Corrosion Behaviour of Carbon Materials and Development of Ceramic Coatings on Graphite Crucibles for Molten Salt Based Applications

By

JAGADEESH SURE

(ENGG02200804028)

Indira Gandhi Centre for Atomic Research,
Kalpakkam

A thesis submitted to the

Board of Studies in Engineering Sciences

In partial fulfillment of requirements
For the Degree of

DOCTOR OF PHILOSOPHY
of
Homi Bhabha National Institute

October, 2013

Homi Bhabha National Institute

Recommendations of the Viva Voce Board

As members of the Viva Voce Board, we certify that we have read the dissertation prepared by **Mr. JAGADEESH SURE** entitled **"Corrosion Behaviour of Carbon Materials and Development of Ceramic Coatings on Graphite Crucibles for Molten Salt Based Applications"** and recommend that it may be accepted as fulfilling the dissertation requirement for the Degree of Doctor of Philosophy.

Date: 10/3/2014

Chairman – **Prof. A.K. Tyagi**

UKamachi Mudali Date: 10/3/14

Supervisor / Convener – **Prof. U. Kamachi Mudali**

M. Kamaraj Date: 10/3/2014

External Examiner- **Prof. M. Kamaraj**

K. Nag Date: 10/3/14.

Member 1 – **Prof. K. Nagarajan**

PKuppusami Date: 10/3/2014

Member 2 – **Prof. P. Kuppusami**

Final approval and acceptance of this thesis is contingent upon the candidate's submission of the final copies of the thesis to HBNI.

I/We hereby certify that I/we have read this thesis prepared under my/our direction and recommend that it may be accepted as fulfilling the thesis requirement

Date: 10/3/14
Place: Kalpakkam

UKamachi Mudali
Prof. U. Kamachi Mudali
(Guide)

STATEMENT BY AUTHOR

This dissertation has been submitted in partial fulfillment of requirements for an advanced degree at Homi Bhabha National Institute (HBNI) and is deposited in the Library to be made available to borrowers under rules of the HBNI.

Brief quotations from this dissertation are allowable without special permission, provided that accurate acknowledgement of source is made. Requests for permission for extended quotation from or reproduction of this manuscript in whole or in part may be granted by the Competent Authority of HBNI when in his or her judgment the proposed use of the material is in the interests of scholarship. In all other instances, however, permission must be obtained from the author.

S. Jagdeesh

(Jagadeesh Sure)

DECLARATION

I, hereby declare that the investigation presented in the thesis entitled "Corrosion Behaviour of Carbon Materials and Development of Ceramic Coatings on Graphite Crucibles for Molten Salt Based Applications" submitted to Homi Bhabha National Institute (HBNI), Mumbai, India for the award of Doctor of Philosophy in Engineering Sciences is the record of work has been carried out by me under the guidance of Prof. U. Kamachi Mudali. The work is original and has not been submitted earlier as a whole or in part for a degree/diploma at this or any other Institution/University.

S. Jagadeesh

(Jagadeesh Sure)

List of Publications

International Journals:

1. **Jagadeesh Sure,** A. Ravi Shankar, S. Ramya, C. Mallika, U. Kamachi Mudali, Corrosion behaviour of carbon materials exposed to molten lithium chloride-potassium chloride salt, **Carbon** **2014**, 67, 643-655.
2. **Jagadeesh Sure**, A. Ravi Shankar, U. Kamachi Mudali, A Nowicki, Baldev Raj, Characterization of pyrolytic graphite exposed to molten LiCl-KCl salt, **Surface Engineering** **2013**, 29, 28-33.
3. **Jagadeesh Sure,** A. Ravi Shankar, B.N. Upadhyay, U. Kamachi Mudali, Microstructural characterization of plasma sprayed Al_2O_3-40 wt.% TiO_2 coatings on high density graphite with different post-treatments, **Surface and Coatings Technology** **2012**, 206, 4741-4749.
4. **Jagadeesh Sure**, A. Ravi Shankar, U. Kamachi Mudali, Surface modification of plasma sprayed Al_2O_3-40wt% TiO_2 coatings by pulsed Nd:YAG laser melting, **Optics and Laser Technology** **2013**, 48, 366–374.
5. **Jagadeesh Sure**, A. Ravi Shankar, S. Ramya and U. Kamachi Mudali, Molten salt corrosion of high density graphite and partially stabilized zirconia coated high density graphite in molten LiCl-KCl salt, **Ceramics International** **2012**, 38, 2803-2812.
6. **Jagadeesh Sure,** S. Ramya, U. Kamachi Mudali, Phase analysis and microstructure correlation of partially stabilized zirconia coatings exposed to molten LiCl-KCl salt, **Journal of Advanced Microscopy Research** **2013**, 8, 150-155.

7. **Jagadeesh Sure**, Ch. Jagadeeswara Rao, P. Venkatesh, C. Mallika, B. Prabhakara Reddy, U. Kamachi Mudali, Evaluation of plasma sprayed alumina-40 wt % titania and partially stabilized zirconia coatings on high density graphite for uranium melting application **Ceramics International** **2014**, 40, 6509-6523.
8. **Jagadeesh Sure**, A. Ravi Shankar, K. Thyagarajan, U. Kamachi Mudali, Molten salt corrosion behaviour of plasma sprayed alumina–40wt% titania coating on high density graphite in molten LiCl-KCl salt, **Materials at High Temperatures** (Revised manuscript under review).
9. **Jagadeesh Sure,** C. Mallika, Ambar Choubey, U. Kamachi Mudali, Corrosion behaviour of laser melted alumina-40 wt % titania coated high density graphite exposed to LiCl-KCl molten salt at 873 K- A microstructural study, **Surface Engineering** (Under review).
10. **Jagadeesh Sure,** A. Ravi Shankar, K. Thyagarajan, C. Mallika, U. Kamachi Mudali, Thermal cycling behaviour of plasma sprayed partially stabilized zirconia coatings on high density graphite substrate, **Journal of Thermal Spray Technology** (Under review).
11. **Jagadeesh Sure,** Ch. Jagadeeswara Rao, C. Mallika, U. Kamachi Mudali, Review on pyrolytic graphite for pyrochemical reprocessing application **Transactions of Indian Institute of Metals** (Manuscript under preparation).

Other related publications:

12. **Jagadeesh Sure,** Maneesha Mishra, M. Tarini, A. Ravi Shankar, N.G. Krishna, P. Kuppusami, C. Mallika, U. Kamachi Mudali, Microstructural characterization and

chemical compatibility of pulsed laser deposited yttria coatings on high density graphite, **Thin Solid Films** **2013**, 544, 218-233.

Chapters in Books

1. **Jagadeesh Sure**, A. Ravi Shankar and U. Kamachi Mudali, Laser surface melting of plasma sprayed alumina-titania coating on high density graphite in: **Functional Materials**, S. Jayakumar, K. Vaideki, R. Balaji (Eds.,) Macmillan Publishers India Ltd, New Delhi, India, 2012, pp. 343-347.

2. **Jagadeesh Sure**, A. Ravi Shankar, S. Ramya and U. Kamachi Mudali, Evaluation of corrosion behaviour of plasma sprayed partially stabilized zirconia coated and uncoated high density graphite in molten LiCl-KCl salt in: **Surface Modification Technologies-XXV**, T.S. Sudarshan, Per Nylén, (Eds.,) VALAR Docs publications, 2012, pp.235-244.

International/National Conferences

1. **Jagadeesh Sure**, A. Ravi Shankar, U. Kamachi Mudali, Corrosion of pyrolytic graphite in molten LiCl-KCl salt, Oral presentation at The National Symposium on Electrochemical Science and Technology NSEST-2010, Indian Institute of Science, Bangaluru, July (2010).
2. **Jagadeesh Sure**, A. Ravi Shankar, U. Kamachi Mudali, Characterization of plasma sprayed alumina-titania coating on high density graphite for pyrochemical reprocessing applications, Poster presentation at 1st International Conference on

Recent Trends in Materials Science and Technology (ICMST), Indian Institute of Space Science and Technology, VSSC, Thiruvananthapuram, Oct **(**2010).

3. **Jagadeesh Sure**, A. Ravi Shankar, S. Ramya and U. Kamachi Mudali, Evaluation of corrosion behaviour of plasma sprayed partially stabilized zirconia coated and uncoated high density graphite in molten LiCl-KCl salt, Oral presentation at 25th International Conference on Surface Modification Technologies (SMT-25), University West, Throllhättan, Sweden, June (2011).
4. **Jagadeesh Sure**, A. Ravi Shankar, S. Ramya, U. Kamachi Mudali, Molten salt corrosion behaviour of partially stabilized zirconia coated high density graphite in LiCl-KCl medium, Oral presentation at 49th National Metallurgists' Day (NMD) and 65th Annual Technical Meeting (ATM), The Indian Institute of Metals, Shameerpet, Hyderabad, Nov (2011).
5. Jagadeesh Sure**,** A. Ravi Shankar, U. Kamachi Mudali, Laser surface melting of plasma sprayed alumina-titania coating on high density graphite, Poster presentation at International Conference on Advanced Materials (ICAM 2011), PSG College of Technology, Coimbatore, Dec (2011).
6. S. Ramya, **Jagadeesh Sure**, A. Ravi Shankar, R.P. George, U. Kamachi Mudali, Laser Raman analysis and imaging of molten salt exposed partially stabilized zirconia coated high density graphite, Poster presentation at Workshop on Electrochemical Techniques for Nano-Scale Surface Engineering, BARC Mumbai, Jan (2012).
7. **Jagadeesh Sure**, A. Ravi Shankar, U. Kamachi Mudali, Degradation of plasma sprayed alumina-40wt%titania coating on high density graphite in molten LiCl-KCl

salt, Poster presentation at International Workshop on Advanced Ceramics for the Future (ACF-2012), Indian Institute of Technology-Madras, Chennai, Jan (2012).

8. **Jagadeesh Sure**, A. Ravi Shankar, S. Ramya, C. Mallika, U. Kamachi Mudali, Corrosion behaviour of carbon allotropes exposed to molten LiCl-KCl salt, Oral presentation at National Conference on Carbon Materials 2012 (CCM12), Bhabha Atomic Research Centre, Mumbai, Nov (2012).
9. **Jagadeesh Sure**, C. Mallika, U. Kamachi Mudali, Corrosion behaviour of carbon materials and development of ceramic coatings on high density graphite for molten salt application, Poster presentation at The International Corrosion Prevention Symposium for Research Scholars (CORSYM-2013), GRT Grand, Chennai, Feb-Mar (2013).
10. **Jagadeesh Sure,** Jagadeeswara Rao, P. Venkatesh, B. Prabhakara Reddy, C. Mallika, U. Kamachi Mudali, Evaluation of ceramic coatings on high density graphite for uranium melting application, Presentation at International Conference on Surface Engineering - Interfinish SERIA 2013, Chennai, Aug (2013).
11. **Jagadeesh Sure**, M. Mishra, M. Tarini, A. Ravi Shankar, N.G. Krishna, P. Kuppusami, C. Mallika, U. Kamachi Mudali, Microstructural characterization and chemical compatibility of pulsed laser deposited yttria coatings on high density graphite, The Sixth International Conference on Technological Advances of Thin Films and Surface Coatings (THINFILMS-2012), July 14-17th, 2012, Singapore Management University(SMU) at Stamford Road, Singapore.

Reports:

1. Pyrolytic Graphite-Potential Candidate Material for Pyrochemical Reprocessing Applications, **IGC Annual Report-2010**, Article No: IV.13, pp.123-124.
2. Ravi Shankar, Ravikumar Sole, **Jagadeesh Sure**, U. Kamachi Mudali, Application of laser processing of materials for high temperature molten chloride environment, **KIRAN 2011**, 22, 33-37.
3. Corrosion behaviour of container and electrode materials for pyrochemical reprocessing exposed to molten LiCl-KCl salt, **IGC Annual Report-2012**, Article No: IV.13, pp.101-102.
4. **Young Researcher's Forum Article:** Corrosion behaviour of carbon materials and ceramic coatings for pyrochemical reprocessing, **IGC News Letter 2013**, 96, 15-19.

Awards and Recognitions

- **Best Poster Presentation Award:**

  Jagadeesh Sure, A. Ravi Shankar, U. Kamachi Mudali, Laser surface melting of plasma sprayed alumina-titania coating on high density graphite in: International Conference on Advanced Materials (ICAM-2011), PSG College of Technology, Coimbatore, Dec (2011).

- **Best Poster Presentation Award:**

  S. Ramya, **Jagadeesh Sure**, A. Ravi Shankar, R.P. George, U. Kamachi Mudali, Laser Raman analysis and imaging of molten salt exposed partially stabilized zirconia coated high density graphite in: Workshop on Electrochemical Techniques for Nano-Scale Surface Engineering, BARC Mumbai, Jan (2012).

- **Best Poster Presentation Award:**

Jagadeesh Sure, C. Mallika, U. Kamachi Mudali, Corrosion behaviour of carbon materials and development of ceramic coatings on high density graphite for molten salt application, International Corrosion Prevention Symposium for Research Scholars (CORSYM-2013), Hotel GRT Grand, Chennai, Feb-Mar (2013).

- **Swarna Jayanti Endowement Fellowship (Young Scientists Category)** from the Indian Institute of Metals (IIM) for attending "The 6th International Conference on Technological Advances of Thin Films and Surface Coatings (THINFILMS-2012)", Singapore, July (2012).
- Travel fellowship from **CICS, Chennai** and **HBNI, Mumbai** (July, 2012).

S. Jagadeesh

(Jagadeesh Sure)

Dedicated to

My Family Members

ACKNOWLEDGEMENT

The thesis work was carried out under the guidance of Prof. U. Kamachi Mudali, Associate Director, Corrosion Science and Technology Group (CSTG), Indira Gandhi Centre for Atomic Research (IGCAR). I sincerely thank him for his outstanding guidance, excellent support and motivation. He taught me with extraordinary patience which gave me immense confidence to initiate my research work. I have benefitted extremely by his teaching in HBNI course work on the fundamentals of corrosion and structural materials for nuclear reprocessing plants. He also trained me to write a scientific article. It is a great privilege for me to work with him. Thanks are due to his constant inspiration, legacy towards learning, and keen interest in the subject. I am deeply obliged to his constructive suggestions, meticulous planning, and effective analytic approach.

I thank Dr. Baldev Raj, former Director, IGCAR, for his support, encouragement and affection to the research scholars which provided us a homely feeling in this institute for pursuing Ph.D. I acknowledge with thanks Shri. S.C. Chetal, former Director, IGCAR and Dr. P.R. Vasudeva Rao, Director, IGCAR for their trust and support on me. Dr. T. Jayakumar, Dean, HBNI-IGCAR Campus and Director, Metallurgy & Materials Group (MMG) for giving support in my research work.

I express my sincere thanks to my doctoral committee members Prof. A.K. Tyagi (Chairman), Prof. K. Nagarajan (Member) and Prof. P. Kuppusami (Member) for their precious suggestions and constant support. I would take this opportunity to thank Dr. M. Sai Baba, Associate Director, Resources Management Group and Convener, Engineering Sciences Standing Committee for providing a pleasant accommodation and encouragement.

I register my sincere thanks to Dr. C. Mallika, Head, ACSCS, CSTG, IGCAR for her valuable suggestions, comments, guidance and support in various aspects constantly with affection. She spent extensive time on my research work while preparing the thesis and manuscripts for journals. I cannot forget her extensive support to my research work with valuable guidance and motivation continuously.

I thank Mr. A. Ravi Shankar for his technical support and guidance during the research work. My very-special thanks to Dr. Ch. Jagadeeswara Rao, for his support during experiments and while thesis writing time with his valuable suggestions.

I am heartfull thanks to Dr. S. Ramya, Shri. K. Thayagarajan Dr. B. Prabhakara Reddy, Shri. P. Venkatesh, Smt. S. Kalavathy,Smt. M. Radhika, Dr. M. Kamarudhin, Mr. P. Shyamala Rao, Dr. S. Ningshen of IGCAR and Shri Rakesh Kaul, Dr. B.N. Upadhyay, Shri Ambar Choubey and Shri P.T Rao of Raja Ramanna Centre for Advanced Technology, Indore for the informative discussions, help and support during my research work. I thank to Prof. Ramesh Chandra of IIT Roorkee for his support during characterization of samples.

I am especially grateful to Dr. Rani P. George for her help in various aspects during my Ph.D tenure and motivation. Special Thanks to Mr. Pradeep Kumar Samantroy, Mr. Arunchandran Chenan, Dr. J. Jayaraj and Dr. Srinivasan Swaminathan and Miss. K. Indira, Miss. Ruth Nithila, Miss. Rasmi and Mrs. Ezhil Vizhi for the their full support and co-operation and help throughout my Ph.D. I would like to specially thank my beloved seniors Dr. N. Padhy and Dr. (Smt.) B. Lipika for their suggestions in research work and help in various aspects.

Also, my acknowledgement is due to for their help and support in various ways Dr. N. Parvathavarthini, Dr. M.G. Pujar, Dr. R. Priya, Dr. Vanitha Kumari, Mr. Nanda Gopala Krishna, Shri. T. Nanda Kumar, Sri. R. Rajendran, Mr. R. Selvam, Mr. Yogesh Kumar, Mr. Avinash Kumar, Mr. Vinod Kumar, Mrs. Namrata, Ms. M. Archana, Smt. Anita Toppo, Smt. N. Sivai Bharasi, Smt. A. Poonguzhali, Smt. Girija Suresh, Sri. T. V. Balaji, Shri. Ravikumar Sole, Mr. Thinakaran, Mrs. M. Jayalakshmi, Shri. P.U. Jalendiran, Mr. R. Sathish and also I would like to extend my thanks to the whole staff of CSTG.

I take this opportunity to thank Mr. Suddhasattwa Ghosh, Dr. Paneerselvam and Mr. Ganapathi, all staff of Pyrochemical studies section in RCL, IGCAR and Dr. Akash Singh PMG, IGCAR.

My very-special thanks to my batchments and friends, D. Srimaha Vishnu, P. Ilayaraja, D. Sharath, Dr. Jammu Ravi, K. Lakshmoji, N. Mariyappa, K. Siva Srinivas, Naveen, M. Bubathi, Kumbar Vijaya Shamrao, Sudhanshu Pati, L. Herojit, Dr. Maneesha Misra, P.

Priyada, Pravati Swain, Debasmita Dash, Shashwat Kumar Swain and other fellow research scholars of IGCAR for their help, support and enjoyable company. Additional thanks to Kunuku. Srinivas, Dr. Haribabu Sata, P. Avinash and Saddu Venkatesh for their support and help in many ways.

Finally, I like to express my heartfelt gratitude to my parents, Shri. Sure Vishnu and Smt. Subbamma, Shri. Sure Durga Madhar and Smt. Sure Siva Nagamani, brother-in law Mr. B. Madhu Babu, Sister Smt. B. Josthana (Hemalatha) and my “Sure” family members and other relatives for their endless love, affection, support, and encouragement. Very special thanks to my Uncle Shri. Gangadhara Ramesh, for his support during my studies and my sister-in-law Smt. Ch. Sukanya constant encouragement for my studies. I would like to thank P. Leela Purnima for her kind information and suggestion about the IGCAR and my friends A. Mallikarjuna, K. Naga Jagadeesh, V. Bharath Kumar, Ramana Chandaka and Kasi Naidu for their constant support to me in the all the ways.

Above all, I thank the Almighty, without whose wish and blessing, this project would never have seen its successful accomplishment. He is the one who knows all the hardships, all my hard works and he is the one, whose satisfaction and acceptance I seek the most.

S. Jagdeesh

(Jagadeesh Sure)

Date: 10-03-14

Place: Kalpakkam

CONTENTS

Introduction to Pyrochemical Processing and Material's Challenges

A Review on the Materials and Coatings for Molten Salt and Uranium Applications

CHAPTER 3 67

Materials, Methods and Characterization Techniques

CHAPTER-5 135

Plasma Sprayed Alumina-40 wt% Titania Coating (A40T) on High Density Graphite

Plasma Sprayed Partially Stabilized Zirconia Coating (PSZ) on High Density Graphite

CHAPTER 7 243

Conclusions, Summary and Scope for Future Work

ABSTRACT

To establish pyrochemical reprocessing plants for reprocessing of spent metallic fuels of Fast Breeder Reactors with various unit operations it is necessary to identify, develop and qualify reliable corrosion resistant materials and coatings for service in molten LiCl-KCl salt and molten uranium environment operating between 773 to 1573 K. Carbon based materials are proposed as candidate materials for salt purification and cathode processor crucibles, vessels and liners in pyrochemical reprocessing involving molten LiCl-KCl salt medium and molten uranium. The present thesis work is focused on evaluation of materials and coatings for salt purification system crucible where molten LiCl-KCl salt will be handled and for the cathode processor crucible where the combined environment of 20 wt% molten salt, cadmium and molten uranium is present. To meet the requirement of pyrochemical reprocessing unit operations, the evaluation and performance of materials and coatings were studies in molten LiCl-KCl salt at 873 K for 2000h as well as in molten uranium at 1623 K. The corrosion behaviour of the carbon materials viz. low density graphite (LDG), high density graphite (HDG), glassy carbon (GC) and pyrolytic graphite (PyG) was investigated in molten LiCl-KCl electrolyte salt medium at 873 K for 2000 h under ultra high pure (UHP) argon atmosphere for selecting the material for salt purification crucible application. Morphological changes in the carbon materials exposed to molten LiCl-KCl salt revealed severe corrosion attack on LDG and HDG and the attack on GC was insignificant due to non-penetration of salt into GC. Removal of carbon particles and surface degradation were not found in PyG exposed to molten LiCl-KCl and these are observed in LDG and HDG. The corrosion

resistance of carbon materials in molten LiCl-KCl salt at 873 K was observed to follow the order: LDG < HDG < GC < PyG.

Owing to its availability and economic viability, HDG is considered as one of the structural materials for salt purification system and as cathode processer crucible. The performance of HDG in molten LiCl-KCl salt clearly indicated that ceramic coatings are desirable on HDG components (crucibles) in order to protect them from corrosion attack by salt and molten uranium and to extend their service life and mechanical integrity at high operating temperatures. Hence, ceramic coatings of partially stabilized zirconia (PSZ) with NiCrAlY bond coat and top alumina-40 wt% titania (A40T) with bond coat of Cr_3C_2-NiCr and without bond coat were developed on HDG substrates by plasma spray process and these were evaluated for deploying these coated materials for crucible, liners and vessels applications in pyrochemical reprocessing. The ceramic coated HDG samples were exposed to molten LiCl-KCl salt for 2000 h at 873 K under UHP argon atmosphere and compatibility test with molten uranium at 1623 K for 20 min under UHP argon atmosphere. The unit operations of salt purification and cathode processor are batch processes in pyrochemical reprocessing. Hence, the durability of coatings developed on HDG substrate need to be evaluated. For this purpose, ceramic coated HDG samples were subjected to thermal cycling to understand the durability of the coatings. The molten salt tested carbon materials and ceramic coated HDG (as-coated and tested) samples were characterized by Scanning electron microscopy (SEM), Energy dispersive X-ray spectroscopy (EDX), Atomic force microscopy (AFM), X-ray diffraction (XRD) and Laser Raman spectroscopy (LRS).

The A40T coating developed cracks and salt deposits were found after exposure to molten salt for 500 h and spallation of A40T coating occurred from HDG substrates after

2000 h of exposure with Cr_3C_2-NiCr bond coated as well as without bond coat. To improve the performance of A40T coating in molten salt, post treatments (annealing and laser melting) were performed. It is evident from the results that denser and compact microstructure can be obtained by pulsed laser melting as compared to vacuum annealing of coatings. Laser melted A40T coatings were exposed to molten salt showed that the laser melted coatings exhibited better corrosion resistance owing to their fully dense top layer. The PSZ coated HDG exhibited excellent corrosion resistance in molten LiCl–KCl salt due to good adherence of the coating to the substrate even after 2000 h of exposure and no change in the morphology as well as in the phases of the PSZ coating was observed.

For selecting a coating for cathode processor crucible, the studies were carried out for testing the PSZ coated samples with molten uranium at 1623 K. A40T coating exhibited poor adhesion on graphite surface and spallation of coating was observed after compatibility test with molten uranium in addition to the adherence of uranium metal on the coating surface. The compatibility of molten uranium with PSZ coatings studies showed that PSZ coating protect the HDG, since the reaction products/layer observed on the surface of the coating was insignificant. A40T coated HDG with Cr_3C_2-NiCr and without bond coat samples were subjected to thermal cycling studies at 873 K exhibited complete coating spallation after 60 and 80 cycles respectively. The failure of A40T coating is due to the poor adhesion strength of the coating to the HDG substrates in both the cases. PSZ coated HDG subjected to thermal cycling studies at 873 and 1023 K showed that PSZ coating did not exhibit any failure of the coating even after 200 cycles and only network of cracks generated in the microstructures still resolved with stable tetragonal phase of the PSZ. The results of the studies reported in this thesis upheld the choice of HDG crucibles and PSZ coating on them for corrosion protection

in molten chloride salt medium and molten uranium based on the performance in both the environments. Finally, PSZ coating was developed on engineering scale facility HDG crucibles for future studies at 1623 K to evaluate the combined (molten salt and molten uranium) environment effect on the coated crucibles.

LIST OF FIGURES

LIST OF TABLES

LIST OF ABBREVIATIONS

PHWR: Pressurized Heavy Water Reactor
FBR: Fast Breeder Reactor
FBTR: Fast Breeder Test Reactor
PFBR: Prototype Fast Breeder Reactor
MFTR: Metallic Fuel Test Reactor
IFR: Integral Fast Reactor
PUREX : Plutonium URanium EXtraction
ANL: Argonne National Laboratory
RIAR: Research Institute of Atomic Reactors
MA: Minor Actinides
FP: fission products
MWF: Metal Waste Form
CWF: Ceramic Waste Form
MSTL: Molten Salt Transfer Line
SLZ: Salt-Loaded Zeolite
DOE: Department of Energy
CRIEPI: Central Research Institute of Electric Power Industry
JAERI: Japan Atomic Energy Research Institute
KAERI: Korea Atomic Energy Research Institute
EBR-II: Experimental Breeder Reactor-II
GC: Glassy Carbon
PyG: Pyrolytic graphite
CVD: Chemical Vapour Deposition
FFC: Fray-Farthing-Chen
MSR: Molten Salt Reactor
MSBR: Molten Salt Breeder Reactors
PyC: Pyrolytic carbon
ADTT: Accelerator Driven Transmutation Technology

AISI: American Institute of Steel Industries

SS: Stainless Steel

A40T: Al_2O_3-40 wt% TiO_2

YSZ: Yttria Stabilized Zirconia

PSZ: Partially stabilized zirconia

PLD: Pulsed Laser Deposition

LDG: Low Density Graphite

HDG or HD graphite: High Density Graphite

APS: Air Plasma Spray or Atmospheric Plasma Spray

RRCAT: Raja Ramanna Centre for Advanced Technology

ASTM: American Society for Testing Materials

MOSTA: Molten Salt Test Assembly

UHP: Ultra High Pure

SEM: Scanning Electron Microscopy

EDX: Energy-Dispersive X-ray spectroscopy

AFM: Atomic Force Microscopy

XRD: X-ray Diffraction

JCPDS: Joint Committee on Powder Diffraction Standards

LRS: Laser Raman Spectroscopy

BSEI: Back Scattered Electron Image

SEI: Secondary Electron Image

LM-1: Laser melted coatings with power density of 640 kW/cm^2

LM-2: Laser melted coatings with power density of 800 kW/cm^2

CHAPTER 1

INTRODUCTION TO PYROCHEMICAL PROCESSING AND MATERIAL'S CHALLENGES

This Chapter introduces the Fast Breeder Reactor programme in India, towards meeting the energy demand in the country. The advantage of closed metallic fuel cycle for future energy security is emphasized. The complete overview on molten salt based pyrochemical reprocessing of the spent metallic fuels is discussed in detail. Various processing steps and the challenges involved in the development of materials for pyro-reprocessing are briefly explained. The main focus of this Chapter is on the materials and identifying protective coatings, issues and their implementation for successful pyrochemical reprocessing in the plant.

1.1 Fast Breeder Reactor Programme in India

Generation of power from nuclear reactors gains importance in India to meet huge demand of power required in the coming decades [1]. India's nuclear power programme emphasizes on closed fuel cycle, in which the spent fuel from natural uranium fuelled Pressurized Heavy Water Reactors (PHWRs) of first stage is reprocessed to obtain the plutonium produced in the reactor. Breeding of the retrieved plutonium from first stage by utilizing it in Fast Breeder Reactors (FBRs) is in the second stage, Thorium based reactors can be setup to convert the vast resource of thorium available in the beach sands of Kerala to ^{233}U sustaining the nuclear reactor programme for a long time in the third stage, and finally use of ^{233}U (fissile element) for future plants [2]. Thorium in association with other heavy elements is present in large quantities in the mineral, monazite in India [3]. Nuclear power does not generate greenhouse gases such as carbon dioxide gas, so it is considered to be one of the promising solutions for the global warming issue [4]. Currently the generation of nuclear power in India is about 3 %, and this it needs to be increased to 25 % by 2050 [5]. Energy security and its sustainability can be achieved through the introduction of fast reactors in phased manner and closing the fuel cycle [5,6]. The successful commissioning and operation of the Fast Breeder Test Reactor (FBTR) loaded with mixed (U,Pu)C fuel of the unique composition 70 % Pu and 30 % U and the reprocessing of the carbide fuels with a burn up of 155 GWd/ton by aqueous route are the major breakthroughs towards achieving this goal at Indira Gandhi Centre for Atomic Research, Kalpakkam in the last 30 years [1]. Extensive research and development in the domain of materials and manufacturing technologies are demanded towards the development of FBRs and their associated fuel cycle technologies [2]. The success of FBR programme depends on the continuous operation of reactor system, reprocessing of the spent fuel waste management facilities to ensure economy and also to achieve sustained fissile material's production for several FBRs planned in future [1]. Based on the rich research experience on sodium cooled FBTR, the construction of a 500 MWe commercial Prototype Fast Breeder Reactor (PFBR) using mixed (U,Pu) oxide fuel is near completion at Kalpakkam [1,3]. A large scale deployment of FBRs towards ensuring future energy security for the country is planned through closed metallic fuel cycled reactors with emphasis on breeding gain and reducing the doubling time of the fuel [3]. It is proposed to construct a metallic fuel fast breeder reactor (MFBR) to evaluate the performance of U-Pu-Zr fuel and reprocessing the spent fuel to gain experience. The developments of metallic fuel and design aspects for MFBR are under way. Beyond 2025, a series of metallic fuelled reactors of

1000 MWe capacity with higher breeding potential are envisaged [1,3,7]. Construction of new reactors for energy production in the country depends on the availability of fuel. Hence, reprocessing of spent fuel, refabrication of fresh fuel and management of radioactive waste for safe disposal are the three major areas of activities to be addressed in order to achieve success in the establishing reactors as well as expanding the nuclear power programme in India.

1.2 Metallic fuel Fast Breeder Reactors for future energy security

Metallic fuel appears to be the most suitable candidate for the FBRs with integral concept, and U-Pu-Zr system is chosen as the metallic fuel which has been under development since late 1960s because of its promising superior performance [8]. Excellent neutron economy and high bumup capability had drawn attention for metallic fuel prior to 1983, and additional features of metallic fuel realized during the formulation of the Integral Fast Reactor (IFR) concept made metallic fuels all the more attractive [9]. The IFR is a design for a nuclear reactor using fast neutrons and without neutron moderator. The advantages of using metallic fuel systems are [9]:

1. Fabrication of metallic fuels is simple and compact
2. Metallic fuel has excellent steady-state and off-normal performance characteristics
3. Metallic fuel has better cladding breach performance characteristics
4. Metallic fuels have higher breeding potential due to superior neutron economy with a hardened spectrum
5. The breeding ratio and burn up for metallic fuels are much higher than oxide or carbide fuels.

6. Because of high neutron economy, the reactivity swing over the operating cycle is minimized and increased cycle length.
7. Compact and simple pyroprocessing of metallic fuel promises dramatic improvement in fuel cycle economics.

In the IFR concept as shown in Fig. 1.1 the reactor and reprocessing plant for metallic fuel will be co-located. The four important features of IFR fuel cycle (Fig.1.1) are: (1) Liquid sodium cooling, (2) Pool type reactor configuration, (3) Metallic fuel and (4) An integral fuel cycle, based on pyrochemical reprocessing and injection casting of fuel fabrication [9].

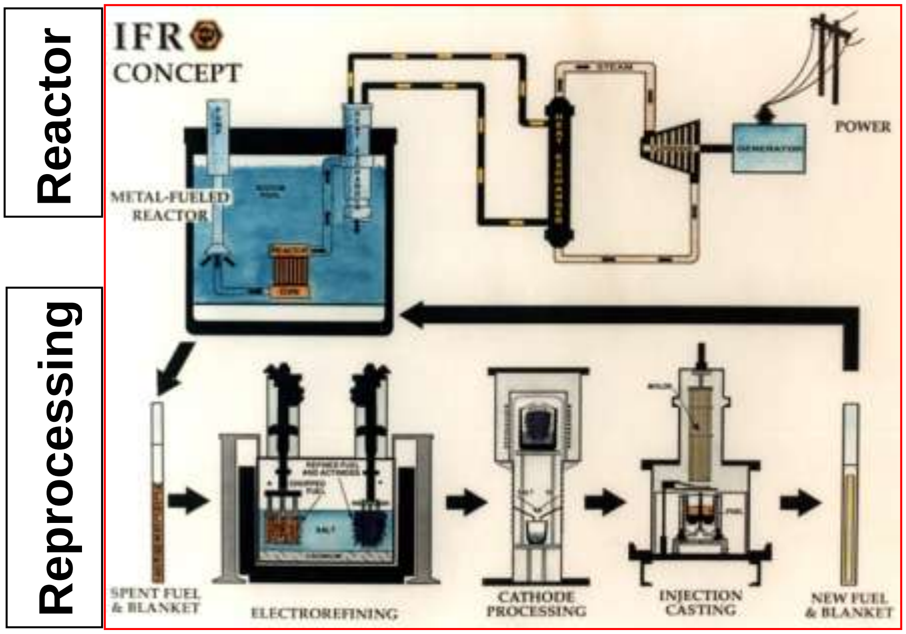

Fig. 1.1 Fuel cycle facility and IFR concept [10].

Fuels based on U-Pu-Zr alloy will be introduced in the future Indian FBRs [11]. Reprocessing of short cooled spent metallic fuels to separate the fuel elements from the fission products is through pyrochemical route involving co-located facilities for reprocessing and refabrication [7,9,12].

1.3 Overview on pyrochemical reprocessing

Countries like USA follow the once-through (also called open) fuel cycle, which does not include reprocessing of spent nuclear fuel. Closing of the fuel cycle is an important part of the strategy to ensure the growth of nuclear energy production at the desired pace [6]. Reprocessing of spent nuclear fuel [6,13] refers to a separation process with the fractionation of useful radionuclides for the fabrication of fresh fuel, and safe waste management. Two types of processes available for the reprocessing of spent nuclear fuel are aqueous reprocessing and pyrochemical reprocessing. In aqueous reprocessing, combination of solvent extraction and ion exchange separation techniques are employed. The spent fuel mechanically or chemically detached from the clad material and dissolved in nitric acid is subjected to solvent extraction for the removal of fission products in the first stage and uranium and plutonium in the later stages. The process is called as Plutonium-URanium EXtraction (PUREX). The PUREX process is well developed and has been used to treat spent nuclear fuels and irradiated uranium for over 40 years [14]. The fission products and other actinides are separated and immobilized with various stabilization matrices like borosilicate glass or pyrochlore based ceramic system and finally disposed. PUREX process is a well suited reprocessing technique for the reprocessing of thermal and fast breeder reactor (oxide/carbide) fuels.

Next generation nuclear fuel cycles require innovative features such as an environmental load reduction, safety, efficient recycle of resources, nuclear proliferation resistance and economics, etc., Considering these points, pyrometallurgical processing of spent fuel has emanated as one of the most promising options for future nuclear systems and closed nuclear fuel technologies [15,16]. The pyrochemical reprocessing is mainly applicable for the reprocessing of mixed oxide [17] and metallic [16] fuels discharged from the fast reactors by using electrochemical techniques. Pyroprocessing or molten salt electrochemical processing has been in use for many years for purification of materials, including plutonium [18]. The Argonne National Laboratory (ANL) in USA first established the technique of pyroprocess for the reprocessing of spent metallic fuels [11,14,19] and this pyrometallurgical route for fuel recycling process is further developed in other countries as well. In early 1980s, the studies on the electro-deposition of uranium at solid cathodes were conducted at ANL towards the development of reprocessing method for IFR metal fuel [20]. The high temperature molten salt based electrochemical process developed by Research Institute of Atomic Reactors (RIAR) Russia on the other hand is suitable only for reprocessing oxide fuels irradiated in fast reactors [17,21]. Pyrochemical reprocessing method offers a number of advantages over the conventional PUREX process employed for the reprocessing of fuels through aqueous medium [6,7,22]. These include:

- The ability to process spent fuels after shorter cooling periods,
- Less criticality problems,
- Low process volumes resulting in compact plant enabling co-location of the reprocessing plant with the reactor,
- Facilitates significant improvement in waste management (less volume of waste in solid form) and destroying toxic waste such as the long-life fission products in spent nuclear fuels.
- Drastically reduces the amount of fuel to be treated in the latter steps, and consequently reduces the fuel cycle cost [15].

The process flowsheet of pyrochemical reprocessing adopted for the processing of spent metallic fuels in India is shown in Fig. 1.2, which involves the following major operations [23]: (i) Dismantling of the fuel pins and shearing of the cladded fuel pins with a pin chopper, (ii) Electrochemical removal of all actinides from the steel cladded fuel element pieces in an electrorefiner, (iii) Distillation of the entrained salt/ cadmium from the electrodeposit and consolidation of the electrodeposited actinides in a cathode processor and (iv) Casting of the actinide product from the cathode processor into an ingot in a casting furnace. Electrorefining and cathode processing are the key steps of the pyroprocess flow sheet. The unit operations of pyrochemical reprocessing based on electrorefining using molten LiCl-KCl eutectic salt as the electrolyte involve the handling of uranium, plutonium, cadmium, minor actinides (MA) and fission products (FP) etc., in metallic form, cadmium, etc. at temperatures ranging from 773 to 1573 K under ultra high pure argon environment [7,11,14]. Electrorefining involves the dissolution of a metal into the molten salt electrolyte and subsequent reduction at a cathode to yield a more (highly) purified form of the metal [12]. During the electrorefining process, the alkali, alkaline earth and rare earth fission products accumulate in the electrolyte and after refining a few batches of the spent fuel, the salt must be treated to remove the fission products [14,23]. The salt purification is carried out by passing the contaminated molten salt through a zeolite column. Prior to this treatment, the actinides present in the salt to an extent of ~ 6 wt % must be recovered in the 'Actinide Drawdown process step' and recycled [23]. The zeolite containing the fission products from the salt purification step is treated with borosilicate glass to make ceramic waste form (CWF) [14,23]. The materials left out in the anode during the electrorefining process such as noble metals and clad constituents are melted with 15 wt% Zr to form a durable metal waste form (MWF) [14,23]. The consolidated radioactive solid waste generated by the above mentioned operations are packed in canisters for safe geological disposal. As pyrochemical reprocessing is a batch-mode process there is flexibility to operate the processing steps in batches [12]. In addition to the above mentioned operations, purification of the LiCl-KCl salt to be used as the electrolyte in the electrorefiner is also one of the important steps. However, this Chapter highlights only on the objectives of the present thesis work and gives a brief description on those processing steps, which are of relevance to the thesis.

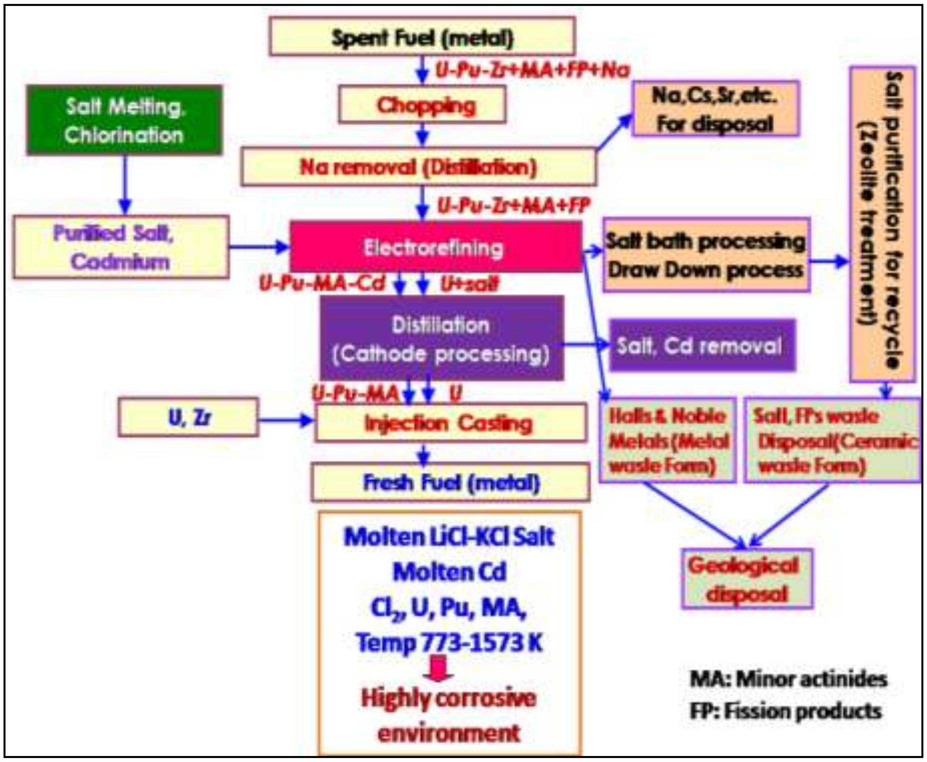

Fig. 1.2 Schematic of the pyrochemical reprocessing of spent metallic fuel [23].

1.3.1 Salt purification system

The LiCl-KCl eutectic salt has been chosen as the electrolyte for electrorefining based on its low melting temperature of 623 K [12]. However, the salt has to be purified from moisture and oxygen impurities before loading into the electrorefiner. For this purpose, anhydrous 44.48 wt % LiCl and 5.552 wt % KCl salts are dried, melted under a flowing stream of chlorine gas and then solidified. The schematic diagram of the salt purification system is shown in Fig. 1.3. The salt purification system consists of three main parts: (i) purification vessel, (ii) a receiving vessel and (iii) a molten salt transfer line (MSTL) [24]. Purification of the chloride salts is carried out in the purification vessel. The vessel consists of a graphite based crucible and lid, liner, outer vessel and a cover plate of the outer vessel. The outer vessel acts as a part of the leak tight boundary of the purification system. The resistance furnace heats this outer vessel to provide the necessary process heat. It is closed at the top by a cover plate and it houses the graphite crucible.

The outer vessel has a graphite liner on its inner surface and bottom, to protect it from corrosion attack by chlorine gas. Sufficient gap has been provided between the crucible and the liner, as the crucible has to be frequently lifted and lowered. The melting of salt for purification is carried out in this graphite crucible, which has a graphite lid (cover). Receiving vessel is used for making the salt moulds out of the molten salt transferred to it from the purification vessel. The MSTL transfers the purified salt from the purification vessel to the receiving vessel by creating vacuum on the receiving vessel made of Cr-Mo steel using a vacuum pump. Selection of ferritic steel is based on the fact that (a) it will not see any chlorine gas and (b) it will be used as the crucible in the electrorefiner, after the solidification of the purified salt. In the receiving vessel the salt is allowed to solidify for some time and then the vessel is removed along with the salt (in the form of mould).

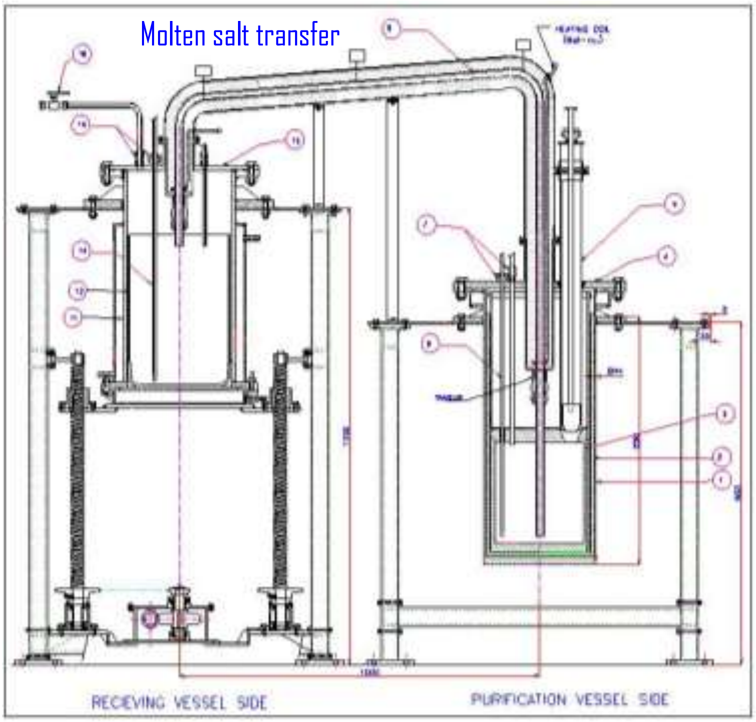

Fig. 1.3 Schematic of salt purification system [24].

The salt purification system should be compatible with the chloride salts heated and melted at about 773 K in the presence of air, moisture and chlorine, without undergoing corrosion or degradation. The purification vessel was observed to undergo high corrosion due to the presence of molten salt under chlorine atmosphere [24]. Thus, identifying materials, with high corrosion resistance to molten chloride salts at high temperatures (about 773 K) for equipment and accessories of salt purification vessel is a challenge. For this purpose, it is essential to identify one or more acceptable materials for the selected medium based on literature research and prior experience, together with a few validation tests. The corrosion rates and mechanisms will then be established with greater precision [17]. Since metallic materials undergo accelerated corrosion under these severe corrosive environment at high temperature, the vessels and crucibles need to be fabricated with corrosion resistant non-metallic materials or with ceramic material/coating. Based on the requirement the materials listed in Table 1.1 have been proposed for the fabrication of the important components in the salt purification system.

Table 1.1 Materials proposed for the different components of salt purification system [24].

Description	Proposed material	Environment
Outer vessel	Inconel-600 with inner ceramic coating or 316 L SS with ceramic coating	Exposed to 973 K
Liner	Non-metallic/ ceramic / graphite material	Chlorine gas
Purification vessel (crucible) and lid (cover)	Non-metallic/ ceramic /graphite material	Molten salt, Chlorine gas
Receiving crucible	9 Cr-1 Mo steel	Purified salt

1.3.2 Electrorefining

In the electrorefining process, an impure metal/alloy is made as anode, from which selected constituents are electrotransported through a salt medium for deposition over a cathode system [12]. The electrorefining step is the heart of the pyrochemical process for separating U, Pu, MA and fission products from spent metallic fuel which acts as an anode [14]. The process is carried out using molten LiCl-KCl as the electrolyte and liquid cadmium layer at the bottom with the operating temperature as 773 K under ultra high purity argon atmosphere as shown in Fig 1.4. The irradiated fuel rods are sent to a chopper, where they are cut into short lengths. The chopped fuel rod segments loaded into perforated steel baskets are placed in the electrorefiner which becomes the anode [12]. Uranium and U-Pu mixture are electrotransported to a solid cathode made of ferritic steel and liquid cadmium cathode respectively.

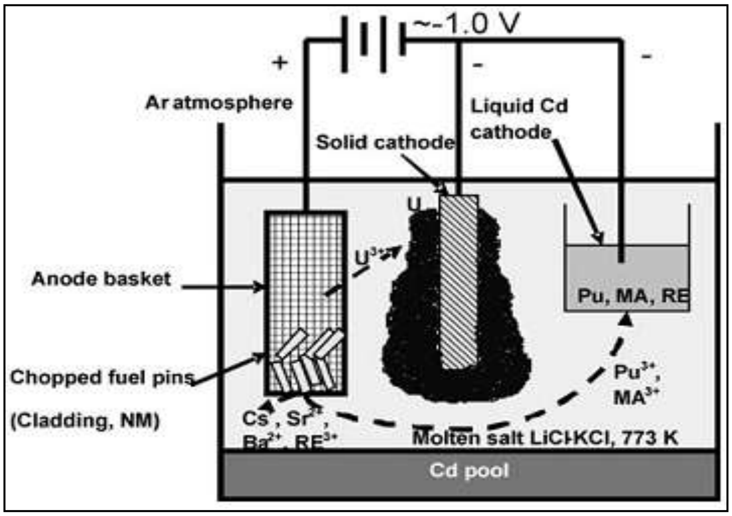

Fig. 1.4 Schematic of electrorefining process [23].

Nickel bearing container materials are not desirable for the electrorefiner, as liquid cadmium is used both as the cathode and as a bottom layer in the electrorefiner to capture the loose deposits of uranium metal that would be falling off from the solid cathode. The molten cadmium present in the bottom of the electrorefiner protects the steel container as $CdCl_2$ is more stable than $FeCl_2$. It is reported that molten cadmium reacts with nickel and therefore the container material should be made with nickel-free material [25,26]. The process depends on the thermodynamic stabilities of the chlorides of U, Pu and fission products. The thermodynamically highly stable chlorides of the fission products such as cesium, strontium, lanthnides etc., will accumulate in the electrolyte salt and the fission products whose chlorides are of very low stability are left out in the anode along with the cladding hulls. The molten chloride salt has to be purified after electrorefining a few batches of the fuel due to accumulation of fission products and then recycled [23]. Thus, the spent fuel is separated into three components; metallic uranium, a MWF the anode, and a highly radioactive salt mixture that subsequently can be converted to a CWF [14]. The proposed materials for electrorefiner are listed in Table 1.2. The material that collects at the cathodes will be processed subsequently in the cathode processing step [14].

Table 1.2 Materials proposed for electrorefiner [24].

Description	**Proposed candidate materials**	**Environment**
Outer vessel	Inconel-600 or SS 310	Inner side exposed to argon gas and outer side heated to 823-973 K
Main vessel	9 Cr-1Mo steel	Argon gas at 923 K, process crucible will be kept in this vessel
Process vessel	9 Cr-1Mo steel	Holds molten salt and molten cadmium and used as a cell for electrorefiner
Top cover	9 Cr-1Mo steel	Exposed to argon gas at 523 K
Anode basket	9 Cr-1Mo steel	Molten salt and molten cadmium
Solid cathode	9 Cr-1Mo steel	Molten salt
Liquid cathode crucible	9 Cr-1Mo with ceramic coating	Liquid cadmium and molten salt

1.3.3 Cathode processor system

In the cathode processor, the cathode from electrorefining operation consisting of uranium deposit, residual salt and cadmium is proposed at high temperatures under vacuum to distill the salt and cadmium first and followed by melting of uranium [12]. Distillation is essential for the removal of entrapped salt along with uranium deposit on the solid cathode and cadmium from the U, Pu and MA deposited in liquid cadmium cathode. The purpose of the cathode processor is twofold: (i) to remove the entrained salt ≈ 20 wt % (and any cadmium) from the uranium electrodeposits by evaporation and (ii) to consolidate the dendritic actinide deposit by melting [14]. The cathode processing operation involves [14]: (i) the cathode deposit with entrapped salt/cadmium is first loaded into a crucible. (ii) The crucible is heated to a temperature of 973 K under pressure of 30 torr to first distill the cadmium from the crucible. (iii) After distillation of cadmium the temperature increased to 1223 K under pressure of 10 torr to removal of salt from the cathode deposit. (iv) The crucible is further heated to a temperature of 1273-1643 K under 600 torr to melt the actinides and consolidate the heavy metal; the crucible and charge are then cooled to form a heavy metal ingot in the crucible mould. The schematic of operation of these processes steps are shown in the Fig.1.5 [27]. After the process crucible has been held at 1473-1573 K for one-half hour, the current to the induction coils is discontinued, and the cathode processor is allowed to cool under vacuum to ambient temperature. (v) Removing the uranium ingots from the crucible for further processing for making fresh fuel by casting.

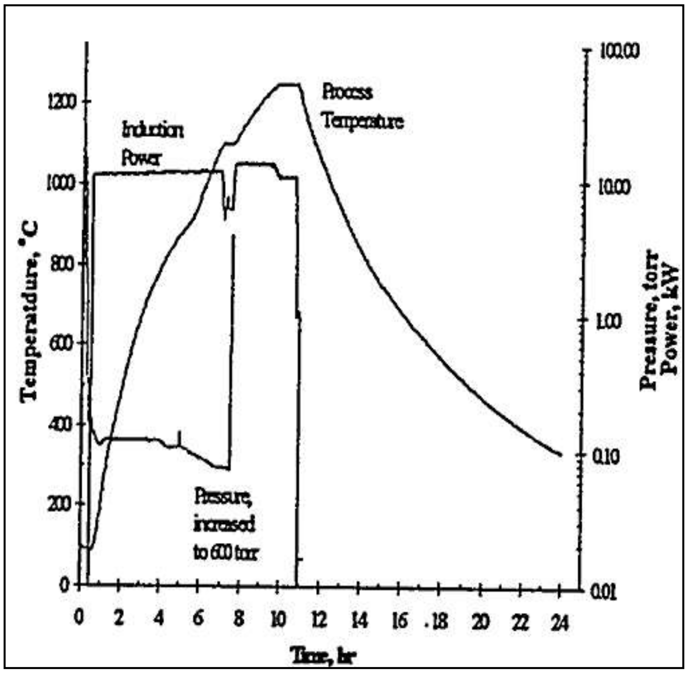

Fig. 1.5 Schematic operation of cathode processor system [27].

The schematic diagram of cathode processing system is shown in Fig. 1.6 [24]. The important parts, operating environment and materials proposed for the construction of cathode processor are tabulated in Table 1.3. The cathode processor (Fig. 1.6) consists of (a) an outer vessel; (b) an induction-heated furnace assembly with coils, liner and insulation; (c) a crucible assembly with a graphite process crucible and cover, (d) a radiation shield, (e) a condenser, and (f) a receiver crucible [24]. The graphite crucible used in the cathode processor is provided with a protective ceramic coating on the interior and exterior of the crucible to prevent contact between heavy metal and graphite and also to reduce the loss of consolidated heavy metal [12,24]. A graphite furnace liner acts as the susceptor in the induction furnace and the induction coils are passively cooled and protected by a vapour barrier. Distillate material is transferred to the condenser region from the process crucible in the vapor phase and collected in a receiver crucible [27]. The metal ingots resulting from the cathode processing operation are sufficiently free of impurities to qualify as feed material for the next operational step namely injection casting [12].

Table 1.3 Materials proposed for cathode processor [24].

Description	Proposed materials	Environment
Process crucible	Graphite coated on both sides with ceramic coating	LiCl-KCl salt + Cd + Uranium + at high temperatures + Pressure
Crucible stand	SS 410	-
Splatter shield	Graphite	-
Furnace liner	Graphite with ceramic coating innerside	Vapour of molten salt
Radiation shield	Ta 10 % W alloy	-
Outer vessel	SS 316 L/ 316 LN	-
Thermo well	Graphite with ceramic coating	High temperature around 1373 K

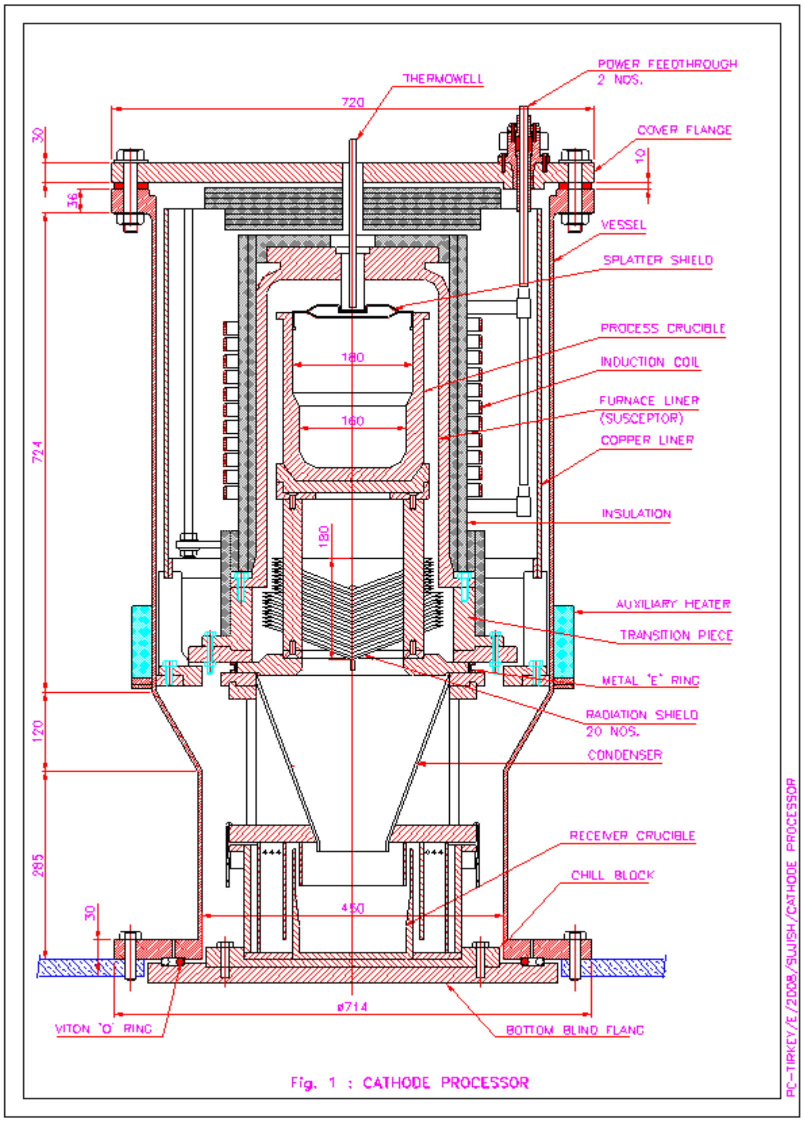

Fig. 1.6 Schematic of cathode processor system [24].

1.3.4 Injection casting system

The function of the injection casting system is to cast the appropriate blend of U, Pu, MA and zirconium, along with some carry-over fission products into slugs suitable for loading as new fuel rods [12]. The fuel batch is first constituted by adding an appropriate mixture of cathode-processor-produced ingots and feed from other external sources such as plutonium or zirconium. Injection casting components are similar to those of the cathode processor except that there is no condenser stage and associated receiver crucible to collect the distillate [14]. Like the cathode processor, the casting furnace comprises an induction furnace and a graphite crucible. The operating parameters associated with the casting furnace include the coating characteristics of the crucible, temperature control, and pressure control [14]. Ceramic coating on graphite crucible is required in the casting furnace to minimize the interaction of molten uranium with graphite and to prevent the cast ingot from adhering to the crucible walls [12,14]. The fuel batch is then induction melted under vacuum and homogenized, after which the system is pressurized and the fuel alloy is injected into closed-end moulds which are rapidly cooled [12]. The fuel-bearing moulds are subsequently sent to the fuel pin processing step. There, the moulds are removed, the fuel slugs cut to length, inspected and inserted into fresh fuel-pin cladding, along with a small amount of sodium for thermal bonding. The top end-caps for the new fuel rods are welded on, and the rods are heated above the melting point of the sodium so that the fuel will sink to the bottom, causing the sodium to distribute itself as a bonding agent [12]. After quality control assurance, the accepted fuel pins are loaded into bundles and installed in new fuel-subassembly for insertion into the reactor [12].

1.3.5 Waste management system

The radioactive waste generated after electrorefining process was consolidated into two forms: the CWF includes actinide elements and fission products in a glass-ceramic matrix and the MWF contains noble metal fission products in a fuel-cladding matrix [14]. Significant amounts of fission products and transuranic elements accumulate in the LiCl-KCl electrolyte after electrorefining process. Although the electrolyte can be recycled, its radioactive components must ultimately be disposed off as high-level radioactive waste [14]. Vitrification methods used to immobilize other high-level radioactive waste materials cannot be used because glass cannot incorporate high concentrations of salt [14]. Extraction of actinide elements from the spent electrolyte salt carried out by liquid–liquid extraction process. The alkali, alkaline earth and rare earth fission products that get accumulated in the electrolyte salt are removed by passing through a zeolite column and the zeolites with trapped fission products are converted to a CWF (Fig. 1.7) known as glass bonded sodalite [7]. In the CWF the active fission products (alkalis, alkaline earths, and rare earths) and transuranic elements of the electrolyte are immobilised with zeolite 4A at 773 K to occlude the waste-loaded salt within the cages of the zeolite crystal lattice [14]. The product of this step is called salt-loaded zeolite (SLZ) [7,14]. The SLZ is converted to glass bonded sodalite by heating a homogeneous mixture of SLZ with boroaluminosilicate glass (25 wt %) in flowing argon atmosphere at 1188 K for 15 h [7]. The CWF thus produced in a batch process by mixing and blending the waste salt, periodically removed from the electrorefiner [14]. The CWF is a multiphase, nonhomogeneous composite consisting of approximately 75% sodalite, 25% borosilicate glass, and up to 5% other minor phases, e.g., aluminosilicates, rare-earth silicates, oxides, and halide (NaCl) [14].

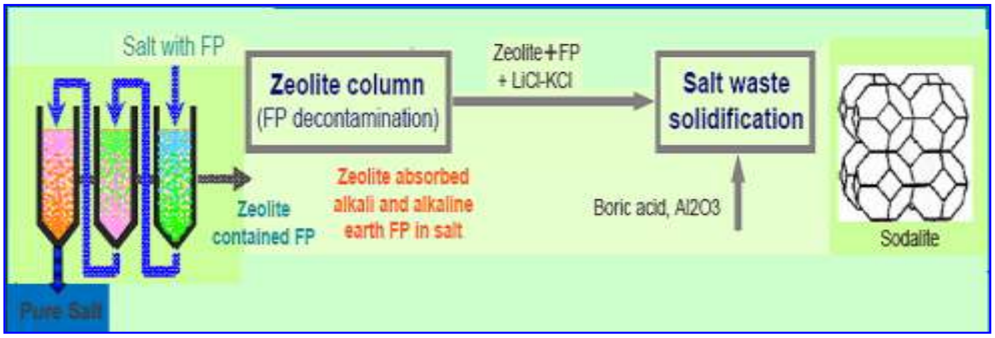

Fig. 1.7 Schematic representation of development of CWF (glass bonded sodalite) [28].

Following the electrorefining operations the stainless-steel cladding hulls are left out in the anode basket, along with the noble metal fission products, some actinides, and adhering salt electrolyte [14]. The maximum uranium content is about 4 wt %. The material in the anode basket is transferred to the cathode processor and heated to 1373 K to distill the salt. The charge from the cathode processor is taken in a ceramic or ceramic coated graphite crucible, about 15 wt % Zr was added and melted at approximately 1873 K in the casting furnace under argon atmosphere [14]. The molten mass is cooled in the crucible and cast into ingots. The ingot constitutes the MWF. The radio nuclides present in these wastes must be sufficiently isolated from the surrounding biosphere for time periods greater than ten thousand years. The baseline waste form reported in the literature for EBR–11 spent metallic fuels was stainless steel–15 wt% Zr alloy for SS clad material and Zr-8 % SS for zircaloy clad material [29]. However, the Zr content of MWF alloys may vary from 5 to 20 wt% depending on the composition of the starting fuel [29,30]. The noble metal content of the waste form depends on the burn up of the treated fuel and the actinide content on the efficiency of the electrorefining process; the waste forms may contain up to 4 wt% noble metals (Ru, Rh and Pd) and up to 10 wt% actinides (mainly U). In the MWF development work on 304 SS - Zr by Argonne National Laboratory, Zr was found to combine with SS and form laves type intermetallics which act as the host phase for actinide and fission products [31,32]. Excellent corrosion and selective leaching resistance properties were reported for the MWF alloys due to the formation of amorphous ZrO_2 layer on the MWF surface [32]. Both the MWF and the CWF are high-level solid waste forms planned for final disposition in a geologic repository.

1.4 Materials challenges for pyrochemical reprocessing plant

The integrity and availability of nuclear fuel reprocessing plants for uninterrupted operation depends on the quality and performance of critical engineering components, vessels and piping. Any failure of the components of reprocessing unit processes would lead to the leakage of radioactivity and slowing down the recovery of useful fissile material required for sustained operation of power plants. Out of several critical issues, material challenges are of utmost important for safe operation of fuel reprocessing plant as well as determining the overall plant life [33]. This demand poses and dictates many challenges with respect to the reprocessing plants, particularly of FBRs as they handle high plutonium content fuels with various fission products and transuranium elements in large yields due to significantly high burn ups in FBRs. The selection criteria of materials of construction for nuclear fuel reprocessing plants is a complicated procedure involving various parameters such as their availability, cost, mechanical properties, corrosion resistance etc., The presence of radiation, corrosive chemicals and high temperature in the operating areas of the plant make it difficult to access for maintenance. These aggressive conditions prevailing in the pyrochemical reprocessing plant demand structural materials and accessories of the unit operations with good mechanical integrity and thermal stability combined with corrosion resistance to provide high performance and long service life [34]. In general metals and alloys can be employed for high temperature operation, but during service in addition to high temperature corrosion and scaling, creep properties begin to dominate their life. The recrystallisation, grain growth, oxidation and scaling, and high temperature corrosion affect the properties and stability of the materials as the temperature of application increases further. Also, depending on the heating and cooling cycles of the process operation, thermal cycling would result in the buildup of thermal stresses, particularly if any ceramic coating has been applied on the surface of the materials [35]. Considering the long term uninterrupted service of the pyrochemical reprocessing plants, the structural materials for the components and accessories to be chosen based on the above considerations is a big challenge. Thus, limited materials only have been identified for these applications at high temperatures and under intense radiation field, to avoid the need for repair and replacement.

1.5 Scope of the present thesis work

Carbon materials are proposed for structural applications are salt purification and cathode processor crucibles for handling molten salt as well as molten uranium at high temperatures during the processing of spent metallic fuels by pyrochemical reprocessing. The objective of the thesis is to (i) understand the corrosion behaviour of different carbon materials and (ii) develop ceramic coatings on graphite crucibles and evaluate the performance of these coatings under pyroreprocessing conditions. Towards reaching this goal, the following issues which arise, while evaluating the performance of materials and coatings need to be addressed.

1. **Corrosion behaviour of carbon materials:** Degradation of carbon materials (if any) in the molten salt and how microstructural changes occur after exposing molten salt for long durations.
2. **Ceramic coatings on graphite:** The technique to be employed for coating and the ceramic material for coatings on graphite need to be identified.
3. **Corrosion behaviour of coatings in molten salt:** Evaluating the performance of ceramic coatings in molten LiCl-KCl salt.
4. **Uranium melting:** Compatibility of the ceramic coatings developed on graphite with molten uranium at and above the melting temperature of uranium.

5. **Thermal cycling:** Predicting the adhesion of ceramic coatings on graphite substrate to withstand the heating and cooling cycles during the operation of process steps.

The present thesis provides optimum solutions for all the above mentioned issues unambiguously by the way of careful testing and evaluation of carbon materials and ceramic coatings in a systematic way.

References

[1] Baldev Raj, Energy Procedia 7 (2011) 186-198.

[2] Baldev Raj, U. Kamachi Mudali, Prog. Nucl. Energy. 48 (2006) 283-313.

[3] S.C. Chetal, P. Chellapandi, P. Puthiyavinayagam, S. Raghupathy, V. Balasubramaniyan, P. Selvaraj, P. Mohanakrishnan and Baldev Raj, Energy Procedia 7 (2011) 64-73.

[4] T. Nishimura, T. Koyama, M. Iizuka, H. Tanaka, Prog. Nucl. Energy. 32 (1998) 381-387

[5] Anil Kakodkar, Energy in India for the Coming Decades, Presentation at the Inter-ministerial Conference on Nuclear Power for the 21st Century, Organized by the International Atomic Energy Agency (IAEA) during March 21-22, 2005, Paris, France.

[6] Baldev Raj, H. S. Kamath, R. Natarajan, P. R. Vasudeva Rao, Prog. Nucl. Energy. 47 (2005) 369-379.

[7] K. Nagarajan, B.P. Reddy, S. Ghosh, G. Ravisankar, K.S. Mohandas, U. Kamachi Mudali, K.V.G. Kutty, K.V. Kasiviswanathan, C. Anand Babu, P. Kalyanasundaram, P.R. Vasudeva Rao and Baldev Raj, Energy Procedia 7 (2011) 431-436.

[8] T. Ogata, Metal Fuel in: Comprehensive Nuclear Materials, R.J.M. Konings (ed.,) Vol. 3 (2012) pp. 1-40.

[9] Y.I. Chang, Nucl. Technol. 88 (1989) 129-138.

[10] Picture courtesy of Argonne National Laboratory Integral Fast Reactor website *http://www.ne.anl.gov/About/reactors/integral-fast-reactor.shtml*

[11] H.S. Kamath, Energy Procedia 7 (2011) 110–119.

[12] J. J. Laidler, J. E. Battles, W. E. Miller, J. P. Ackerman, E. L. Carls, Prog. Nucl. Energy. 31 (1997) 131-140.

[13] P. Hogselius, Energy Policy 37 (2009) 254-263.

[14] Electrometallurgical Techniques for DOE Spent Fuel Treatment: Final Report, National Academy Press, Washington, D.C., ISBN: 0-309-51482-7 (2000) pp. 1-128.

[15] Spent Nuclear Fuel Reprocessing Flowsheet, A Report by the WPFC Expert Group on Chemical Partitioning of the NEA Nuclear Science Committee, NEA/NSC/WPFC/DOC (2012)15, June (2012) p.1-120.

[16] S.X. Li, D. Vaden, B.R. Westphal, G.L. Frederickson, R.W. Benedict, T.A. Johnson, Nucl. Technol. 166 (2009) 180-186.

[17] Pyrochemical Separations in Nuclear Applications- A status report by Nuclear Energy Agency, ISBN 92-64-02071-3, (2004).

[18] M.R. Coops, J.B. Knighton, L.J. Mullins, Plutonium Chemistry, W.T. Carnall and G.R. Choppin (eds.,), ACS Symposium Series 216, American Chemical Society, Washington, D.C., (1983) pp. 381-400.

[19] T. Koyama, M. Iizuka, Y. Shoji, R. Fujita, H. Tanaka, T. Kobayashi, M. Tokiwai, J. Nucl. Sci. Tech. 34 (1997) 384-393.

[20] J.L. Willit, W.E. Miller, J.E. Battles, J. Nucl. Mater.195 (1992) 229-249.

[21] M.V. Kormilitsyn, A.V. Bychkov and V.S. Ishunin, Pyroelectrochemical reprocessing of irradiated fuel of fast reactors. VI. Generalization of experience on BOR-60 spent nuclear fuel reprocessing using approaches “$UO_2 \rightarrow UO_2$” “MOX→ PuO_2” and “MOX→MOX”, Proc. of Global 2003, New Orleans, (2003), pp 782-783.

[22] T. Subramanian, B. Prabhakar Reddy, S. Ghosh, K. Nagarajan, Report No: CG/2005/33, (2005).

[23] B. Prabhakar Reddy, K. Nagarajan, Development of pyrochemical reprocessing flow sheet for fast reactor fuels, in: K.L. Ramakumar, S.C. Parida, S.M. Mukerjee, R.V. Pai, S.K. Rakshit (eds.,) Proceedings of Conference on Molten Salts in Nuclear Technology, (2013), pp. 56-61.

[24] U. Kamachi Mudali, A. Ravi Shankar, C. Mallika, K. Thyagarajan, S. Ningshen, B.P. Reddy and K. Nagarajan, Materials and Coating Technologies for Pyrochemical Reprocessing of Spent Metallic Fuel from Fast Breeder Reactors, Report: IGC/MMG/CSTG/2011. pp. 1-47.

[25] J.E. Herceg, K.J. Belcher, L. Bova, H.J. Haupt, S.A. Kamal, J.G. Saiveau, Engineering and Acquisition of Equipment for Electrometallurgical Treatment of Spent Nuclear Fuel, Proceedings of 8th International Conference on Nuclear Engineering, Baltimore, USA, (2000) pp. 1

[26] L. Burris, R.K. Steunenberg, W.E. Miller, The Application of Electrorefining for Recovery and Purification of Fuel Discharged from the Integral Fast Reactor, AlChE Symposium Series No.254, 83, (1987): pp. 135.

[27] A.R. Brunsvold, P.D. Roach, B.R. Westphal, Design and development of a cathode processor for electrometallurgical treatment of spent nuclear fuel, Proceedings of ICONE 8: 8th International Conference on Nuclear Engineering, Apri12-6, 2000, Baltimore, MD USA.

[28] T. Inoue, An overview of CRIEPI pyroprocessing activities, 9th OECD/NEA P&T IEM Nimes, France, (2011).

[29] S.M. McDeavitt, D.P. Abraham and J.Y. Park, Evaluation of stainless steel-zirconium alloys as high-level nuclear waste forms, J. Nucl. Mater. 257 (1998) 21-34.

[30] D.D. Keiser, D.P. Abraham, W. Sinkler, J.W. Richardson, S.M. McDeavitt, J. Nucl. Mater. 279 (2000) 234-244.

[31] D.P. Abraham, S.M. McDeavitt, J.Y. Park, Met. Mater. Trans. A 27 (1996) 2151-2159.

[32] D.P. Abraham, J.W. Richardson, S.M. McDeavitt, Mater. Sci. Engg. A 239–240 (1997) 658–664.

[33] Baldev Raj, U. Kamachi Mudali, T. Jayakumar, K.V. Kasiviswanathan, R. Natarajan, Sadhana 25 (2000) 519–559.

[34] T. Jayakumar, U. Kamachi Mudali, Materials and Coating Technology for Pyrochemical Reprocessing Applications, Proceedings of Conference on Molten Salts in Nuclear Technology, Eds. K.L. Ramakumar, S.C. Parida, S.M. Mukerjee, R.V. Pai, S.K. Rakshit (2013), pp. 122-133.

[35] U. Kamachi Mudali, A. Ravi Shankar, S. Ningshen, Plasma sprayed thermal barrier coatings for molten chloride environment, Surface Modification Technologies-XXV, Eds. T.S. Sudarshan, Per Nylén, VALAR Docs publications (2012), pp. 143.

CHAPTER-2

A REVIEW ON THE MATERIALS AND COATINGS FOR MOLTEN SALT AND URANIUM APPLICATIONS

This Chapter introduces the developmental aspects of pyrochemical reprocessing of spent metallic nuclear fuel. A brief overview of the carbon materials graphite, glassy carbon and pyrolytic graphite, their processing and applications to nuclear technology have been presented. Description of the ceramic coating materials and development of coating methods aspects with emphasis on plasma spray process are included. This Chapter reviews the materials and coatings developed for high temperature molten salt and uranium consolidation applications. The up to date literature on materials and coatings and their characterization and performance in molten salt and uranium applications are also covered in this chapter.

2.1 International experience on pyrochemical reprocessing

The evolution of nuclear technology encompasses the development of numerous methods for processing irradiated nuclear fuel. Separation techniques were initially developed in the 1940s and were applied to the separation of plutonium for military purposes [1]. Later, reprocessing of civilian irradiated nuclear fuel was introduced as a means of extending the uranium resources for future needs. The purpose of more complex fuel cycle schemes and the development of reprocessing methods are for achieving the goal of minimizing waste generation and reducing costs. This has resulted in renewed interest in dry reprocessing methods, known as “pyrochemical” processing [1]. Such processes have been studied in the past by various countries. Pyrochemical processes attract strong interest, as they offer the potential for more compact (and hence, lower cost) facilities and the ability to handle irradiated nuclear fuel, cooled for shorter times [1]. Applications of pyrochemical processing for irradiated fuel vary from country to country. Some countries are oriented towards the treatment of thermal reactor fuel for the purpose of recycling and recovering actinides (primarily the transuranic elements) in fast spectrum reactors in order to provide sustainable nuclear energy systems. Other countries focused on fast reactor fuel cycle with processes being developed for treating metal [2], oxide [1] and nitride [3] fuels.

Electrochemical treatment of spent nuclear fuel using molten salt systems has progressed significantly over the last 20 years. Development, testing and demonstration operations have been performed with spent fuel for flowsheet development. This technology is expected to provide benefits over conventional aqueous options for treating spent nuclear fuel and enable the deployment of next generation nuclear power systems [4]. Pyrochemical processing has been implemented for the treatment of spent fuel from the Experimental Breeder Reactor-II (EBR-II) at Idaho National Laboratory since 1996 [5]. A successful demonstration of the technology was performed from 1996 to 1999 by the Department of Energy (DOE). Electrorefining is the central technology for pyrochemical processing. The experiences on electrorefining of spent fuels of EBR-II were summarized by Li et al. [5]. Central Research Institute of Electric Power Industry (CRIEPI), Japan started research and development work on metal fuel cycle in 1986, had initiated a joint study on pyrometallurgical technology with the United States DOE and showed progress in electrorefining of metal fuel and treatment of wastes [6]. Japan has two proposals under consideration. One is to separate the minor actinides and long lived fission products from irradiated oxide fuels by electrorefining after reducing them to metals and transmute them in critical or sub-critical reactors. The other is to use the nitride fuels in fast reactors and reprocess them by either molten salt electrorefining or nitriding in molten cadmium [1,6]. Research Institute for Atomic Reactors (RIAR) has used the pyroelectrochemical process for the production of tonnes of granulated UO_2 and $(U,Pu)O_2$ fuels for use as vipac fuel pins and for reprocessing enriched UO_2 and $(U,Pu)O_2$ irradiated fuels [1]. France has proposed to use pyrochemical processes for the separation of minor actinides and long lived fission products [1]. Korea Atomic Energy Research Institute (KAERI) has been developing pyroprocessing technology to handle the spent oxide fuel since 1990s [7].

Lee et al. [8] performed electrorefining using graphite as cathode in eutectic LiCl-KCl salt. The steel cathode proposed to be used in the electrorefiner was replaced by a graphite cathode, as graphite exhibited self-scraping behavior in which the electrodeposited uranium dendrite falls from the cathode surface on its own without any kind of further processing. The self scraping nature of graphite cathode would increase the efficiency of electrorefining process due to the elimination of mechanical scraping as well as the stripping of the cathode [8]. Recovery of uranium from the electrorefiner vessels containing a LiCl-KCl eutectic salt has been the on-going research work in the pyrometallurgical processing of used nuclear fuels for more than a decade. Usually, austenitic stainless steels are utilized for LiCl-KCl salt systems; however, the cadmium in the electrorefiner dictates an alternate material. A 2.25Cr-1Mo steel (ASME SA-387) was chosen due to the absence of nickel in the alloy, which has considerable solubility in cadmium. The vessel made up of 2.25Cr-1Mo was used as the electrorefiner vessel for the processing of EBR-II fuel. The corrosion of 2.25Cr-1Mo alloy in LiCl-KCl eutectic was evaluated to be uniform (i.e. non-localized corrosion) [9]. Without cadmium, the selection of a material for the containment of LiCl-KCl salt would have been an austenitic stainless steel (304 SS or 316 SS) based on corrosion studies [10,11]. Evaluating the corrosion resistance of materials in molten chloride salts at high temperature is of prime importance for their use as equipment like electrorefiner and salt purification vessel in pyrochemical reprocessing plants. In order to overcome the corrosion of metallic materials in molten chloride environment, efforts were made to develop coatings on structural materials for various unit operations like salt preparation, electrorefining and cathode processing. Selecting materials and coatings for a critical application in reprocessing plants is a challenge where extended life of a material is demanded. Hence studies to identifying different materials and understanding their behaviour in molten salts by various research groups in the world become essential.

From international experience it is evident that pyrochemical reprocessing is leading technology worldwide and materials development for such critical applications is a challenging task. This chapter focusses on the corrosion behaviour of materials in lithium based molten chloride environment at high temperature, which is the medium for pyrochemical processing. Various materials were evaluated in molten chloride salts by different research groups in order to understand their corrosion behaviour, and the need for the development of coatings has been discussed in detail.

2.2 Carbon materials

Carbon exists in several physical forms which are known as polymorphs (or allotropes), with different names like graphite, diamond, lonsdalite, fullerene and others. The term “carbon material” is used to qualify such as carbon fiber, pyrolytic carbon, vitreous carbon and others [12]. These carbon materials have a sp^2 atomic structure and are essentially graphitic in nature. Graphite is composed of series of stacked parallel layers with the trigonal sp^2 bonding. The carbon atoms are arranged in a hexagonal lattice with a separation of 0.142 nm, and the distance between the planes is 0.335 nm [12]. Graphite materials such as pyrolytic graphite (PyG), carbon-fiber-carbon-matrix composites (carbon-carbon), vitreous carbon, carbon black and many other forms are actually aggregates of graphite crystallites and these all are called as polycrystalline graphites. The crystallite sizes in these graphites may vary considerably [12]. Carbon and graphite form a unique class of high temperature materials due to their strength and stiffness up to 2673 K under non-oxidizing environments [13]. The major disadvantage of carbon materials is their low oxidation resistance under oxygen containing environment. Because of this oxidizing nature, the strength of these materials reduce by nearly 50 % [13]. In the present thesis three kinds of carbon materials viz. graphite, glassy carbon (GC) and PyG have been studied for their possible applications in pyrochemical reprocessing. Hence, this chapter deals with the preparation of these carbon materials and their testing under various environments as reported in the literature.

Graphite materials can be prepared as dense or as very light body as well as highly anisotropic or as an isotropic material [14]. Graphite materials are prepared by heat treating a mixture of petroleum coke and coal tar pitch at high temperatures. The carbon product is further heat treated in an electric furnace in the temperature range 2773-3073 K to produce amorphous to crystalline graphite [13,14]. The manufacturing process steps were discussed in detail by Castro at al. [13]. Graphite possesses lubricity, strength, dimensional stability, thermal stability and ease of machining; a combination of these properties has led to its use in a variety of applications in industries. Its properties, through process modifications are tailorable to meet an array of design criteria for survival under extremely harsh environmental operations. Carbon and graphite exhibit excellent resistance to the corrosive actions of acids, alkalies, and organic and inorganic compounds, an attribute that has attracted the use of graphite in process equipment [12]. Manufactured carbon and graphite parts exhibit varying degree of porosity. Because of their unique combination of physical and chemical properties, manufactured products of carbon and graphite are widely used in several forms in high temperature processing of metals, ceramics, glass, and fused quartz. Industrial carbon and graphite are available in a broad range of shapes and sizes. The resistance of graphite to thermal shock, its stability at high temperatures, and its resistance to corrosion permit its use as self-supporting vessels to contain reactive materials at elevated temperatures (1023–1973 K); self-supporting reaction vessels are used for the direct chlorination of metal and alkaline-earth oxides. Several grades of low density porous carbon and graphite are commercially available [15].

GC is an amorphous form of carbon with isotropic nature in properties [16,17]. GCs are produced by pyrolysis of thermosetting resins (eg. phenolformaldehyde) under controlled heating process at typical temperatures around 1173 to 1273 K [16-19]. The GC structure consists of randomly oriented hexagonal graphite-like layers [16,19] and it has very low porosity with moderately bulk density [17]. Depending on the preparation methods and process parameters the porosity can vary from near zero to several tens [19,20].

Synthetic form of graphite manufactured by chemical vapour deposition (CVD) is referred as PyG. It is a high purity form of carbon (< 1 atom % hydrogen). According to Kotlensky [21], thermal decomposition of hydrocarbon gases give rise to three products in the field of carbon namely (i) pyrolytic carbon (PyC), (ii) CVD carbon and (iii) PyG. All these names or terms refer to the same material. The two terms pyrolytic carbon and CVD carbon are related to the deposition of carbon material by the pyrolysis of a hydrocarbon vapour. The term “PyG” is a particular high temperature form of PyC or CVD carbon. There are two ways to obtain PyG; one is deposition of PyC followed by graphitization at temperatures above 2273 K. In the second method deposition is carried out at temperatures above 2273 K. PyG has the following excellent desirable properties among other forms of synthetic graphite because of the highly oriented crystallinity present in the structure: (i) Its strength increases with temperature especially at high temperatures above 2773 K (ii) Greater oxidation resistance and (iii) Low porosity (high density) etc,. The main application of PyG is in the form of coatings, and also in the bulk form, by making the coatings sufficiently thick over the substrate and machining for different shapes [12]. A free standing object can be made after separating PyG from the substrate, with sufficiently thick deposition [22,23]. PyG can be deposited on the substrate up to a thickness of approximately 7 inches [23] and it can be deposited over moulded graphite, carbon fibers and porous carbon-carbon structures [12]. The microstructure [24], structural features and other properties [25] of PyG depend upon the deposition conditions [26]. PyG has been chosen as a coating material over graphite because it has greater oxidation resistance, chemical inertness and good thermal shock resistance and is stronger than normal graphite [22]. PyG has considerable technological importance as a coating as well as structural (container) material in the field of nuclear technology.

2.3 Application of carbon materials in nuclear technology

Carbon and graphite find wide ranging applications as electrode, refractories and crucible components, moderator and structural components in gas-cooled nuclear reactors, and air craft brakes, rocket engine components and nose tips in aerospace applications [13]. Application of graphite in aerospace and nuclear reactor demand high reliability and reproducibility of properties, mechanical integrity of product and product uniformity [15]. Different forms of carbon materials are employed for various applications in nuclear technology.

PyG is used in the front and back end of nuclear fuel cycle. Triso-coated fuel particle is used in high temperature reactor. Each particle contains a kernel of uranium dioxide or uranium oxycarbide (UO_2 or UCO) of 500 to 800 μm in diameter. The confinement barrier is managed by means of a coating of ceramic multilayer [27]. PyG is one of the crystalline forms of carbon and it can be deposited on graphite for providing high temperature corrosion resistance in aggressive molten salt environments [28,29]. It is used as crucibles and as coating material on graphite crucibles in RIAR for fuel reprocessing in corrosive molten salt environment [28-30] and also as electrode material for the electrochemical reduction of oxides into metals in LiCl melt [31]. PyG crucible has been used as anode in the electrolysis process of pyrochemical method [32]. Corrosion studies carried out by Takeuchi et al. [29] on PyG and other ceramic materials like mullite and cordierite in molten NaCl-KCl salt (for oxide fuel reprocessing) at 1023 K for 24 h showed negligible corrosion rate (0.01 mm/y) under Cl_2 bubbling conditions. However, in Cl_2-O_2 (1:1) atmosphere in molten salt medium the corrosion rate was more than 0.5 mm/y. This clearly indicated that oxygen environment is not conducive to PyG [29]. The weight loss in PyG was insignificant compared to GC weight loss (0.5 wt%), when tested in molten fluoride environment at 813 K for the duration of 1-10 h and at 1268 K for about 1 h [20]. Magdziarz [33] investigated the thermal oxidation behaviour of general grade graphite, GC, pre-baked and pyrolytic carbon in air and nitrogen atmospheres at 833 K for application in molten salt based Fray-Farthing-Chen (FFC) electro reduction process and had recommended the use of GC and PyC as anodes for electro reduction at lower temperatures because of their high resistance to oxidation compared to graphite and pre-baked carbon. GC is widely used as electrode and crucible material for various processes [34]. It was also used as anode crucible and as working electrode in electrochemical measurements in pure LiF-NaK-KF, LiF-NaK-KF-UO_2 and UF_4 melt [35].

Graphite crucibles are extensively used in pyrochemical reprocessing of metallic nuclear fuels as cathode processor material and casting furnace crucibles [36,37], liners [36] and as electrodes and tubes for chlorination at 973 K [30]. Graphite served as the crucible for cathode processing for the purpose of consolidating uranium from the cathode deposit comprising uranium, cadmium and 20-30 wt.% of salt [5]. Graphite crucible along with liner has been used for melting and purification of molten salt under chlorine atmosphere [38]. Bernardet et al. [39] carried out the interaction studies between nuclear graphite and graphite protected by a glassy carbon coating and a double coating of PyC/GC in molten fluoride salt. The behaviour of unprotected graphite was far from satisfactory after two days of immersion of graphite in molten salt at 773 K. The best way of protecting graphite surface, with maximum inertness towards molten salt, has been obtained by providing a double coating of PyC/GC. The importance of PyC/GC coating for molten salt applications was highlighted in their study. Further, the coating layer exhibited perfect adhesion on the surface of nuclear grade graphite and a very weak adherence towards the molten salt [39].

Selection of materials is one of the critical issues in the accelerator driven transmutation technology (ADTT) [20]. GC, PyG and Hastelloy B are considered as candidates for structural materials of the ADTT systems. The interaction of molten fluoride salt with these materials in a bath of the molten salts either as one-component LiF (100%) at the temperature of 1268 K or in a mixture of LiF (46.5 wt%) + KF (42 wt%) + NaF (11.5

wt%) (FLiNaK) with a melting point of 813 K has been investigated [20,40]. Pyrolitic graphite was found to be chemically intact; corrosion attack was evident on GC and particularly on the surface of Hastelloy B [20,40]. Different carbon allotropes and metallic foils (Ni, Ti, V and Mo) were exposed to molten LiF based salt mixture at 813 K (1 to 10 h) and 1268 K (1 h) and their weight loss (%) measured after the corrosion test by Vacik et al. [40] are listed in Table 2.1. Very low values of corrosion were observed for GC and PyG compared to metallic foils [40].

Table 2.1 Weight losses in carbon materials and metallic foils in molten LiF based salt [40].

Specimen	**LiF 995°C, 1 h**	**LiF+KF+NaF 813 K, 1 h**	**LiF+KF+NaF 813 K, 5 h**	**LiF+KF+NaF 813 K, 10 h**
GC	0	0	~11	~ 0.5
PyG	0	0	0	0
Reactor graphite	~24	~11	dissolved	-
Nickel	0	0	0	~0.5
Titanium	~52	~42	dissolved	-
Vanadium	~35	~15	~23	dissolved
Molybdenum	~50	~12	~26	dissolved

Molten salt reactor systems demand structural materials to effectively resist corrosion by fluoride salt mixtures. In order to select the best suited materials for molten salt reactor extensive corrosion studies were carried out with graphite in molten fluoride salt up to 1000 h exposure at 978 K. After corrosion test, graphite indicated penetration of salt to a great extent through the available pores. [41]. Development of PyC coating on nuclear grade graphite is a promising method for to resist the attach of fluoride salt its application in Molten Salt Reactor

(MSR). Pyrolytic carbon (PyC) coatings were deposited on nuclear grade graphite (IG-110) by thermal decomposition of methane at 2103 K. The PyC coating was pretty dense and anisotropic with nanopores. Helium gas permeability into nuclear grade graphite was significantly decreased after PyC coating. These results indicate that the PyC coating is dense and pore free to protect the nuclear graphite against the permeation of molten fluoride salts and the diffusion of fission gases [42]. These studies recommended the use of impervious grades of graphite for molten salt applications in order to control corrosion. Graphite is also used as moderator in molten salt breeder reactors (MSBR) as it resists radiation and tolerates fission product accumulation. The type of graphite to be used in the MSBR should not undergo any chemical reaction with molten fluoride mixtures [43].

2.4 Molten salt corrosion behaviour of structural materials

The specific type of corrosion of metals and alloys in molten salt at high temperature is known as hot corrosion [44]. Corrosion reaction in molten salts is a fairly complex phenomenon. Loss of material after corrosion test could be attributed to the corrosion reaction and homogeneous or heterogeneous attack on the surface [45]. Material's behaviour in molten salt was studied mainly by gravimetric method or by weight change measurements and subsequent surface examination/characterization [45]. Uniform metal oxidation and dissolution is a common form of molten salt corrosion. Selective leaching is very common at higher temperatures, while pitting and crevice corrosion are seen at lower temperatures [46]. All the forms of corrosion observed in aqueous systems including stress-assisted corrosion, galvanic corrosion, erosion-corrosion and fretting corrosion have occurred in molten salts. Many of the principles that apply to aqueous corrosion, such as anodic reactions leading to metal dissolution and cathodic reduction of an oxidant also apply to molten salt corrosion

[46]. The corrosion process is mainly electrochemical in nature because of the excellent ionic conductivity of most of the molten salts [45,46]. Even though the corrosion mechanism is similar, there are major differences between molten salt and aqueous corrosion as listed in Table 2.2. The differences arise mainly from the fact that molten salts are partially electronic and ionic conductors, which allows reduction reactions to take place in the melt as well as at the metal-melt interface. Molten salt systems operate at higher temperatures than aqueous systems, and cause different forms of corrosion attack. High-temperature corrosion in molten salts often results in selective dissolution and internal oxidation [46].

Table 2.2 The difference between aqueous and molten slat corrosion mechanisms.

Aqueous corrosion	Molten salt corrosion
Simple anodic and cathodic reactions	Complex situation with several oxidants
Passive state can be easily maintained (e.g. SS, Ti)	Passive state maintenance is less promising due to salt
Pourbaix diagram can be used to understand M -H_2O corrosion (Potential-pH)	Basicity diagrams can be used to understand M-salt corrosion (Potential-pO^{2-})
Anodic reaction involves dissolution of metal and formation of metal oxides	Anodic reaction involves dissolution of metal and formation of salt times
Cathodic reaction involves reduction of species	Cathodic reaction is complicated and depends on oxidants and trace impurities

Evaluation of molten salt corrosion is essential to understand the material behaviour under aggressive molten salt environment. AISI 316L stainless steel (SS) was envisaged as a candidate material for the fabrication of components for various unit operations in pyrochemical reprocessing [47]. The corrosion of 316L SS after immersion in molten LiCl-KCl salt up to 250 h at 773 K under UHP argon resulted in sever corrosion and formation of voids. Enrichment of Cr toward the top surface and underlying Cr-depleted layer with voids was observed in exposed 316L SS [47]. The thickness of the degraded layer containing voids increased with increase in the duration of exposure from 25 to 250 h and the spallation of chromium-rich compound could be seen in the sample exposed for 250 h. From international experience, Cr-Mo steels were considered for use as container material as molten Cd present in the electrorefiner protects the steel container [48]. The percentage weight loss values of 2.25Cr-1Mo and 9Cr-1Mo exposed to molten LiCl-KCl salt at 873 K indicated that 2.25Cr-1Mo suffers more corrosion attack when compared to 9Cr-1Mo steel. Hence, 9Cr-1Mo steel is the most preferred material than 2.25Cr-1Mo steel because of its good corrosion resistance in chloride environment and high temperature properties. Thus, 9Cr-1Mo is proposed as an alternative candidate material for electrorefiner vessel in pyrochemical reprocessing plant [49]. It has been widely accepted that Nickel-rich alloys suffer less from corrosion attack in chlorine containing environment than carbon steels and stainless steels [50]. Therefore, INCONEL alloys were considered as candidate materials for the fabrication of transfer lines of salt purification system where Cd free molten LiCl-KCl salt is handled [49]. INCONEL (600, 625 and 690) exposed for 500 h at 873 K exhibited weight gain due to the formation of adherent corrosion products on the surface of the sample. Microstructural analysis of INCONEL (600, 625 and 690) exposed for 100 h showed two regions: corrosion attacked regions rich in Cr and Fe and Ni rich matrix adjacent to the corrosion products. Accidental ingression of moisture and oxygen will aggravate the corrosion of structural materials used and hence the materials selected should withstand such aggressive environment. A study was initiated to understand the corrosion behaviour of 316L SS, INCONEL alloy (600, 625 and 690), electroformed (EF) Ni and EF Ni with Ni-W coating in molten LiCl–KCl at 673, 773 and 873 K for 2 h in the presence of air and the corrosion resistance was found to be in the following order: INCONEL 690 > INCONEL 600 > INCONEL 625 > EF Ni with Ni-W coating > EF Ni > 316L SS [49,51]. Preferential leaching of Cr from the surface and formation of Cr rich corrosion products appeared to be the common mechanism of corrosion for all the alloys exposed to molten LiCl-KCl salt [49].

Corrosion is an important issue during salt purification as the high temperature molten salt picks up oxygen and moisture and salt purification is carried out by passing chlorine gas which is highly corrosive in nature; therefore, the effect of Cl_2 on the INCONEL alloys needs to be understood. INCONEL 600, 625 and 690 base and weldments were tested in molten LiCl-KCl eutectic salt at 873 K for 30 min under Cl_2 gas [52]. INCONEL 690 exhibited better corrosion resistance than INCONEL 600 and INCONEL 625. INCONEL welds exhibited marginally higher corrosion rate than the base alloy [52]. Beryllia (BeO) crucibles are used as the container for liquid cadmium cathode as they are highly resistant to attack of molten salt and were not even wetted by uranium [48]. Hosoya et al. [53] studied the corrosion behaviour of Ni-based superalloy, Hastelloy-X and refractory metals (Ta and W) in molten $NdCl_3$-NaC1-KC1salt at 773 -1023 K for 60 min. Hastelloy-X showed no evidence of attack and refractory metals (Ta and W) retained glossy surfaces even after immersion test. Tantalum, tungsten and Hastelloy-X had sufficient corrosion-resistance against molten chlorides when moisture and oxygen were appropriately removed [53]. Indacochea et al. [54,55] tested tantalum, 316 L SS, 422 SS, 430 SS and 2.25 Cr-1 Mo steel in molten LiCl-3.5 wt % Li_2O and 1 wt % Li_3N salt saturated with Li metal at 998 K for 30 days whereas 304 SS, 316L SS, INCONEL 600 and INCONEL 625 were tested in molten LiCl-3.5 wt % Li_2O and 1 wt % Li_3N salt saturated with Li metal at 923 K for 6 days under argon and argon + 10 % O_2

atmosphere. Corrosion attack was minimum in the case of materials tested under pure argon as the cover gas. Corrosion was severe when a cover gas of argon + 10 % O_2 was used, even after the test temperature was reduced to 923 K and exposure time was shortened to 6 days. Oxygen gas plays a crucial role in corrosion and not as an oxide. Types 316L SS and 304 SS had similar corrosion behaviour even with the presence of Mo in 316L SS. The 316L SS welded specimen was severely corroded and intergranular attack was detected in the heat affected zone despite the low carbon content of this steel. INCONEL 600 showed the best corrosion performance among all the alloys tested and INCONEL 625 performed poorly as a consequence of higher amount of Mo and Cr present in the alloy [55].

The high temperature refractories ZrN and HfN are known for their chemical inertness in extreme corrosive environments. Periasamy et al. [56] investigated the compatibility of ZrN and HfN in molten salt mixture (28.5% LiCl–36.3% KCl–29.4% NaCl–5.8% UCl_3) at 998–1173 K for 4–485 h. Both ZrN and HfN experienced weight loss under all experimental conditions due to the formation of volatile products and electrochemical dissolution. Formation of volatile Zr–Cl and Hf–Cl products was believed to occur due to the reaction of the nitrides with Cl_2(g) or Cl^-, which in turn was generated by the reaction of UCl_3 species present in the salt with oxygen [56]. Effect of uranium, plutonium and trans-uranium elements on the corrosion behaviour of ceramics was required to select them as high corrosion resistant materials for RIAR process. For this purpose investigations using simulated trans-uranium elements added molten salt was carried out [29]. Takeuchi et al. [29] tested SiC, Si_3N_4, BN, AlN, ZrB_2, Al_2O_3, Y_2O_3, $Al_6Si_2O_{13}$, $Mg_2Al_3(AlSi_5O_{18})$ and pyrolytic graphite in 2CsCl-NaCl molten salt and its vapour phase at 923 K under Cl_2 + O_2 gas. The corrosion resistances of these ceramics were excellent and were less than 0.1 mm/y. No cracks were observed on the materials and mechanical strength did not drop remarkably after 480 h of corrosion test under Cl_2+O_2 atmosphere. Pyrographite suffered from severe damage by the effect of oxygen in molten salt. Silicon nitride, mullite and cordierite were promising for severe corrosion environment, particularly in RIAR process [29].

Since metallic and carbon materials undergo accelerated corrosion under severe corrosive environment and high temperatures, the vessels and crucibles made up of these materials need to be coated with corrosion resistant ceramic materials by efficient and flexible processes. It is also necessary to identify and develop of high temperature materials and coatings which are amenable to remote handling operations under highly aggressive and radioactive molten salt atmosphere.

2.5 Materials and coatings

In the process of selection of appropriate coatings for any application the following requirements should be satisfied: (1) The coating must have adequate mechanical–thermal resistance, (2) Thermophysical parameters of coating and substrate must be nearly identical, (3) Coating must have minimum chemical interaction with the environment, (4) Adhesion with substrate should be strong, (5) Possibility of multiple restoration of coating and (6) Coating material should be relatively economical and commercially available. According to Shifler [57], the performance of high temperature coatings are chosen depending on the following important parameters: (1) the environment, (2) temperature, (3) quality control of the coating application, (4) coating structure and chemistry, (5) fuel contaminants and (6) nature of substrate. Before selecting a material for high temperature molten salt applications, the thermodynamic stability of the coating material at the temperature of interest should be assessed. Based on the Gibbs energy data SiO_2, ZrO_2, BeO, ZrO_2-SiO_2 and yttria stabilized zirconia were found to be the candidate materials, [28,47,58-60] for molten salt environment at temperatures up to 1273 K. Various ceramic materials used for developing thicker coatings (i.e. thermal barrier coatings), their properties, advantages and limitations were listed by Cao et al [61].

High purity alumina coatings are widely used for insulation purpose of metals and alloys. Alumina composites rather than pure Al_2O_3 have certain advantages. Ananthapadmanaban et al. [62] reported that TiO_2 with a lower melting point effectively binds alumina grains, contributing to high density. Alumina powder with the addition of TiO_2 in the range of 3, 13 and 40 wt% is widely used for coating applications using thermal spray process [63-65]. Increasing TiO_2 content in the sprayed powder leads to a decrease in the melting temperature of the alumina-titania coating, resulting in the tendency to diminish the porosity [64] and increasing the fracture toughness of the coating [66,67]. The percentage of porosity of the 60/40 Al_2O_3-TiO_2 mixtures was lower than other compositions (i.e. 97/3 and 87/13). The microhardness of Al_2O_3-TiO_2 composite coatings depends essentially on their composition. The hardness decreased linearly with increase of TiO_2 content or decreasing alumina content [66,68]. The doping of TiO_2 into alumina could partially stabilize the α-phase of Al_2O_3 [63]. Alumina-titania coatings are excellent candidates for providing protection against abrasive wear, and are resistant to high temperature erosion. Such coatings are desirable for electrical insulation and anti-wear applications; for example in protective coatings for sleeve shafts, thermo-couple jackets, pump shafts etc. In addition to exhibiting good wear; these coatings exhibits corrosion and thermal shock resistance [69].

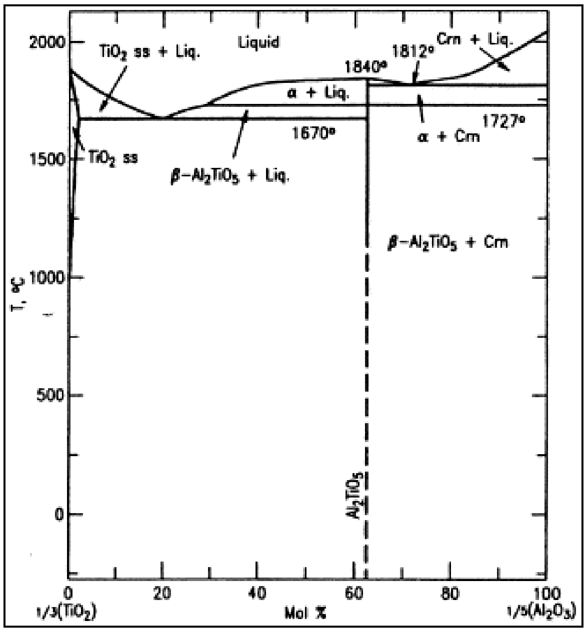

Fig. 2.1 Al_2O_3–TiO_2 phase diagram [70].

Porosity of Al_2O_3-40 wt% TiO_2 was reduced when agglomerated powder was used which also improved the homogeneity of the coating, owing to the formation of a new compound, Al_2TiO_5 [70]. Al_2O_3 and TiO_2 react together to form Al_2TiO_5, in accordance with the Al_2O_3–TiO_2 phase diagram shown in Fig. 2.1 [70]. The formation of this compound in the coating process improves the coating performance with respect to corrosion and thermal shock resistance. Based on the experience available in literature and its beneficial properties Al_2O_3-40wt% TiO_2 coating has been selected for the current study.

The performance of zirconia is reported to be satisfactory among the materials presently used for thermal barrier coatings. Zirconia (ZrO_2) has high melting and boiling points; it exhibits polymorphism with three stable phases up to its melting point of 2690°C [71]. The following characteristics of pure zirconia are evident from the phase diagram shown in Fig. 2.2 [72] : Melting point: 2690°C/2963 K; Cubic (C) to tetragonal (T) phase change: 2370°C/ 2643 K; Tetragonal (T) to monoclinic (M) phase change: 1170°C/ 1443K. The details of the phase transitions in ZrO_2 are listed in Table 2.3 [73].

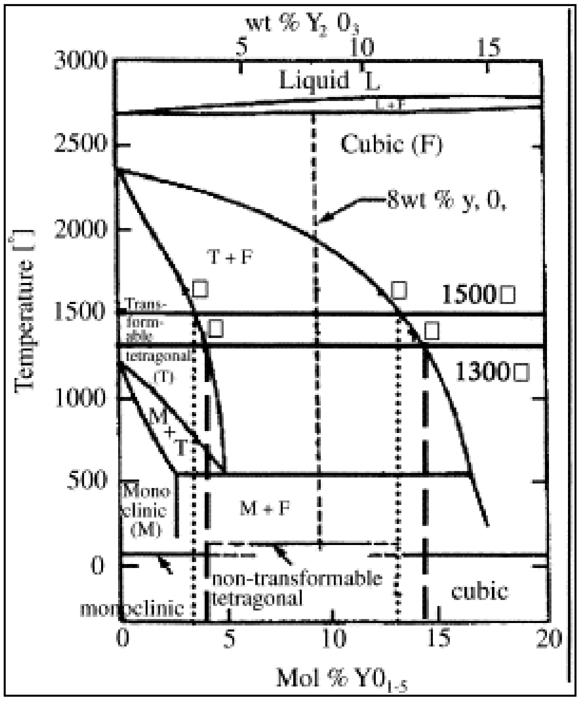

Fig. 2.2 Phase diagram of ZrO_2–Y_2O_3 [72].

Table 2.3 The details of the phase transition in ZrO_2 [73]

Parameters for the phase transition in ZrO_2					
Phase	**Monoclinic**		**Tetragonal**		**Cubic**
Space group	C_{2h}^5		D_{4h}^{15}		O_h^5
$T_{c\,(cooling)}^{a\,(heating)}$		1150°C 900°C		2370°C 2355°C	
Order		1st		1st	
Z	4		2		1
Lattice parameters	a=5.142 Å b=5.206 Å c=5.313 Å β=99°18' (30°C)		a=3.653 Å c=5.293Å (1390°C)		a=5.272 Å (2400°C)

Monoclinic ZrO_2 is seldom used in high temperature applications because of its polymorphic transformation accompanied by dimensional changes [74,75]. The tetragonal-to-monoclinic phase transformation is martensitic in nature because it does not require diffusion and occurs by small displacement of atoms in the structure. The transformation occurs on cooling zirconia from high temperature and it involves 3-5% volume increase. The volume change induces a significant shear strain, as high as 10%, in the structure, affecting the integrity of the coating [71]. Alloying zirconia with other oxides such as CaO, MgO, Y_2O_3, CeO_2, Sc_2O_3 and In_2O_3 inhibits the phase transformation, stabilizes the high-temperature phase and eliminates the volume change [76,77,71]. Among these stabilizers, the most commonly used is yttria, because of the long term stability of the resulting oxide. The optimum content of approximately 6-8 wt % yttria stabilizer in zirconia exhibits longer lifetime because of the presence of maximum amount of non equilibrium, “non transformable” tetragonal phase formed during the quenching process as indicated in the phase diagram (Fig. 2) [71,78,79]. Significantly lower yttria contents do not inhibit the transformation to monoclinic phase, while higher levels stabilize the cubic phase which lacks adequate strength, thermal shock resistance and toughness. As a result, 7 wt % yttria stabilized zirconia (named as 7YSZ) has become the industrial standard [71].

Coatings are applied to high temperature components to resist environmental degradation [80]. According to Heath et al. [81] four important critical properties to protect components from high temperature/molten salt corrosion are: chemistry of the coating, coating thickness, adhesion and thermal expansion co-efficient of coating and base material. Thermal spray coatings find extensive applications in aerospace, chemical, waste incineration, power generation, pulp and paper, petroleum, infrastructure, medical prosthesis and automotive industries for protection against corrosion [81,82]. The application of thermal spray coatings for reprocessing of nuclear fuel was initiated around 1990s and widely used now for the molten salt environment. Thermal spray coating represents a group of processes in which plasma spray is one of the versatile and widely used processes [71,78,83]. The principle behind the thermal spray is to melt the material feedstock (wire or powder), accelerate the melt to impact on a substrate where rapid solidification and deposit buildup occur. Thus, a heat source and a means of accelerating the material are required. This is pictured schematically in Fig. 2.3 [84].

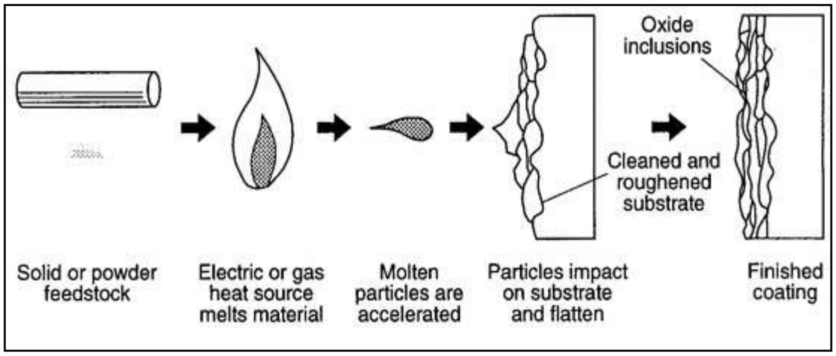

Fig. 2.3. A schematic over view of thermal spray process [84].

Thermal spray technique was recommended for ceramic coatings on graphite and graphite ceramic systems [85,86]. The most important advantage of thermal spray coatings is the possibility of on-site application and repair of components, given a sufficient accessibility for the sprayer and it equipment [81]. Plasma spraying is one of the extensively used thermal spray processes because of the ability to deposit several metallic and ceramic materials with high deposition rate [87,88] of coating to reduce high temperature oxidation and molten salt corrosion. In economical point of view, cost performance ratios of thermal sprayed coatings are of special interest [81]. Plasma spray process is capable of producing micrometer range thick coatings with deposit efficiency < 50 to 90% and deposit rate <3 kg/h to 50 kg/h for reproducible and durable coatings [81]. Plasma spray process is a straight forward technique scaling from laboratory experiments to industrial production [89]. All materials can be sprayed by plasma spray process on any type of substrate [90]. The adhesion of ceramic coatings to metallic and non-metallic materials is poor. For improving the adhesion of ceramic coatings to the substrates a bond coat was used as an intermediate coating. Many review articles [91,92] provide extensive details of plasma spray process in the literature. Therefore, detailed discussion on the plasma spray process is not attempted, but the performance of plasma sprayed coatings in molten salt is focused in the following section, as it is of relevance to the present work.

YSZ (7-9 wt%) with an intermediate metallic bond coat (NiCrAlY) is considered as one of the options to protect the structural materials (viz. type 316L SS) of salt purification vessel. Corrosion studies carried out on YSZ coated 316L SS in molten LiCl-KCl salt at 773 K for 500 and 1000 h exhibited better corrosion resistance compared to uncoated 316L SS [47,58]. Weight loss studies indicated that the percentage of weight loss for 500 and 1000 h exposed samples was negligible and no significant degradation or penetration of salt across the coating was observed [58]. Partially stabilized zirconia (PSZ) coated on 9Cr-1Mo samples and tested in molten LiCl-KCl salt up to 2000 h showed marginal increase in weight, but the coating exhibited large number of cracks and buckling [49]. The results indicated that premature spallation of PSZ coating on 9Cr-1Mo could have occurred due to accidental ingress of oxygen and moisture [49]. YSZ and Al_2O_3 coatings on Inconel 713LC by plasma spraying were tested in molten LiCl-3 wt % Li_2O salt at 923 K in a mixed gas of Ar-10 wt% O_2 for 24 to 168 h. The corrosion rate for the Al_2O_3 coating was 5.8×10^{-2} μm/h while for YSZ coating, it is nearly zero. A porous reaction layer was formed due to reaction of Al_2O_3 with Li_2O. The dense amorphous reaction layer on the surface of the YSZ coating offered better protection and provided an effective barrier against the LiCl-Li_2O molten salt [59].

Plasma sprayed ZrO_2 and ZrO_2-SiO_2 coatings on graphite and pyrolytic graphite coating on high density graphite by chemical vapour infiltration were tested in NaCl-KCl-CsCl-UO_2Cl_2 (5 wt % U) for 6 h at 873 and 923 K under Cl_2 +O_2 gas. Based on the corrosion results, the life time of ZrO_2 is shortest compared to ZrO_2-SiO_2 and pyrolytic graphite while the lifetime of ZrO_2-SiO_2 was estimated to be three times longer than that of ZrO_2 and pyrolytic graphite. ZrO_2-SiO_2 material was found to be the most promising compared to pyrolytic graphite [28]. ZrO_2-Y_2O_3 and Al_2O_3-Cr_2O_3 coatings on IN713LC by plasma spraying were tested in molten LiCl-3 wt% Li_2O salt at 948 K in a mixed gas of Ar-10% O_2 for 216 h. Superior corrosion resistance shown by ZrO_2-Y_2O_3 and Al_2O_3-Cr_2O_3 top coat was attributed to their chemical and thermal stability [60,93]. Adhesion and chemical stability tests were conducted on graphite coated with TiN and TiC by chemical vapor deposition by Maiya et al. [94]. The coated specimens were exposed to a corrosive molten salt $CaCl_2$ and a liquid metal alloy (Zn-10 wt.% Mg) at 1073 K for 168 h to determine the corrosion resistance. No reaction discontinuity of coatings along the interface was detected by scanning electron microscopy or energy-dispersive X-ray spectroscopy. TiN and TiC coatings on graphite were chemically stable in corrosive and reducing molten salt and liquid metal alloy baths in addition to displaying good adherence. It is apparent that graphite coated with TiC and TiN by chemical vapour deposition is a promising container material for pyrochemical processing [94]. High density graphite substrates have been coated with Y_2O_3 using pulsed laser deposition technique and were exposed to molten LiCl-KCl salt at 873 K. The results revealed that Y_2O_3 coating offers better compatibility and provides protection to high density graphite from the attack by molten chloride salt [95**]**.

2.6 Coatings for heavy metal consolidation application

For various applications, uranium and its alloys are generally melted by induction heating in ceramic coated graphite crucibles under vacuum [96]. Graphite has been the proposed crucible material for such applications, because of its high-temperature strength and resistance to thermal shock. The crucible material for processing of molten uranium should satisfy the following requirements: (a) withstand the thermal cycle, (b) ease of release of uranium ingot, (c) should not interact with and contaminate the ingot, (d) should be reusable and (e) preferably does not require extensive preparation methods. As carbon readily reacts with uranium, it must be coated to prevent reaction with uranium. Even very little contact between the molten uranium and graphite causes an interaction that lead to the ingot being firmly stuck with the crucible. This usually requires destruction of the crucible to recover the ingot. Other crucible materials such as ceramics and metals have also been tested due to the stringent requirements. Owing to the presence of 20-30 wt % chloride salt along with uranium deposited in the cathode, it is all the more difficult to select materials for such processes [97]. Holcombe et al. [98] estimated the chemical reactivity of different ceramic oxide coating materials with both uranium and carbon based on the temperatures of interaction and summarized the oxide/uranium interactions. Al_2O_3, Y_2O_3 and ZrO_2 coatings obtained by sponging, brushing or spraying on graphite were tested under cathode processor operating conditions up to 1573 K under vacuum. Al_2O_3 coating failed to adhere well to graphite, yttria was attacked by the chloride salts and zirconia coating resulted in degradation [97]. Plasma sprayed multilayered coatings on graphite crucibles also gradually deteriorated and flaked off due to lower adhesion strength [97]. Cho et al. [99] employed plasma sprayed alumina and YSZ top coated on graphite for cathode processor application, not only to reduce the reaction between uranium and graphite but also to reduce the interaction between molten salt containing UCl_3 and graphite. Ceramic lined crucibles were developed based on the experience with zirconia coatings. Zirconia based castable liner (78 wt% ZrO_2, 20 wt% Al_2O_3 and 2 wt% C) was developed on graphite crucible for testing under cathode processor operating conditions at 1473 K (< 100 Pa). Ceramic liners improved the performance of graphite crucible for the separation of salt during uranium processing [100].

As Y_2O_3 is highly compatible to molten metals and salts at high temperatures and because of its high melting point and thermal stability, Y_2O_3 was used as coating material for high temperature corrosive environment [101,102]. Y_2O_3 coating is reported to be stable with graphite up to 1873 K without initiation of a reaction with graphite substrate [102]. Plasma sprayed Y_2O_3 coatings on graphite were tested in molten uranium at 1573-1773 K for 30 min. Superior corrosion protection was observed up to 1573 K and above, but it became less satisfactory above 1723 K when applied directly on graphite due to the interaction of graphite with yttria at that temperature [96]. The performance of yttria coating was improved using a bilayer of Nb/ZrO_2 in between Y_2O_3 and graphite up to 1773 K. The Nb/Y_2O_3 coating on graphite crucible was used for seven melts at 1723 K without degradation of coating [96]. Padmanabhan et al. [102] investigated the reaction of Y_2O_3 with uranium using a thermogravimetric TG/DTA analyser at 1473 K for 2 h under helium gas. There was absolutely no reaction of Y_2O_3 coatings with molten uranium. Sticking of uranium pellet to Y_2O_3 buttons was also not observed by them. Based on these results, Y_2O_3 coating was plasma sprayed on tantalum for processing liquid uranium at 1573 K and tested for 80 h [103]. The Y_2O_3 coating exhibited excellent corrosion resistance against liquid uranium. No reaction products were observed at the uranium-Y_2O_3 interface. Instabilities leading to crack and spallation of the coating were not observed indicating that the coating had good adhesion to the tantalum substrate [103].

Kim et al. [104] used plasma spray process to deposit HfN, TiC, ZrC, and Y_2O_3 coatings on niobium substrate and conducted melt interaction studies with U-Zr fuel at 1823 K for 15 min under vacuum. HfN and Y_2O_3 didn't form significant reaction layers between U–20wt % Zr melt and the coating layer. Y_2O_3 coating was found to be the most promising coating material compared to HfN, TiC and ZrC for re-usable crucibles for metallic fuel processing due to good thermal compatibility with U–20 wt.% Zr melt. Thermal cycling tests were conducted up to 1723 K at a rate of 193 K/min, held for 30 min, followed by cooling to room temperature. The results indicated that HfN, TiC, ZrC, and Y_2O_3 coatings possessed good thermal cycling characteristics with the development of only a few interconnected cracks in ZrC and no interconnected cracks in the other materials even after 20 cycles, exhibiting a good thermal shock resistance [104]. Al_2O_3 substrates coated with TiN by ion beam assisted deposition technique were tested with uranium at 1773 K for 4 h under a vacuum of 10^{-4} Pa. TiN thin film was appeared to protect alumina, because no reaction between TiN and uranium was observed even at 1700 K. However, TiO_2 was formed at the interface of substrate-coating because of the reaction between TiN and Al_2O_3 [105]. HfN plasma sprayed on niobium crucible was tested under cathode processor conditions (heated to 1473 K at pressure less than 100 Pa) and coated crucibles were found to perform for 15 runs with uranium and salt. No apparent degradation on the crucible or its HfN coating was observed. No difficulties were encountered on ingot dumping [106]. Holcomb et al. [107] used aluminium titanate (Al_2TiO_5) coated titanium crucible for melting uranium at 1413-1523 K for 5 to 45 min, under a vacuum of $< 1 \times 10^{-5}$ torr. No cracking and spallation of Al_2TiO_5

coating was observed after melting, and the pellets could be detached easily from the crucibles. Brown coloured uranium oxide films were observed on the surface of coating due to the slow and time dependent reduction of aluminium titanate by molten uranium. Uranium titanate was not detected probably due to its unstable nature above 1313 K [107]. BeO crucible showed good chemical stability with process materials and could withstand thermal stresses of the process cycle. BeO crucibles are expected to provide reliable multi-use in addition to avoiding special preparation procedures [97]. Nevertheless, because of its high toxicity, usage of BeO coatings or its substrates is avoided. Reaction of lanthanum phosphate ($LaPO_4$) with uranium evaluated by differential thermal analysis at 1473 K for 2 h under helium gas showed no reaction between molten uranium and $LaPO_4$. The chemical stability of $LaPO_4$ with molten uranium and its stability against hydration reaction indicated its usefulness for molten uranium handling as well as thermal barrier applications [108]. Refractory oxides (Y_2O_3), carbides (NbC, VC, ZrC), nitrides (AlN, NbN, TaN, ZrN, VN, TiN) and sulfides (CeS) applied quartz and refractory metals were examined as mould coating materials for casting metallic fuel of IFRs [109]. Sessile drop tests were employed to study the interaction between ceramic coatings and molten U-10 wt% Zr at 1823 K. Among these coatings NbC, TiN and Y_2O_3 were found to be non-wetting with U-10%Zr; however, Y_2O_3 coating alone completely avoided adhesion of the fuel [109]. Coating materials such as CaO,ThO_2, Er_2O_3, MgO, HfO_2, Al_2O_3 and BeO plasma sprayed on W-Re, W, AlN, TiN, ZrB_2 and TiC were tested for their compatibility in cathode processor operation in order to identify a durable coating which would facilitate easy ingot release, minimize contamination and avoid loss of uranium metal. However, these coatings did not perform up to the required level of satisfaction [100].

For the purpose of corrosion protection, nanostructured coatings have been developed on structural materials for reprocessing applications [110]. Nitrides possessing high hardness, melting point and thermodynamic stability against reactive materials and molten LiCl–KCl salts have greater potential for coating graphite crucibles [111]. Gibb's free energy values calculated for the reactions of TiN, ZrN and HfN with uranium from 373-1773 K indicated that these nitrides are stable in molten uranium [111]. Nanocrystalline TiN, ZrN and Ti–Si–N coatings were developed by DC/RF magnetron sputtering on high density graphite disc and crucibles for uranium melting experiments [111]. No significant coating detachment was observed after blank run and with uranium melting even at a very high heating rate of 358 K/min. TiN and Ti-Si-N coating appeared to offer better stability in comparison to ZrN [111]. Nanostructured thin film yttria was coated by pulsed laser deposition (PLD) on plasma sprayed thick Y_2O_3 coatings to seal and fill up the pores and cracks generated on the surface of the sprayed coatings in order to improve the performance of coatings on moulds and crucibles for handling molten uranium [101]. Uranium melting experiments were conducted on Y_2O_3 coated HD graphite crucibles by pulsed laser deposition at 1623 K for 20 min [112]. Phase identification by XRD revealed only cubic Y_2O_3 phase and peaks corresponding to uranium were absent. No detachment of coating was observed after uranium melting [95,112].

2.7 Post treatments on plasma sprayed coatings

The presence of porosity and microcracks in plasma sprayed coatings is a drawback and these may cause corrosion of the substrate on prolonged exposure to molten salts. The microstructure of plasma sprayed coatings can be modified by post treatments [113]. The commonly used post spray treatments for thermal spray coatings to protect from different corrosive environments are: chemical/physical (organic sealing, aluminizing and chromizing), thermal (fusion, heat treatment, diffusion, recrystallization, laser glazing and hot isostatic pressing) and mechanical (machining, grinding, shot peening and polishing) treatments [114]. Heat treatments induce grain growth, initiate precipitation and interlamellar porosity will change to spherical porosity [92]. Among the four approaches proposed by Jones [115], to mitigate the corrosion of thermal barrier coatings one of them is laser based glazing or melting or sealing of coating to obstruct the penetration of salt into the coating. There are many literatures available reported related to the surface modification of plasma sprayed coatings by post treatments like annealing and laser melting for molten salt applications for aerospace and gas turbine blades [116-118]; hence this review highlights the literature related to the post treatments for plasma sprayed coatings for pyrochemical reprocessing activity alone. Ravi shankar et al. [119] performed laser melting using a continuous wave CO_2 laser of 10.6 mm wavelength with a beam diameter of 1.5 mm to eliminate porosity and microcracks in the YSZ coating. The surface morphology of laser melted YSZ coating exhibited dense layer with segmented cracks on the surface. After laser melting the porosity decreased from 10% in the as-coated sample to 0.5% in the laser treated samples. Delamination occured near the bond coat/ceramic interface in the coating as the thickness of the melted layer was high for higher laser power. With increasing laser power, the non-transformable tetragonal phase increased marginally in YSZ coating, which is beneficial for resisting to thermal shock [119]. Laser remelted surface exhibited a sharp interface with coarse and fine grains which was attributed to the reheating effect. The segmented crack on the surface of laser remelted sample decreased further by applying ZrO_2 and ZrO_2 + SiO_2 sealant and heat treating [120]. From the foregoing discussions, it is evident that post-plasma-spray treatments enhance surface properties and chemical bonding at the substrate/ceramic interface and the modified microstructure would improve the physical, chemical and mechanical properties of the plasma-sprayed coatings. Based on the literature, post spray treatments were employed for the plasma sprayed ceramic coatings in the present work to enhance the properties of the coatings for molten salt applications in pyroreprocessing.

2.8 Need for the present study

The literature review suggests that the alloys and carbon materials employed for high temperature molten salt and uranium applications are prone to undergo degradation and attacked by molten salt and uranium medium; hence, providing ceramic coatings is the most appropriate method to protect the structural and container materials from molten salt as well as to control the reactivity with molten uranium. The corrosion studies reported in the literature were carried out on various materials in different molten salt systems, which are not relevant to the present application of carbon materials under molten LiCl-KCl salt medium to be used for the reprocessing of spent metallic fuels. Hence, this study assumes importance as there are not many reports on the corrosion behaviour of carbon materials in LiCl + KCl salt is available. The present work also attempts to emphasis the need for developing coatings on carbon materials for pyroreprocessing applications. The ceramic coatings identified were deposited on graphite for handling molten salt as well as melting of uranium. The developed ceramic coatings will be evaluated under demanding environments (molten salt, reactive metallic uranium at high temperatures) of the salt purification vessel and cathode processor crucible. The complete and in-depth microstructural analysis is carried out on carbon and coated materials by various characterization techniques to understand the mechanism of interactions and phase changes affecting the performance of the coated as well as uncoated carbon materials under the above environments.

References

[1] Pyrochemical Separations in Nuclear Applications, A Status Report, Prepared by nuclear energy agency, organization for economic co-operation and development, ISBN 92-64-02071-3 (2004) pp. 1-179.

[2] K. Nagarajan, T. Subramanian, B. Prabhakara Reddy, P. R. Vasudeva Rao, Baldev Raj, Nuclear Technology 162 (2008) 259-263

[3] Y. Arai, T. Ogawa, Research on nitride fuel and pyrochemical process for MA transmutation, pp. 445-457. *https://www.oecd-nea.org/pt/docs/iem/madrid00/Proceedings/Paper37.pdf*

[4] K.M. Goff, Idaho National Laboratory, Report on Non-Aqueous Processes (2005), pp-1-9.

[5] S.X. Li, T.A. Johnson, B.R. Westphal, K.M. Goff, R.W. Benedict, Electrorefining Experience For Pyrochemical Processing Of Spent EBR-II Driver Fuel, Proceedings of GLOBAL 2005, Tsukuba, Japan, Oct (2005) Paper No. 487.

[6] T. Nishimura, T. Koyama, M. Iizuka, H. Tanaka, Prog. Nucl. Energ. 32 (1998) 381-387.

[7] H. Lee, G-I. Park, K-H. Kang, J-M. Hur, J-G. Kim, D-H. Ahn, Y-Z. Cho, E.H. Kim, Nucl Eng Technol. 43 (2011) 317-28.

[8] J.H. Lee, Y.H. Kang, S.C. Hwang, J.B. Shim, E.H. Kim, Nucl. Technol. 162 (2008) 135-143.

[9] B.R. Westphal, S.X. Li, G.L. Fredrickson, D. Vaden, T.A. Johnson, J.C. Wass, Evaluation of 2.25cr-1mo alloy for containment of LiCl/KCl eutectic during the pyrometallurgical processing of used nuclear fuel, INL/CON-10-19580, March (2011).

[10] F. Colom, A. Bodalo, Melts,Corr. Sci.12 (1972) 731-38.

[11] J.E. Battles, F.C. Mrazek, W.D. Tuohig, Materials Corrosion Molten-Salt Lithium/Sulfur Cells, Corrosion Problems in Energy Conversion and Generation, C.S. Tedmon, Jr (ed.,) Princeton, NJ: The Electrochemical Society (1974) pp. 20-31.

[12] H.O. Pierson: Handbook of carbon, graphite, diamond and fullerenes, 1st edn, Noyes publications, Park ridge, New Jersey (1993).

[13] L.D.D Castro, B. McEnaney, Corros. Sci. 33 (1992) 527-543.

[14] R.E. Nightingale, Graphite: Advantages, limitations, and applications, Status report of Pacific Northwest laboratories, Richland, Washington, (1966) pp. 1-16.

[15] J. M. Criscione, R. L. Reddy, C. F. Fulgenzi, D. J. Page, F. F. Fisher, A. J. Dzermejko, J. B. Hedge, Graphite, Applications of Artificial, in: Kirk-Othmer Encyclopedia of Chemical Technology, (2000).

[16] M. Inagaki, New Carbons-Control of structure and functions, Elsevier Science Ltd, Oxford (2006).

[17] J. Rautavuori, P. Tormala, J. Mater. Sci. 14 (1979) 2020-2022.

[18] T. Noda, M. Inagaki, S. Yamada, J. Non-Crystalline Solids 1 (1969) 285-302.

[19] G.M. Jenkins, K. Kawamura, Polymeric carbons-Carbon fiber, glass and char, Cambridge University Publications, Cambridge (1976).

[20] J. Vacik, H. Naramoto, J. Cervena, V. Hnatowicz, I. Peka, D. Fink, J. Nucl. Mater. 289 (2001) 308-314.

[21] W.V. Kotlensky, Deposition of pyrolytic carbon in porous solids in Chemistry and physics of carbon, Marcel Dekker publication, Vol.9 (1973) pp.173-262,

[22] A. W. Moore, Carbon 5 (1967) 159-162.

[23] M. Turkat, W. A. Robba, US Patent 2442617, 1969.

[24] S. Yajima, T. Satow, T. Hirai, J. Nucl. Mater. 17 (1965) 127-135.

[25] J. Pappis, S. L. Blum, J. Am. Ceram. Soc. 44 (1961) 592-597.

[26] S. Yajima, T. Satow, T. Hirai, J. Nucl. Mater. 17(1965) 116-126.

[27] X. Bourrat, O. Dugne, Pyrocarbon-based multilayer for HTR fuel particles, pp.1-8 *http//:acs.omnibooksonline.com/data/papers/2004_M036.pdf*

[28] M. Asou, S. Tamura, T. Namba, H. Kamoshida, Y. Shoji, K. Mizuguchi, T. Kobayashi, The corrosion resistance tests of crucible materials for oxide pyro-process, in: Proceedings of International Conference on Future Nuclear Systems (Global'99), Jackson Hole, WY, USA, Aug (1999).

[29] M. Takeuchi, T. Kato, K. Hanada, T. Koizumi, S. Aose, J. Phys. Chem. Solids 66 (2005) 521–525.

[30] www.nea.fr/pt/iempt8/abstracts/Abstracts/Sakamura.pdf

[31] T. Inoue, L. Koch, Nucl. Eng. Technol. 40 (2008) 183-190.

[32] H. Hayashi, T. Koizumi, T. Washiya, K. Koizumim, US Patent 6793894, 2004.

[33] A. Magdziarz, Arch Metall Mater 51 (2006) 471-474.

[34] Nakamura K, Morooka H, Tanabe Y, Yasuda E, Akatsu T, Shindo H. Corros Sci. 53 (2011) 4010-13.

[35] H. Boussie, Pyrometallurgical processing research program "PYROREP"-final report, (2003).

[36] Electrometallurgical techniques for DOE spent fuel treat: By Committee on Electrometallurgical Techniques for DOE Spent Fuel Treatment, Board on Chemical

Sciences and Technology, National Academy Press, Washington, D.C. (2000) pp. 1-116.

[37] R.W. Benedict, S.P. Henslee. EBR-II spent treatment demonstration project status. 5th international nuclear conference on recycling, conditioning and disposal, Nice, France (1998) pp. 149-55.

[38] U. Kamachi Mudali, A. Ravi Shankar, C. Mallika, K. Thyagarajan, S. Ningshen, B.P. Reddy, K. Nagarajan, Materials and coating technologies for pyrochemical reprocessing of spent metallic fuel from fast breeder reactors. Kalpakkam, India, IGC/MMG/CSTG/2011, (2011) pp. 1-47

[39] V. Bernardet, S. Gomes, S. Delpeux, M. Dubois, K. Guérin, D. Avignant, G. Renaudin, L. Duclaux, J. Nucl. Mater. 384 (2009) 292–302.

[40] J. Vacik, H. Naramoto, J. Cervena, R. Mach, Czechoslovak Journal of Physics 49 (1999) 997-1002.

[41] W.D. Manly, J.W. Allen, W.H. Cook, J.H. DeVan, D.A. Douglas, H. Inouye, H. Jansen, P. Patriarea, T.K. Roche, G.M. Slaughter, A. Taboada, G.M. Tolson, Construction materials for molten salt reactors. In: MacPherson HG, editor. Molten salt reactors, Part-II, Tennessee; Oak Ridge National Laboratory Press, (1958) pp. 595-625.

[42] S. Feng, L. Xu, L. Li, S. Bai, X. Yang, X. Zhou, J. Nucl. Mater. (2013), doi: http://dx.doi.org/10.1016/j.jnucmat.2013.06.035

[43] W.R. Grirnes, Chemical Research and Development for Salt Breeder Reactors, Oak Ridge National Laboratory, ORNL-TM-1853, pp.1-133.

[44] R.A. Rapp, Pure. Appl. Chem. 62 (1990) 113-122.

[45] A. Nishikata, H. Numata and T. Tsuru, Mater. Sci. Eng. A 146 (1991) 15-31.

[46] R.D. Kane, Molten salt corrosion, ASM Handbook, Volume 13A: Corrosion: Fundamentals, Testing, and Protection, S.D. Cramer, B.S. Covino, Jr. (eds.,) (2003) pp. 216-219.

[47] A. Ravi Shankar, U. Kamachi Mudali, Mater. Corros. 59 (2008) 878-882.

[48] L. Burris, R.K. Steunenberg and W.E. Miller, The Application of Electrorefining for Recovery and Purification of Fuel Discharged from the Integral Fast Reactor, AIChE Symposium Series No.254, 83 (1987): pp. 135.

[49] A. Ravi Shankar, K. Thyagarajan, U. Kamachi Mudali, Corrosion 69 (2013) 655-665.

[50] M.A. Uusitalo, P.M.J. Vuoristo, T.A. Mantyla, Corros. Sci 46 (2004) 1311-1331.

[51] A. Ravi Shankar, S. Mathiya, K. Thyagarajan, U. Kamachi Mudali, Metall. Mater. Tran. A 47 (2010) 1815-1825.

[52] A. Ravi Shankar, U. Kamachi Mudali, Corrosion (Under review)

[53] Y. Hosoya, T. Terai, T. Yoneoka, S. Tanaka, J. Nucl. Mater. 248 (1997) 348-353.

[54] J.E. Indacochea, J.L. Smith, K.R. Litko, E.J. Karell, J. Materials Research 4 (1999) 1990-1995.

[55] J.E. Indacochea, J.L. Smith, K.R. Litko, E.J. Karell,A.G. Raraz, Oxidation of Metals 55 (2001) 1-16.

[56] P. Periasamy, M.F. Hurley, B.M. Marx, M.F. Simpso, D.P. Butt, J. Nucl. Mater. 405 (2010) 266–273.

[57] D.A. Shifler, Factors that Influence the Performance of High Temperature Coatings, CORROSION 2006, Paper id: 06475, San Diego Ca, NACE International, March (2006).

[58] A. Ravi Shankar, U. Kamachi Mudali, R. Sole, H.S. Khatak, Baldev Raj, J. Nucl. Mater. 372 (2008) 226–232.

[59] H.-Y. Lee, K.-H. Baik, Met. Mater. Int. 15 (2009) 783–787.

[60] S.-H. Cho, B.-H. Park, J.-M. Hur, H.-S. Lee, K.-C. Song, J.-H. Lee, Corros. Sci. 52 (2010) 2353–2364.

[61] X.Q. Cao, R. Vassen, D. Stoever, J. Europen Ceram. Soc. 24 (2004) 1-10.

[62] P.V. Ananthapadmanabhan, T.K. Thiyagarajan, K.P. Sreekumar, R.U. Satpute, N. Venkatramani, K. Ramachandran, Surf. Coat. Technol. 168 (2003) 231-240.

[63] Z. Znamirowski, L. Pawlowski, T. Cichy, W. Czarczynski, Surf. Coat. Technol. 187 (2004) 37-46.

[64] K.A. Habib, J.J. Saura, C. Ferrer,M.S. Damra, E. Gimenez, L. Cabedo, Surf. Coat. Technol. 201 (2006) 1436-1443.

[65] R. Tomaszek, L. Pawlowski, J. Zdanowski, J. Grimblot, J. Laureyns, Surf. Coat. Technol. 185 (2004) 137-149.

[66] V. Fervel, B. Normand, C. Coddet, Wear 230 (1999) 70-77.

[67] Y. Jin, Y. Yang, Surf. Coat. Technol. 88 (1997) 248-254.

[68] V. Fervel, B. Normand, H. Liao, C. Coddet, E. Beˆche, R. Berjoan, Surf. Coat. Technol. 111 (1999) 255-262.

[69] Steeper, T.J.; Riggs II, W.L.; Rotolico, A.J.; Nerz, J.E.; Varacalle, D.J.; and Wilson, G.C. A taguchi experimental design study of plasma sprayed alumina-titania coatings. Proceedings of 4th National Thermal Spray Conference on Thermal spray coatings: Properties, Processes and Applications, Pittsburgh, Pennsylvania, USA, - ASM International, Materials Park, Ohio, May (1991) pp.13-20.

[70] B. Normand, V. Fervel, C. Coddet, V. Nikitine, Surf. Coat. Technol.123 (2000) 278-287.

[71] S. Bose, High Temperature Coatings, Butterworth-Heinemann Publications, USA (2007) pp. 155-232.

[72] J. Moon, H. Choi, H. Kim, C. Lee, Surf. Coat. Technol. 155 (2002) 1-10.

[73] K. Negita, Acta. Metall. 37 (1989) 313-317.

[74] O. Ruff, E. Ebert, Z. Anorg. Allg. Chem. 180 (1929) 19.

[75] D.K. Smith, C.F. Cline, J.Am. Ceram. Soc. 45 (1962) 249-250.

[76] D.P. Duwez, F. Odell, J. Am. Ceram. Soc. 33 (1950) 274-283.

[77] K.S. Mazdiyasni, C.T. Lynch, J.S. Smith II, J. Am. Ceram. Soc. 50 (1967) 532-537.

[78] R.L. Jones, Thermal barrier coatings, in: K.H. Stern (Ed.), Metallurgical and Ceramic Protective Coatings, Chapman and Hall, London, (1996) pp.194–235.

[79] E. Lugscheider, I. Kvernes, Thermal barrier coatings: powder spray process and coating technology, in: N.B. Dahotre, T.S. Sudarshan (Eds.), Intermetallic and Ceramic Coatings, Marcel Dekker Inc., New York/Basel, 1999, pp. 267–306.

[80] J. Stringer, Mater. Sci. Eng. 87 (1987) 1-10.

[81] G.R. Heath, P. Heimgartner, G. Irons, R. Miller, S. Gustafsson, Mater. Sci. Forum 251-254 (1997) 809-816.

[82] H. Singh, B. S. Sidhu, D. Puri, and S. Prakash, Mater. Corros. 58 (2007) 92-102

[83] P. Chagnon, P. Fauchais, Ceram. Int. 10 (1984) 119-131.

[84] H. Herman, S. Sampath, Metallurgical and Ceramic Protective Coatings: in Thermal spray coatings, K.H. Stern (ed.,) Springer Netherlands (1996) pp. 261-289.

[85] N. Mesrati, H. Ajhrourh, N. Du, D. Treheux, Thermal spraying on graphite, in: C. Coddet (Ed.), Thermal Spray: Meeting the Challenges of the 21st Century, Proceedings of the 15th International Thermal Spray Conference, ASM International, Ohio (1998) pp. 1501–1512.

[86] N. Mesrati, H. Ajhrourh, N. Du, D. Treheux, J. Therm. Spray Technol. 9 (2000) 95-99.

[87] J.T. DeMasi-Marcin, D.K. Gupta, Surf. Coat. Technol. 68/69 (1994) 1-9.

[88] H. Singh, D. Puri, S. Prakash, Surf. Coat. Technol. 192 (2005) 27–38.

[89] H.D. Steffen, M. Mack, Pure and Applied Chemistry 62 (1990) 1801-1808.

[90] E. Pfender, Surf. Coat. Technol. 34 (1988) 1-14.

[91] R. Sivakumar, S.V. Joshi, Trans. Ind. Ceram. Soc. 50 (1991) -14.

[92] H.D. Steffen, M. Mack, Pure. Appl. Chem. 62 (1990) 1801-1808.

[93] S-H. Cho, S-B. Park, D-S. Kang, M-S. Jeong, H. Park, J-M. Hur, H-S. Lee, J. Nucl. Mater. 399 (2010) 212–218

[94] P.S. Maiya, R.A. Erck, B.M. Moon, Surf. Coat. Technol. 102 (1998) 218-222.

[95] Jagadeesh Sure, Maneesha Mishra, M. Tarini, A. Ravi Shankar, N.G. Krishna, P. Kuppusami, C. Mallika, U. Kamachi Mudali, Thin Solid Films 544 (2013) 218- 233.

[96] J. W. Koger, C. E. Holcombe, J. G. Banker, Thin Solid Films 39 (1976) 297-303.

[97] A.R. Brunsvold, P.D. Roach, B.R. Westphal, Proceedings of 8th International Conference on Nuclear Engineering, , ASME, Baltimore, USA, April 2000.

[98] C.E. Holcombe, J.G. Banker, Metall. Trans. B 9 (1978) 317-319.

[99] C-h Cho, Y-s Lee, E-s Kim, J-g Kim, H-s Lee, J. Radioanal. Nucl. Chem. 287 (2011) 485-490.

[100] B.R. Westphal, K.C. Marsden, J.C. Price, Met. Mater. Trans. A 40 (2009) 2891-2866.

[101] A.K. Singh, T.R.G. Kutty, S. Sinha, J. Nucl. Mater. 420 (2012) 374-381.

[102] P.V.A. Padmanabhan, S. Ramanathan, K.P. Sreekumar, R.U. Satpute ,T.R.G. Kutty, M.R. Gonal, L.M. Gantayet, Mater. Chem. Phys. 106 (2007) 416-421.

[103] N. Alangi, J. Mukherjee, P. Anupama, M.K. Verma, Y. Chakravarthy, P.V.A. Padmanabhan, A.K. Das, L.M. Gantayet, J. Nucl. Mater. 410 (2011) 39–45.

[104] K.H. Kim, C.T. Lee, C.B. Lee, R.S. Fielding, J.R. Kennedy, Thin Solid Films 519 (2011) 6969-6973.

[105] G. de Vasconcelos, L. C. O. Dacal, M. E. Sbampato, N. A. S. Rodrigues, J. R. Martinelli, Phys. Stat. Sol. a 201 (2004) 2351–2355.

[106] B.R. Westphal, K.C. Marsden, J.C. Price, D.V. Laug, Nucl. Engg. Technol. 40 (2006) 163-174.

[107] C.E. Holcomb, G.L. Powell, J. Nucl. Mater. 49 (1973/74) 238-240.

[108] P.V. Ananthapadmanabhan, K.P. Sreekumar, T.K. Thiyagarajan, R.U. Satpute, K. Krishnan, N.K. Kulkarni, T.R.G. Kutty, Mater. Chem. Phys. 113 (2009) 417–421.

[109] P.S. Chen, W.C. Stevens, C. L. Trybus, Reusable molds for casting u-zr alloys, 6th International Conference on Surface Modification Technology, Chicago, Illinois, November (1992).

[110] U. Kamachi Mudali, S. Ningshen, A. Ravi Shankar, Pure. Appl. Chem. 83 (2011) 2079.

[111] A. Ravi Shankar, B. Prabhakara Reddy, Vipin Chawla, M. Jeya Preyanga, Ramesh Chandra, U. Kamachi Mudali, Surf. Coat. Technol. 204 (2010) 3214-3221.

[112] Jagadeesh Sure, IGC News Letter 96 (2013) 15-19.

[113] S.S. Chatha, H.S. Sidhu, B.S. Sidhu, Role of post treatment in thermal spray coatings, National Conference on Advancements and Futuristic Trends in Mechanical and Materials Engineering, October (2011).

[114] J.R. Davis and associates, ASM Handbook, Metallography and microstructure, ASM International, Materials Park, Ohio, Vol. 9 (2004) pp. 1038-1046.

[115] R.L. Jones, J. Thermal Spray Technol. 6 (1997) 77-84.

[116] I. Zaplatynsky, Thin Solid Films 95 (1982) 275-284.

[117] A. Petitbon, L. Boquet, D. Delsart, Surf. Coat. Technol. 49 (1991) 57-61.

[118] C. Batista, A. Portinha, R.M. Ribeiro, V. Teixeira, M.F. Costa, C.R. Oliveira, Appl. Surf. Sci. 247 (2005) 313-319.

[119] A. R. Shankar, B. J. Babu, R. Sole, U. Kamachi Mudali, H. S. Khatak, Surf. Eng. 23 (2007) 147-154.

[120] A. Ravi Shankar, U. Kamachi Mudali, Surf. Eng. 25 (2009) 241-248.

CHAPTER 3

MATERIALS, METHODS AND CHARACTERIZATION TECHNIQUES

This Chapter presents the carbon materials and their properties and evaluated using various tests. The experimental details of ceramic coatings on graphite by plasma spray process. The complete experimental testing information and characterization techniques used for microstructural analysis are also discussed.

3.1 Materials selection, their properties and their composition

3.1.1 Carbon materials

Four different types of carbon materials namely low density graphite (LDG), high density graphite (HDG), glassy carbon (GC) and pyrolytic graphite (PyG) were selected for the molten salt corrosion experiments. The PyG investigated for corrosion behavior in molten salt was deposited by chemical vapour deposition (CVD) at 2323–2373 K in an indirect heating reactor by pyrolysis of methane gas. The detail of the CVD technique and the optimized deposition parameters for PyG were described by Nowicki et al. [1] and was received from Poland. The optimized deposition parameters for developing PyG for the purpose of corrosion studies are listed in Table 3.1. PyG was deposited on graphite up to dimensions approximately 20 cm length, 6 cm width and 2.5 mm thickness. The properties of the four carbon materials are compared in Table 3.2. The variation in the physical properties of LDG, HDG, GC and PyG is mainly due to the method of preparation of these four carbon materials. Even though the method of preparation for LDG and HDG is same, they differ significantly in density, porosity, grain size and specific surface area because of variation in the baking temperature and the parameters used for compaction. LDG and HDG materials were of origin from Japan and supplied by M/s. Nickunj Pvt Ltd, Mumbai. GC was procured from M/s. SIGRADUR®HTW GmbH, Germany. The open porosity of GC was negligible and its bulk density was moderate. The temperature of formation of PyG is the main controlling parameter in obtaining very fine graphite crystallite size, high density, negligible open porosity and low impurity content compared to other carbon materials. LDG, HDG and PyG were crystalline materials, whereas GC used in the present study was amorphous.

Table 3.1 Deposition parameters for pyrolytic graphite [1].

Deposition parameters	
Heating method	Indirect
Temperature (K)	2323-2373
Pressure (Torr)	10-15
Hydrocarbon gas	CH_4
Flow of methane gas (CH_4) (kg C/sec x 10^6)	4.7 -5.5

3.1.2. Plasma spray materials

Powder size, morphology and composition of the coating materials can have a significant effect on the behaviour during spraying and thus influence the properties of the coatings. Therefore, before spraying the coating the spray powders size, chemistry, method of preparation and composition of the powders should be understood. For the production of reliable coatings by plasma spray process it is essential to have an understanding on the coating composition and selection, spray parameters, surface preparation, substrate properties, heat input etc. [2].

Table 3.2 Properties of the carbon materials LDG, HDG, GC and PyG.

Property	LDG	HDG	GC	PyG
Bulk density (g/cm^3)	1.66	1.85	1.54	2.22
Open porosity (%)	20-22	11-12	negligible	negligible
Average grain size (µm)	32	20	-	0.2
Specific surface area (m^2/g)	25.2	18.6	-	4.7
Impurity content (ppm)	Si -13.824, Ca-4.206, Al-0.134, Fe-0.175, Ni-0.292, Cr-0.007, Cu-0.042, Na-0.247, K-0.024, Mg-0.068	Si-8.253, Ca-3.475,Al-0.046, Fe-0.047, Ni-0.282, Cr-0.001, Cu-0.008, Na-0.004, K-0.003, Mg-0.051	Si -3.873, Al-0.274, Fe-0.925, Ni-0.127, Cr-0.092, Cu-0.034, Na-0.785, K-0.346, Ti-0.092, Zr- 0.063	Si-0.927, Fe0.256,Impurities of La, Nd, Ta, W, Na, Mg, A1, Sc, V, Mn in the order of 10^{-5} % and 2 to 3 % soot
Flexural strength (MPa)	40-43	78	210	120
Hardness (Shore)	67	83	48	37

3.1.2.1 Chemical composition and particle size distribution

Commercially available NiCrAlY and yttria stabilized zirconia (YSZ), Cr_3C_2-25NiCr and Al_2O_3-40wt% TiO_2 (A40T) powders were utilized for coating application. The manufacturing methods and the powder characteristics like particle size distribution, purity and chemical composition are presented in Table 3.3.

Table 3.3 Characteristics and composition of Cr_3C_2-25NiCr, A40T, NiCrAlY and YSZ powders used for plasma spraying.

Powder	Manufacturing process	Particle size distribution (µm)	Purity (%)	Chemical Composition (wt %)
YSZ	Agglomerated	-125 +11	99.9	ZrO_2-Balance Y_2O_3-7-9 SiO_2 – 0.7 Fe_2O_3 – 0.2 TiO_2 - 0.2 Al_2O_3 - 0.2
NiCrAlY	Gas atomization	-106 +53	99.9	Ni - Balance Cr - 21-23 Al – 9-11 Y – 0.8-1.2
A40T	Fused and crushed	-22 +5	99.9	Al_2O_3 – base% TiO_2 - 40.0 % SiO_2 - 0.50% Fe_2O_3 - 0.40% MgO - 0.20% CaO - 0.10%
Cr_3C_2-25NiCr	Agglomerated and sintered	-45 +15	99.9	Ni - 20.0% C - 10.0% Cr - Remaining %

3.1.2.2 Powder morphology

The morphology of the powders is also important because it determines the ability to flow and melt [3]. Representative micrographs of individual particles showing the different particle morphologies of Cr_3C_2-25NiCr, A40T, NiCrAlY and YSZ powders are shown in Fig. 3.1. Cr_3C_2-25NiCr and A40T powders were characterized by SEM-EDX to find out the particle shape and size. To prevent charging, coatings were sputtered with gold prior to SEM analysis. The Cr_3C_2-NiCr powder (Fig. 3.1a) exhibited spherical shaped hollow spheres and these were porous. The elemental composition analysis by EDX yielded Cr as the major (59.79 wt %) content with minor amounts of Ni (17.90 wt %) and C (22.31 wt %). The SEM image of A40T powder (Fig. 3.1b) clearly showed that the particles were irregular in shape and dense in nature. The EDX analysis of A40T powder showed coating elements: Al (37.04 wt %), Ti (27.54 wt %) and O (35.42 wt %) in its composition. NiCrAlY (Fig. 3.1c) and YSZ (Fig. 3.1d) powders consisted of spherical particles of different morphologies with a dense outer shell and a porous core [4,5]. A spherical geometry is beneficial for good flow in the powder feed line, which in turn can lead to high feed and deposition rates.

3.1.2.3 Phase constitution of the starting powders

The XRD patterns for the feedstock Cr_3C_2-NiCr and A40T powders are shown in Fig. 3.2. Figure. 3.2a reveals that the XRD patterns are composed of diffraction peaks for Cr_3C_2 and Ni-Cr phases in Cr_3C_2-NiCr powder. The pattern observed for Ni-Cr may be related to the process of preparation of Cr_3C_2-NiCr powder. However, the major diffraction peaks corresponded to Cr_3C_2. The two major phases identified from XRD pattern in the A40T powder (Fig. 3.2b) are α-$A1_2O_3$, rutile (R-TiO_2) and a small amount of titanium suboxides (Ti_2O_3 and Ti_3O_5).

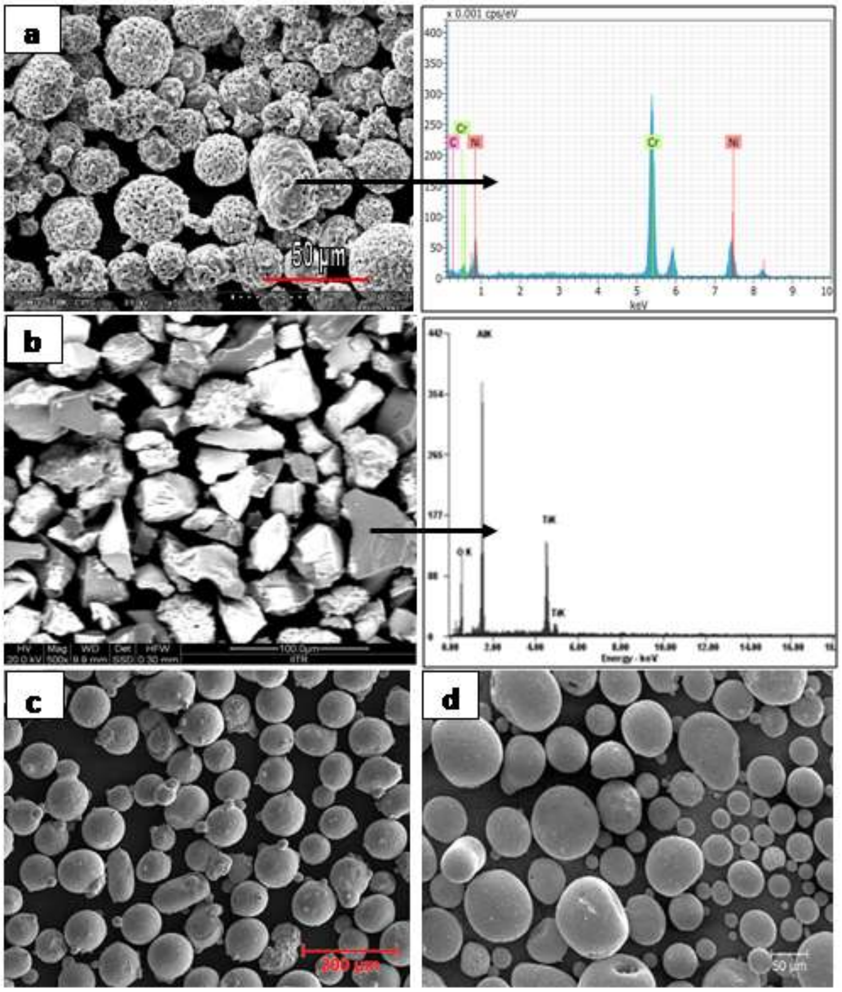

Fig. 3.1 Morphology of (a) Cr_3C_2-25NiCr, (b) A40T, (c) NiCrAlY [4] and (d) YSZ powders [5].

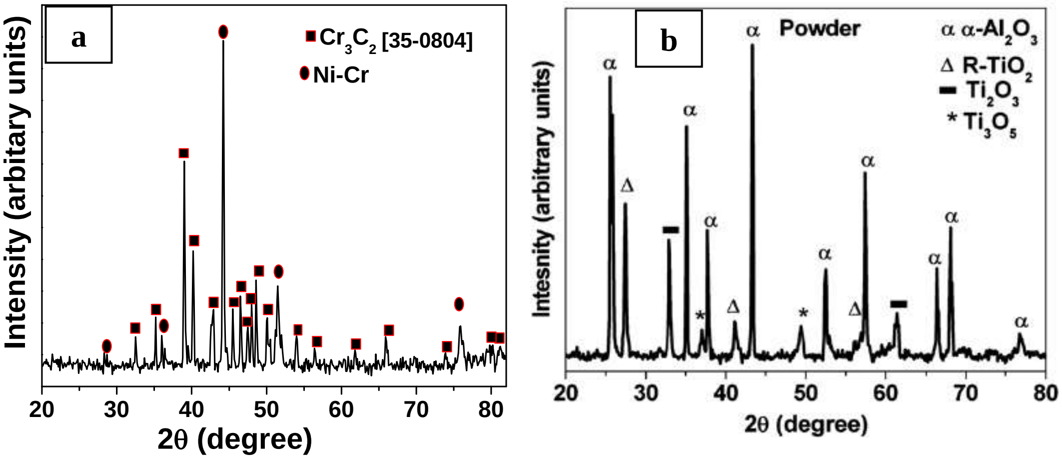

Fig. 3.2 XRD patterns of (a) Cr_3C_2-NiCr and (b) A40T powders.

The powder of YSZ comprised of a mixture of monoclinic and tetragonal zirconia. The X -ray pattern confirmed that the additive resulted in partial stabilization of the tetragonal phase of the zirconia polymorph. The phase constitution of the as-received YSZ powder was in good agreement with the expected compositions as per the phase diagram literature [3].

3.1.3 Coating procedure and post treatments

3.1.3.1 Preparation of substrate

The substrate material used for developing ceramic coatings in the present study was HDG. The sample dimensions used for plasma spraying process were: circular discs of 12 mm diameter and 6 mm thickness and rods of 6 mm diameter and 100 mm length; blocks and crucibles of dimensions of height - 150 mm, OD - 150 mm, ID - 135 mm and height - 100 mm and OD - 100 mm, ID - 85 mm. The properties of HDG substrate have been already discussed in Table 3.2. Plasma spraying requires careful surface preparation of substrate. The preliminary treatment consisted of grit blasted before spraying and cleaning. The main purpose of blasting is to obtain enough surface roughness to ensure proper mechanical anchoring of the coating. Also, impurities present on the surface of HDG substrates can be removed by blasting. For obtaining good adhesion between the substrate and coating, the surface of graphite sample was sand blasted for 10 min in the present study. Cleaning process was carried out using compressed air to remove residual sand particles and thorough cleaning was done with a degreasing agent. The cleaning process was done just before plasma spraying, to avoid recontamination.

3.1.3.2 Plasma spraying

Plasma spraying is relatively straight forward in concept but buildup of a plasma sprayed coating is a chaotic process. The gases used for creating plasma are argon, hydrogen, helium, nitrogen and any mixture of these gases. The plasma is created in a plasma gun as shown in Fig. 3.3a operating on direct current, which sustains a stable non-transformable electric arc between cathode and a water cooled anode. This will cause ionization of the arc-gas atoms when passing through the burning arc [6]. When the desired powder composition is allowed to enter into the plasma jet along with carrier gas, it melts and the molten droplets move towards the path to the substrate with high speed (100-500 m/s), where they impact and undergo rapid solidification as deposit on the substrate (‘splat’) [6]. Like this, molten particles spread out and splatter as they strike the target, initially locking onto the irregularities of the roughened surface and then interlocking with one another. Figure 3.3b shows the schematic cross-section microstructure of plasma sprayed coating containing voids, unmelted particles and oxide particles. Voids result as the growing deposit traps air. In some cases particles get overheated in the flame and become oxidized; some particles may not melt and simply get embedded in the deposit **[7]**.

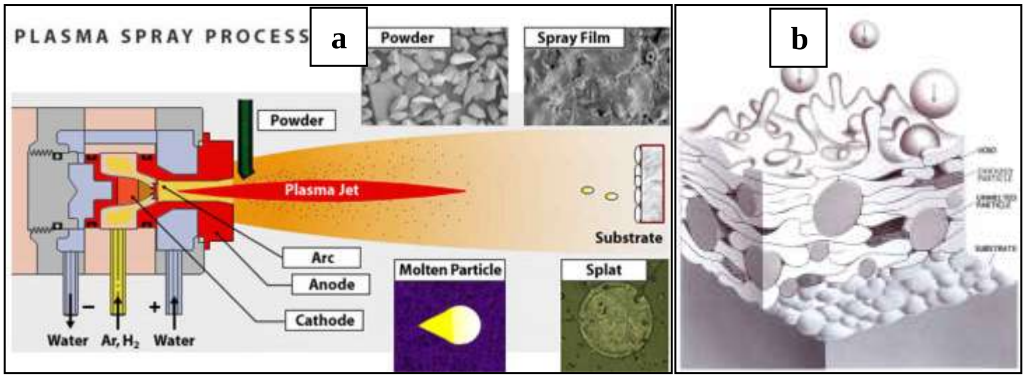

Fig. 3.3 (a) Schematic of a plasma spray process and (b) typical cross-section morphology of sprayed coating [7].

Spraying was performed in a plasma spraying unit is containing double skinned, water cooled, stainless steel chamber. As this process is conducted in air, it is called as air plasma spray

(APS) or atmospheric plasma spray (APS) process. The gun pattern and speed are programmed from a control console. The spray unit is controlled by a dedicated computer system. Windows based control software allows the adjustment of different parameters of the spraying process. The difference in the coefficient of thermal expansion of ceramic top coat and substrate necessitates the use of an intermediate bond coat. The bond coat reduces the stresses developed owing to thermal expansion mismatch during heating and cooling and also improves the adhesion of the coating. The commonly used bond coats are MCrAlY, where M could be Fe, Ni and NiCo or NiAl depending on the nature of the substrate. The bond coat need to be selected based on the substrate material and its properties. In the present work one metallic coating and one ceramic coating were chosen as bond coats: NiCrAlY bond coat for PSZ, while Cr_3C_2-25NiCr for A40T top coating respectively. Cr_3C_2-25NiCr and A40T coating were produced by APS process using a METCO 3 MB type plasma gun. The intermediate bond coat of Cr_3C_2-25NiCr (20-25 µm) was sprayed on the substrate and above this bond coat, a top ceramic coating of A40T (100 µm) was deposited. A40T coating was also sprayed on HDG without bond coat. The NiCrAlY and PSZ coatings were produced at M/s. Plasma Spray Processors, Mumbai, India using a METCO 9 MB type plasma gun. The thickness of a NiCrAlY bond coat was 50 µm and that of the top ceramic PSZ coating was 300 µm. The optimized spray parameters used for the deposition of PSZ and A40T coatings are listed in Tables 3.4. These A40Tand PSZ coatings deposited by APS process acts as a corrosion protective coatings in addition to acting as a thermal barrier. The thermal expansion behavior of HD graphite, bond coat (BC) of Cr_3C_2-NiCr, NiCrAlY and top coat (TC) of A40T, PSZ was reported in Table 3.5 to assess the relative influence of substrate, BC and TC thermal expansion behavior on durability of plasma sprayed coatings.

Table 3.4 APS parameters employed for coating of A40T and PSZ on HDG.

Process parameters (Units)	**A40T coating**	**PSZ coating**
Plasma arc current (A)	470	600
Arc voltage (V)	50	64-70
Powder carrier gas	Ar	Ar
Secondary gas	H_2	H_2
Powder feed rate (g/min)	50	46
Spraying distance (mm)	100	100
Argon flow rate (l/min)	80	38
Hydrogen flow rate (l/min)	12	10
Carrier gas flow rate (l/min)	40	37

Table 3.5 Thermal expansion co-efficient of HD graphite and coatings

Material	**Co-efficient of thermal expansion (K^{-1}) in the temperature range 293–1273 K**
HD graphite	5.9×10^{-6}
Cr_3C_2-NiCr (BC)	10.9×10^{-6}
Al_2O_3-40 wt% TiO_2 (TC)	3.5×10^{-6}
NiCrAlY (BC)	17.1×10^{-6}
Partially stabilized zirconia (TC)	10.7×10^{-6}

3.1.3.3 Post spray treatment techniques

Thermal spraying is a popular surface modification technology; however, after spraying the coating contains pores, oxides and voids originating at the splat boundaries, which will be attacked when exposed to highly aggressive environments, resulting in coating spllation or attack on the substrate [8]. Post-spray treatment has been widely recognized in the last decade as the key to improve the quality of coatings and their properties. With post-spray treatments the shortcomes in the sprayed coatings can be overcome to achieve better performance. In the present thesis, two kinds of post treatments performed on A40T coating to eliminate the defects/inhomogeneities of the coating were vacuum annealing and laser melting.

3.1.3.3.1 Vacuum annealing

As post spray heat treatment is one of the ways to improve the properties of plasma sprayed coatings [9]. Vacuum annealing of the plasma sprayed A40T coating on HDG discs was carried out in a high vacuum-high temperature furnace for the purpose of minimizing the surface porosity and for homogenizing the microstructure. The coated samples were annealed at 1373 K for 5 h under a vacuum of 10^{-4} mbar. The heating rate for the annealing treatment was 1°C/s.

3.1.3.3.2 Laser melting

Lasers are powerful tools to modify the microstructures of materials for improvement in properties [10]. Considerable interest is shown on the application of laser technology in conjunction with thermal-spraying process to improve the overall performance of the coatings [11] by eliminating porosity and unmelted/partially melted particles and generating an external dense layer. Laser surface melting permits selective heating and melting of the surface. Rapid heating and quenching in the laser melting process produces homogeneous microstructures [10]. Pulsed lasers find extensive applications in surface modification by melting the surface or in developing coating by laser ablation. Pulsed lasers can be used for the melting of very thin surface layer of ceramic coatings to form a solidified layer because of high thermal gradients [12].

Laser melting of plasma sprayed A40T coating on HDG substrates was carried out by using high power pulsed Nd:YAG laser at Raja Ramanna Centre for Advanced Technology (RRCAT), Indore. The Nd:YAG laser beam has been generated from a cylindrical rod and has a circular spot. However, in the present investigation laser beam has been focused to a line by means of a cylindrical lens. Laser output has a circular spot of laser beam of 6 mm diameter and a full angle beam divergence of 5 mrad. A cylindrical lens of 30 mm focal length has been used in the beam path to produce a line focus of 6 mm x150 μm size on the sample. The schematic diagram of the pulsed Nd:YAG laser system used for melting of A40T coating is shown in Fig 3.4. The details of rectangular pulsed Nd:YAG laser beam profile have been discussed elsewhere [13,14]. The overall process parameters employed for melting of plasma sprayed A40T coatings are listed in Table 3.6. Argon gas was provided for shielding during the laser melting process. The coated sample was fixed on the X-Y direction movable stand. The movement of stand was controlled automatically. Argon gas was purged into the main chamber and blown directly over the laser processing area with optimized flow rate and velocity to avoid the formation of pores during the laser melting process. The vertical and horizontal overlap of 640 and 800 kW/cm^2 is 20 to 30 % between consecutive tracks. The melting experiments were repeated with a number of samples to ensure data reliability and reproducibility.

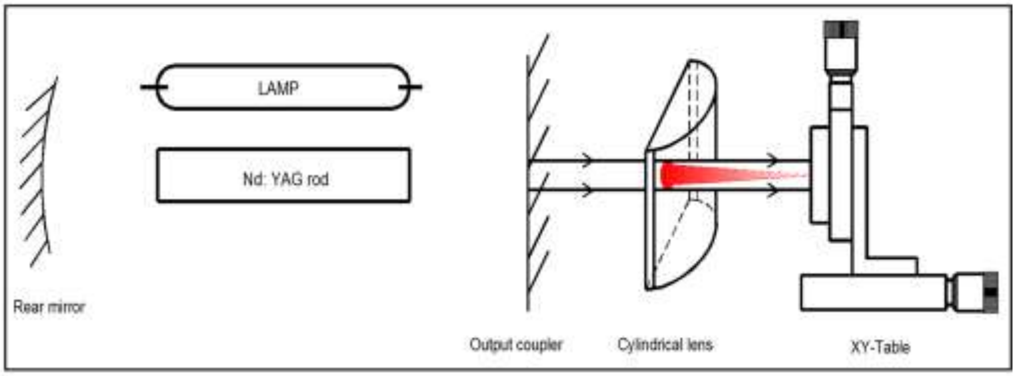

Fig. 3.4 Schematic of pulsed Nd:YAG laser system used for surface modification of A40T coating.

Table 3.6 Laser processing parameters used for melting of plasma sprayed A40T coatings.

Laser system	**Nd:YAG**
Mode of operation	Pulsed mode
Laser wavelength (µm)	1.064
Line of focus	6 mm x 150 µm (length x width)
Repetition rate (Hz)	20
Pulse width (µsec)	55
Pulse energy (mJ)	320 400
Pulse peak power (kW)	5.8 7.3
Peak power density (kW/cm^2)	640 800
Speed (mm/s)	1

3.1.3.4 Sample preparation for metallographic observation

For characterizing the coatings, metallographic preparation of the cross section was required. For cross section examination, as-coated and tested samples (corrosion tested, uranium melted and thermal cycled) were cold mounted with epoxy resin and the mounted samples were prepared according to ASTM E 1920-03 standard [15]. Care was taken to minimize the polishing and grinding duration, in order to avoid unnecessary material removal and smearing of small pores during the polishing. The cross sections of coatings were prepared and covered with gold coating prior to the examination by back scattered as well as secondary electron detector in SEM.

3.2 Methods

3.2.1 Specimen preparation

For corrosion testing, cylindrical samples were fabricated from rods of LDG, HDG and GC by machining without disturbing the as-received surface finish received from the Supplier, for molten salt corrosion experiments. PyG, HDG and LDG flat samples machined out from a plate were also tested in molten salt.

3.2.2 Molten salt preparation

The melting temperature of a salt mixture is the most important criteria in the selection of a salt. One way to lower the melting point of a salt is to combine multiple salts to form a salt of eutectic composition. These eutectic compositions have a much lower melting temperature than the individual salt components and are characterized by a single melting point [16]. In recent years, the eutectic composition of lithium chloride (LiCl)-potassium chloride (KCl) binary system has attracted more attention as a low-temperature and low-viscosity electrolyte for electric power cells and for refining metals [17,18]. Molten LiCl-KCl eutectic salt has been considered as the process medium for electrorefining of spent metallic fuels. This eutectic salt has been chosen as the electrolyte based on its low melting temperature of 633 K. Anhydrous LiCl and KCl salts (greater than 99 % purity; from Sigma-Aldrich) weighed and mixed in proper proportions (44.48 wt % LiCl – 55.52 wt % KCl) were used to prepare the eutectic composition. Most suppliers of halide salts do not provide materials that can be used directly. The major impurities that must be removed to prevent severe corrosion of the container metal are moisture/oxide contaminants. Once removed, these salts must be kept from atmospheric contamination by handling and storage in sealed containers [19]. These chlorides are highly hygroscopic in nature; hence, all the salt handling operations were done in an UHP argon atmosphere glove box. The as-received LiCl and KCl salts were dried at 423 K under vacuum (10^{-3} mbar) for 48-72 h to remove the moisture. The vacuum dried salt mixture was loaded in an alumina crucible inside the glove box. The salt loaded crucible was kept inside a leak-tight quartz tube as shown in Fig. 3.5 and it was further transferred to the salt purification furnace; UHP argon gas was continuously purged through the inlet into the salt purification quartz tube. The salt mixture was subsequently heated up to 773-873 K while purging of UHP argon gas, followed by chlorination process. For chlorination, high purity dry chlorine gas (99.99 %) was purged into the molten salt through the inlet and the excess chlorine was let out through NaOH solution. The process of chlorination was continued for purification of salt about 1-2 h. After chlorination, UHP argon was purged inside the salt containing quartz tube to remove the excess chlorine; otherwise it would accelerate the corrosion of the structural materials of corrosion testing facility. After cooling to room temperature, the molten salt contained alumina crucible was removed from the quartz tube inside the glove box. The purified salt was then transferred into corrosion test cell. Throughout the process of salt preparation and handling, UHP argon gas atmosphere was maintained in order to avoid the ingress of oxygen and moisture which affect the purity of salt.

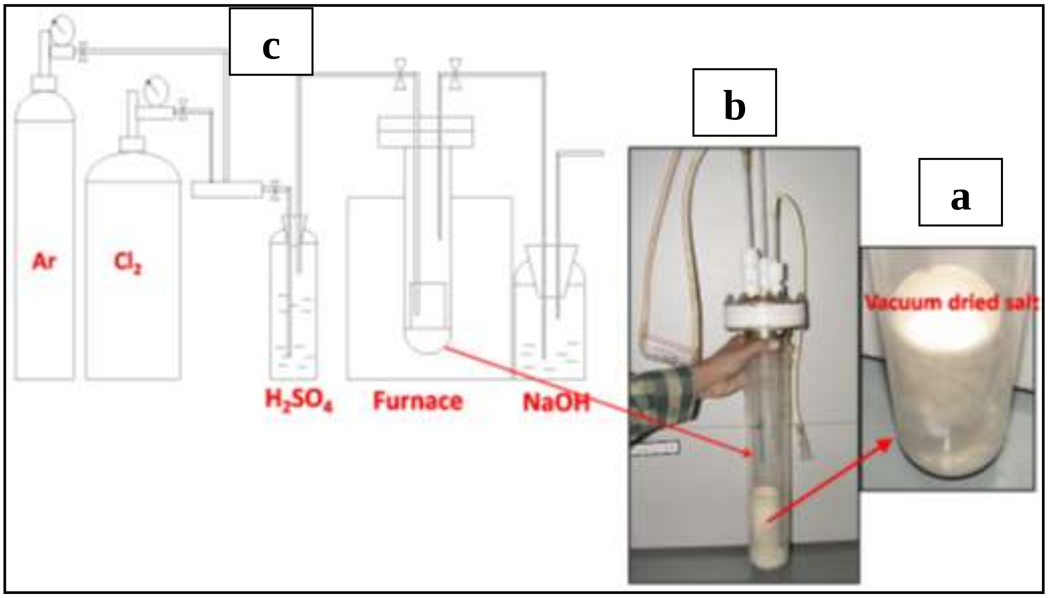

Fig. 3.5. Schematic representation of molten LiCl-KCl salt preparation for corrosion studies; (a) vacuum dried salt in alumina crucible, (b) alumina crucible loaded inside the leak-tight quartz tube and (c) salt preparation furnace with purification gas system.

3.2.3 Molten salt test assembly for corrosion studies

Corrosion of materials in molten salt depends on the composition, temperature, environment and exposure time. The complete experimental setup used for molten salt corrosion experiments is shown in Fig. 3.6. It consists of three important assemblies namely (i) corrosion test vessel with furnace, (ii) atmosphere modular glove box for handling salt operations and (iii) argon gas supply for maintaining inert atmosphere throughout the experiments. Corrosion studies were carried out in molten salt test assembly (MOSTA) comprising of an alumina crucible in a structural stainless steel cell, a thermocouple and provision for argon gas inlet and outlet. The stainless steel cell was sealed in the glove box along with the thermocouple and was transferred to the MOSTA setup. Purified salt was loaded in the corrosion test cell and the cell in turn was loaded in MOSTA under ultra high pure (UHP) argon atmosphere. The cell was connected to the argon lines of the furnace. The samples were loaded inside the cell by suspending them in the molten salt cell kept in the furnace (Fig. 3.6) and heated to the desired temperature. When the test temperature was reached the samples were dipped inside the molten salt.

In present work corrosion studies were carried out in purified molten LiCl-KCl salt with the following materials and coatings to evaluate the corrosion behaviour.

(i) Samples of LDG, HDG, GC and PyG were immersed in molten LiCl-KCl eutectic salt at 873 K for 2000 h with continuous UHP argon flowing throughout the experiment.

(ii) Uncoated and PSZ coated HDG samples at 873 K for 250, 1000 and 2000 h in continuous flowing UHP argon atmosphere.

(iii) A40T coated HDG samples without and with Cr_3C_2-NiCr bond coat for 500, 1000 and 2000 h under continuous flowing UHP argon atmosphere.

(iv) Laser melted A40T coated HDG samples at 873 K for 24 h under continuous flowing UHP argon atmosphere. The samples were positioned at about 5 cm from the bottom of the container crucible and the purified LiCl-KCl salt was spreaded over the surface of coated discs.

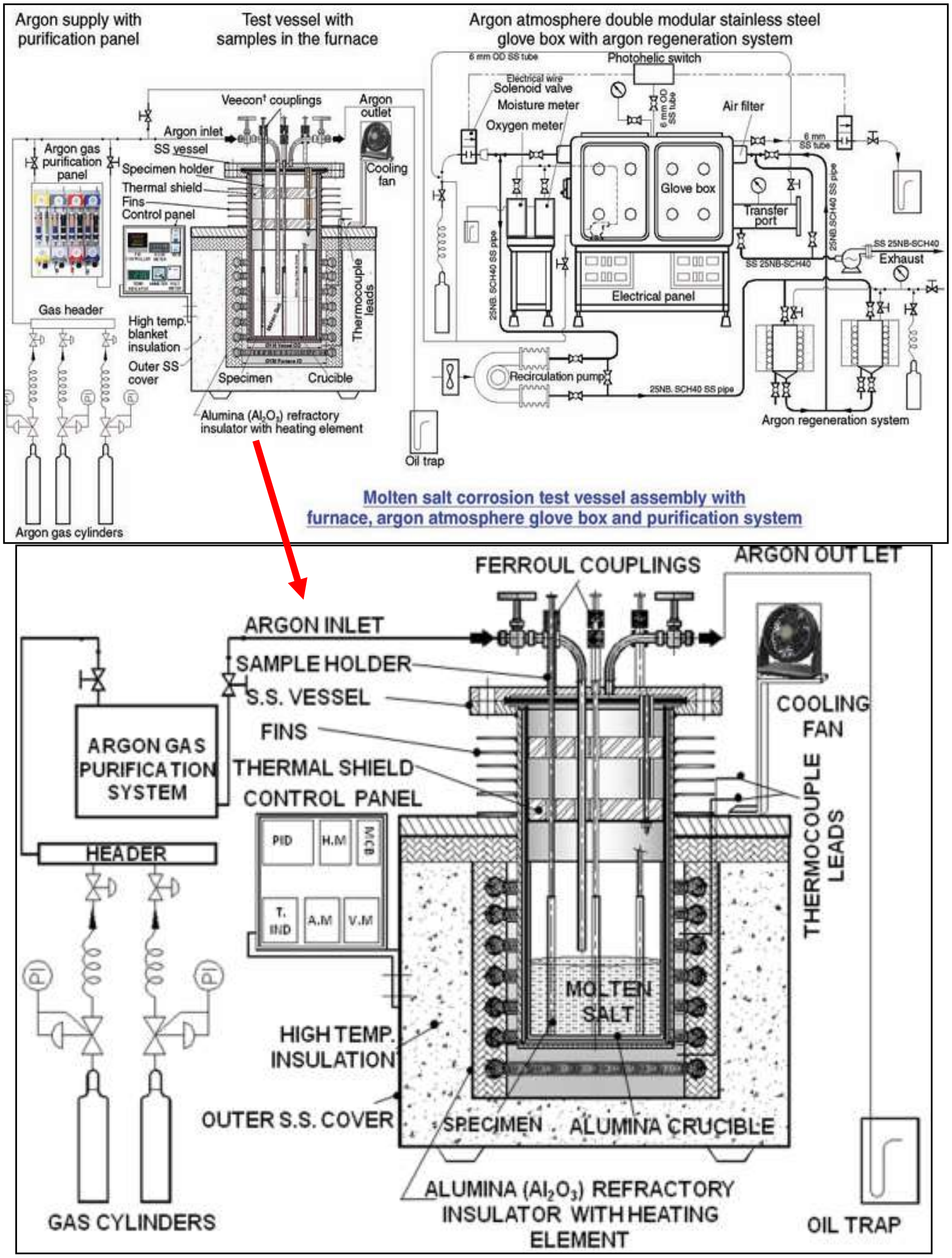

Fig. 3.6 Molten salt corrosion test assembly (MOSTA) with glove box and gas purification system.

3.2.4 Thermal cycling studies

The thermal cycling experiments were conducted in furnace (Fig. 3.7a) at 873 and 1023 K on ceramic coated HDG samples using a Model TC-1200-M furnace made by Ducom Instruments, Bangalore which can heat up and cool down the specimens automatically. All HDG specimens were coated on only one face. Figure 3.7b shows the photographs of as-coated surface and the vacuum sealed samples in the quartz tube. A40T and PSZ coated HDG samples were sealed under a vacuum of 10^{-3} torr in a quartz tube to avoid the oxidation of coating and uncoated side of HDG and also to simulate the pyroprocessing conditions. After reaching the desired temperature samples were loaded into the heating tray to hold for10 minutes to heat up, followed by a forced air cooling for 10 minutes to ambient temperature. Figure 3.7c shows the schematic diagram of thermal cycle test carried out in the present study to assess the durability of the coating. The following steps constitute one thermal cycle: (i) the furnace is opened by lowering the floor of the furnace and the samples are placed on the floor. The samples are leaned against a refractory holder such that the coated circular face, which is almost normal to the floor, does not make contact with the refractory holder. (ii) The floor is raised and the furnace is closed; the time is set to zero. (iii) After 10 min, the floor is lowered and the samples are conventionally forced air cooled using a fan for 10 min. Steps (ii) and (iii) are repeated. The cycle length is fixed. Two coated HDG disc samples of dimensions 12 mm diameter and 8 mm thickness were simultaneously subjected to different number of cycles ranging from 50 to 200. The samples were removed from vacuum sealed quartz tubes after every 50 cycles and were visually examined, weighed and surface characterization and phase analysis were carried out. Vacuum sealed coated samples were again loaded into the for further thermal cycle testing.

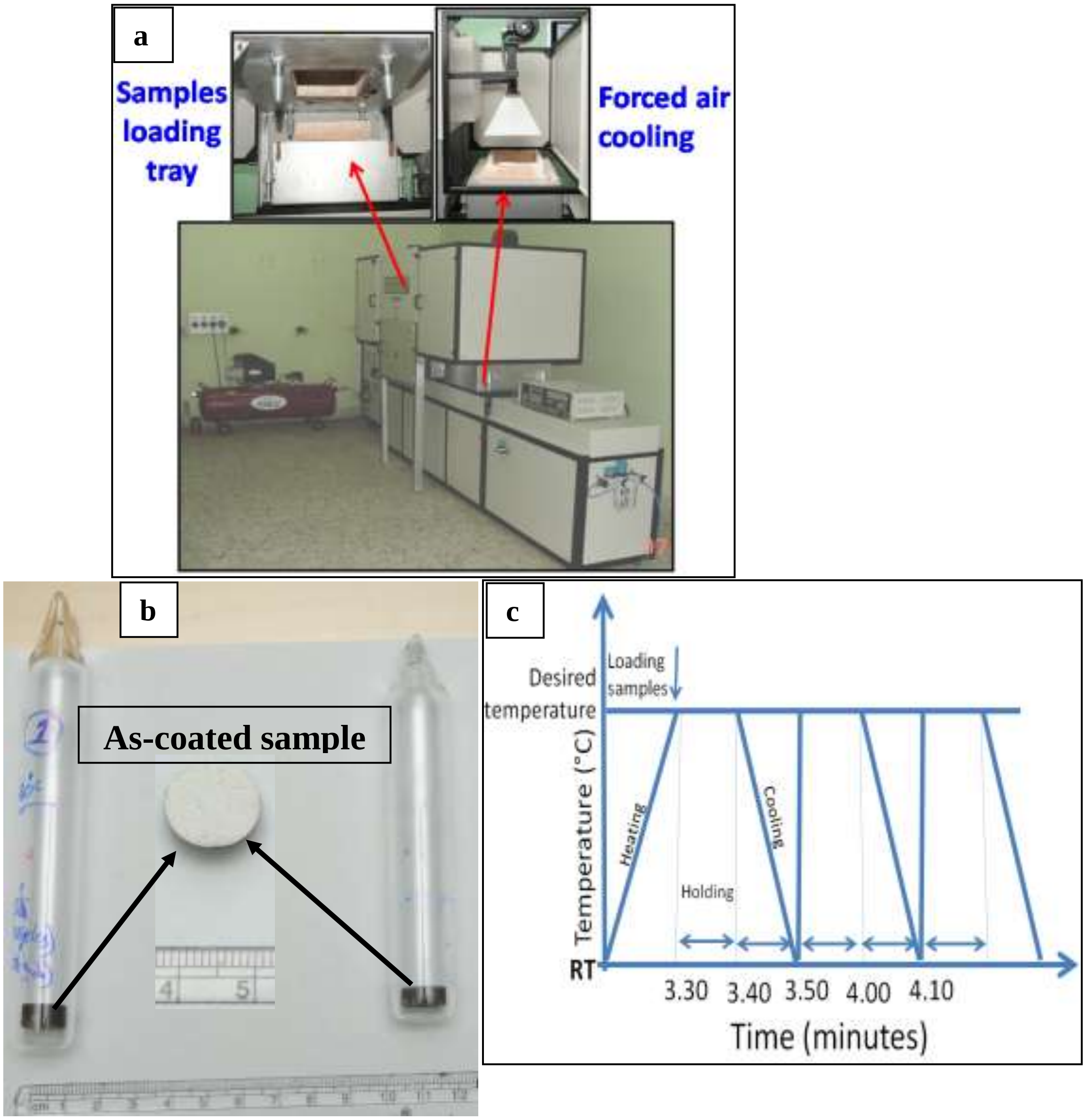

Fig. 3.7 (a) Photographs of thermal cycling setup used for testing of the ceramic coatings, (b) Photograph of as-sprayed PSZ coated HDG sample vacuum sealed in quartz tube for thermal cycling testing and (c) schematic representation of heating and cooling cycles for thermal cycling experiments.

3.2.5 Computation of Gibb's free energies

To predict the chemical reactivity of molten uranium with the coating materials, the Gibbs free energy change (ΔG_R) was calculated using FactSage® Version 6.2 software for the chemical reactions in the temperature range 300–2000 K.

3.2.6 Uranium melting

Uranium melting experiments were carried out in an induction melting setup shown in Fig. 3.8. This setup consists of a holder made of HDG, in which the coated HDG sample was loaded and a piece of uranium metal was kept on the top surface of coating. The HDG holder acts also as a susceptor for induction heating. The sample containing graphite holder was placed inside a quartz tube surrounded by induction heating coils capable of heating to the maximum temperature of 1773 K. The entire setup was placed in the UHP argon atmosphere glove box and heated at the rate of 90°C/min to reach the temperature of 1623 K in 15 min and was held at this temperature for 20 min to melt the uranium. The molten uranium was subsequently cooled down to room temperature inside the UHP argon glove box. Uranium metal shots of ≈5 mm diameter were used for single time melting and second time melting was performed with uranium shots of ≈10 mm diameter placed on coated graphite samples. Some of the YSZ and A40T coated samples were tested by melting uranium metal on the coating surface in the same holder. All the melting experiments were repeated twice to check the reproducibility.

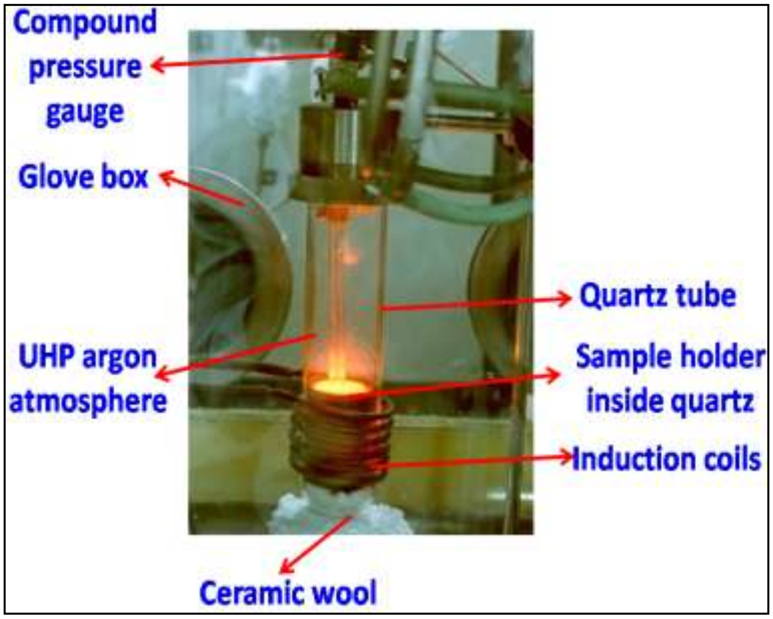

Fig. 3.8 Photograph of induction melting experimental set up used for uranium melting on ceramic coated HDG discs and crucibles.

3.3 Characterization of materials and coatings

3.3.1 Weight change measurement

Weight change measurements are widely used to assess the extent of corrosion of materials tested in molten salts at high temperatures. In the present study weight changes measured as a function of duration to estimate the extent of corrosion of material with time. After corrosion testing in the molten salt, the samples were cleaned ultrasonically in distilled water for about 10-15 minutes to remove salt sticking on the surface, followed by drying the samples under hot air. The initial and final weight of the carbon materials, coated HDG and molten salt tested samples were measured using an analytical balance (A&D Company. Ltd, Japan) and the percentage weight change was calculated. The ceramic coated (A40T and YSZ) samples subjected to thermal cycling test were weighted initially and after thermal cycles using an analytical balance (A&D HM-202, Japan) with a precision of ±0.01 mg.

3.3.2 Visual examination

The human eye is one of the mankind's most fascinating tools and is capable of assessing many visual characteristics and identifying various types of surface discontinuities [20]. Visual examination of objects, parts or components is the oldest and reliable non-destructive testing method. Generally, this test method is applied to almost every material as a quality assurance test. The basic principle in the visual examination is illuminating the test specimen with light or examines the specimen with the eye. Many defects, cracks and surface breaking can be detected by careful visual examination. The eye can perform accurate inspection to detect size, shape, color, depth, brightness, contrast, and texture [20]. For the present work, the surface of the as-received and corrosion tested carbon materials as well as ceramic coated and tested HDG samples (molten salt corrosion, uranium melted and thermal cycled) were examined visually to detect the surface variation/degradation/attack/cracks formation and change in dimensions. After visual examination the materials and coatings were microscopically examined for in-depth analysis.

3.3.3 Optical microscopy

Optical microscope is the oldest and the most commonly used instrument for characterization of a variety of materials from micron to sub-micron level. Optical microscope is the conventional and the most familiar device for magnifying a small specimen which cannot be viewed by naked eye. Optical microscopy is a simple lens system consisting of an objective lens with a short focal length (few mm), which creates an image of the object in the intermediate image plane. This image in turn can be viewed with another lens, the eye-piece, which can provide further magnification [21]. Conventional optical microscopy still maintains its position as the easiest, fastest and the most widely used method of micro-characterization tools before switching over to the advanced microscopy techniques. Optical microscope (Leica DM ILM, Germany) model was used for the characterization of the following materials and coatings in the thesis:

1. The as-deposited and corrosion tested PyG surfaces before and after the immersion test in molten LiCl-KCl salt.
2. The as-coated ceramic coatings on HD graphite were characterized for porosity and the percentage porosity of coatings was determined using ASTM E 2109, by following method A, and comparing with seven standard images (direct manual) [22].

3.3.4 Scanning electron microscopy/Energy dispersive X-ray spectroscopy

Scanning electron microscope (SEM) is one of the most advanced imaging tools for microstructural analysis wherein the images of the specimen are formed by scanning it with a high-energy electron beam. The interaction of electrons with the atoms of the specimen produces signals which provide information mainly about the specimen's surface topography and composition. The electron beam is thermionically emitted from an electron gun fitted with a tungsten filament cathode or lanthanum hexaboride (LaB_6) cathode. The accelerated electron beam of energy around 0.2 to 40 keV is focused by one or two condenser lenses to a spot of about 0.4 to 5 nm in diameter. The accelerated electron beam (primary electron beam) interacts with the surface of the specimen and the electrons lose their energy by repeated random scattering and absorption within a teardrop-shaped volume of the specimen known as the interaction volume. Secondary electron (SE), back scattered electron (BSE) and absorbed electrons are produced due to energy exchange between the electron beam and the specimen, each of which can be detected by specialized detectors. Various types of electronic amplifiers are used to amplify the signals and are displayed as variations in brightness on a cathode ray tube (CRT). The raster scanning of the CRT display is synchronised with that of the beam on the specimen in the microscope, and the resulting image is therefore, a distribution map of the intensity of the signal being emitted from the scanned area of the specimen. The image can be captured by photography from a high-resolution cathode ray tube, but in modern technology it can be digitally captured and displayed on a computer monitor and saved in a computer's hard disk [23].

In the present thesis SEM attached with energy dispersive X-ray spectroscopy (EDX) was used to characterize the as-received/deposited and tested materials and coatings for microstructural and elemental composition analyses. Various models of SEM used in the present thesis are: (1) FE-SEM of FEI, Quanta 200F, (2) ESEM of Philips XL-30, (3) Mini-SEM (Model SNE-3000M) and (4) Carl Zeiss-SUPRA55 and the studies included:

1. As-received and immersion tested carbon materials (LDG, HDG, GC and PyG) in the molten salt.
2. Cross sections and surface morphology of the as-sprayed and post treated A40T coated HDG samples at different regions along with cross sections.
3. Tested (corrosion, uranium melted, thermal cycled) A40T coated HDG samples to obtain quantitative chemical analysis and the microstructural features in the A40T coatings.
4. Laser melted A40T coated HDG after molten salt corrosion test for chemical composition of the tested surfaces and cross sections.
5. The as-sprayed and tested PSZ coatings (corrosion, uranium melted, thermal cycled) for the elemental composition of the surface and cross sections of the coatings.

3.3.5 Atomic force microscopy

Atomic force microscope (AFM) is one of the important analytical instruments in the field of material science for surface investigation from micron to nano-meter range. AFM has certain advantages over conventional microscopy techniques in obtaining three dimensional image of a sample surface, with good e resolution in the x-y plane ranging from 0.1 to 1.0 nm and is 0.01 nm (atomic resolution) in the z-direction [24]. Atomic force microscopy is currently applied to various environments (air, liquid, vacuum) and all types of materials surfaces such as metal, non-metal, semiconductors, soft, biological, conductive and non-conductive materials [24,25]. In this technique, a tip interacts with the sample surface through a physical phenomenon. The AFM measures the forces acting between the fine tip and a sample. The tip is attached to the free end of a cantilever and is brought very close to the surface. Attractive or repulsive forces resulting from interactions between the tip and surface will cause a positive or negative bending of the cantilever. Measuring a “local” physical quantity related with the interaction, allows constructing an image of the studied surface [25]. AFM is a vital tool for studying surface roughness at the nanoscale, with resolution far exceeding that of other stylus and optical based methods.

In the present work, the surface morphology and surface roughness analysis of the as-received and corrosion tested LDG, HDG and PyG samples were carried out using an NT-MDT make Solver Pro EC electrochemical scanning probe microscope. The samples were analysed in semicontact mode using a standard conical silicon tip attached to a cantilever under ambient condition. The average roughness (Eq. 1) and Root Mean Square (RMS) (Eq. 2) value of the surfaces were calculated using NOVA software to evaluate the extent of corrugation present on the surface.

$$R_a = \sum_{i=1}^{n} Z_i - \overline{Z} \qquad \text{- (1)}$$

$$R_q = \sqrt{\frac{\sum_{i=1}^{n} \left(Z_i - \overline{Z}\right)^2}{n}} \qquad \text{- (2)}$$

where Z_i is the height of each single point, $\overline{Z}$ is the mean of all the height values and n is the number of data points within the image.

3.3.6 X-ray diffraction

XRD is a rapid and non-destructive analytical technique used for phase identification of a crystalline material and can provide detailed information about the crystallographic structure of naturally occurring and synthetic materials [26]. XRD is based on the constructive interference of monochromatic X-rays and a crystalline material. The X-rays are generated by a cathode ray tube, filtered to produce monochromatic radiation, collimated to concentrate and directed towards the specimen. A constructive interference (and a diffracted ray) is produced by the interaction of the incident rays with the specimen by satisfying Bragg's Law (nλ=2dsin θ). This law relates the wavelength of electromagnetic radiation (λ) with the diffraction angle (θ) and the lattice spacing (d) in a crystalline specimen. The diffracted X-rays are then detected, processed and counted. By scanning the specimen over a range of 2θ values, all possible diffraction directions of the lattice could be obtained due to the random orientation of the powdered material. Conversion of the diffraction peaks to d-spacing allows the identification of the crystalline materials because each material has a set of unique d-spacing. Typically, this is achieved by the comparison of d-spacing with standard reference patterns [27]. Important information that can be obtained from the XRD analysis are: (1) identification of crystalline phases and orientation, (2) Determination of structural properties: Lattice parameters (10-4Å), strain, grain size, expitaxy, phase composition, preferred orientation, order-disorder transformation and thermal expansion), (3) Measurement of thickness of thin films and multi-layers and (4) Determination of atomic arrangement.

In the present work XRD studies were carried out for the following specimens. The XRD patterns obtained were compared with the standard JCPDF database and available literature.

1. As-received and corrosion tested LDG, HDG and PyG coupons using a Philips X'pert MPD diffractometer (40 kV, 30 mA, Cu K_α radiation; $\lambda = 0.1542$ nm).
2. PyG powder samples using a STOE diffractometer with Cu Kα radiation. The interlayer spacing or distance (d_{002}) and crystallite size along the c axis $L_c(002)$ were calculated using Bragg's and Scherrer formula [27].

$$d = n\lambda / 2 \sin\theta \quad - (3)$$

$$L_c = 0.9\, \lambda / \beta \cos\theta \quad - (4)$$

3. Powder, as-sprayed, annealed and laser melted A40T coatings using Bruker AXS D8 diffractometer (40 kV, 30 mA, CuKα radiation; $\lambda = 0.1542$ nm) to identify the phase changes due to post treatments.
4. Corrosion tested A40T coatings on HD graphite using Philips X'pert MPD diffractometer (40 kV, 30 mA, Cu $_{K\alpha}$ radiation, $\lambda = 0.1542$ nm) after exposure to molten LiCl-KCl salt.
5. Laser melted A40T coatings before and after corrosion testing and as-sprayed and corrosion tested PSZ coatings using Bruker AXS D8 diffractometer.
6. PSZ coating before and after uranium melting using PAN alytical X'Pert (45 kV, 30 mA, 2θ= 20 to 80°) instrument.

7. Thermal cycled A40T and PSZ coatings using normal mode PAN alytical X'Pert, diffractometer (40 kV, 30 mA, Cu K_α radiation $\lambda = 0.1542$ nm). The coatings were examined in continuous scan mode in the range $20° < 2\theta > 80°$ at the san rate of 2° per minute.

3.3.7 Raman spectroscopy

Raman spectroscopy is a relatively easy and non-contact method to probe the inelastic scattering of light from a sample surface at room temperature and ambient pressure [28]. Raman spectroscopy involves molecular and crystal lattice vibrations and is therefore, sensitive to the composition, bonding, chemical environment, phase and crystalline structure of the material in any physical form: gases, liquids, solutions, and crystalline or amorphous solids [29].

The Raman phenomenon is a consequence of the interaction of materials with a monochromatic photon beam (laser), most of which are absorbed, reflected or transmitted by the sample. However, a small fraction of photons are scattered. During this interaction, some energy is transmitted to elementary particles of which materials are constituted (electrons, ions etc.). This causes their transition from ground energy levels to 'virtual' excited states. These excited states are highly unstable and the particles decay instantaneously to the ground state by one of the following three different processes, as shown in Fig. 3.9.

(a) Rayleigh scattering (elastic scattering): the emission of a photon of the same energy allows the molecule to relax to its ground vibrational state [29]. Rayleigh scattering, therefore, bears no information on vibrational energy levels of the sample.

(b) Stokes and (c) anti-Stokes Raman photons (inelastic scattering): Emission of a photon with energy either below or above that of Rayleigh photons generates a set of frequency-

shifted ‘Raman’ photons. The energy difference of the Stokes and anti-Stokes Raman photons with respect to the excitation energy gives information about molecular vibrational levels [29]. These photons are collected by a detector and transformed to electrical signals and finally to the corresponding Raman spectrum. Usually, Stokes bands which are more intense than anti-stokes bands are called “Raman spectrum” of the sample. The Rayleigh band is filtered out before reaching the detector [29].

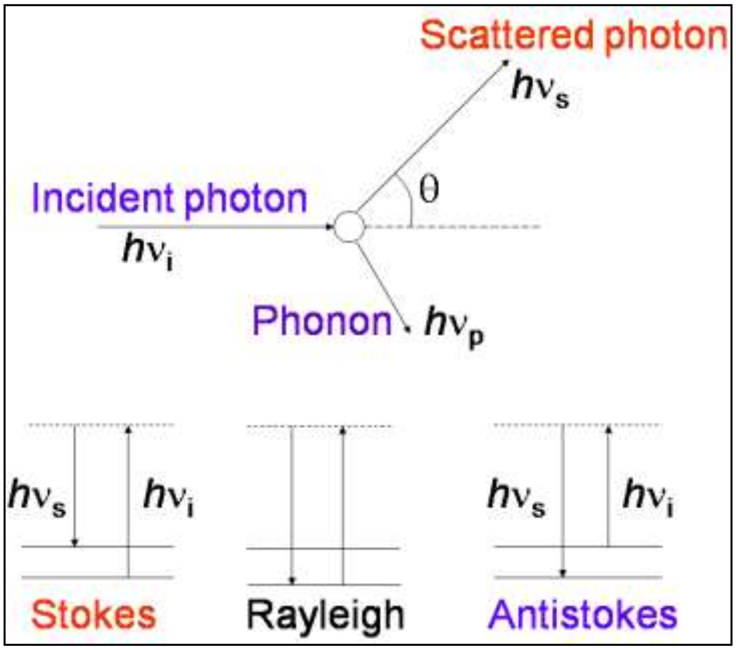

Fig. 3.9 Energy level diagram showing the states involved in Raman signal.

Raman imaging is an extension of Raman microspectroscopy [30]. One key benefit of Raman imaging is that the powerful Raman spectral information can be presented in a visual format and which can be more easily understood [30]. Raman imaging combines Raman spectroscopy with digital imaging technology in order to visualize chemical composition and molecular structure of materials to produce molecular chemical images of materials [30]. Typically, image contrast reveals the distribution of molecular composition based on the “fingerprint” Raman spectral identification. Raman spectroscopy is also considered as a bulk technique because the optical penetration depth of the visible lasers typically used as excitation sources is too long to have a large collection of volumes [31].

In the present thesis, Raman spectral analysis of carbon materials were carried out and the Raman mapping results of disorder-induced D peak of LDG, HDG and PyG samples before and after corrosion test in molten salt had been analyzed. Raman experiments were also carried out on the as-sprayed, corrosion and thermal cycle tested and uranium melted PSZ coatings to identify the phase changes in PSZ coatings. Raman microscopic experiments were performed using a HR800 (Jobin Yvon) Raman spectrometer equipped with 1800 grooves/mm holographic grating. The samples were placed under an Olympus BXFMILHS optical microscope mounted at the entrance of the Raman spectrograph. Low energy He-Ne laser of wavelength 633 nm was used as the excitation source for Raman studies on carbon materials since higher energy argon line was reported to affect the structure of carbon materials due to absorption effect [32]. The laser power at the sample was 5 mW. The slit width of the monochromator was 300 μm corresponding to a resolution of 4 cm^{-1}. Argon ion laser of 488 nm was used as the excitation source for Raman studies on PSZ coatings. The laser power at the sample was ≈ 15 mW. The slit width of the monochromator was 400 μm. The laser spot size of 3 mm diameter was focused tightly on the sample surface using diffraction limited 10x (NA = 0.25) long distance objective. The back scattered Raman spectra were recorded using super cooled (<-163 K) 1024 x 256 pixels charge coupled device (CCD) detector, over the range 80–2000 cm^{-1} with 5 s exposure time and 20 CCD accumulations. All the spectra were baseline corrected and deconvoluted. Data for Raman maps were collected over a selected area of interest on exposed carbon materials and PSZ coatings and processed by associated software.

3.3.8 Vickers microhardness testing

Hardness is the property of a material that enables it to resist plastic deformation, usually by penetration. The term hardness may also refer to resistance to bending, scratching, abrasion or cutting. [33]. Different type of hardness measurement techniques such as Rockwell hardness test, Rockwell superficial hardness test, Brinell hardness test, Vickers hardness test, Mohs hardness test, Scleroscope and other hardness testing methods are available. The term microhardness test usually refers to static indentations made with loads not exceeding 1 kgf [33]. The methods that have persisted to this day may be divided into two broad categories: (1) those where a hardened steel ball or cone is pressed into a surface under a known load; and (2) those methods, where sharp diamond of various shapes are pressed into a surface under a known load [34]. The Vickers hardness measurement is simpler than other hardness measurements since the required calculations are independent of the size of the indenter, and the indenter can be used for all materials irrespective of hardness. The Vickers hardness test method consists of indenting the test material with a diamond indenter, in the form of a right pyramid with a square base and an angle of 136° between opposite faces, which is subjected to a load of 1 to 100 kgf. The full load is normally applied for 10 to 15 second. The two diagonals of the indentation left out on the surface of the material after removal of the load are measured using a microscope and their average calculated.

In the present study, microhardness of the as-sprayed, vacuum annealed and laser melted A40T coatings was determined with a load of 200 g applied for 15 s on various regions of the coatings using SHIMADZU-HMV-2 microhardness tester. The testing body was a four side diamond-pyramid which locks in an angle of 136°. On the coating, a quadrangle impression is made by the plastic deformation caused by the diamond indenter.

With a videographic system, the user marks the diagonals of the quadrangle and the area of the sloping surfaces of the indentation is calculated automatically, which gives Vickers hardness value. Average value of five Vicker indentations made on the coatings was calculated and used.

3.3.9 Surface profilometery

Surface roughness plays a crucial role in determining the functional performance of many devices especially in the field of surface and coating technology. The concept of roughness is often described with terms such as ‘uneven’, ‘irregular’, ‘coarse in texture’, ‘broken by prominences’, and other similar ones [35]. Surface roughness is defined as the arithmetic average of deviation of the surface from a mean line or centerline [36,37]. Physically, the surface roughness value depends on the microstructure of the surface and it gives information on the uniformity of the surface. Stylus profilers are the most common instruments used today for roughness measurement. Stylus instruments are based on the principle of running a probe across a surface in order to detect variations in height as a function of distance [38].

In the present thesis, the surface roughness of the as-coated, vacuum annealed and laser melted A40T coated HDG samples was measured using the Taylor Hobson surface profilometer (surtronic 3+ roughness tester) at RRCAT, Indore. The surface roughness is denoted as average surface roughness (R_a) and expressed in micrometer (μm) unit.

References

[1] R. Wlodarski, A. Nowicki, L. Pealska, Obtaining of pyrographite in the indirect heating method, INCT-2059/I/ME/A (1988).

[2] G.R. Heath, P. Heimgartner, G. Irons, R. Miller, S. Gustafsson, Mater. Sci. Forum 251–254 (1997) 809–816.

[3] S. Bose, High Temperature Coatings, Butterworth-Heinemann Publications, USA (2007) pp. 155–232.

[4] Amdry 962, NiCrAlY powder specifications from Sulzer Metco Ltd., Switzerland

[5] Mecto 204NS, YSZ powder specifications from Sulzer Metco Ltd., Switzerland

[6] H. Herman, S. Sampath, Thermal spray coatings, in Metallurical and Ceramic Protective Coatings, K.H. Stern (eds.,), Chapman & Hall publisher, London, UK (1996) pp.261-305.

[7] H. Herman, Sci. Am. 259 (1988) 112–117.

[8] S.S. Chatha, H.S. Sidhu, B.S. Sidhu, Role of post treatment in thermal spray coatings, National Conference on Advancements and Futuristic Trends in Mechanical and Materials Engineering, October (2011).

[9] L.C. Lim, S.C. Lim, M.O. Lai, S.F. Chong, S. Alli, Surf. Coat. Technol. 79 (1996) 151-161.

[10] S.T. Picraux, L.E. Pope, Science 226 (1984) 615–622.

[11] A. Gisario, M. Barletta, F. Veniali Optics. Laser Technol. 44 (2012) 1942–1958.

[12] A. Ibrahim, H. Salem, S. Sedky, Surf. Coat. Technol. 203 (2009) 3579–3589.

[13] M.P. Mateo, M.C. Luisa, J.J. Laserna, Appl. Optics. 42 (2003) 6057–6062.

[14] A. Choubey, R. Singh, S.C. Vishvakarma, P. Misra, D.M. Vachhani, R.K. Jain, K.K. Pant, R. Arya, B.N. Upadhyaya, S.M. Oak , Development of fiber-coupled short pulsed Nd: YAG laser for cleaning applica- tions, In: Proceedings of the 19th National Laser Symposium (NLS-19), Raja Ramanna Centre for Advanced Technology, Indore, December (2010).

[15] ASTM E 1920-03, Standard Guide for Metallographic preparation of Thermal sprayed coatings, American Society for Testing and Materials (ASTM), Philadelphia, USA.

[16] P. Sabharwall, M. Ebner, M. Sohal, P. Sharpe, M. Anderson, K. Sridharan, J. Ambrosek, L. Olson, P. Brooks, Report no: INL/EXT-10-18090, Molten Salts for High Temperature Reactors: University of Wisconsin Molten Salt Corrosion and Flow Loop Experiments – Issues Identified and Path Forward, March (2010) pp. 1-43.

[17] A. Adachi, Y. Katayama, T. Miura, T. Kishi, J. Power. Sources 68 (1997) 348–351.

[18] O. Shirai, M. Iizuka, T. Iwai, Y. Suzuki, Y. Arai, J. Electroanal. Chem. 490 (2000) 31–36.

[19] V. Ignatiev, A. Surenkov, Comprehensive Nuclear Materials 5 (2012) 221–250.

[20] G. A. Matzkanin, Selecting a Nondestructive Testing Method, Part II: Visual Inspection, The AMMTIAC Quarterly, 1, pp. 7-10.

http://ammtiac.alionscience.com/pdf/TechSolutions02.pdf

[21] http://www.molphys.leidenuniv.nl/monos/students/pdf/smon02.pdf

[22] ASTM E 2109-00, Test methods for determining area percentage porosity in thermal sprayed coatings, American Society for Testing and Materials (ASTM), Philadelphia, USA.

[23] J. Goldstein, D.E Newbury, D.C. Joy, C.E. Lyman, P. Echlin, E. Lifshin, L. Sawyer, J.R. Michael, Scanning Electron Microscopy and X-ray Microanalysis, Plenum, New York (1981).

[24] C.R. Blanchard, The Chemical Educator 1 (1996) 1–8.

[25] Physics of Advanced Materials Winter School (2008).

[26] http://web.pdx.edu/~pmoeck/phy381/Topic5a-XRD.pdf

[27] B.D. Cullity, Elements of X-ray diffraction, Prentice Hall publication, 3rd edition (2001).

[28] M.A. Pimenta, G. Dresselhaus, M.S. Dresselhaus, L.G. Cancado, A. Jorio, R. Saito, Phys. Chem. Chem. Phys. 9 (2007) 1276–1290.

[29] *http://alpha1.infim.ro/cost/pagini/handbook/chapters/raman.htm#4.1.7.1*

[30] P.J. Treado, R. J. Priore, M.P. Nelson, Raman Spectroscopic Imaging, J.M. Chalmers, P.R. Griffiths (eds.,) Handbook of Vibrational Spectroscopy, John Wiley & Sons Ltd., (2002) pp. 1429-1459.

[31] A.M. Bolon, M.M. Gentleman, J. Am. Ceram. Soc. 94 (2011) 4478–4482.

[32] T. Jawhari, A. Roid, J. Casado Carbon 33 (1995) 1561–1565.

[33] http://www.gordonengland.co.uk/hardness/

[34] S.M. Walley, Mater. Sci. Technol. 28 (2012) 1028–1044.

[35] T.R. Thomas, Rough Surfaces, 2nd ed., Imperial College Press, London (1999).

[36] T.J. Steeper, W.L. RiggsII, A.J. Rotolico, J.E. Nerz, D.J. Varacalle, G.C. Wilson, in: T.F. Bernecki (ed.), Thermal Spray Coatings: Properties, Processes and Applications, Proceedings of the Fourth National Thermal Spray Conference, Pittsburgh, Pennsylvania, ASM International, Ohio, (1991), pp. 13.

[37] S. Yilmaz, Ceram. Int. 35 (2009) 2017–2022.

[38] R. Amaral, L.H. Chong, Surface Roughness, (2002). *http://www.sjsu.edu/faculty/selvaduray/page/papers/mate210/surface.pdf*

CHAPTER 4

CORROSION BEHAVIOUR OF CARBON MATERIALS IN MOLTEN LiCl-KCl SALT

The corrosion behaviour of four carbon materials namely, low density graphite, high density graphite, glassy carbon and pyrolytic graphite was investigated in molten LiCl-KCl electrolyte medium at 873 K for 2000 h under ultra high pure argon atmosphere. Structural and microstructural changes of the carbon materials after exposure to the molten chloride salt were investigated. Microstructural analysis of the samples revealed poor corrosion resistance of high density and low density graphite with severe attack on their surfaces. While glassy carbon and pyrolytic graphite exhibited relatively inert behaviour, pyrolytic graphite possessed the best resistance.

4.1 Introduction

Carbon based materials are considered as the potential candidates for the fabrication of various structural materials viz vessels, lids, crucibles and liners in the reprocessing of spent metallic fuels by pyrochemical route [1]. The major advantages of carbon materials are the ease with which they can be fabricated into various shapes, mechanical integrity at high operating temperatures, high temperature strength, thermal shock resistance and their inertness towards chlorine atmosphere. The Gibbs free energy of formation of CCl_4(g) from carbon(s) and chlorine(g) is +13 kJ/mol at 923 K. This positive value indicates that the reaction is not spontaneous and the solid phase of carbon is stable in chlorine environment [2]. The reaction of chlorine gas with graphite is reported to occur at temperatures not below that of the electric arc [3]. Different forms of carbon materials are employed for various applications in molten salt environment [2-21] complete details are reported in Chapter-2 (Literature Review).

Since the operating conditions for pyrochemical reprocessing in molten salt medium create an aggressive corrosive environment for the process crucibles, liners and vessels, they undergo drastic degradation, leading to replacement of components and disposal of the solid waste becomes a critical issue. Hence, there is considerable interest in the selection of materials and coatings for pyrochemical reprocessing application and it is essential to understand the behaviour of materials in molten salt environment [22,23]. Evaluation of long term corrosion behaviour is very important to understand the mechanism of degradation of materials under such aggressive environment. It should be noted that pyrochemical reprocessing operations are carried out in high pure argon atmosphere containing <1 ppm oxygen and water vapour and <15 ppm of nitrogen [24]. The corrosion behaviour of various structural materials in molten salt medium under inert (argon) and reactive oxygen gas atmosphere and the mechanisms involved were investigated by several researchers [25-29].

Characterization techniques like Laser Raman spectroscopy, X-ray diffraction (XRD), scanning electron microscopy (SEM) and atomic force microscopy (AFM) have a key role in understanding the microstructural features of carbon materials exposed to different environmental conditions [4,30]. Donnet and Wang [31] studied the surface morphology of four commercially available carbon materials (highly oriented pyrolytic graphite, synthetic graphite powder, carbon black and carbon fiber) using AFM and had compared the results with those obtained from scanning tunneling microscopy. Though there are several studies on the surface characterization of carbon materials using SEM, AFM and Laser Raman spectroscopy (LRS), the surface morphological changes associated with molten LiCl-KCl salt corrosion have not been reported in the literature.

In this thesis work, the corrosion performance of the carbon materials, namely low density graphite (LDG), high density graphite (HDG), GC and PyG was investigated and the morphological changes in the samples induced by molten LiCl-KCl salt after continuous exposure to 2000 h were evaluated at the micrometer scale using SEM, EDX, AFM, XRD and LRS. The results are presented along with probable mechanism by which surface degradation occurred during molten salt corrosion.

4.2 Experimental

1. The PyG investigated in this study was deposited at 2323 – 2373 K by pyrolysis of methane gas and in an indirect heating reactor of chemical vapour deposition (CVD) [32].
2. X-ray diffraction studies were carried out on as-deposited PyG powder and flat plate samples for calculating the interlayer spacing or distance (d_{002}) and crystallite size along the c-axis $L_c(002)$ using Bragg and Scherrer formula.
3. Corrosion studies were conducted in molten salt test assembly (MOSTA). The carbon samples LDG, HDG, GC and PyG were immersed in molten LiCl-KCl eutectic at 873 K for 2000 h under ultra high pure (UHP) argon atmosphere.
4. The weights of the samples before and after the molten salt corrosion test were used to calculate the weight change percentage due to corrosion.
5. The surface of the as-received and corrosion tested carbon materials was examined visually and were characterized with SEM, EDX, AFM, XRD and LRS.

4.3 Results and Discussion

4.3.1 Visual examination and corrosion behaviour of carbon materials

The LDG, HDG and PyG samples after 2000 h of exposure to LiCl-KCl salt is shown in Fig 4.1. Visual examination of LDG (Fig. 4.1a) and HDG (Fig. 4.1b) revealed the formation of pores on the surfaces compared to as-received samples and uniform attack was observed on the entire surface after exposure. Both as-deposited and corrosion tested PyG top and bottom surfaces had a silvery appearance as shown in Figs. 4.1c and 4.1d respectively. The top surface showed spherical nodes and it a black shadow which formed on the surface at the time of deposition. The bottom surface was small curve shaped and it appeared to be the inverse of the top surface nodes [33]. The impurities and irregularities present on the graphite substrate surface are the growth centers for the nodes during deposition process. After corrosion test, the surfaces (top and bottom) did not show any observable change and no attack was found on the surfaces of PyG; however, the brightness of the surface increased. The as-received GC surface exhibited mirror like finish and after corrosion test the surface became marginally dull without any attack on the surface. Dimensional variation after corrosion testing was significant in the case of LDG, less pronounced in HDG and no change in dimensions was observed in GC and PyG samples. Weight gain of about 0.1875 % and 0.0335 % were observed in the case of LDG and HDG, respectively; however, GC (9.2×10^{-4} %) and PyG (4.0×10^{-4} %) showed negligible weight loss after exposure to LiCl-KCl salt indicating the possibility of penetration of molten salt into porous LDG and HDG compared to GC and PyG. It was observed that LDG and HDG samples lost weight by degradation and gained weight by absorption of salt. Weight gain was more pronounced in LDG compared to

HDG. The insignificant weight change in case of GC and PyG materials suggest that they have limited interaction and their compatibility with molten LiCl-KCl salt is excellent.

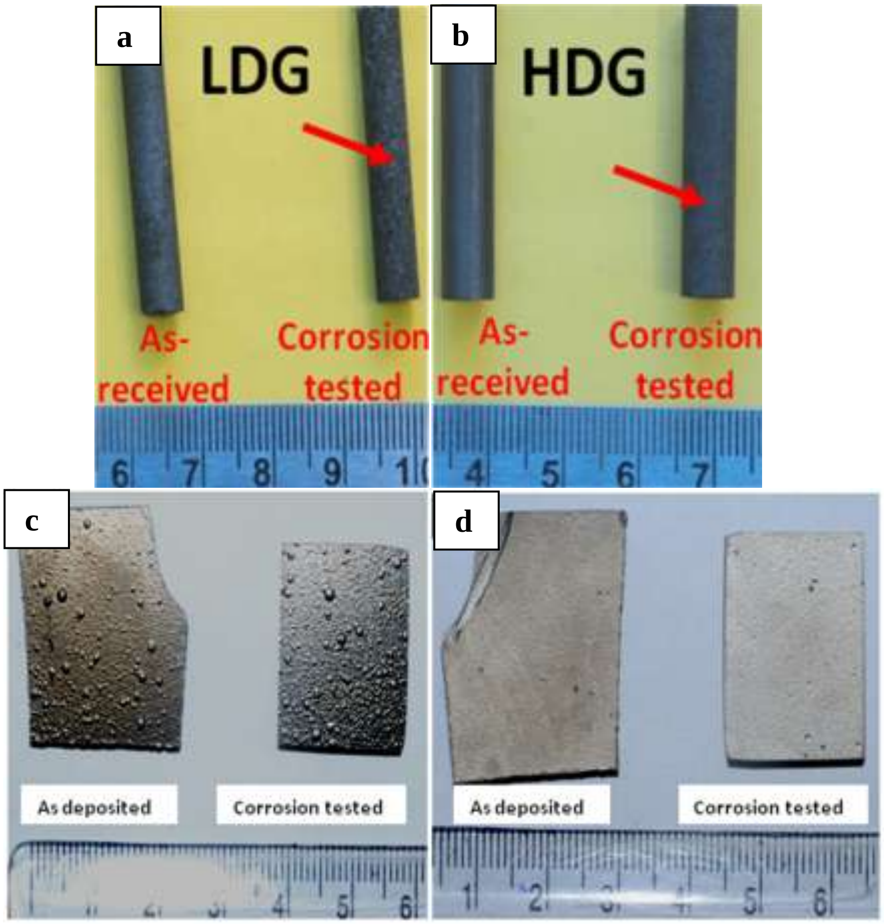

Fig. 4.1 As-received and corrosion tested samples: (a) LDG, (b) HDG and PyG (c) top and (d) bottom surfaces immersed in molten LiCl-KCl salt for 2000 h at 873 K.

4.3.2 Microstructural studies and surface morphology of low and high density graphite

4.3.2.1 SEM-EDX and AFM studies

The surface morphology of as-received and corrosion tested LDG and HDG samples are shown in Figs. 4.2 and 4.3 respectively. The microstructures of as-received LDG (Fig. 4.2a) and HDG (Fig. 4.3a) revealed pores, defects and micro cracks, which become active sites for molten salt to penetrate into the bulk and cause internal corrosion. According to Vacik et al.

[6] the penetration of molten salt depends on the exposure time and the temperature of the molten salt system. It is well known that graphite materials have significant porosity (as shown in Figs. 4.2 and 4.3) and according to the mass transport proposed by Castro et al. [34], the salt penetration into the graphite structure is practically controlled by in-pore diffusion and by boundary layer diffusion at high temperatures. Baumli and Kaptay [35] evaluated the wettability of molten alkali chlorides on graphite surfaces by sessile drop method and had measured the critical contact angle of spontaneous penetration (infiltration) of the molten chlorides into a porous graphite substrate to be below 90°, in the interval between 31°and 58°. The contact angle indicated that molten salts have favorable wettability on graphite surfaces and penetration of different molten salts into the inner porous structure of graphite substrate will occur. Generally molten salt corrosion is caused by the dissolution of the constituents of the material, selective leaching/attack, pitting, uniform surface corrosion and chemical reactions [26]. Any one or more of the above corrosion processes can take place depending on the nature of materials, testing medium, temperature and environment. Thermodynamic data for the reaction of carbon with LiCl and KCl are not available in the literature, and hence, the values of Gibbs free energy of these reactions could not be calculated. However, the reactions that can occur assumed to be as follows at 873 K are:

$C + 4LiCl \rightarrow 4\,Li + CCl_4;\ \Delta G = 1372\ kJ/mol$ (1)

$C + 4KCl \rightarrow 4K + CCl_4;\ \Delta G = 1438\ kJ/mol$ (2)

The ΔG values at 873 K for reactions (1) and (2) were calculated using FactSage Version 6.2 software. The positive values of ΔG of reactions (1) and (2) reveal that spontaneous chemical reaction between carbon and the molten salt is not possible at 873 K. In the case of LDG and HDG materials, carbon particles detaching from the surfaces of graphite and dispersed into the molten salt and uniform surface attack (Figs. 4.2b and 4.3b) were clearly observed and the pores were found to be widening after exposure to molten LiCl-KCl salt at high temperatures and leaving behind a relatively more porous graphitic structure. The other possibility for significant corrosion behaviour of LDG and HDG materials is due to the presence of trace impurities in the chloride salt [6,26], hetero-elements (e.g. H, O, N, S) bound to the edges and impurities present in the specimen. The corrosion of carbon materials depends on the impurity (inorganic residues) content also. These impurities may form corrosive and gaseous products at high temperature and attack the carbon materials. SEM/EDX single spot analysis at higher magnification confirmed the presence of salt within the pores. The X-ray microanalysis (using EDX) showed the presence of molten salt (K: 04.53 wt % and Cl: 03.47 wt %) along with carbon (C: 92.04 wt %) in the microstructure of corrosion tested LDG; likewise salt was present in the microstructure of corrosion tested HDG. The salt (K and Cl) was observed to distribute randomly and co-existed with carbon on a microscopic scale (within the pores). Adsorption of the alkali chloride salt on the surface of graphite substrate could not be examined since the corrosion tested samples were washed with water as soon as they were removed from the cell assembly for the purpose of preventing any interaction of salt particles with ambient air. The carbon particles flake off from the graphite materials (LDG and HDG) after immersion test as observed in magnified SEM images (Figs. 4.2b and 4.3b). The major difference between LDG and HDG in terms of corrosion behaviour is their density and macro porosity. The nature of molten salt attack on LDG and HDG appeared to be similar; however, the extent of attack varied. Penetration of molten salt into LDG and HDG samples up to a few micro meter depth could be observed, due to the interconnected pores present in these materials. The penetrated salt was found to be distributed randomly within the pores of graphite on a microscopic scale. Molten salt can penetrate or adsorb into LDG compared to HDG, because of high specific surface area, lower density and high porosity features accelerating the degradation of LDG by uniform surface attack, pore widening and dislodging carbon particles into molten salt. This ultimately led to the enhancement of adsorption of molten salt and weight gain.

AFM is a powerful tool for accurate determination of surface roughness values along with the surface topography of carbon materials [30,31]. Figure 4.4 shows the AFM morphology of as-received and corrosion tested LDG and HDG materials in molten LiCl-KCl salt for 2000 h at 873 K. Aggressive attack of molten salt was observed on the surface of LDG (Figs. 4.4a and b) and HDG (Figs. 4.4c and d). The topography of LDG and HDG surfaces showed imperfections owing to surface attack induced by molten salt and the removal of surface layer as flakes (Figs. 4.4b and d) with formation of plenty of pores. The surface roughness values of these carbon materials calculated from AFM measurements are listed in Table 1. The roughness of as-received LDG and HDG surfaces increased after exposure to molten salt. The increase in the surface roughness was due to the increase in the size of pores and creation of new pores over the surface because of dispersion of carbon particles from HDG and LDG into molten salt. Deposition and penetration of salt particles through the surfaces of LDG and HDG also resulted in increased roughness.

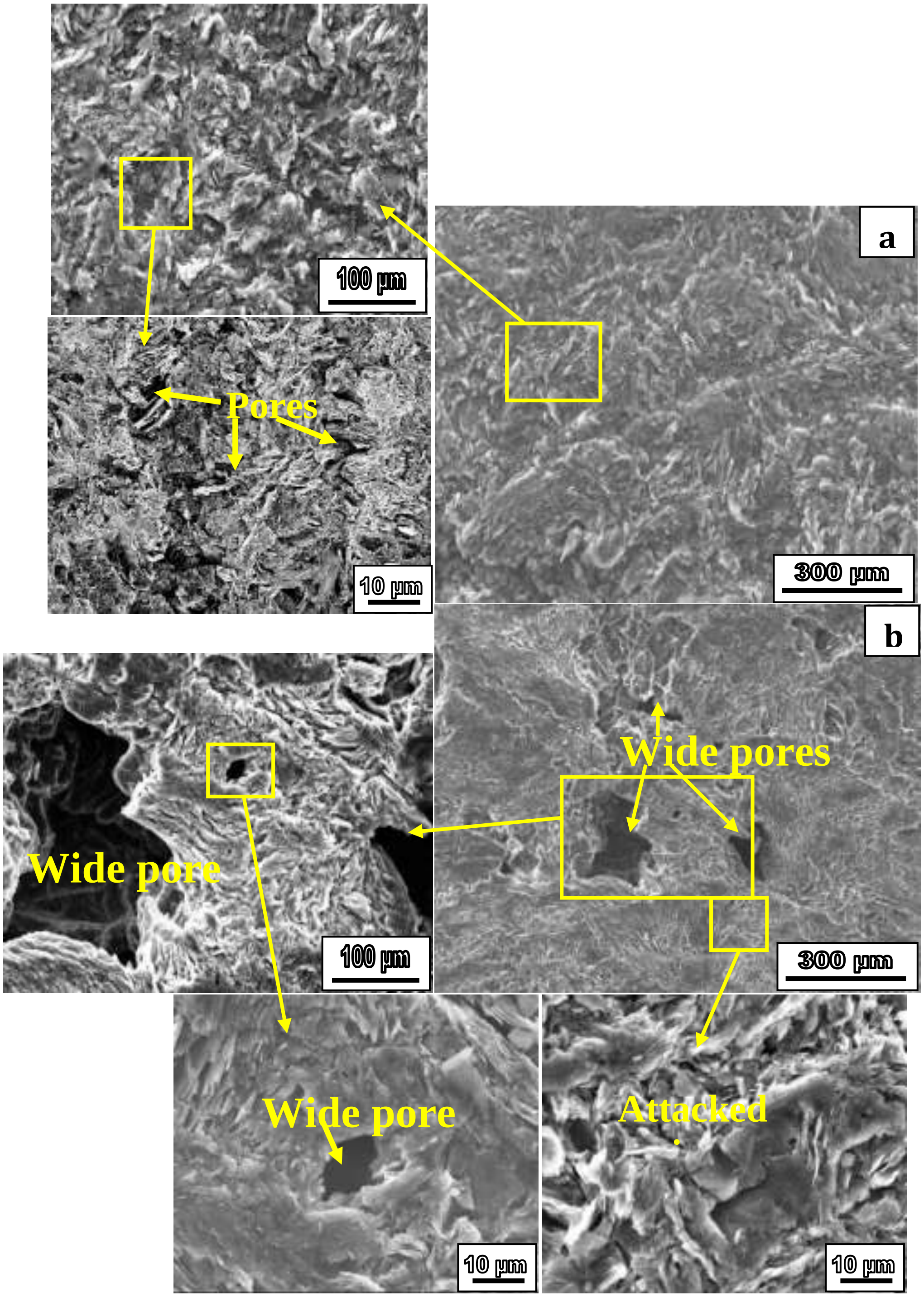

Fig. 4.2 Surface morphology of (a) as-received and (b) corrosion tested LDG in molten LiCl-KCl salt for 2000 h at 873 K.

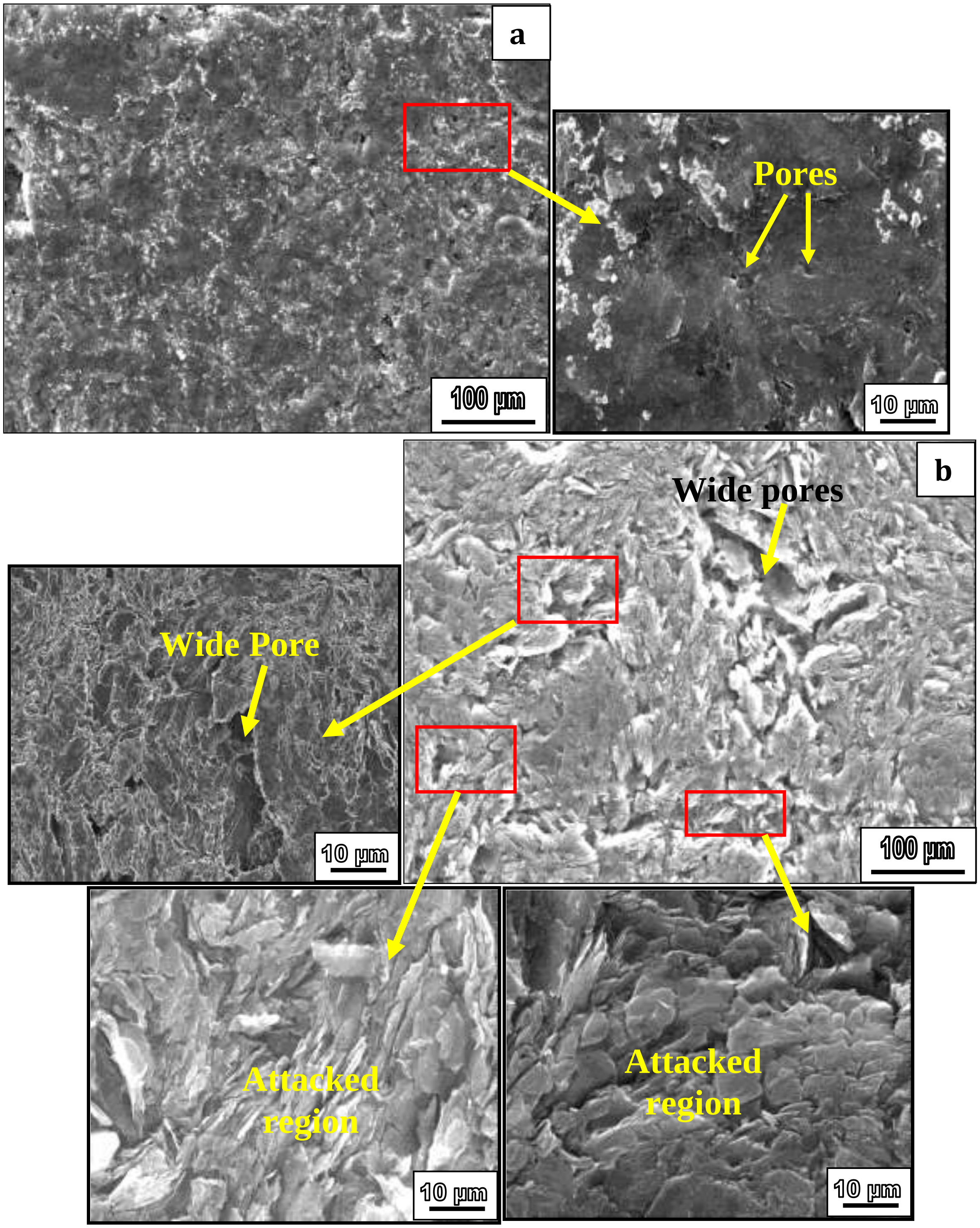

Fig. 4.3 Surface morphology of (a) as-received and (b) corrosion tested HDG in molten LiCl-KCl salt for 2000 h at 873 K.

Table 4.1 Surface roughness of as-received and corrosion tested LDG and HDG by AFM.

Carbon material	Average roughness (nm)		RMS roughness (nm)	
	As-received	Corrosion tested	As-received	Corrosion tested
LDG	294.3	520.5	400.1	640.8
HDG	104.5	252.1	135.9	321.4

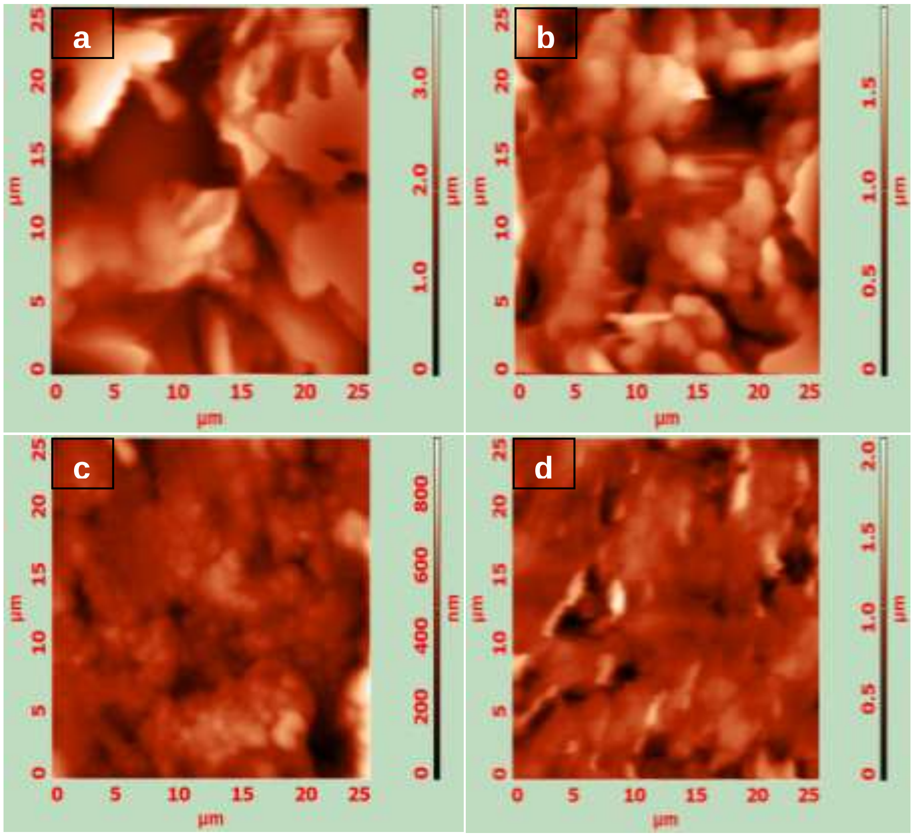

Fig. 4.4 Topography of as-received and molten salt corrosion tested LDG (a and b) and HDG (c and d).

4.3.2.2 X-ray diffraction studies

The XRD patterns of the as-received and immersion tested LDG and HDG samples in molten LiCl-KCl salt are shown in Figs. 4.5a and b. The lattice planes observed for both LDG and HDG were (002), (100), (101), (004) and (110). The XRD data revealed neither any major change nor the formation of any new compound after the corrosion test. Salt phase could not be identified in the diffraction patterns since to the amount of salt absorbed into the porous structure was less than the detection limit of XRD. However, the salt present in the LDG and HDG was identified by EDX point analysis. The diffraction patterns of LDG and HDG were observed to be similar, because of the same processing method and no structural variation in them. The FWHM values of the (002) peak of the LDG, HDG and PyG were calculated to understand the disorder in the carbon materials from as-received to corrosion tested ones. The FWHM of the as-received samples are 0.299 and 0.478° while in case of corrosion tested materials are 0.391 and 0.492° for LDG and HDG respectively. Although the differences are small, an increase in FWHM of

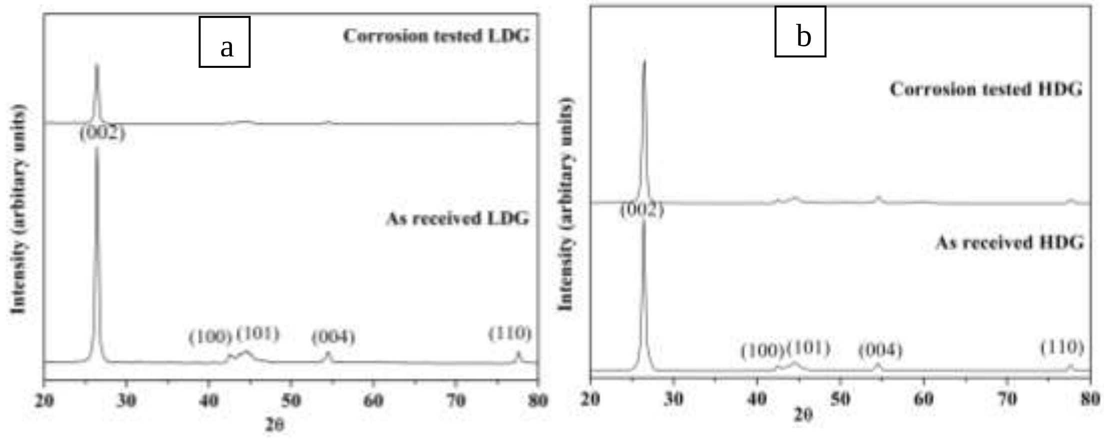

Fig. 4.5 XRD patterns of (a) LDG and (b) HDG samples before and after corrosion test in molten salt at 873 K for 2000 h.

(002) peak of LDG and HDG indicating that an increasing structural disorder of the graphite after the corrosion test in molten salt. XRD patterns confirmed the absence of reactivity of graphite materials with molten LiCl-KCl salt at 873 K. The peaks corresponding to intercalation compounds were not observed on LDG and HDG upon exposure to molten salt for 2000 h.

4.3.3 Surface morphology of glassy carbon

The surface morphologies of as-received and corrosion tested GC samples are shown in Figs. 4.6a and 4.6b respectively. The lines in the micrograph of the as-received GC (Fig. 4a) sample may be due to preparation of the surface by milling/machining of the material. After corrosion test in LiCl-KCl salt the surface morphology appeared to be smooth (Fig. 4b) and there was no significant attack. The surface of GC was flat after corrosion test since the lines formed during milling/machining of the GC disappeared. Due to the non-wetting characteristic of GC by molten salt initiation of pores was not observed on the surface even after corrosion testing for 2000 h. The density of GC is quite low, but it is nonporous in nature due to the absence of large open pores and the presence of small closed pores of a few nanometer in size [36]. Owing to closed porosity, penetration of molten salt into GC was not evident. High temperature stability and absence of long-range order in the structure also make GC chemically more inert towards molten salt than LDG and HDG materials [6]. Albeit GC showed excellent corrosion resistance towards molten LiCl-KCl salt, it was not considered for present applications as structural material in pyroprocessing due to the constraints like cost and commercial availability. Thus for the detailed microstructural characterization LDG, HDG and PyG were only chosen in the present work.

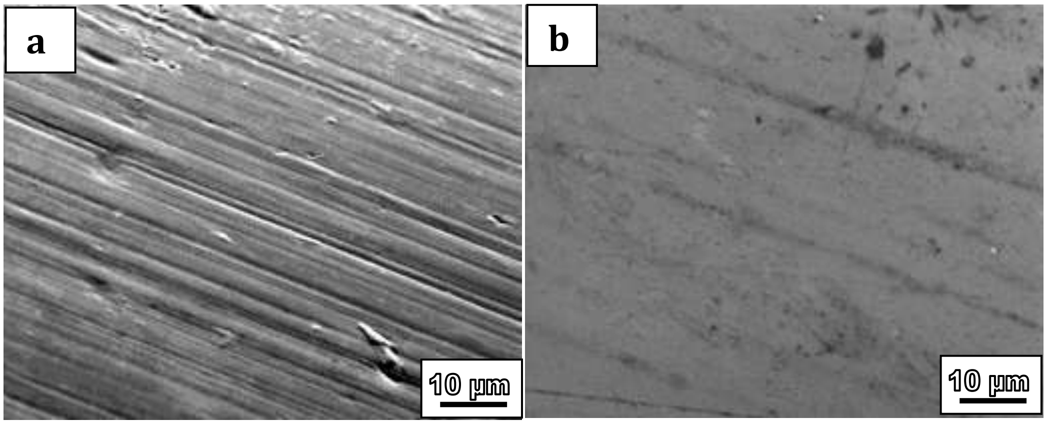

Fig. 4.6 Surface morphology of (a) as-received and (b) corrosion tested GC in molten LiCl-KCl salt for 2000 h at 873 K.

4.3.4 Microstructural studies and surface morphology of pyrolytic graphite

4.3.4.1 Optical Microscopy, SEM-EDX and AFM studies

The fine spherical growth features on the top surface of PyG are shown in Figs. 7a and b. These spherical shapes were observed to grow in the perpendicular direction to the substrate. The PyG top surface examined under optical microscopy bright field view showed nodules like structure [37]. Inside the nodules cauliflower structure (Figs. 4.7a and 4.7b) could be seen. The bottom face contained very small nodules in comparison to the top face as shown in Figs. 7c and d respectively. These nodules were large in diameter and the size was observed to increase as the deposition process continued [37]. The surface morphology of corrosion tested samples did not show any change and was similar to that of the as-deposited surface of PyG. The SEM microstructures of the top and bottom surfaces of the as-received as well as corrosion tested PyG samples are shown in Fig. 4.8. These microstructures revealed major feature of concave and convex asperities on the top and bottom surfaces respectively [33,38]. The top surface exhibited characteristic bumps which could be seen clearly in optical microscope (Fig. 4.7a & 4.7b). These bumps are correlated to the smoothness of the graphite substrate and to the characteristics of the soot in the deposition processes [38,39].

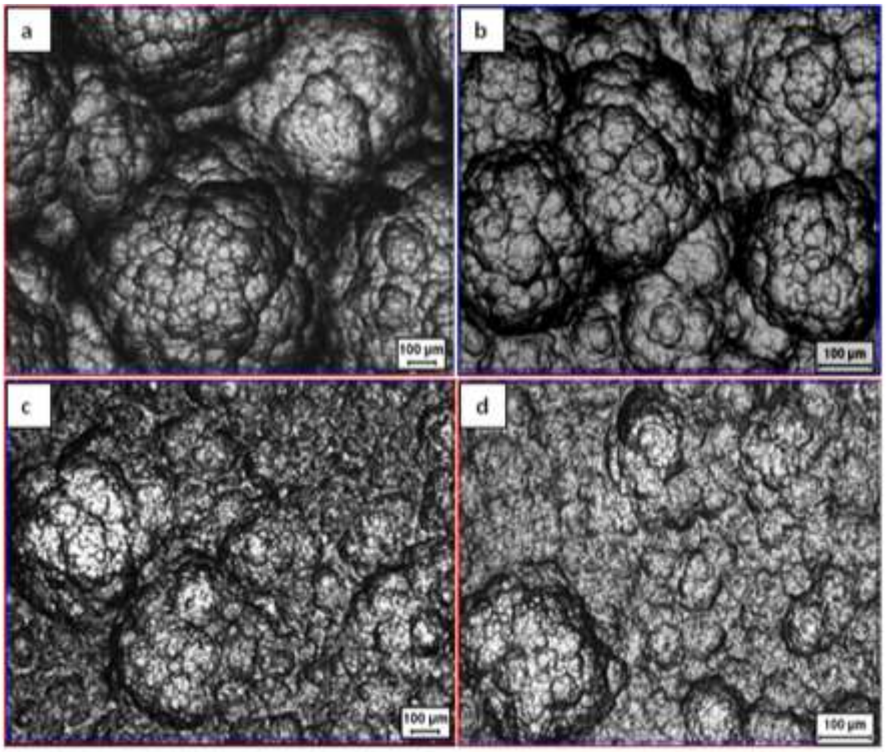

Fig. 4.7 Bright field optical microscopic images of PyG: (a) as-deposited top surface; (b) exposed to molten LiCl-KCl for 2000 h: (c) bottom surface (as-deposited) and (d) bottom surface exposed to molten LiCl-KCl for 2000 h.

The SEM micrographs of the bottom surface before and after corrosion test are shown in Figs. 4.8c and d respectively. The bottom surface appears to be the inverse of the top surface. As-received PyG surface exhibited convex feature and absence of pore morphology in the back scattered SEM micrograph (Fig. 4.8a). After corrosion test in molten salt PyG did not show any evidence of degradation and attack on the surface (Fig. 4.8b). Magnified SEM images and the corresponding EDX spectra of PyG surface before and after corrosion test are shown in Figs. 4.8e and f. The EDX spectrum of as-received PyG was found to possess the impurities

Si (0.91 wt%) and O (9.25 wt%) along with C (89.84 wt%), while the EDX spectrum of molten salt corrosion tested PyG after 2000 h showed 100 wt% C only.

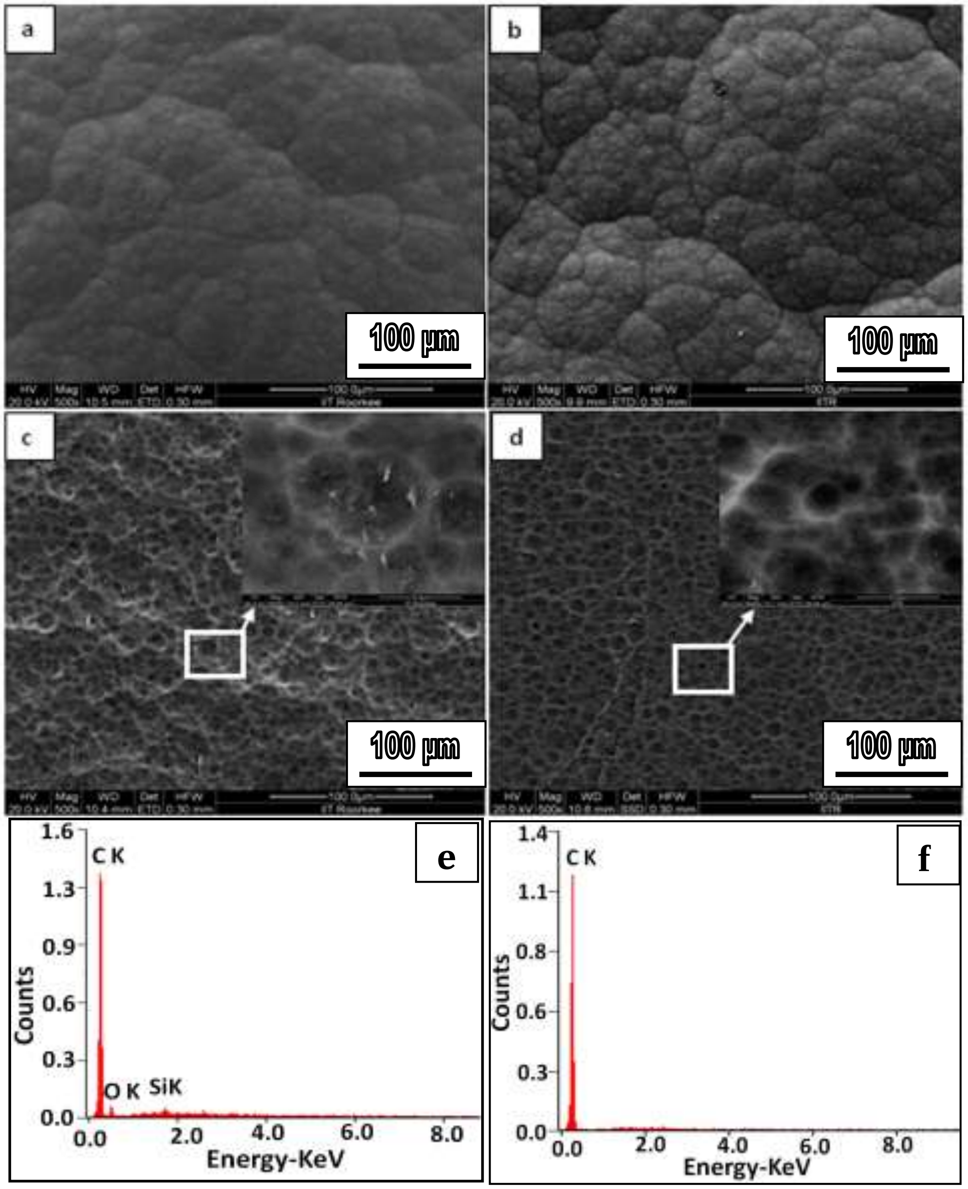

Fig. 4.8 SEM microstructures of PyG top surface: (a) as-deposited, (b) corrosion tested and (c) as-deposited bottom surface; (d) corrosion tested bottom surface; (e) EDX spectrum of as-deposited bottom surface and (f) EDX spectrum of bottom surface exposed to molten LiCl-KCl salt for 2000 h at 873 K.

According to Lewis et al. [37] traces of impurities present in PyG could be from the starting material. The EDX pattern before and after the corrosion test are similar, which confirmed that no significant change occurred in elemental composition. In the preparation method for PyG, higher temperature caused high graphitization, less active sites and absence of hetero-elements in its structure resulting in lower corrosion rate than GC, HDG and LDG.

The surface topography of as-received and corrosion tested PyG is shown in Figs. 4.9a-d respectively. The nodular morphology observed is characteristic of PyG [37]. The surface roughness values calculated with Nova software using average and RMS roughness formula are listed in Table 4.2. These values indicated that top surface had less roughness compared to bottom surface of PyG. Also, corrosion tested top surface had less roughness compared to that of the as-deposited surface. After immersion in molten salt, the surface roughness of PyG further decreased (Table 4.2) and the surface became smoothened. The decrease in surface roughness could be attributed to the removal of soot formed during deposition of PyG on the surface. This feature was also observed in the SEM images of PyG as shown in Figs. 8c and d. The top surface analyzed by AFM also ascertained the nodular morphology. After corrosion test in molten chloride medium there was no appreciable change in nodular morphology (Fig. 4.9b). The concave asperity present on the bottom surface resembled as cavities in AFM (Figs. 4.9b and d). There was no attack on the bottom side of PyG surface. The topographical feature present on the bottom surface of as-deposited PyG is resembled the same as that of the corrosion tested surface. White regions present in AFM micrographs are topographically elevated portions. The roughness profiles at the bottom surface showed nearly equal roughness. After 2000 h exposure in chloride environment, the top and bottom of corrosion tested surfaces appeared similar to the as-deposited surfaces.

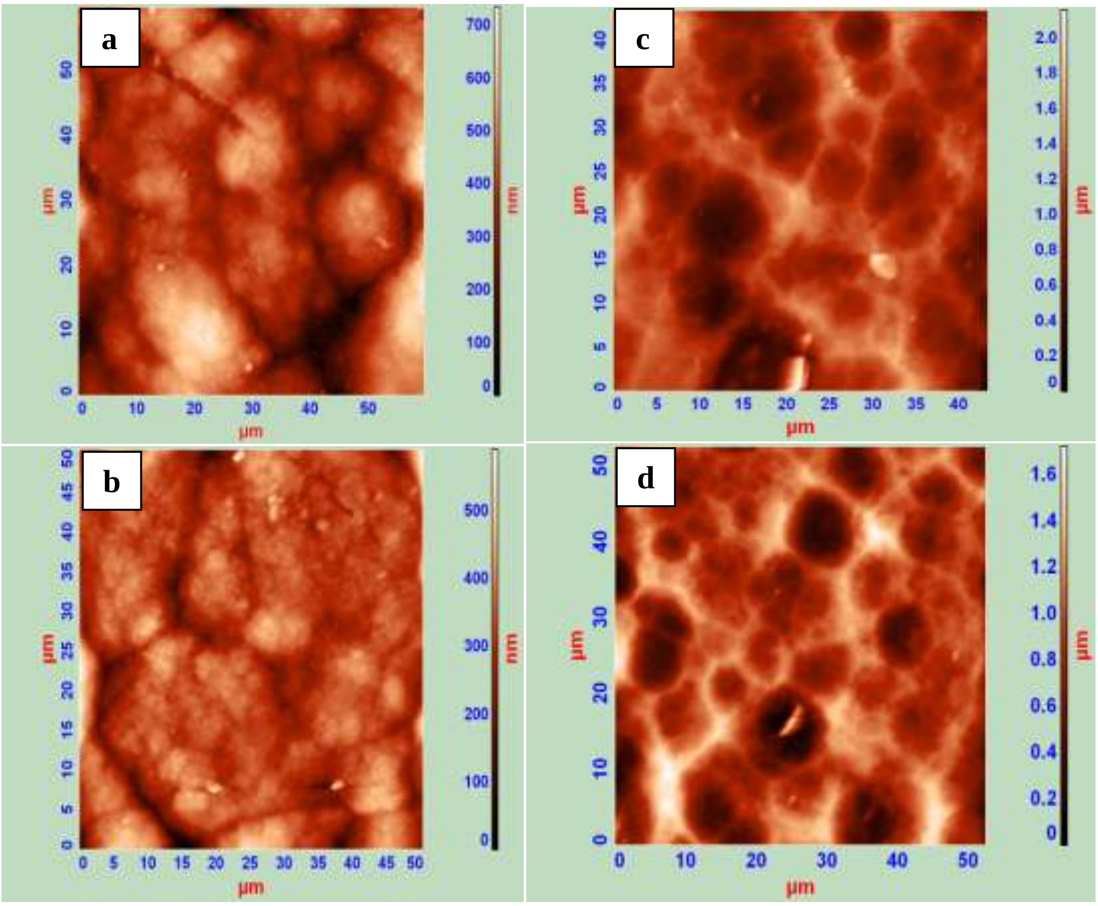

Fig. 4.9 AFM micrographs of pyrolytic graphite: (a) as-deposited top surface; (b) top surface exposed to molten LiCl-KCl for 2000 h; (c) as-deposited bottom surface and (d) bottom surface exposed to molten LiCl-KCl for 2000 h.

Table 4.2 Surface roughness values of PyG measured from AFM.

PyG sample	**Surface roughness values (nm)**			
	Top surface		**Bottom surface**	
	RMS	Average	RMS	Average
As-deposited	113	89	269	218
Corrosion tested	71	55	270	213

4.3.4.2 X-ray diffraction studies

The structural features of the as-deposited PyG samples characterized by X-ray diffraction technique are shown in Fig. 4.10. The interlayer spacing of the PyG measured by Brag's formula found to be 3.42 Å. This interlayer spacing is much larger than that of the ordered graphite (for well oriented graphite the value is 3.35 Å). The diffraction lines of as-deposited PyG showed considerable broadening effect. The breadth of a diffraction peak is significant in the determination of crystallite size. The crystallite size (L_c) of PyG was estimated using (002) peak was found to be 249.4 Å. The broadening is caused by finer crystallite particles present in the PyG. The crystallite sizes indicated that the layer order is nearly random [40]. The unique and important structural feature of PyG is the preferred orientation parameter. In this study the preferred orientation of PyG was calculated from (002) reflections using the following formula.

$$\text{Preferred orientation} = I\,(002)_{\max} / I\,(002)_{\min} \quad [40]$$

Where the data are normalized to $I\,(002)_{\min} = 1$

The value in order of 10^3:1 clearly indicates that the preferred orientation of the (002) plane is high. PyG exhibited a high degree of preferred orientation along one particular direction. The individual crystallites present in the PyG tend to have their basal planes (002) aligned parallel to the surface of deposition [10]. The hexagonal layered structure of PyG has the preferred orientation along 'c' axis. During deposition, atoms of the hexagonal network could be displaced along the c-direction [41]. The arrangement of crystallites in turbostratic structure of PyG is reported to have high degree of preferred orientation [42]. The high temperature CVD (≥ 2000°C) method plays a key role in obtaining such preferred orientation in PyG [32,43]. Close interlayer spacing and finer crystallite particles revealed that PyG has nearly ordered graphite structure. The diffraction pattern of PyG after immersion studies in molten salt is also shown in Fig.4.10. PyG showed only (002) and (004) lattice planes with highly preferred orientation along (002) plane before and after the corrosion test. The increase in FWHM of (002) was quite low from as-received to corrosion tested PyG; hence, much pronounced disorder was not observed in the PyG after exposed to molten LiCl-KCl salt. The turbostratic structure, graphitization, high preferred orientation and high density of PyG prevent the permeability of molten salts into its structure. It is evident that PyG is chemically inert to molten salt since no corrosion products were identified.

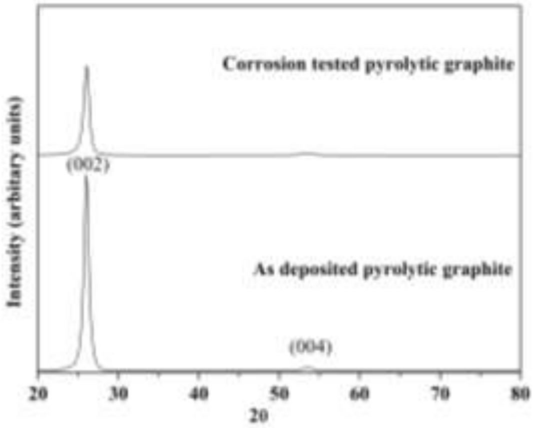

Fig. 4.10 XRD patterns of PyG samples before and after corrosion test in molten salt at 873 K for 2000 h.

4.3.5 Laser Raman spectroscopic studies on low density graphite, high density graphite and pyrolytic graphite

Raman spectroscopy plays an important role in the structural characterization and it provides the most valuable data on the microstructure of carbon/graphite materials [44,45]. Raman investigation of different carbon materials was conducted elaborately by different research groups in the past [45,46]. However, very limited information is available [4] on the Raman analysis of carbon materials after corrosion test in molten salt and up to now, no

Raman mapping (imaging) study has been reported after the molten salt corrosion test. Carbon based materials in the wave number region between 1000 and 2000 cm^{-1} give interesting information related to microstructural features. However, the sensitivity of the Raman peaks to short range disorder and the complexity in the microstructure of carbon materials create ambiguity in the interpretation of various band frequencies. The Raman spectrum of single hexagonal crystal of graphite belonging to D^4_{6h} generally gives a first order band (E_{2g2}) at 1582 cm^{-1} (referred to as G band), which is attributed to the displacement of carbon strongly coupled in hexagonal sheets [45]. Disorderness due to structural imperfection and interstitial defects in the graphite structure broaden the Raman peaks. In addition, new peaks around 1357 (D band) and 1620 (D′) cm^{-1} will also appear due to disordered carbon atoms [45]. The basal plane in graphite consisting of strong C-C bonding conserve highly ordered structure. However, the graphite crystals are affected by disorder through the c-axis. The Raman analysis on highly ordered pyrolytic graphite (HOPG) gives a single strong peak at 1582 cm^{-1} [45,47]. The Raman spectra recorded on the graphite surfaces before and after molten salt immersion in the present study are shown in Fig. 4.11. In order to quantify the effect of molten salt exposure, Raman spectra of unexposed graphite specimens were compared with that of molten salt exposed samples. The as-received and corrosion tested LDG, HDG and PyG samples showed peaks around 1337, 1582 and 2700 cm^{-1}, which were attributed to D, G and G′ bands respectively. Apparently all the spectra obtained had similar spectral signatures around 1337 and 1582 cm^{-1}, implying that the fraction of disorder in the microstructures of all three graphite materials is about the same. Even the PyG used in the present analysis was not highly ordered as reported in the literature. The position of the D band was shifted to several wave numbers than expected. It was supposed to occur at 1357 cm^{-1}, but was not the case in the present study. Dependency of D band on laser wavelengths has been reported in the literature [47-50]. The D band was shifted from 1360 to 1330 cm^{-1} when the excitation wavelength was increased from 488 to 647 nm.

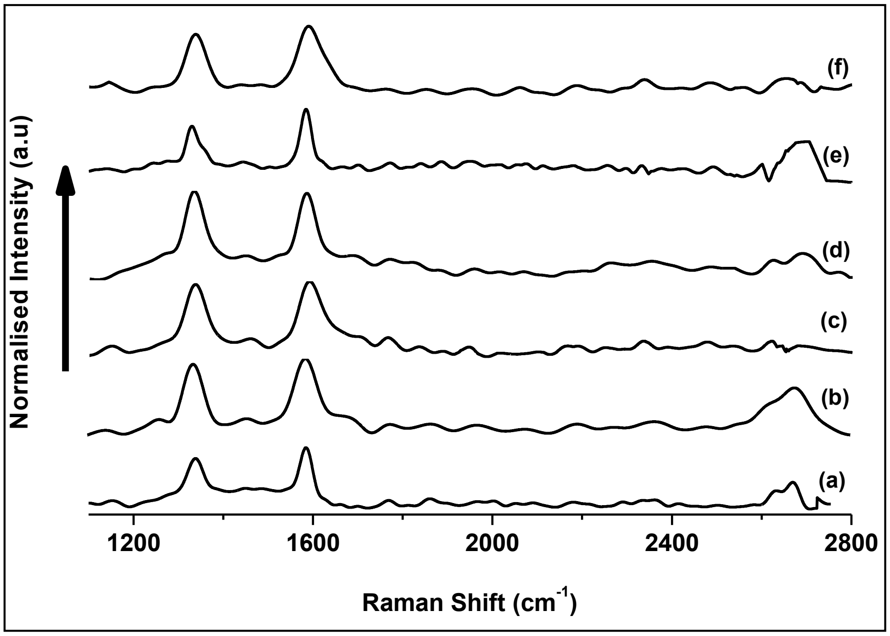

Fig. 4.11 Raman spectra of as-received and molten salt exposed carbon materials: (a) as-received LDG; (b) molten salt exposed LDG; (c) as-received HDG; (d) molten salt exposed HDG; (e) as-received PyG; and (f) molten salt exposed PyG.

The wavelength used in the present Raman investigation was 633 nm, and the observed D band values were matching with the reported values [47]. The D band frequency was found to be consistent in all types of carbon materials irrespective of whether exposed or unexposed to molten salt. Wang et al. [47] reported that the intensity of D band depends on edge density and the laser wavelength and not on the size of the micro-crystallites. The peak around 2700 cm^{-1} referred as G′ was accounted generally for crystalline graphite [51]. In imperfect graphites, G′ is reported to occur as a single component; but in highly ordered structure, it has two close and broad components. In the present study, similar G′ band was observed.

Interestingly, the characteristics of D and G′ were totally opposite and the D band occured in structurally imperfect graphites [51]. The Raman spectra of all the graphite materials in the present studies showed the presence of both D and G′ bands. This has raised a question whether our graphite materials are crystalline or not. It was earlier reported that the spectrum of polycrystalline graphites also give D band, called as disorder-induced D mode and become active in small graphite crystallites of polycrystalline graphites. From the normal Raman spectral analysis, it is inferred that all the graphite materials under investigation were partially disordered polycrystalline in nature.

Rigorous analysis of intensity, peak position and band width gave exciting information on microstructural features of carbon materials. The integrated intensity ratio, I_D/I_G for the D and G bands is widely used for quantifying the defect in graphitic materials [44,45]. The band width and I_D/I_G ratio calculated from Raman spectra of as-received and corrosion tested LDG, HDG and PyG are listed in Table 4.3. The I_D/I_G ratio of LDG was comparatively higher than HDG and PyG materials, indicating that the disorder in LDG was more compared to the other two. The I_D/I_G ratios of the corrosion tested samples were also higher than that of the as-received specimens. The corroded LDG samples were observed to possess higher I_D/I_G ratio than that of corroded HDG and PyG specimens. The band width of the corroded LDG was also higher than that of other carbon materials. Generally, greater the band width, higher is the degree of disorderness in graphite samples [47]. All these observations from Raman investigation revealed that PyG and HDG samples have more degree of ordered structure and are free from interstitial defects when compared to LDG samples and the degree of disorder was the least in PyG. This structural variation could be detected from the I_D/I_G ratio.

Table 4.3 Raman spectroscopic parameters derived for LDG, HDG and PyG.

Sample		**Peak position** **υ (cm^{-1})**	**D Band width** **$\omega_{1/2}$ (cm^{-1})**	**I_D / I_G**
LDG	As-received			
	D	1336	48	1.03
	G	1588		
	Corrosion tested			
	D	1334	59	1.36
	G	1584		
HDG	As-received			
	D	1330	43	0.87
	G	1584		
	Corrosion tested			
	D	1333	56	1.26
	G	1586		
PyG	As-received			
	D	1342	40	0.83
	G	1592		
	Corrosion tested			
	D	1340	42	1.21
	G	1590		

Since Raman spectrum from single spot will not give a clear picture about the bulk sample, information from spatial Raman mapping is considered to be more reliable and relevant than single spectral analysis. Raman mapping was carried out on corrosion tested samples of surface area 80 x 80 μm^2 to find out the D band variation semi quantitatively which in turn would provide information about the effect of molten salt on the degree of disorder. Raman map generally gives the intensity distribution of one particular spectral range from which the changes in the composition of a specific component can be determined. Raman map also provides the image distribution of one particular wave number range (corresponding to one component). Average Raman spectra and imaging (mapping) were recorded before and after testing the graphite materials in molten salt. The Raman imaging confirmed that the molten

LiCl-KCl salt induced a disorder in the microstructure of carbon material, particularly in LDG.

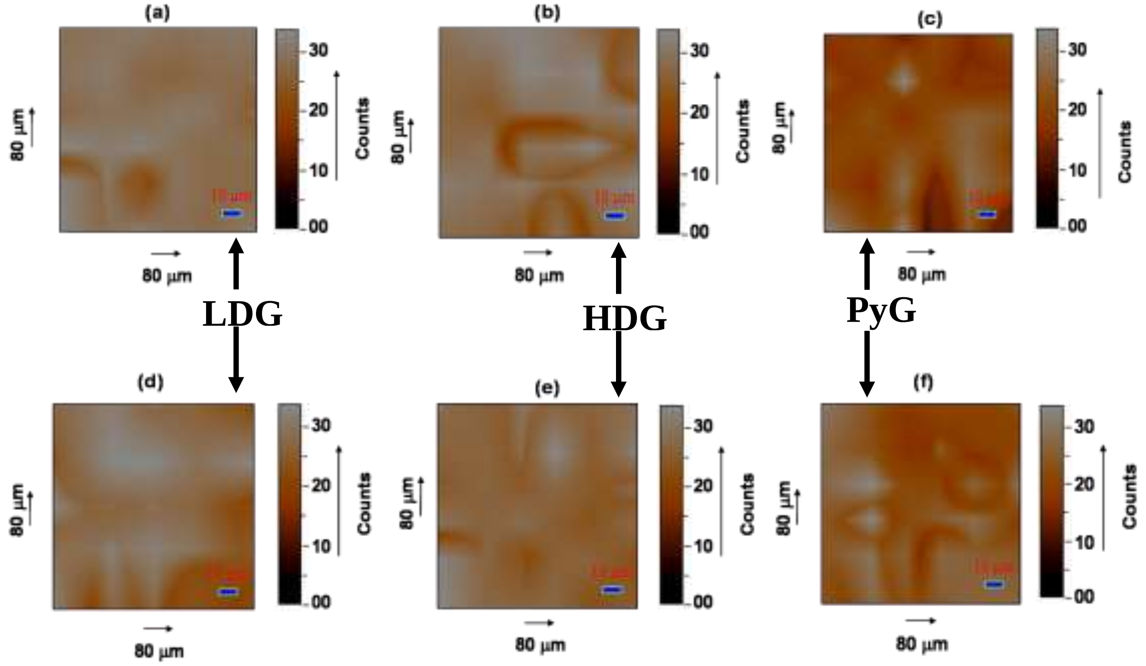

Fig. 4.12 Raman mapping of the D band of carbon materials: (a), (b) and (c) are for the as-received LDG, HDG and PyG respectively and (d), (e), and (f) correspond to that of molten salt exposed LDG, HDG and PyG respectively.

Figure 4.12 shows the Raman mapping of D band of unexposed and molten salt exposed LDG, HDG and PyG samples. It is evident that the D line distribution is low in as-received graphite samples when compared to molten salt exposed samples. Also, the degree of disorder (high D band distribution) was high in LDG (Figs. 4.12a and d) when compared to HDG (Figs. 4.12b and e) and PyG (Figs. 4.12c and f), which was indicated as white colour in the mapping image. Raman mapping analysis of molten salt exposed carbon materials revealed that high disorder (indicated by white colour intensity) was introduced in the graphitic structure of LDG and HDG and the modification in the D band of PyG was negligible. Raman study by Bernardet et al. [4] confirmed the molten salt induced disorder in the structure of the three carbon materials. Analysis of integrated intensity ratio upheld the introduction of minor defects in HDG and PyG after molten salt corrosion test. Raman mapping ascertained the quantum of disorder introduced in PyG to be less than that in HDG.

4.3.6 Degradation mechanisms of carbon materials

The penetration and adsorption of molten salt into graphitic structures can proceed in different ways depending on the arrangement of graphite planes in the structure. Vacik et al. [6] reported the restricted penetration of molten salt into non-porous material and accelerated penetration of salt into porous materials. The degradation of graphite depends on the degree of structural disorder, surface uniformity, preparation method and density of the material. The AFM observations of the carbon materials (LDG, HDG & PyG) are in accordance with the SEM microstructures. Structural disorder increased in the case of LDG and HDG due to high corrosion in molten salt. The degradation and corrosion behaviour of carbon materials depend upon the nature of hetero-elements present at the edges of carbon planes, the precursors, defects and heat treatment conditions at the time of manufacturing [34]. The major differences among LDG, HDG, GC and PyG are in the graphite structure, macro porosity and the impurity content. The structural features and absence of open porosity in GC and PyG resulted in high inertness towards molten LiCl-KCl salt at 873 K under UHP argon atmosphere when compared to LDG and HDG. The degradation of carbon materials in molten salt could be attributed to one or more of the following mechanisms: 1. Adhesion of salt to graphite, 2. Diffusion and filling the pores in graphite [4], 3. Formation of intercalation compounds [52] and/or 4. Removal of carbon particles. In the present investigation, formation of intercalation compounds was not evident by XRD and Raman analysis. Analysis of the cross-section of the long term corrosion tested samples by XRD, Raman spectroscopy and

SEM/EDX did not reveal the formation of any intercalation compound/phase. In the case of PyG the possibility of diffusion or penetration of molten salt is very remote because of the non-porous structure and highly preferred orientation of crystallites, which makes the PyG chemically inert to molten LiCl-KCl salt. The salt penetration depth of molten LiF into GC and PyG samples found to be negligible [6]. Thus, GC and PyG are called as impermeable grades of carbon materials [53]. The penetration and absorption of molten salt into graphite materials strongly depend upon the microstructure of the material. The present study suggests that the penetration of molten salt into carbon materials can be minimized by using impermeable graphite grades like GC and PyG. It is understood from the foregoing discussions that PyG has excellent corrosion resistance in LiCl-KCl salt at high temperatures under UHP argon atmosphere.

However, based on commercial availability and economic viability, HDG is preferred for plant applications. Corrosion studies on HDG indicated that a protective ceramic coating is essential to prevent its degradation during prolonged exposure in molten salt. For this purpose, the following two ceramic coatings have been identified:

1. Alumina-40 wt% Titania
2. Yttria Stabilized Zirconia

The development of these coatings and their performance in molten salt form Chapters 5 and 6.

4.4 Summary

The as-deposited PyG has a high preferred orientation along the (002) plane. The measured values of interlayer spacing (3.42 Å) and crystallite size (249.4 Å) indicated that PyG has a nearly ordered structure. Visual examination of the samples exposed to molten salt indicated no surface attack on PyG and uniform attack was observed on the surfaces of LDG and HDG. Among the carbon materials LDG, HDG, GC and PyG, excellent corrosion resistance was exhibited by PyG and GC when exposed to molten LiCl-KCl salt medium for 2000 h at 873 K under UHP argon atmosphere. Morphology of carbon materials by SEM and AFM analyses revealed that the surface of LDG and HDG were severely attacked in molten LiCl-KCl salt and the penetration of salt into GC and PyG was insignificant. X-ray diffraction analysis of carbon materials after immersion test showed no evidence of salt phase on the surface because the amount of salt absorbed by the carbon materials was below the limit of detection by XRD. The integrated intensity (I_D/I_G) ratio and band width analysis by Raman mapping confirmed that the extent of disorder created by molten salt was the least in PyG. Leaching of carbon particles from PyG or surface degradation after exposure to molten LiCl–KCl salt was negligible. This study revealed the excellent corrosion resistance of PyG in molten LiCl–KCl salt, required for Pyrochemical reprocessing applications. The corrosion data derived from this study indicated that the resistance of carbon materials to molten LiCl-KCl salt under UHP argon atmosphere at 873 K follows the order: LDG < HDG < GC < PyG. To extend the service life of carbon materials in pyrochemical processing, it is recommended that PyG may be used as a material (bulk form) or coating on graphite and HDG requires to be provided with a protective ceramic coating on the surface.

References

[1] K.C. Song, H. Lee, J.M. Hur, J.G. Kim, D.H. Ahin, Y.Z. Cho, Nucl. Eng. Technol. 42 (2010) 13-44.

[2] M. Takeuchi, T. Kato, K. Hanada, T. Koizumi, S. Aose, J. Phys. Chem. Solids. 66 (2005) 521–525.

[3] H.O. Pierson. Handbook of carbon, diamond and fullerenes. Park Ridge NJ: Noyes (1993) pp. 67.

[4] V. Bernardet, S. Gomes, S. Delpeux, M. Dubois, K. Guerin, D. Avignant, G. Renaudin, L. Duclaux, J. Nucl. Mater. 384 (2009) 292–302.

[5] M. Asou, S. Tamura, T. Namba, H. Kamoshida, Y. Shoji, K. Mizuguchi, T. Kobayashi, The corrosion resistance tests of crucible materials for oxide pyro-process, Proc. Int. Conf. on Future nuclear systems (Global’99), Jackson Hole, WY, USA, August–September (1999).

[6] J. Vacik, H. Naramoto, J. Cervena, V. Hnatowicz, I. Peka and D. Fink, J. Nucl. Mater. 289 (2001) 308–314.

[7] www.nea.fr/pt/iempt8/abstracts/Abstracts/Sakamura.pdf

[8] T. Inoue, L. Koch, Nucl. Eng. Technol. 40 (2008) 183-190.

[9] S. Yajima, T. Satow, T. Hirai, J. Nucl. Mater. 17 (1965) 127-135.

[10] J. Pappis, S. L. Blum, J. Am. Ceram. Soc. 44 (1961) 592-597.

[11] S. Yajima, T. Satow, T. Hirai, J. Nucl. Mater. 17 (1965) 116-126.

[12] A.W. Moore, Carbon 5 (1967) 159-162.

[13] M. Turkat, W. A. Robba, US Patent 2442617, (1969).

[14] H. Hayashi, T. Koizumi, T. Washiya, K. Koizumi, US Patent 6793894, (2004).

[15] A. Magdziarz, Arch. Metall. Mater. 51 (2006) 471-474.

[16] K. Nakamura, H. Morooka, Y. Tanabe, E. Yasuda, T. Akatsu, H. Shindo, Corros. Sci. 53 (2011) 4010-4013.

[17] H. Boussie, Pyrometallurgical processing research program “PYROREP”-final report, (2003).

[18] Electrometallurgical techniques for DOE spent fuel treat: By Committee on Electrometallurgical Techniques for DOE Spent Fuel Treatment, Board on Chemical Sciences and Technology, National Academy Press, Washington, D.C. (2000) pp.1-116.

[19] R.W. Benedict, S.P. Henslee. EBR-II spent treatment demonstration project status. 5th International Nuclear Conference on Recycling, Conditioning and Disposal, Nice, France, (1998) pp. 149-155.

[20] H. Lee, G-I. Park, K-H. Kang, J-M. Hur, J-G. Kim, D-H. Ahn, Y-Z Cho, E.H. Kim, Nucl. Eng. Technol. 43 (2011) 317-328.

[21] U. Kamachi Mudali, A. Ravi Shankar, C. Mallika, K. Thyagarajan, S. Ningshen, B.P. Reddy, K. Nagarajan, Materials and coating technologies for pyrochemical reprocessing of spent metallic fuel from fast breeder reactors. Kalpakkam India, IGC/MMG/CSTG/2011, (2011).

[22] U. Kamachi Mudali, A. Ravishankar, S. Ningshen, S. Girija, S. Ravikumar, K. Thyagarajan, Energy Procedia 7 (2011) 463–473.

[23] T. Jayakumar, U. Kamachi Mudali, Materials and Coating Technology for Pyrochemical Reprocessing Applications, Proceedings of Conference on Molten Salts in Nuclear Technology, K.L. Ramakumar, S.C. Parida, S.M. Mukerjee, R.V. Pai, S.K. Rakshit (Eds.) (2013), pp. 122-133.

[24] J.J. Laidler, J.E. Battles, W.E. Miller, J.P. Ackerman, E.L. Carls, Prog. Nucl. Energ. 31 (1997) 131-140.

[25] A. Ravi Shankar, U. Kamachi Mudali, Mater. Corros. 59 (2008) 878-882.

[26] J.E. Indacochea, J.L. Smith, K.R. Litko, E.J. Karell, J Mater. Res. 14 (1999) 1990-1995.

[27] A. Ravi Shankar, U. Kamachi Mudali, S. Ravi Kuma, H.S. Khatak, Baldev Raj. J Nucl Mater. 372 (2008) 226-232.

[28] A. Ravi Shankar, S. Mathiya, K. Thyagarajan, U. Kamachi Mudali, Metall. Mater. Trans A. 41 (2010) 1815-1825.

[29] S-H Cho, S-S H, D-S Kang, J-M Hur, H-S Lee, Met. Mater. Int. 15 (2009) 51-55.

[30] Z. Vakar, E.A. Denisov, T.N. Kompaniets, I.V. Makarenko, V.A. Marushchak, A.N. Titkov, Tech. Phys. 46 (2001) 773–777.

[31] J.B. Donnet, T.K. Wang, Analusis 22 (1994) M24-M26.

[32] R. Wlodarski, A. Nowicki, L. Pealska, Obtaining of pyrographite in the indirect heating method, Report INCT-2059/I/ME/A, Poland, (1988).

[33] W. S. Horton, D. B. Ballard, Carbon 10 (1972) 499–500.

[34] L.D.D. Castro, B. McEnaney, Corros. Sci. 33 (1992) 527-543.

[35] P. Baumli, G. Kaptay, Mater. Sci. Eng. A 495 (2008) 192–196.

[36] E. Fitzer, W. Schaefer, S. Yamada, Carbon 7 (1969) 643-646.

[37] J.C. Lewis, I.J. Floyd, J. Mater. Sci.1 (1966) 154–159.

[38] G.S. Rellick, P.A. Thrower, P.L. Walker, Carbon 13 (1975) 71–80.

[39] I.F. Coffin Jr., J. Am. Ceram. Soc. 47 (1964) 473–478

[40] O.J. Guentert, J. Chem. Phys. 37 (1962) 884–191.

[41] S. Eroglu, B.M. Gallois, Ceram. Int. 22 (1996) 483–487.

[42] A.S. Fialkov, A.L. Baver, N.M. Sidorov, M.L. Chalkun, S.M. Rabinovich, Russ. Chem. Rev. 34 (1965) 46-58.

[43] T. Hirai, Trans. JIM 8 (1967) 190–194.

[44] M.A. Pimenta, G. Dresselhaus, M.S. Dresselhaus, L.G. Cancado, A. Jorio, R. Saito, Phy. Chem. Chem. Phy. 9 (2007) 1276–1291.

[45] T. Jawhari, A. Roid, J. Casado, Carbon 33 (1995) 1561-1565.

[46] M. Nakamizo, R. Kammereck, P.L. Walker JR, Carbon 12 (1974) 259-267.

[47] Y. Wang, D.C. Alsmeyer, R.L. McCreery, Chem. Mater. 2 (1990) 557-563.

[48] R.P. Vidano, D.B. Fischbach, L.J. Willis, T.M. Loehr, Solid State Commun. 39 (1981) 341-344.

[49] A.V. Baranov, A.N. Bekhterev, Y.S. Bobovich, V.I. Petrov, Opt. Spectrosc. (USSR) 62 (1987) 613.

[50] T.P. Mernagh, R.P. Cooney, R.A. Johnson, Carbon 22 (1984) 39-42.

[51] R. Wdanqb, D.B. Fpschbach, J. Amer. Ceram. Soc. 61 (1978) 13-17.

[52] O. Tanaike, M. Inagaki, Carbon 37 (1999) 1759-1769.

[53] W.D. Manly, J.W. Allen, W.H. Cook, J.H. DeVan, D.A. Douglas, H. Inouye, H. Jansen, P. Patriarea, T.K . Roche, G.M. Slaughter, A. Taboada, G.M. Tolson, Construction materials for molten salt reactors In: Molten salt reactors, Part-II, H.G. MacPherson (ed.,), Oak Ridge National Laboratory Press, Tennessee (1958) pp. 595-625.

CHAPTER 5

PLASMA SPRAYED ALUMINA-40 Wt% TITANIA COATING ON HIGH DENSITY GRAPHITE

The present study focuses on the deposition of alumina–40 wt.% titania (A40T) coating on high density graphite by plasma spray process and investigation of its corrosion behaviour in molten LiCl-KCl salt at 873 K for the time periods of 500, 1000 and 2000 h under ultra high pure argon atmosphere. The microstructural analysis of corrosion tested A40T coatings revealed better corrosion resistance up to 500 h. A40T coatings with Cr_3C_2-*NiCr bond coat on high density graphite showed complete spallation of top coating and oxidation of bond coat. To improve the performance of A40T coating, post treatments viz. vacuum annealing and pulsed Nd:YAG laser melting were carried out. Laser melted coatings exhibited homogenous microstructure and better properties when compared to vacuum annealed and as-sprayed coatings. Laser melted A40T coatings were exposed to molten LiCl-KCl salt to investigate their corrosion behaviour. The probable protection mechanism offered by laser melting to A40T coatings was proposed. The compatibility of A40T coating with molten uranium evaluated at 1623 K showed that uranium was sticking to the coating and the coating spalled off after uranium melting. Thermal cycling responses of A40T coating at 873 K and failure mechanisms have been discussed in detail.*

5.1 Introduction

The structural materials to be employed in pyrochemical reprocessing should possess high resistance to corrosion at high temperatures in molten LiCl-KCl salt environment [1].

Studies pursued earlier to understand the corrosion behaviour of structural materials in molten salts under different environments and the mechanisms involved have been reported [2-5]. High density (HD) graphite has been selected as one of the structural materials in pyrochemical reprocessing for salt purification vessel and covering lid based on its performance evaluation discussed in Chapter 4. The results reported in Chapter 4 on the investigation of corrosion behaviour of HD graphite in molten salt at 873 K indicated that a protective ceramic coating is essential to reduce the attack of graphite by molten LiCl-KCl salt. The reactivity and permeability of oxygen towards graphite was reduced by thermal spraying of Al_2O_3 or ZrO_2 with different bond coats (SiC or Cr_3C_2) on graphite [7,8]. Oxides such as zirconia, yttria, titania, alumina and silica are the most stable ceramics in molten chloride salts [9]. Alumina is stable with low solubility and exhibits good corrosion resistance in molten salt [10,11], but possesses lower toughness [12]. Therefore, it is beneficial to choose ceramic composites rather than individual ceramics for coating application. Alumina, combined with titania are generally used as hard coatings because of their high wear resistance [13,14]. Al_2O_3-40 wt% TiO_2 (A40T) was selected for the present application because of the superior characterization of A40T than the other combinations as discussed in Chapter 2, section 2.5. The A40T coating possesses high dielectric strength [15], wear resistance [13], heat resistance and is resistant to most of the acids and alkalies [15,16]. Al_2O_3-13 wt.% TiO_2 coating deposited on graphite by vacuum plasma spray process indicated that no cracking or degradation of the coating upon tested under oxidation environment [17]. Al_2O_3 coating on yttria stabilized zirconia (YSZ) layer had reduced the infiltration of molten salt into YSZ layer and increased the hot corrosion resistance of thermal barrier coatings [18]. Sapra et al. [19] investigated the hot corrosion behaviour of D-gun sprayed Al_2O_3-3 wt.%

TiO_2 coating in Na_2SO_4-V_2O_5 molten salt, and observed improvement in the corrosion resistance of boiler steel with alumina-titania coatings. Plasma sprayed Al_2O_3-Cr_2O_3 coating on superalloys exhibited chemical and thermal stability and superior corrosion resistance in LiCl-Li_2O molten salt [20]. Though plasma sprayed Al_2O_3 based coatings offer good corrosion resistance to molten salts, the interconnected porosity, interlamellar pores and cracks present in the sprayed coating provide easy paths for the molten salt to penetrate [21] and attack the underlying bond coat and substrate material resulting in the degradation on prolonged exposure [21,22]. The large fraction of both open and closed pores in plasma spray coatings might lower their strength, create poor coating adhesion and decrease their corrosion resistance [23]. Hence, the porosity levels are required to be kept below 10% [24]. Further, the coatings were found to be attacked mainly by oxides and voids originating from the spraying process at the splat boundaries [25]. In order to overcome these drawbacks post treatments are necessary for plasma sprayed coatings to improve their characteristics and performance.

Post-spray treatments have been widely recognized since the last decade as the key technique to increase the quality and performance of coatings for different corrosive environments. These treatments are one of the ways to reduce the porosity, other surface defects and to modify the thickness of the coating by a few microns. After post treatment the expected improvement in the coatings are modified microstructure, enhanced bond strength, relaxation of residual stresses, closure and reduction of porosity, improved homogeneity and chemical modification [25]. The corrosion, wear and erosion resistance of the plasma sprayed coatings depend on their microstructure, particularly on the densification of microstructure and distribution of chemical composition of the coatings [26]. As microstructure is the common factor linking all coating properties, it needs to be studied in detail [27]. Annealing, laser melting and sealing are widely used for improving the properties of thermally sprayed ceramic coatings in corrosive environments. Heat treatment of the as-sprayed A40T coatings was carried out by Pawlowski et al. [28] to stabilize the super-cooled phases in the coating. McPherson et al. [29] demonstrated the possibility of converting sprayed alumina deposits completely into α-Al_2O_3 by heat treatment.

Laser melting is an excellent process to seal porosity on the surface, for reducing the corrosion attack and to increase the spalling resistance to thermal shock [30] in order to improve the lifetime of alumina-titania coatings. Thus, laser melting of A40T coating is an approach to reduce the penetration of molten salt by decreasing the surface porosity, generating an external dense top layer and consolidating the as-sprayed microstructure for better surface properties. Sreedhar et al. [31] modified the surface of alumina-titania coatings with varying of power intensity, process speed and beam focusing distance. Laser melting improved the durability of plasma sprayed coatings because the segmented cracks that are generated during melting are beneficial for accommodating thermal stress and resulting in two to six times higher durability [32]. Tomaszek et al. [33] analyzed the changes in modified microstructure of laser engraved plasma sprayed TiO_2 and Al_2O_3+TiO_2 coatings for electron emitter applications. Laser melting of plasma sprayed coatings showed improved corrosion resistance with lower number of defects [26]. Pulsed lasers can be used for the melting of thin top surface (few microns thickness) of ceramic coatings to form a solidified layer due to high thermal gradients [34,35]. Sidhu et al. [36] had used pulsed Nd:YAG laser to improve the hot corrosion behaviour of Ni_3Al coating in molten sodium sulfate-60% vanadium pentoxide salt environment. Pulsed Nd:YAG laser could reduce the thermally affected zone in the coating because of the highly localized action and controlled energy input during the treatment and these features will reduce undesirable side effects such as horizontal cracking of the top ceramic coating [37]. Limited studies are reported on pulsed Nd:YAG laser melting of plasma sprayed A40T coatings [31].

For purifying the cathode product in pyrochemical reprocessing, ceramic coating deposited on HD graphite crucible is required to avoid the reaction with molten uranium (as discussed in Chapter 1, Section 1.3.3). Hence, studies on the interaction of molten uranium with the coating assume importance. Generally, uranium and its alloys are induction melted in ceramic coated graphite crucibles under vacuum for various applications [38]. Asbury [39] employed crucibles and crucible liners made up of aluminum titanate (Al_2O_3. TiO_2 or Al_2TiO_5) for molten uranium applications and reported the non-wetting and non-reactive nature of the coating with molten uranium. As the processing steps involved in the pyrochemical process are in batch mode, the coating should withstand thermal stresses generated due to heating and cooling of various processes. Hence, it is desirable to study the effect of temperature variation on the coated HD graphite to evaluate the thermal cycle life of coating [40]. There is no literature reported on the thermal cycling behaviour of A40T coating. In the present study, in order to improve the compatibility and durability of HD graphite towards molten LiCl-KCl salt, ceramic A40T coatings were proposed on HD graphite without and with Cr_3C_2-NiCr bond coat by plasma spraying process. All the cited literature pertain to wear and tribological properties [13,14,41] and the aqueous corrosion behavior [16] of A40T coatings. Studies on the molten salt corrosion behaviour of A40T coatings are not reported. Hence, the molten salt corrosion behaviour of A40T coating on HD graphite in LiCl-KCl salt at 873 K has been evaluated in the present study for pyrochemical reprocessing applications. The plasma sprayed A40T coatings on HD graphite were post spray treated by means of vacuum annealing and laser melting to achieve better properties.

The objectives of this Chapter are to develop of A40T coating on HD graphite and evaluate coating performance under various conditions. This Chapter contains four sections related to the evaluation of A40Tcoating: (1) Investigation of corrosion behaviour in molten salt, (2) Surface modification by post treatments and subsequent corrosion testing, (3) Compatibility studies with molten uranium and (4) Thermal cycling behaviour.

5.2 Experimental

The experiments carried out to evaluate the performance of A40T coatings (detailed description about the testing and characterization techniques is provided in Chapter 3) are as follows:

1. Deposition of A40T coating on HD graphite by plasma spray process with and without Cr_3C_2-NiCr bond coat employing optimized parameters at M/s. Spraymet Surface Technologies Pvt Ltd, Bangalore, India and characterization by SEM-EDX and XRD techniques.
2. The corrosion studies were carried out in molten salt test assembly (MOSTA). The A40T coated HD graphite rod samples were immersed in molten LiCl-KCl eutectic at 873 K for 500, 1000 and 2000 h under ultra high pure (UHP) argon atmosphere.
3. Post spray treatments were performed by annealing of A40T coating at 1373 K under vacuum of 10^{-4} mbar for 5 h and laser melting of A40T with high power micro pulsed Nd:YAG laser at RRCAT, Indore.
4. Laser melting was carried out with two different power densities; 640 and 800 kW/cm^2 and the modified surfaces were characterized using SEM-EDX,

microhardness tester, profilometry and XRD techniques. Laser melted coatings with power density of 640 and 800 kW/cm^2 are designated as 'LM-1' and 'LM-2' respectively.

5. The laser melted coatings were exposed to molten LiCl-KCl salt at 873 K for 24 h under UHP argon atmosphere and the microstructures were analysed by SEM-EDX and XRD.
6. Uranium metal was melted on A40T coated HD graphite samples at 1623 K and after melting experiments, the microstructural changes were characterized by visual examination and SEM-EDX.
7. Thermal cycling studies on A40T coated HD graphite samples were conducted in an automated furnace at 873 and 1023 K under a vacuum of 10^{-3} torr and failure analysis done using with SEM-EDX.

5.3 Results and discussion

5.3.1 Characterization of as-sprayed coatings

The A40T coatings deposited on HD graphite substrate without and with bond coat by plasma spray process is shown schematically in Fig. 5.1. The surface, cross sectional morphologies and X-ray elemental maps of A40T coating on HD graphite with the bond coat of Cr_3C_2-NiCr are shown in Figs. 5.2a, 5.2b and 5.2c respectively. X-ray elemental maps from the cross section micrograph of sprayed coatings (Fig. 5.2c) clearly indicated the presence of Al, Ti and O elements in the top coat and Cr, Ni and C in the bond coat. Thin bond coatings are more beneficial during the service under operating conditions because of the lower stresses developed at the interface between substrate and the bond coat. The micrograph showed the lamellar microstructure of top A40T coating, which is characteristic of thermal spray coatings [24]. The lamellae of thermal sprayed coatings depend on the particle size distribution of the starting powder and the parameters for the thermal spray process. In general, complete melting of powder particles is necessary to minimize porosity in the coating [42]. EDX line profiles (Fig. 5.3) of the as-sprayed cross-section of the samples showed the elemental distribution as a function of distance, from top ceramic coating to HD graphite substrate. The EDX line profiles clearly distinguished the Al_2O_3-TiO_2 topcoat, bond coat and HD graphite regions. The absence of Ni, Cr and C in top coat and their presence in bond coat could be visualized from the top coat and bond coat regions in Fig. 5.3. Al, Ti and O were present in their appropriate ratios on top ceramic coating. The significant increase in carbon peak intensity in Fig. 5.3 indicates bond coat-HD graphite interface.

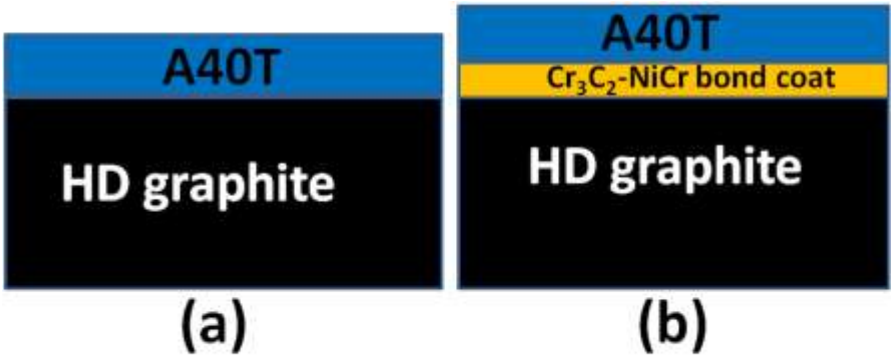

Fig. 5.1 Schematic representation of A40T coating deposited on HD graphite (a) without and (b) with bond coat of Cr_3C_2-NiCr.

The as-sprayed top A40T coating with Cr_3C_2-NiCr bond coat (Fig. 5.2a) and without bond coat (Fig. 5.4a) exhibited similar morphology. Cross section micrograph of A40T coating on HD graphite and corresponding EDX spectra are shown in Figs. 5.4b and 5.4c respectively. The thickness measured for the as-sprayed coatings of Cr_3C_2-NiCr and A40T were 15 μm and 75-100 μm respectively. Plasma sprayed A40T coated surface was composed of alternate splats of completely melted splats, unmelted and partially melted regions as observed in Fig. 5.4a. The coated surface exhibited wavy nature with high roughness. From the micrograph (Fig. 5.2a), it could be noticed that the completely melted region has splat structure (region-1) and these splats are formed by rapid solidification of ceramic powders over the substrate during plasma spray process [24].

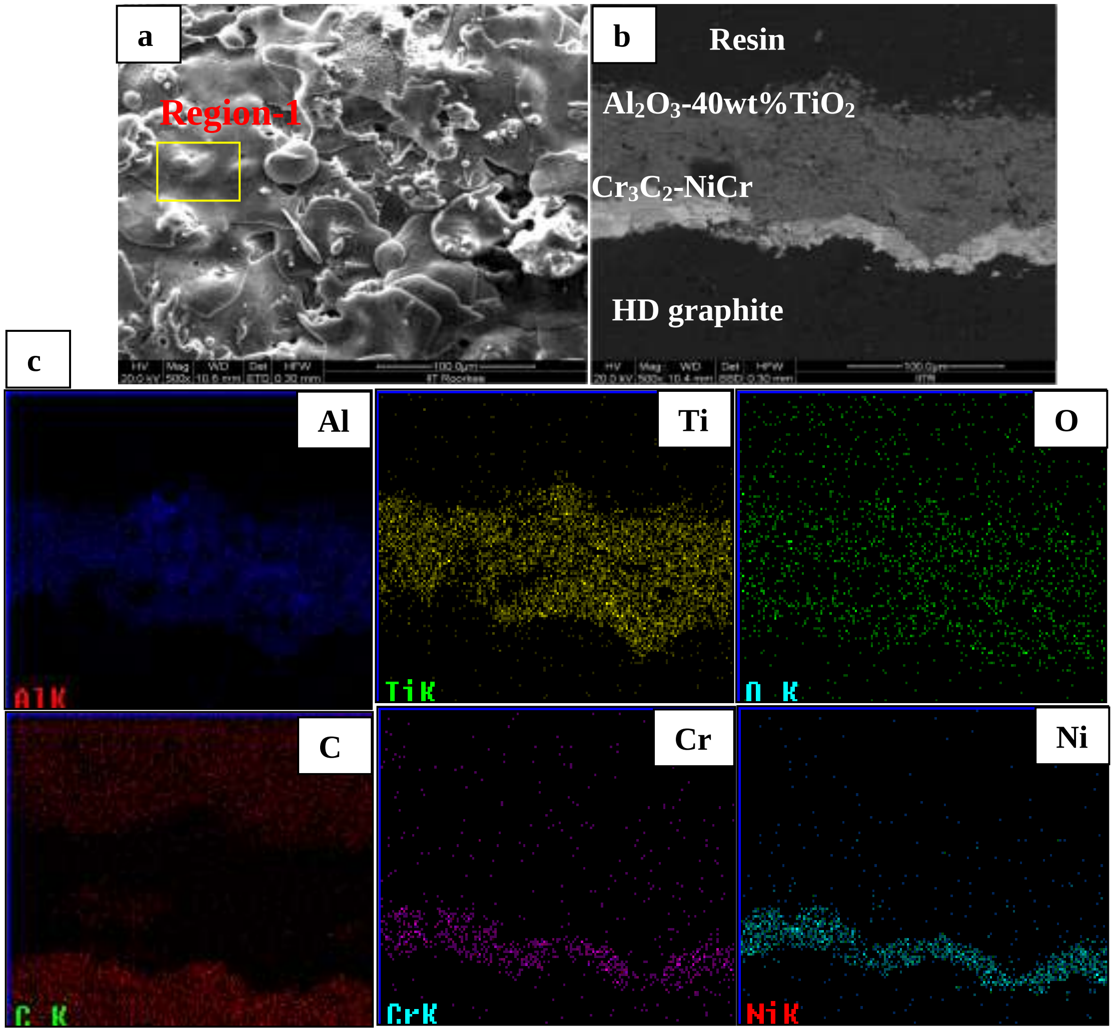

Fig. 5.2 SEM micrographs of (a) surface morphology and (b) cross section of Cr_3C_2-NiCr bond coated top A40T coating on HD graphite and (c) X-ray elemental mapping of Al, Ti, O, C, Cr and Ni.

Observation at higher magnification of as-sprayed A40T coating revealed two distinct types of morphologies of unmelted regions (Fig. 5.5a and b). Figure 5.5a shows irregular or coarse morphology and EDX analysis revealed significant titanium content. The other region identified and shown in Fig. 5.5b contains small sized particles and the EDX analysis showed significant aluminum content. During plasma spraying a part of titania did not react with alumina and vice versa as could be seen in the micrographs (Fig. 5.5). In composite coatings, some of the ceramic particles are not melted completely as these particles would be entering into the lower temperature region of the plasma tail. The elemental composition of unmelted (region-2 and 3) and melted regions (region-1) obtained by EDX analysis are given in Table 5.1. It is well known that plasma sprayed coatings contain up to 10% porosity, partially melted portions, completely melted and deformed splats [24]. During plasma spraying, the powders are heated to high temperatures by plasma. While majority of the particles are completely melted and solidified, some particles are unmelted due to less spraying time and rapid melting of the powder.

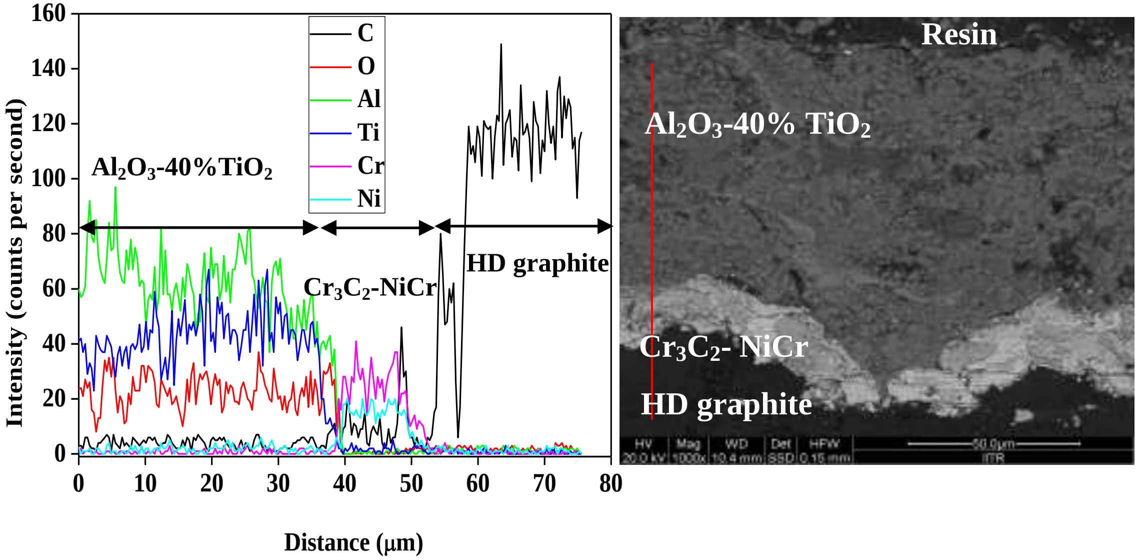

Fig. 5.3 EDX line profiles of Cr_3C_2-NiCr bond coat, top A40T coating and HD graphite substrate along with cross section.

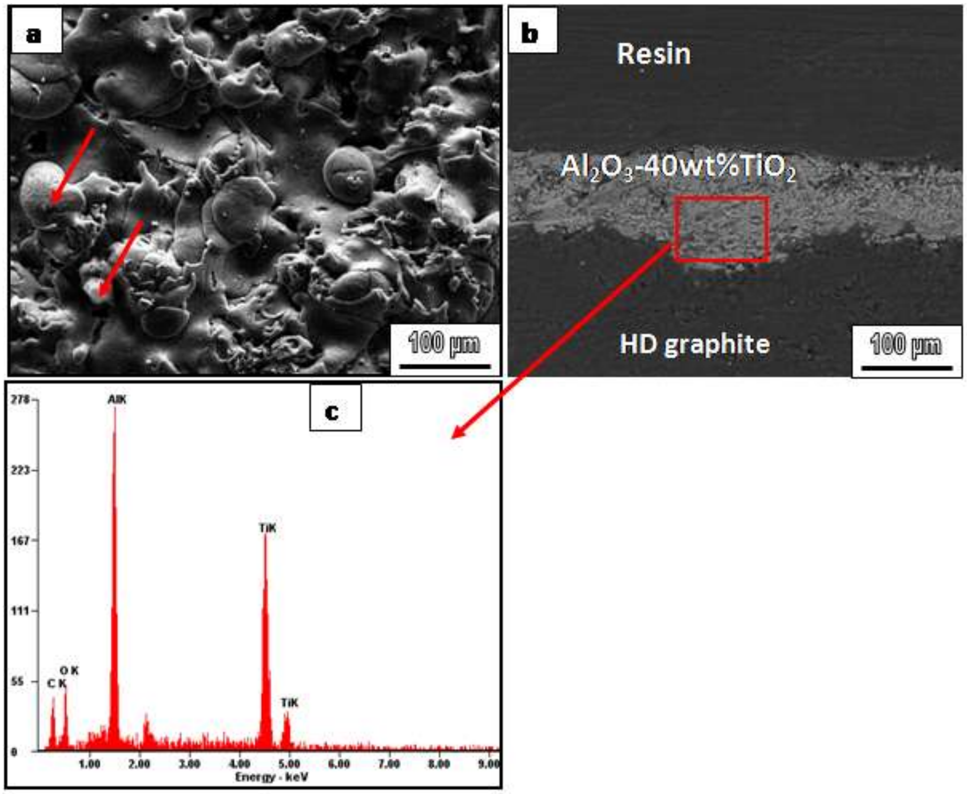

Fig. 5.4 SEM micrographs of (a) surface morphology, (b) cross section of A40T coating on HD graphite and (c) EDX spectrum of A40T coating.

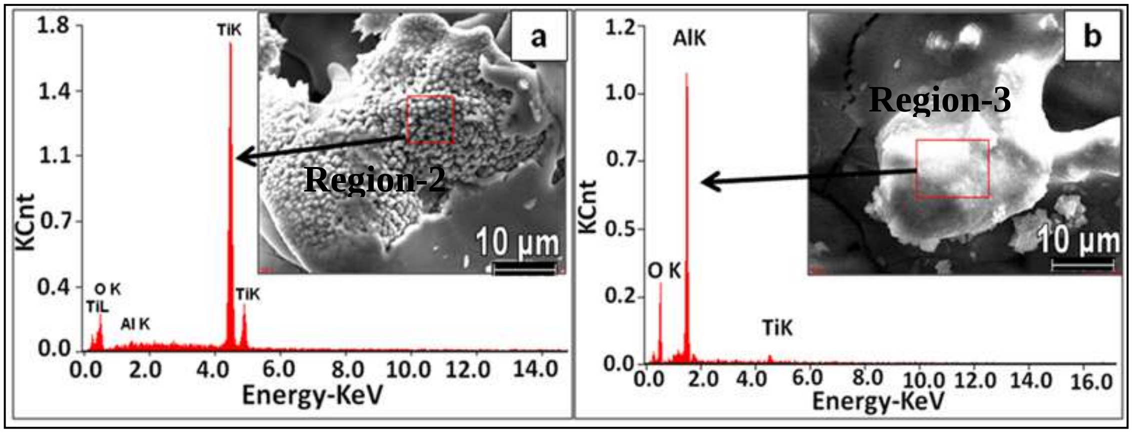

Fig. 5.5 Morphologies of unmelted/partially melted regions in as-sprayed A40T coatings: (a) titanium particles rich region and corresponding EDX spectrum and (b) aluminum particles rich region and corresponding EDX spectrum.

Table 5.1 Elemental composition of different regions in as-sprayed A40T coatings by EDX analysis.

Region	Element (wt %)		
	Al	Ti	O
Completely melted region-1 in Fig. 5.2a	33.41	31.61	34.98
Partially or unmelted region-2 in Fig. 5.5a	1.04	68.64	30.32
Partially or unmelted region-3 in Fig. 5.5 b	58.50	03.76	37.74

Berndt et al. [42] reported the possibilities of three different locations of the unmelted particles, namely (i) at the substrate surface, (ii) at the lamellar boundaries within the coating, and (iii) within a completely solidified particle. By carefully choosing the spraying parameters, the number of pores and other defects in the coating can be minimized. Few voids were observed in between the splats because of less cohesive strength. These complex microstructures are formed due to the following reasons: (1) For very short time of residence of powders in the stream of plasma, some of the particles melt completely and deposit as splat morphologies and some particles will remain as unmelted particles. (2) Stresses can be generated in the microstructure owing to the contraction of individual sprayed splats during rapid cooling (10^6 -10^8 K/s) and deposit on the colder substrate or on a layer of previously solidified splats [43,44]. (3) Volume changes associated with the phase changes in the coating during spraying process also lead to generate stresses in the coating [43]. The non-uniform microstructure of the sprayed coating could be made homogeneous by reducing the irregularities present in the coating through post treatments.

5.3.2 Corrosion behaviour of A40T coatings in molten LiCl-KCl salt

5.3.2.1 Corrosion assessment

Weight change in A40T coated HD graphite exposed to molten LiCl-KCl salt at 873 K for different period of exposure is shown as histograms in Fig. 5.6. The percentage weight loss/gain of the as-sprayed coatings (without bond coat) after exposure to the eutectic salt for 500, 1000 and 2000 h were +0.58, -0.56 and -8.4 respectively. The percentage weight loss/gain of Cr_3C_2-NiCr bond coated samples exposed for 500 and 2000 h was +0.6 and -1.1 respectively.

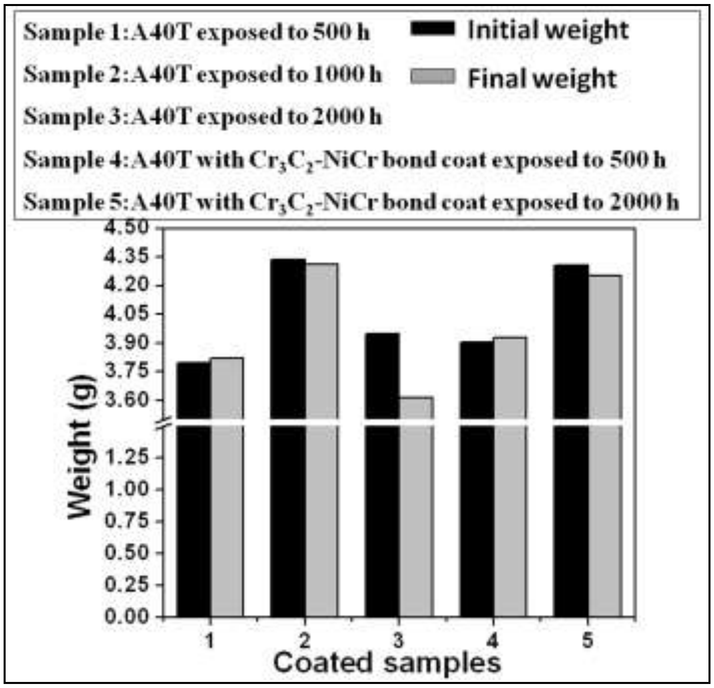

Fig. 5.6 Weight change in A40T coated HD graphite exposed to molten LiCl-KCl salt at 873 K for different time periods (without and with Cr_3C_2-NiCr bond coat).

The weight losses could be explained by the corrosion attack on the coating and the spallation of the coating during experiment. The 500 h exposed samples with and without bond coat gained weight owing to the deposition of salt on the surface. In both the cases, the percentage weight loss/gain increased with increase in the duration of exposure to molten LiCl-KCl salt. As-sprayed A40T coating on HD graphite sample exposed for 2000 h showed significant weight loss because of the complete removal of A40T coating and subsequent attack on the graphite surface. Compared to as-sprayed A40T coating, Cr_3C_2-NiCr bond coated sample of A40T coating exposed for 2000 h showed a lower percentage of weight loss owing to the spallation of top coat only and presence of bond coat (without spallation) on graphite substrate.

5.3.2.2 Morphology of corrosion tested A40Tcoated HD graphite

The corrosion behaviour of plasma sprayed coatings depends on coating microstructure, phase composition, corrosive medium, testing temperature and duration of exposure [16]. Surface morphology of A40T coated HD graphite exposed to molten LiCl-KCl salt are presented in Fig. 5.7. As the exposed time increased from 500 to 1000 and 2000 h, the coating spallation increased, as observed from the SEM micrographs. In the case of 500 h (Fig. 5.7a) exposed sample the surface showed salt deposits, particles (Fe) and a few cracks. The surface morphology of 1000 h exposed sample showed the presence of voids on the surface indicating that the salt had intiated attack on HD graphite (Fig. 5.7b). The morphology of 2000 h exposed coating (Fig. 5.7c) clearly showed that coating got completely spalled off from HD graphite and molten salt had attacked the underlying HD graphite substrate. After 1000 (Fig. 5.7b) and 2000 h (Fig. 5.7c) of exposure to molten LiCl-KCl salt, the A40T coating spalled off from the substrate and the surface morphology resembled that of degraded graphite morphology as observed for HD graphite (viz. Chapter 4). To ascertain the degrdation of coating, EDX anlysis was carried out on the exposed surface of the coatings.

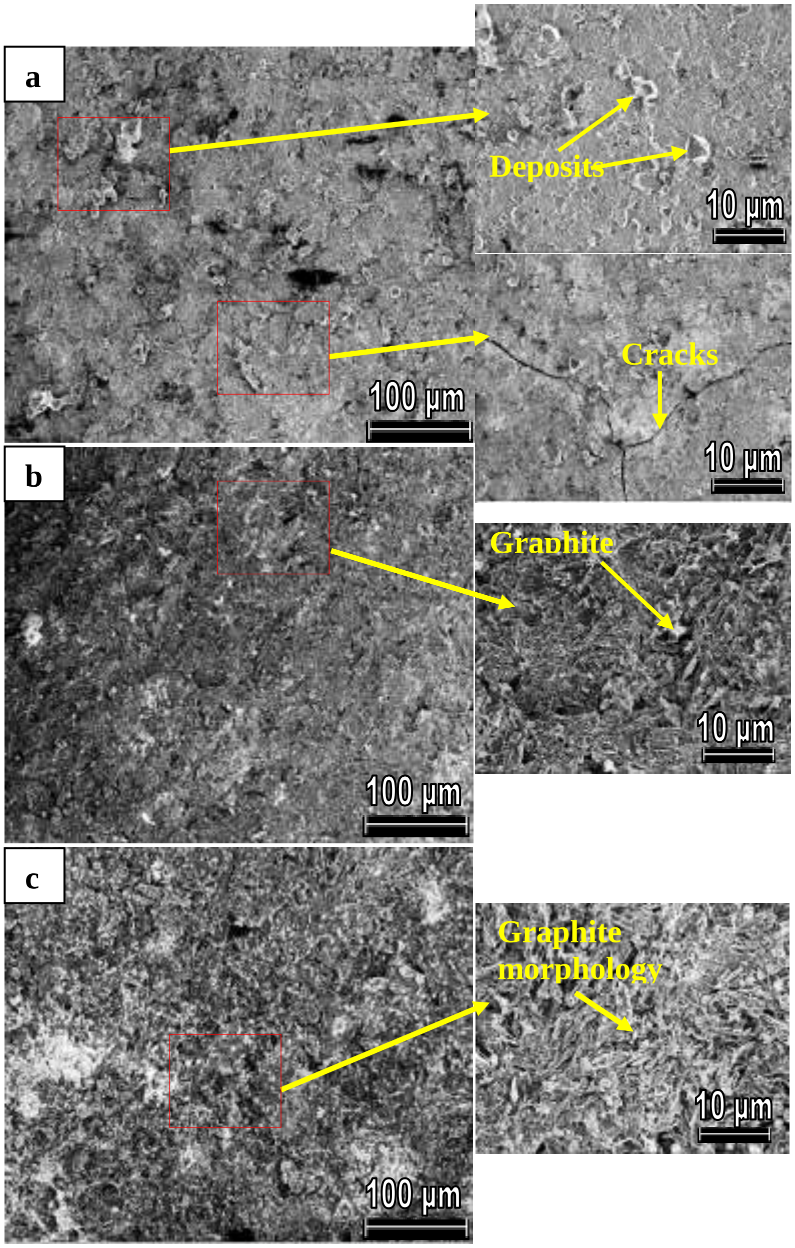

Fig. 5.7 Surface morphology of A40T coating on HD graphite exposed to molten LiCl-KCl salt at 873 K for (a) 500 h, (b) 1000 h and (c) 2000 h.

The SEM micrograph and corresponding EDX spectra of the surfaces of 500 and 1000 h exposed samples are shown in Fig. 5.8a, b and c respectively. The composition (in wt.%) of the 500 and 1000 h exposed coatings as determined by EDX is shown in Fig. 5.8a and 5.8b respecitvely.

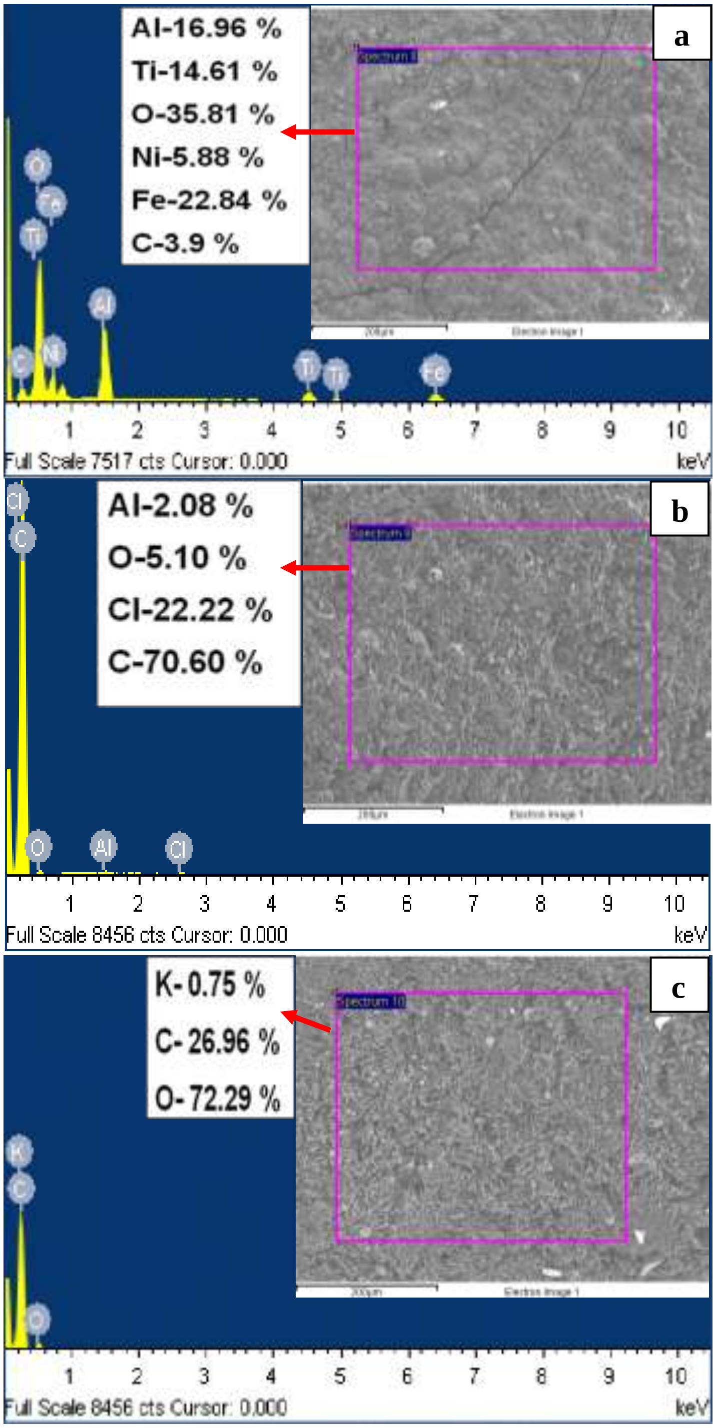

Fig. 5.8 Surface morphology and EDX spectra of A40T coated HD graphite exposed to molten LiCl-KCl salt at 873 K for (a) 500 h, (b) 1000 h (c) 2000 h.

The 500 h exposed coating showed the presence of Al, Ti and O (Fig. 5.8a). The SEM micrograph and the corresponding EDX spectrum of 2000 h exposed samples surface shown in Fig. 5.8c revealed carbon and salt deposits. This implies that the coating on HD graphite spalled off from the 1000 and 2000 h exposed samples. The EDX analysis on 500, 1000 and 2000 h exposed surfaces confirmed the increase in the deposition of salt particles and the drastic decrease in the composition of coating elements with increase in the exposed time. Oxidants (O_2, H^+, H_2O and OH^-) [45] and impurities present in the molten salt were found to accelerate the corrosion process by dissolution and leaching of the elements into molten salt [4]. Porosity, voids and microcracks observed in the as-sprayed coating (Fig. 5.4a and Fig. 5.5a) could have allowed the penetration of salt leading to the degradation of coating as observed by Toma et al. [16]. Penetration of the salt had led to coating spallations from the substrate and attack of underlying substrate material which resulted eventually in the degradation after long exposure to aggressive molten salt [46]. In the present study, the A40T coating withstood upto 500 h, and degradation in the molten salt was severe at 1000 h and the coating got completely spalled off after 2000 h exposure.

Figure 5.9 shows the surface morphology and EDX spectra of A40T coated HD graphite with Cr_3C_2-NiCr bond coating exposed to molten LiCl-KCl salt at 873 K for 500 and 2000 h. The 500 h exposed sample exhibited a dense layer (Fig. 5.9a) comprising bond coat elements, salt deposits and impurity, as determined by EDX. The top coat morphological features had diminished and salt rich deposits appeared on the surface of bond coat. This implies that the top A40T coating was completely detached from graphite substrate and only bond coat of Cr_3C_2-NiCr was present on the surface. It was noticed that chromium carbide present in the bond coat had undergone oxidation with the formation of chromium oxide rich regions over the surface as evidenced from the EDX spectrum shown in Fig. 5.9a. The composition in wt% shown by EDX spectrum was Cr-44.82, Ni-2.32, O-30.56, C-2.69 and Fe-19.62. Similar kind of chromium oxide morphology was observed when 316L SS was exposed to molten LiCl-KCl salt at 873 K [2]. Figure 5.9b shows the surface morphology after 2000 h exposure to LiCl-KCl salt. The spllation of top A40T coating followed by attack on the bond coat of Cr_3C_2-NiCr was observed. The attack on bond coat was deeper after exposure to molten salt for 2000 h compared with 500 h exposure. In the case of 500 h exposed surface (Fig. 5.9a), the bond coat and salt deposits were uniformly spread over the surface while on the 2000 h exposed sample lot of surface discontinuty and porous nature of coating was observed (Fig. 5.9b). Formation of porous chromim oxide rich regions (Fig. 5.9a) was also observed in 2000 h exposed sample. It is evident that as the exposure time increases, the degradation of bond coat as well as the salt attack on the substrate also increase. The EDX analysis of 2000 h exposed sample confirmed the presence of Cr-8.31 wt.%, Ni-28.79 wt.%, O-19.40 wt.%, Fe-17.55 wt.% and K-10.86 wt.%, and Cl-15.09 wt.% in the deposit. Spallation of top ceramic coating after 500 and 2000 h exposure indicated the poor adhesion of A40T top coat to the Cr_3C_2-NiCr bond coat. During plasma spraying of Cr_3C_2-NiCr coating, the chromium carbide present in the powder gets oxidized and oxide formation occured [47] due to recation of chromium with the oxygen from the atmosphere [48,49]. Spallation of A40T coating from bond coat was due to high stresses at the bond coat/top coat interface and formation of porous chromium oxide. Stresses can generate at the interface of coating and substrate owing to thermal expansion coefficient mismatch leading to loss of adhesion strength and spallation of coating [46]. Complete spallation of bond coat of Cr_3C_2-NiCr from graphite substrate was not observed even after 2000 h of exposure.

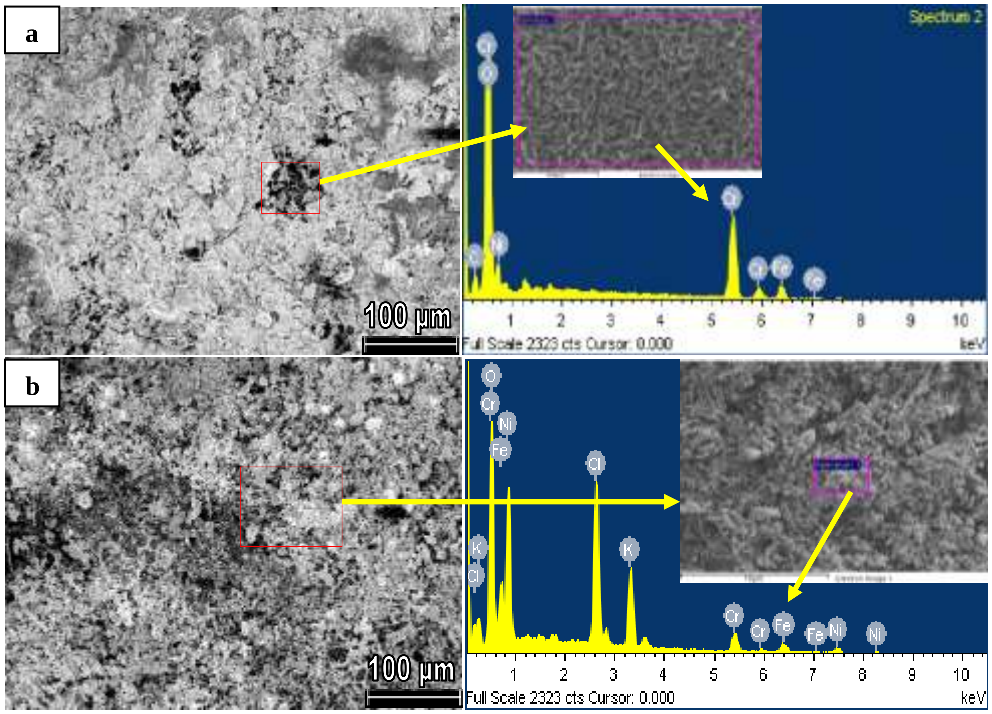

Fig. 5.9 Surface morphology and EDX spectra of A40T coated HD graphite with Cr_3C_2-NiCr bond coated exposed to molten LiCl-KCl salt at 873 K for (a) 500 h (b) 2000 h.

5.3.2.3 XRD studies on corrosion tested A40T coated HD graphite

The XRD pattern of as-sprayed and 1000 h exposed A40T coatings (without bond coat) are shown in Figs. 5.10a and 5.10b respectively. The as-sprayed coating (Fig. 5.10a) consisted of β-Al_2TiO_5 as the major (41-0258) phase, γ-Al_2O_3 (10-0425), rutile-TiO_2 (21-1276) and α-Al_2O_3 (10-0173). The aluminium titanate (Al_2TiO_5) is the major phase in the 1000 h exposed coating also. Addition of 40-44wt% TiO_2 to Al_2O_3 results in the formation of Al_2TiO_5 phase at high temperatures [50]. The reaction of alumina with titania could have occurred either subsequent plasma spraying during or contact with substrate afterwards [51]. The properties of Al_2TiO_5 differ from those of Al_2O_3 and TiO_2 and it exhibits good wear, corrosion resistance to acids [16] and excellent thermal shock resistance [52]. The plasma spraying process transforms corundum (α-$A1_2O_3$) phase into γ-Al_2O_3 for all Al_2O_3–TiO_2 compositions. It is well known that γ-$A1_2O_3$ commonly nucleates in preference to α-Al_2O_3 due to lower energy of nucleation during rapid solidification of the liquid droplets [29]. Titania exists in the crystallographic form of rutile (R-TiO_2) phase. The presence of corundum phase in the sprayed coating might be owing to the unmelted or partially melted particles in the coating (Fig. 5.5b) [53] and the presence of rutile phase in the sprayed coating is the unreacted $TiO_{2.}$ These results are corroborated by the SEM micrograph (Fig. 5.5a) and EDX analysis (Table 5.1) of partially or unmelted region. After corrosion test in molten LiCl-KCl salt for 1000 h at 873 K, the coating on the graphite substrate spalled out during cleaning in distilled water because of poor adhesion after exposure to molten salt. The spalled coating was subjected to phase analysis in order to identify the phase changes. The phases in the as-sprayed coating were present even after corrosion test in molten salt for 1000 h (Fig. 5.10b). The major phases present were β-Al_2TiO_5, γ-Al_2O_3, TiO_2 (rutile) and α-Al_2O_3. XRD studies clearly showed that no major phase change had occurred in the coating and the coating peeled off from graphite substrate due to poor adhesion between coating and HD graphite substrate after exposure to molten salt. XRD studies on molten salt exposed A40T coated HD graphite with Cr_3C_2-NiCr bond coat for 500 and 2000 h are shown in Fig. 5.11. The Al_2TiO_5 phase in the top coat of as-sprayed coating (Fig. 5.10a) disappeared after corrosion test for 500 (Fig. 5.11a) and 2000 h (Fig. 5.11b). The exposed coatings contained only chromium based phases due to spallation of the top ceramic coat into molten LiCl-KCl salt. The bond coat of Cr_3C_2-NiCr changed to brown colour and was still present on the surface of HD graphite after 500 and 2000 h exposure. XRD studies on this sample revealed distinct phases of chromium oxide and chromium carbide. The major phases observed were Cr_3C_2 (35-0804), $Cr_{23}C_6$ (35-0783), Cr_7C_3 (36-1482), Cr_2O_3 (38-1479) and Cr_3O_4 (12-0559). It was reported that [48,49] at high temperatures and in oxidation atmosphere, several reactions can participate in the decomposition of chromium carbide and formation of new phases. The formation of porous chromium oxide from chromium carbide present in the bond coat decreased the bond strength [54] leading to spallation of top ceramic coating into molten LiCl-KCl salt. To improve the adherence of A40T (Cr_3C_2-NiCr bond coated) coating, post treatments were carried out to modify the surface properties and corrosion resistance in molten salt medium.

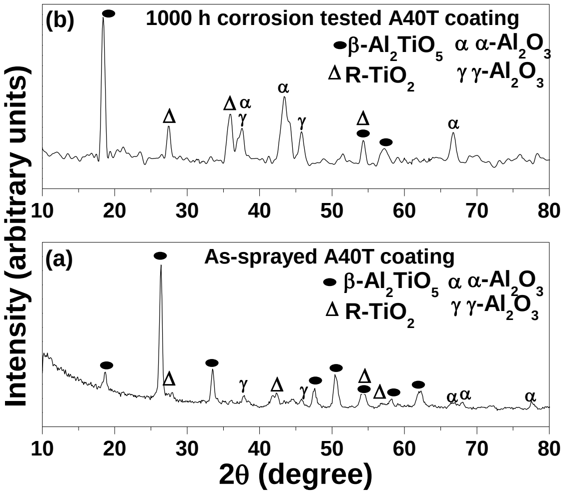

Fig. 5.10 XRD analysis of (a) as-sprayed and (b) corrosion tested A40T coating exposed to molten LiCl-KCl salt for 1000 h.

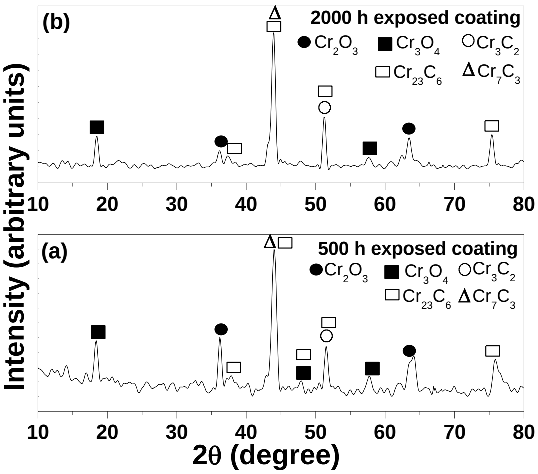

Fig. 5.11 XRD analysis of A40T coating with Cr_3C_2–NiCr bond coat exposed to molten LiCl-KCl for (a) 500 and (b) 2000 h.

5.3.3 Surface modification by post treatments

5.3.3.1 Vacuum annealing of A40T coating

Post heat treatment at high temperatures results in changes in the amount and shape of porosity due to phase transformations and sintering. Sintering occurs to various extents in the sprayed coating during annealing at 1373 K. However, in the present study the surface morphology of the coating after vacuum annealing treatment at 1373 K (shown in Fig. 5.12a) did not reveal any major change; only the unmelted or partially melted regions (Fig. 5.5b) in sprayed coating became densified as shown in Fig. 5.12b.

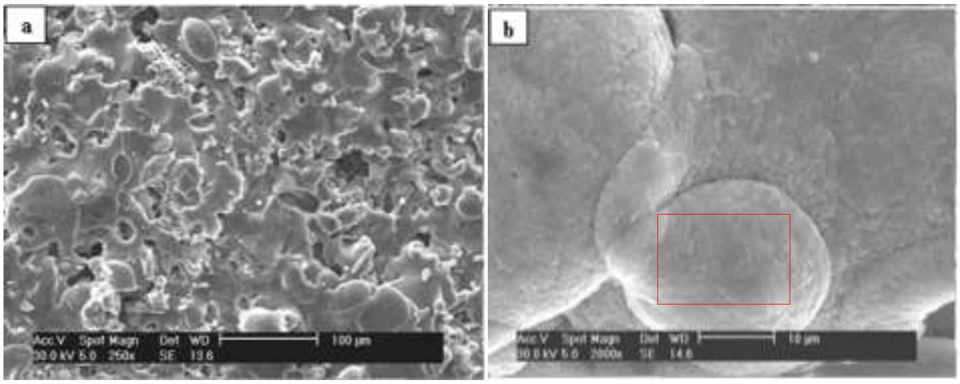

Fig. 5.12 (a) Surface morphology of vacuum annealed A40T coating and (b) agglomerate region in the annealed coating.

During heat treatment (soaking time: 5 h) the unmelted or partially melted ceramic particles absorb sufficient energy to form agglomerates in the coating. These agglomerates are not completely densified at 1373 K. The agglomerated and unmelted or partially melted particles, formed as clusters (Fig. 5.12b) were observed in the vacuum annealing coating. The EDX analysis of cluster morphology (Table 5.2) also showed the presence of high amount of Ti similar to that of the unmelted or partially melted region-3 in the as-sprayed coating (Fig. 5.5a). This indicated that the annealing temperature should be higher than 1373 K to completely densify or modify the sprayed coating. Densification of the coating through vacuum annealing requires longer time.

5.3.3.2 Pulsed laser melting of A40T coating

The spallation of the sprayed coating exposed to molten salt occurred due to low cohesive strength between the sprayed particles, the presence of porosity, partially and unmelted particles and microcracks [21,22]. The complex microstructures observed in Fig. 5.5 had been eliminated by glazing the coating with high power lasers. Visual examination showed the laser melted (LM) coating produces a light black to a shining glassy appearance. Figure 5.13 shows the unmelted and laser melted regions. High irregularities found in sprayed coatings were minimized in the laser melted coatings. Some voids found on the surface were located mostly over the cracks and they were formed due to the release of entrapped gases from the gas pockets before solidification process [26,55,56].

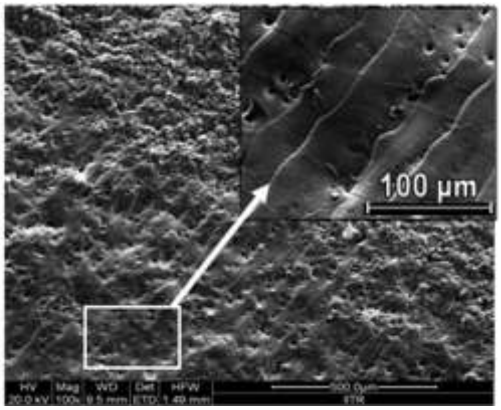

Fig. 5.13 SEM micrographs of laser melted and unmelted regions in A40T coating.

The morphology of laser melted and unmelted as-sprayed A40T coating is shown in Fig. 5.13. The laser melted region had become smooth and dense compared to unmelted region. The individual splats, voids between splats, connected pores disappeared and unmelted or partially melted surface of the sprayed coating got fully melted after laser treatment. The surface of laser melted A40T coating (Fig. 5.14a) exhibited uniform and homogeneous microstructure in contrast to the as-sprayed coating (Fig. 5.2a) because heating and melting the surface inhomogeneties. Laser radiation annihilated the surface defects. The porous nature of the sprayed coating was transformed into consolidated microstructure by laser melting; surface became denser and pores and other defects were reduced significantly. Surface homogeneity improved from as-coated (Fig. 5.14a) to laser melted coatings (Fig. 5.14b and 5.14c). As could be seen in Fig. 5.14b and 5.14c surface homogeneity improved with increasing laser power.

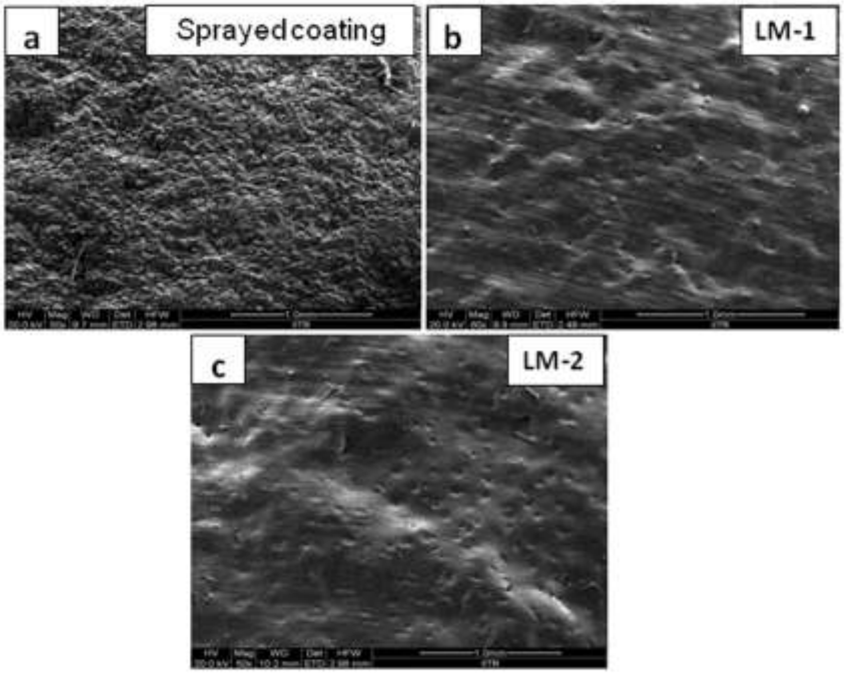

Fig. 5.14 Surface morphology of A40T coating (a) as- sprayed, and laser melted coatings of (b) LM-1 and (c) LM-2.

SEM microstructures of LM-1 (Figs. 5.15a and b) and LM-2 (Figs. 5.15c and d) shows that microcracks are nucleated during the laser melting process. It is well known that such cracks in the laser melted coatings originate from high localized temperature gradients, relief of thermal induced stresses and volume change during solidification of molten ceramic particles. The formation of segmented network of cracks in laser melted coatings is beneficial to increase the thermal shock resistance and the thermal cycle life [32]. LM-2 coatings were denser with reduced pores and other defects when compared to the LM-1 coatings which had some partially melted zone with growth features. These growth features are in a columnar shape (Fig. 5.15b). During laser melting the distribution of heat energy on the coating causes the growth of unmelted and partially melted regions into different shapes, particularly in the growth direction which increases the consolidation of coating. EDX analysis of this region (Fig. 5.15b) revealed high concentration of titanium as listed in Table 5.2. The TiO_2 rich regions act as barriers for thermal energy generation during laser melting and eventually contribute to loss of heat energy at the molten surface [65]. Commonly observed microstructural inhomogeneities in the sprayed coatings were considerably diminished in LM-2 coatings. Higher magnified microstructure of LM-2 coating (Fig. 5.15d) did not exhibit any growth features and all the regions were melted. The EDX analysis of this region revealed high concentration of aluminum as listed in Table 5.2. EDX analysis on laser melted coatings (Figs. 5.15b and 5.15d) revealed improved homogeneous elemental composition of the modified layer due to redistribution of elements by laser melting. The difference in the microstructural changes (Figs. 5.15b and 5.15d) in LM-1 and LM-2 coatings imply that the surface quality and homogenization of the coatings depend on the process parameters used for the laser melting.

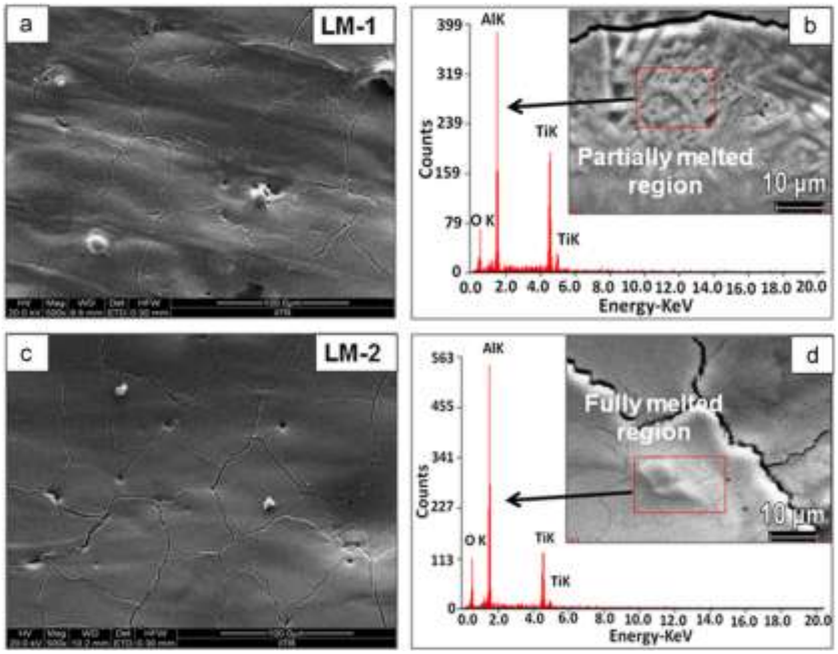

Fig. 5.15 Surface morphology and EDX spectra of laser melted A40T coatings: (a and b) LM-1 and (c and d) LM-2.

Table 5.2 EDX analysis of elemental composition of vacuum annealed and laser melted coatings.

Region	Element (wt %)		
	Al	**Ti**	**O**
Annealed coating (Fig.5.12b)	39.18	60.82	-
LM-1 coating (Fig.5.15b)	33.04	38.05	28.91
LM-2 coating (Fig.5.15d)	41.30	22.84	35.85

Figure 5.16 depicts the cross section of LM-2 coating of A40T with Cr_3C_2-NiCr bond coat. Cross sectional morphology clearly indicated that only a thin layer of the ceramic coating was consolidated by laser melting. The absorption of laser energy and depth of melting depend on the nature of surface and the structure of the material [57]. Pulsed laser

melting is confined to a highly localized region of about a few micron thickness because of the pulsed mode energy supplied during laser treatment [34,37]. Pulsed mode Nd:YAG laser reduced the thermally affected zone (small zones) in the coating because of the highly localized action and controlled energy input during the treatment [35,56]. These laser features would reduce undesirable side effects such as horizontal cracking of the top ceramic coating [37]. Chehrghani et al. [58] reported that the absorption of the laser energy on the surface of the material depends on the thermal effects/properties of laser irradiation with different materials. Further, laser parameters can be optimized for altering the absorption and penetration of the laser beam into the sprayed coating.

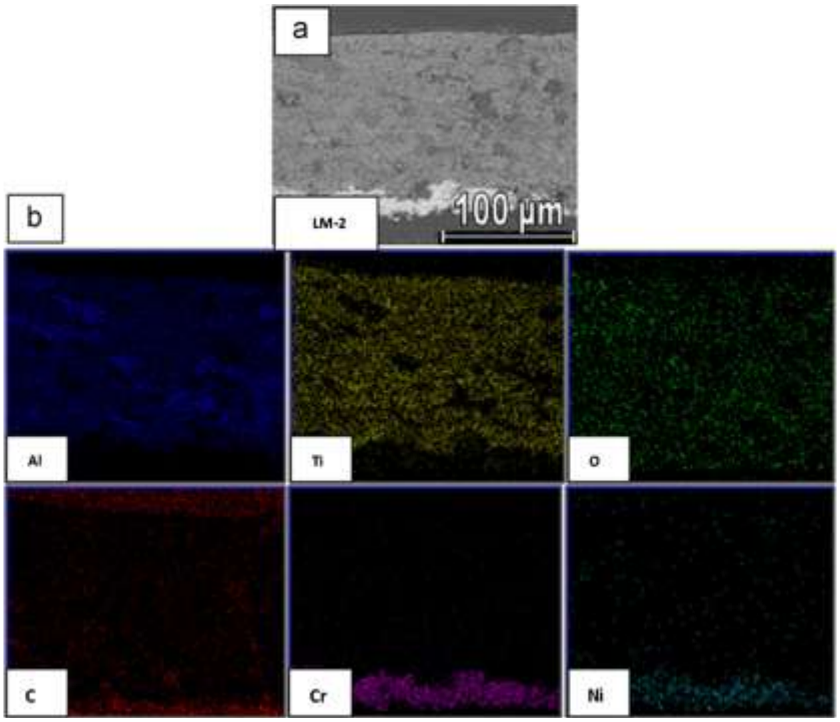

Fig. 5.16 (a) Cross-sectional micrograph and (b) EDX elemental mapping of LM-2 A40Tcoating.

Vertical cracks were observed after laser melting of plasma sprayed coatings with very high power CO_2 laser [59,60]. In the present study, the coating was devoid of cracks and delamination of the coating occurred in the cross section of the laser melted coatings due to the controlled supply of laser energy (Fig. 5.16a). X-ray elemental maps did not show any elemental change along the cross section of LM-2 coatings. Top coat elements Al, Ti and O were not mixed with bond coat elements at the bond coat/ top coat interface after laser melting. The top A40T coating was densified and there was no effect on bond coat as well as on HD graphite substrate. The cross section of LM-1 coatings showed similar characteristics. Therefore, it is evident that the unmelted/partially melted regions present on the surface of plasma sprayed A40T coatings decrease as the laser irradiation power density is increased. A comparison of the microstructure revealed that partially melted regions were present in annealed A40T coatings (Fig. 5.12); but these regions were completely eliminated in laser melted LM-2 coatings (Fig. 5.15). Annealing of A40T coating at 1373 K did not show any marked effect, while laser melting improved the surface homogeneity of the coatings. Laser melting is superior to vacuum annealing process with respect to densification, smoothness and hardness.

5.3.3.3 Phase analysis of post spray treated A40T coatings

The microstructural phase modifications occurred on the surface of A40T coatings, analyzed by XRD are in the following sequence: sprayed coating→ annealed coating→ LM-1→LM-2. The XRD pattern of the sprayed coating shown in Fig. 5.17a, confirmed the presence of $\beta\text{-Al}_2\text{TiO}_5$ phase, $\gamma\text{-A}1_2\text{O}_3$, R-TiO_2 and $\alpha\text{-A}1_2\text{O}_3$. The XRD analysis clearly indicated that the $\alpha\text{-A}1_2\text{O}_3$ and R-TiO_2 present in the initial powder (Chapter 3 Section 3.1.2.3) reacted in the plasma during spraying process and solidified as $\beta\text{-Al}_2\text{TiO}_5$ phase. After heat-treatment under vacuum for 5 h at 1373 K, the XRD pattern of coating (Fig. 5.17b) consisted of $\alpha\text{-Al}_2\text{O}_3$, Al_2TiO_5 and TiO_2 (rutile) phases. $\gamma\text{-Al}_2\text{O}_3$ phase was absent in the annealed coatings as the polymorphic phase of alumina, γ-Al$_2$O$_3$ phase present in the sprayed coating transformed to α-Al$_2$O$_3$ during annealing process. The intensity of α-Al$_2$O$_3$ was significant in heat treated coatings in comparison to sprayed coating. The stable α-Al$_2$O$_3$ phase had improved the thermal and chemical stability of the A40T coating. The rutile phase present in vacuum annealed coating indicates that the unmelted titanium dioxide particles were densified (Fig. 5.12b) in annealed coatings.

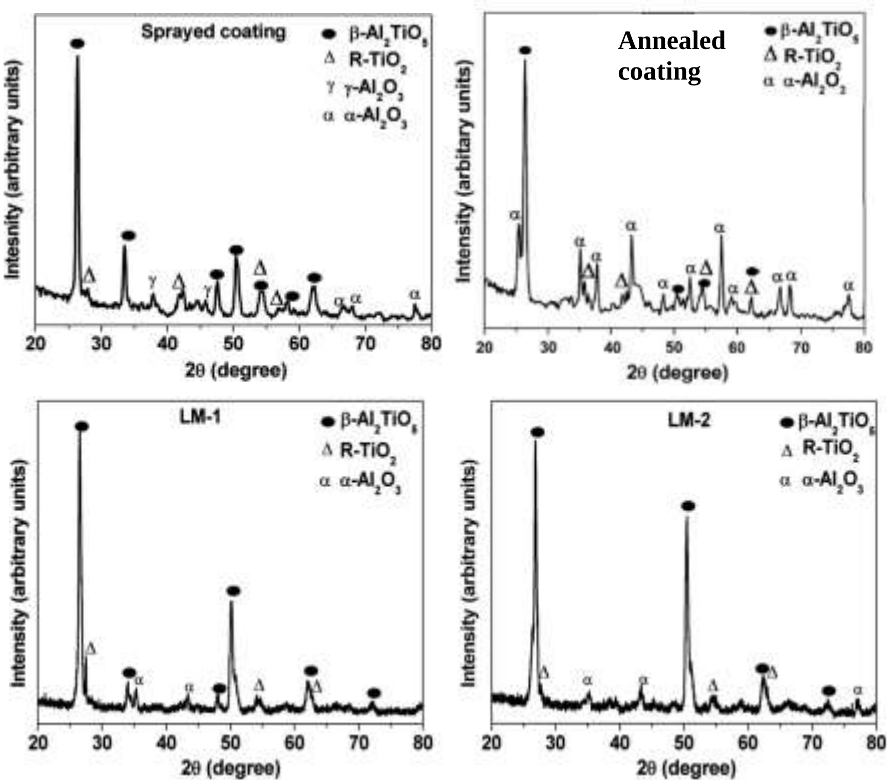

Fig. 5.17 XRD patterns of Al$_2$O$_3$-40 wt.% TiO$_2$ coatings: (a) as-sprayed, (b) vacuum annealed, (c) LM-1 and (d) LM-2 coatings.

Figures 5.17c and 5.17d show the XRD pattern of the LM-1 and LM-2 coatings. The metastable γ-A1$_2$O$_3$ phase in the sprayed coating transformed into stable phase of α-A1$_2$O$_3$ because of melting and recrystallization of the coating [61]. This phase transformation resulted in the opening of voids between lamellae and a few cracks were also found in annealed and laser melted A40T coatings. The beneficial Al_2TiO_5 became the predominant phase in the case of laser melted coatings. Laser melting allowed the stable phases of α-Al_2O_3, R-TiO_2 and β-Al_2TiO_5 to solidify as a smooth surface. Variation in the pulse energy/power density of the laser melting process did not vary the phase content significantly; however, significant amount of R-TiO_2 phase was present in LM-1 coatings compared to LM-2 coatings.

5.3.3.4 Microhardness of post spray treated A40T coatings

Microhardness measurements were carried out on the as-coated and post spray treated coatings randomly at different regions on A40T coatings. During microhardness measurement, Vickers indentation impressions were difficult to observe on the sprayed coating and vacuum annealed coatings because of the irregularities present in the coating morphology; nevertheless, the hardness values were recorded in those regions where clear indentation was possible and the average value was measured. The increment in microhardness from sprayed coating to vacuum annealed and laser melted coatings (LM-1 and LM-2) are shown in Fig. 5.18. The microhardness of as-sprayed A40T coating was low because of the presence of porosity, microcracks, voids and unmelted or partially melted regions on the surface. LM-2 coating showed high hardness because of the increase in microstructural compactness and surface homogeneity due to melting and solidification of unmelted or partially melted and other heterogeneities in the coating. Elimination of the microstructural irregularities increased the hardness of LM-2 coatings. The percentage of increase in microhardness from sprayed coating to vacuum annealed, LM-1 and LM-2 coatings is 6, 3 and 11% respectively. The hardness of pure alumina coatings is higher (≈1000-1100 HV) than the as-sprayed A40T coatings because hardness depends on the percentage of titania content present in the coating [13]. Microhardness of the coatings depends on the composition as well as the phases present in the coating [13,14,41]. In the present study there was no variation in the composition of the coating. Hence, the hardness was dependent on the phases and microstructure of the coating. Vacuum annealing treatment had produced stable α-Al_2O_3 phase, which increased the hardness of the coating. However, the surface defects could not be completely eliminated by annealing [13]. The percentage increase in the hardness value from sprayed coating to laser melted coatings (LM-1 and LM-2) is due to the synergistic effect of the reduction in hardness by the predominant Al_2TiO_5 phase and enhancement due to the formation of α-Al_2O_3 phase after laser melting [13,14,41]. The increase is less in hardness for all four cases because Al_2TiO_5 was one of the major phases in the coatings as evident in Fig. 5.17. The increase in hardness is attributed to decrease in porosity, microstructural modification and nucleation of α-Al_2O_3 phase in the laser melted coatings [13,14].

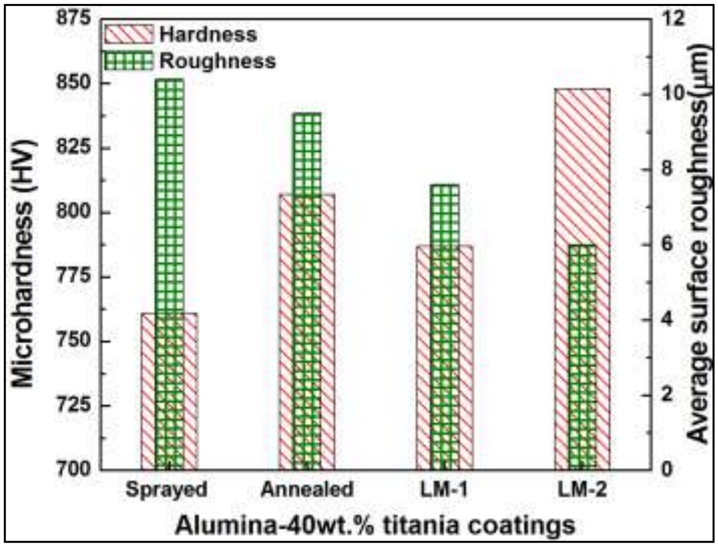

Fig. 5.18 Vickers microhardness and average surface roughness (R_a) of as-sprayed, annealed and laser melted (LM-1 and LM-2) A40T coatings.

Microhardness increased by 3% in the annealed coating when compared to the LM-1 coating, while it increased by 5 % in the LM-2 coating when compared to the annealed coating. This is due to the partially unmelted regions present in the LM-1 coating and also in annealed coating; however, annealed coating contained stable α-Al_2O_3. Microhardness results imply that laser energy plays a major role in the modification of surface hardness of the A40T coating compared to the annealing temperature. Microhardness of laser melted coatings increased with increase in laser power density [62]. The increase in microhardness from LM-1 to LM-2 is about 8% in the present study. The significant increase in microhardness value from LM-1 to LM-2 coating is due to significant reduction in the surface porosity, other defects and increase of microstructural homogeneity produced by high laser energy.

5.3.3.5 Surface roughness of post treated A40T coatings

Plasma spayed coatings exhibit significant roughness due to voids, microcracks, unmelted and partially melted regions present in the coating. The average surface roughness (R_a) values measured for the sprayed coating, vacuum annealed and laser melted coatings (LM-1 and LM-2) are shown in Fig. 5.18. It is evident that the surface roughness of the sprayed coating decreased after vacuum annealing and more significantly after laser melting. It is obvious that as-sprayed coatings have higher roughness compared to the post treated coatings. The decrease in R_a from sprayed coating to vacuum annealed coatings was 12%, however, it was 37 and 80% in the case of laser melted coatings LM-1 and LM-2, respectively. The decrease in surface roughness after post spray treatment from vacuum annealed to laser melted (LM-1 and LM-2) coatings was 20 and 37% respectively. These results indicated that the coating surface did not change drastically after annealing at 1373 K for 5 h; only the partially melted regions were consolidated during heat treatment. Hence, the roughness value of vacuum annealed surface was not far from the sprayed coating. The decrease in R_a from as-sprayed to laser melted (LM-1 and LM-2) samples was 27 and 42%, respectively. The decrease in R_a from LM-1 to LM-2 was about 21%. It is apparent that the surface finish improved considerably with a glazing effect upon laser melting. The surface defects present on the sprayed coating which contribute to high roughness were minimized by laser melting. Among the laser treated specimens LM-2 exhibited lower roughness than LM-1 due to the smooth surface caused by the large overlap of laser tracks. The partially melted regions were still present in LM-1 coating compared to LM-2. The decrease in the roughness values clearly indicated that high power density was beneficial to obtain more uniform microstructure (Fig. 5.18) owing to the formation of denser and homogeneous structure by way of eliminating surface defects/splat morphology. Hence, the average surface roughness followed the order: sprayed coating > vacuum annealed coating > LM-1 coating > LM-2 coating.

5.3.3.6 Corrosion studies on pulsed laser melted A40T coating (morphology and phase analysis)

The objective of this Section is to examine and compare the corrosion behaviour of laser melted A40T coatings with as-sprayed A40T coating for short time duration. The laser melted samples after corrosion test in molten LiCl-KCl salt had a glazy appearance with shining black colour. However, after ultrasonic cleaning, the tested and untested samples were similar in appearance. For the purpose of comparison the microstructure of HD graphite before and after corrosion test for 24 h in molten salt are shown in Fig. 5.19. The surface of the as-received HD graphite (Fig. 5.19a) had substantial porosity and after exposure to molten salt, and the existing pores were widened and new pores were created (Fig. 5.19b). It is evident from Fig. 5.19 that even short period of exposure leads to significant attack and protective coatings are required on HD graphite to prevent the attack by molten salt corrosion (as per the detailed discussion in Chapter 4).

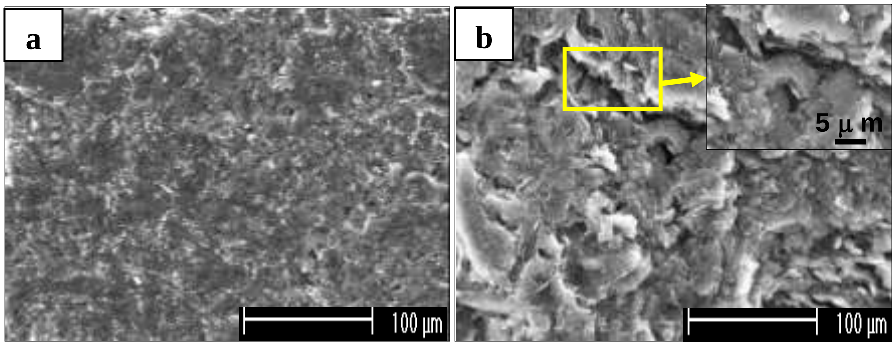

Fig. 5.19 Surface morphology of HD graphite (a) as-received and (b) corrosion tested for 24 h in molten LiCl-KCl salt at 873 K.

The SEM micrographs of as-sprayed A40T coatings exposed to molten LiCl-KCl salt for 24 h are shown in Fig. 5.20. Unmelted/partially melted surface with coating defects such as interlamellar gaps, open pores and microcracks present in the sprayed coatings are generally the effective penetration paths for molten salt to accelerate corrosion [63], leading to detachment of coating (vide section 5*.3.2.2*). Severe corrosion attack at the unmelted region was noticed in the present work at higher magnification (Fig. 5.20b). The affected regions in the as-sprayed coating after molten salt corrosion test were due to salt attack which would spread from the coating surface to HD graphite substrate as the exposure time increased. The corrosion studies on as-sprayed coatings (short and long durations), revealed that coating defects alter the corrosion behaviour of A40T coating in molten salt system and these are the effective penetration paths for molten salt. Corrosion behaviour of sprayed coatings depends to a large extent on the surface properties of the coating.

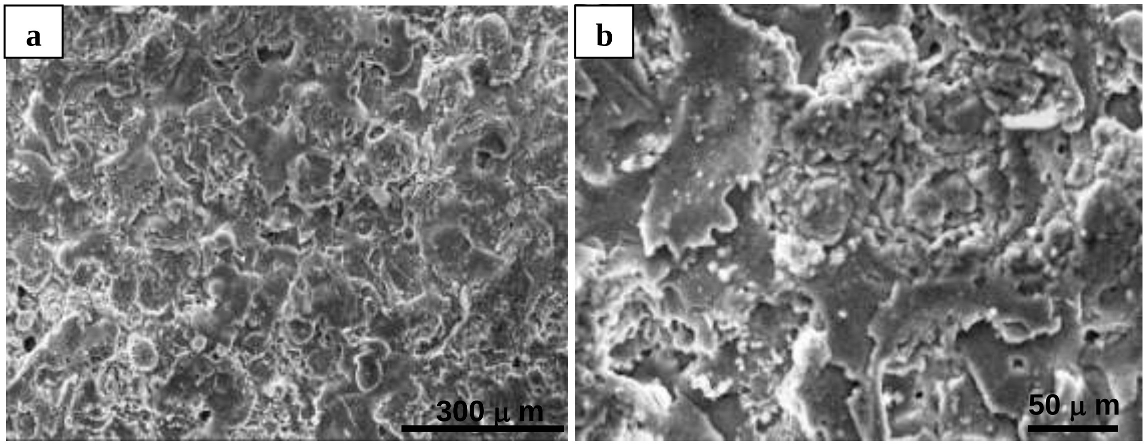

Fig. 5.20 (a) Surface morphology of corrosion tested as-sprayed coating exposed to molten LiCl-KCl salt at 873 K for 24 h (b) at higher magnification morphology.

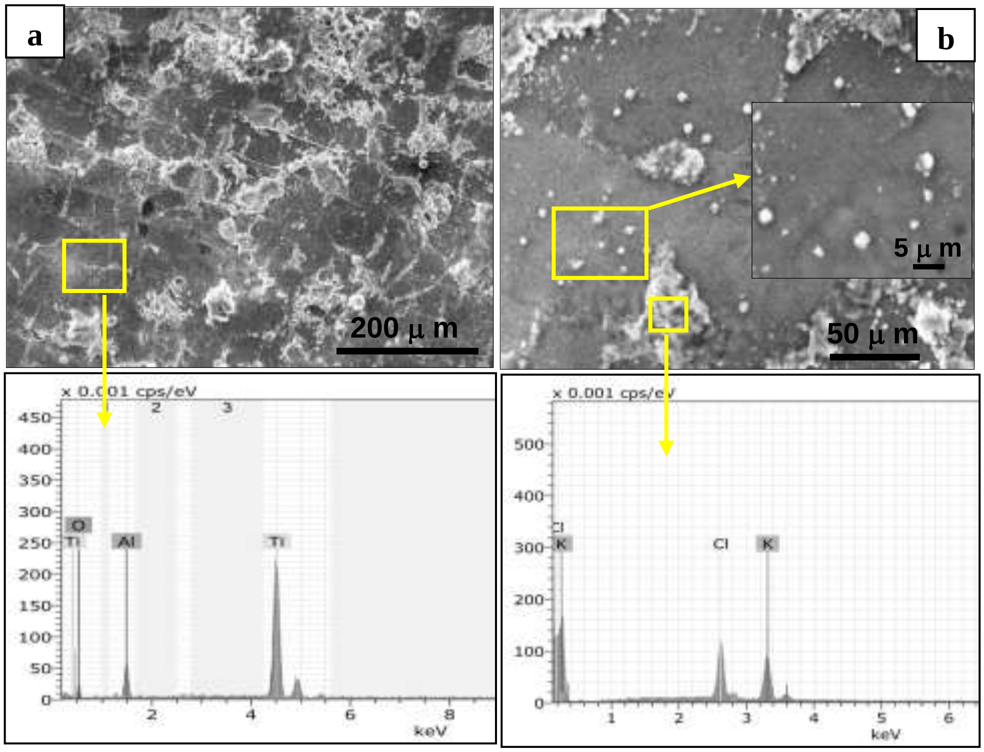

Fig. 5.21 (a) Surface morphology and EDX spectrum of LM-1 A40T coating exposed to molten LiCl-KCl salt at 873 K for 24 h and (b) at higher magnification morphology of coating with EDX spectrum.

Variation in laser power density from 640 to 800 kW/cm^2 showed a remarkable change in the surface properties (as discussed in Section 5.3.3.2.). The surface modified A40T coatings by laser melting process were exposed to molten LiCl-KCl salt at 873 K for 24 h. Figures 5.21 show the surface morphology of LM-1 coating after corrosion test in molten salt. The cracks formed in the coating during laser melting were found to be filled with molten salt after corrosion test (Figs. 5.21a and b). EDX analysis of corrosion tested LM-1 (Fig. 5.21a) revealed the presence of the elements of A40T coating listed in Table 5.3 and the white spot regions were identified as molten salt. The segmented cracks formed on the laser melted coatings were not beneficial with respect to corrosion; however, the reduction of specific surface area by the formation of compact dense melted layer would enhance the performance of coatings [22]. The LM-2 coating exposed to LiCl-KCl salt showed (Figs.5.22a and b) the degradation and corrosion attack on the surface to be marginal. The generation of dense microstructure by laser melting with 800 kW/cm^2 power density significantly reduced the penetration of molten salt into the coating (Fig. 5.22b) and corrosion attack compared to the as-sprayed coating (Fig. 5.20). Cracks surrounded by the salt on the laser melted coatings were due to initial penetration of salt into the cracks during the corrosion test. After testing for 24 h, salt penetration and macroscale damage in the LM-2 samples were observed to be lower than that in LM-1 coatings. Zhong et al. [64] also reported that the external dense layer generated by laser melting restrained the penetration of the molten salt into the coating to a certain extent. The microstructural features of corrosion tested laser melted coatings (Figs. 5.21b and Fig. 5.22b) upheld the observation that contamination by molten salt on the coated surface decreased as the laser pulse energy was increased from 640 to 800 kW/cm^2.

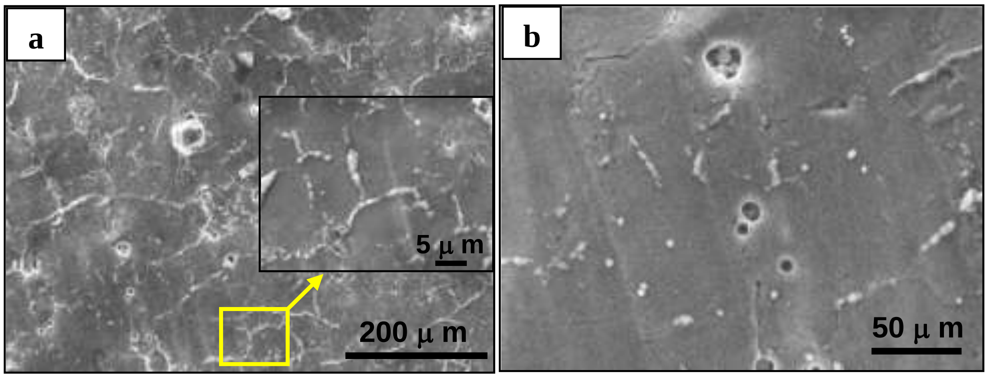

Fig. 5.22 (a) Surface morphology of corrosion tested LM-2 A40T coating exposed to molten LiCl-KCl salt at 873 K for 24 h; (b) morphology at higher magnification.

Table 5.3 EDX analysis on the microstructure of corrosion tested laser melted A40T coatings.

Microstructure of sprayed and corrosion tested laser melted A40T coatings.	**Elements (wt %)**				
	Al	**Ti**	**O**	**K**	**Cl**
Fig. 5.21a (on coating)	41.30	22.84	35.85	-	-
Fig. 5.21b and Fig. 22 a (White regions)	-	-	-	58.53	41.47

The mechanism of protection of laser melted A40T coatings from the corrosive attack by molten LiCl-KCl salt is schematically shown in Fig. 5.23. The attack of molten salt on plasma sprayed coatings described by Park et al. [63] comprises a three step corrosion mechanism process. Salt infiltration into the entire thickness of the top coating is the first step; the penetrated salt reacts with the phases in the ceramic coating is the second step and finally the coating is damaged by diffusion controlled salt attack in the third step. In the case of A40T top coating there is no reaction between the molten salt and top ceramic coating. Hence, a probable mechanism proposed for molten salt corrosion attack of laser melted A40T coating is as follows: the penetration of molten salt into the coating is very low because the surface was modified by laser melting and the dense microstructure created restricts the penetration of salt into the coating due to reduction in the specific surface area. Hence, the molten salt will settle on the surface of the coating (Fig. 5.23). The main reason for the improvement in the performance of A40T coating after laser melting is attributed to the formation of dense structure, uniform microstructure and distribution of phases. The corrosion control in A40T coatings by laser melting process is attributed to the improvement in the surface quality of the coating in terms of microstructure caused by higher pulse energy.

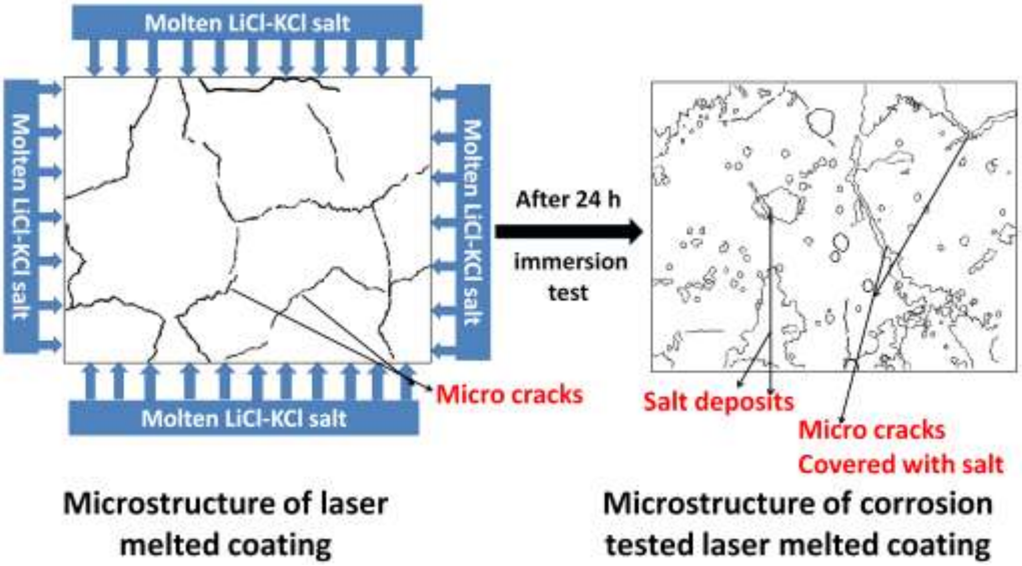

Microstructure of laser melted coating

Microstructure of corrosion tested laser melted coating

Fig. 5.23 Schematic diagrams showing the microstructures of as-melted and corrosion tested laser melted coating after testing in molten salt.

The phases identified on the corrosion tested as-sprayed and laser melted A40T coatings in molten LiCl-KCl salt at 873 K for 24 h are listed in Table 5.4. The XRD pattern of LM A40T coating exposed to molten salt comprised diffraction peaks for β-Al$_2$TiO$_5$, α-A1$_2$O$_3$

and R-TiO_2 phases. For the purpose of comparison the XRD results of powder, as-sprayed and laser melted coatings before corrosion testing are also listed in Table 5.4. In the corrosion tested LM A40T coatings the predominant phase observed was β-Al_2TiO_5 similar to the as-melted A40T coatings (as discussed in Section 5.3.3.3).

Table 5.4 Phase identification by XRD on powder, sprayed coating, and laser melted coating and corrosion tested A40T coatings after exposed to molten LiCl-KCl salt.

Coating	Phases	Remarks
A40T powder	α-$A1_2O_3$, R-TiO_2, Ti_2O_3, Ti_3O_5	Highest intensity for α-$A1_2O_3$, R-TiO_2
As-sprayed A40T coating	β-Al_2TiO_5, γ-$A1_2O_3$, R-TiO_2 α-$A1_2O_3$	β-Al_2TiO_5 with highest intensity and unstable γ-$A1_2O_3$ observed
Laser melted A40T coating with 640 kW/cm^2	β-Al_2TiO_5, α-$A1_2O_3$, R-TiO_2	β-Al_2TiO_5 as the predominant phase
Laser melted A40T coating with 800 kW/cm^2	β-Al_2TiO_5, α-$A1_2O_3$, R-TiO_2	β-Al_2TiO_5 as the predominant phase
Corrosion tested sprayed A40T coating for 24 and 1000 h	β-Al_2TiO_5, γ-$A1_2O_3$, R-TiO_2, α-$A1_2O_3$	β-Al_2TiO_5 had highest intensity
Corrosion tested Laser melted A40T coating with 640 kW/cm^2	β-Al_2TiO_5, α-$A1_2O_3$, R-TiO_2	Maximum intensity for β-Al_2TiO_5
Corrosion tested Laser melted A40T coating with 800 kW/cm^2	β-Al_2TiO_5, α-$A1_2O_3$, R-TiO_2	Maximum intensity for β-Al_2TiO_5

5.3.4 Uranium melting studies

5.3.4.1 Compatibility studies based on Gibbs free energy and visual examination

To assess the chemical reactivity of molten uranium with the coating components, the Gibbs free energy change (ΔG_R) was calculated using FactSage® version 6 software for the following reactions in the temperature range 300 - 2000 K.

$U + C \rightarrow UC$ (1)

$Al_2O_3 + 1.5\ U \rightarrow 1.5\ UO_2 + 2Al$ (2)

$TiO_2 + U \rightarrow UO_2 + Ti$ (3)

ΔG_R values computed for the reactions (1) to (3) are plotted as a function of temperature in Fig. 5.24. The thermodynamic stability of the A40T coatings with respect to molten uranium can be ascertained from the values of Gibbs free energy change for the formation of all probable binary compounds from the constituents of coating materials and molten uranium in the temperature range of investigation. The negative values of Gibbs free energy change for the formation of UC indicates that the interaction of uranium with graphite and protection of graphite is required to process uranium in a graphite crucible. Figure 5.24 shows that Al_2O_3 is stable with uranium up to 900 K, beyond which, the free energy change continuously decreased with increase in temperature and becomes more negative indicating the occurrence of a spontaneous reaction. The reaction of TiO_2 with uranium has the highest negative value for Gibbs free energy change compared to other reactions. This suggested that spontaneous reaction will occur with uranium as the chemical affinity of TiO_2 towards uranium is high. In temperature range of 900 - 2000 K, the Gibbs free energy change for these reactions (2) and (3) are negative revealing that uranium may react with A40T. This can be further verified by experientially by uranium melting experiments.

Figure 5.25 shows the pictures of the ceramic coatings of A40T on HD graphite before and after uranium melting experiments. Visual examination of the A40T coating without bond coat showed that the coated layer did not peel off from the surface of HD graphite substrate after uranium melting. However, a portion of the coating spalled off after the uranium melting was carried out for second time. This observation suggested that A40T coating exhibits poor adhesion to HD graphite. After uranium melting, A40T coating on HD graphite did not spall off, whereas Cr_3C_2-NiCr bond coated A40T coating on HD graphite spalled off.

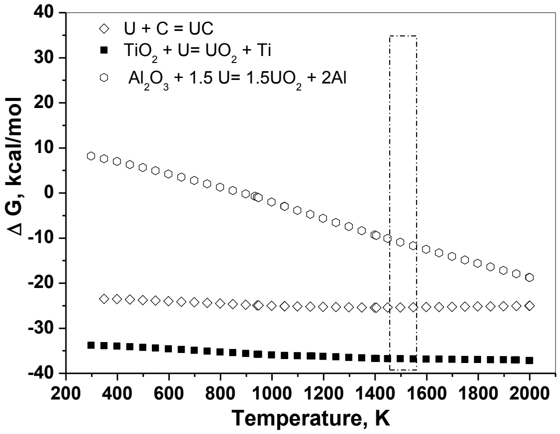

Fig. 5.24 Gibbs free energy change of possible chemical reactions as a function of temperature.

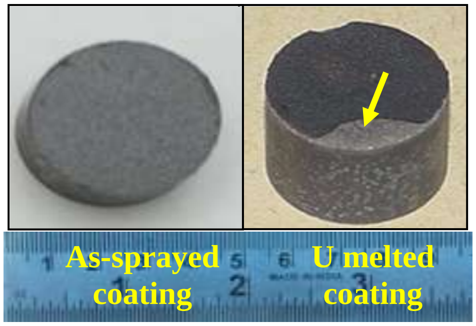

Fig. 5.25 Pictures of as-coated and second time uranium melted A40T coatings on HD graphite samples.

5.3.4.2 Morphology of A40T coatings

After a single run of uranium melting on A40T coated HD graphite without bond coat the splat morphology was still present (Fig. 5.26a). However, the morphology at higher magnification (Figs. 5.26b and 5.26c) showed uranium metal particles sticking on the splats of the coating. EDX analysis was performed at two different regions of A40T coating (Fig. 5.26b). The EDX spectrum (Fig. 5.26d) recorded on the white spot region-1 showed the elemental peak of U along with Al, Ti and O elements.

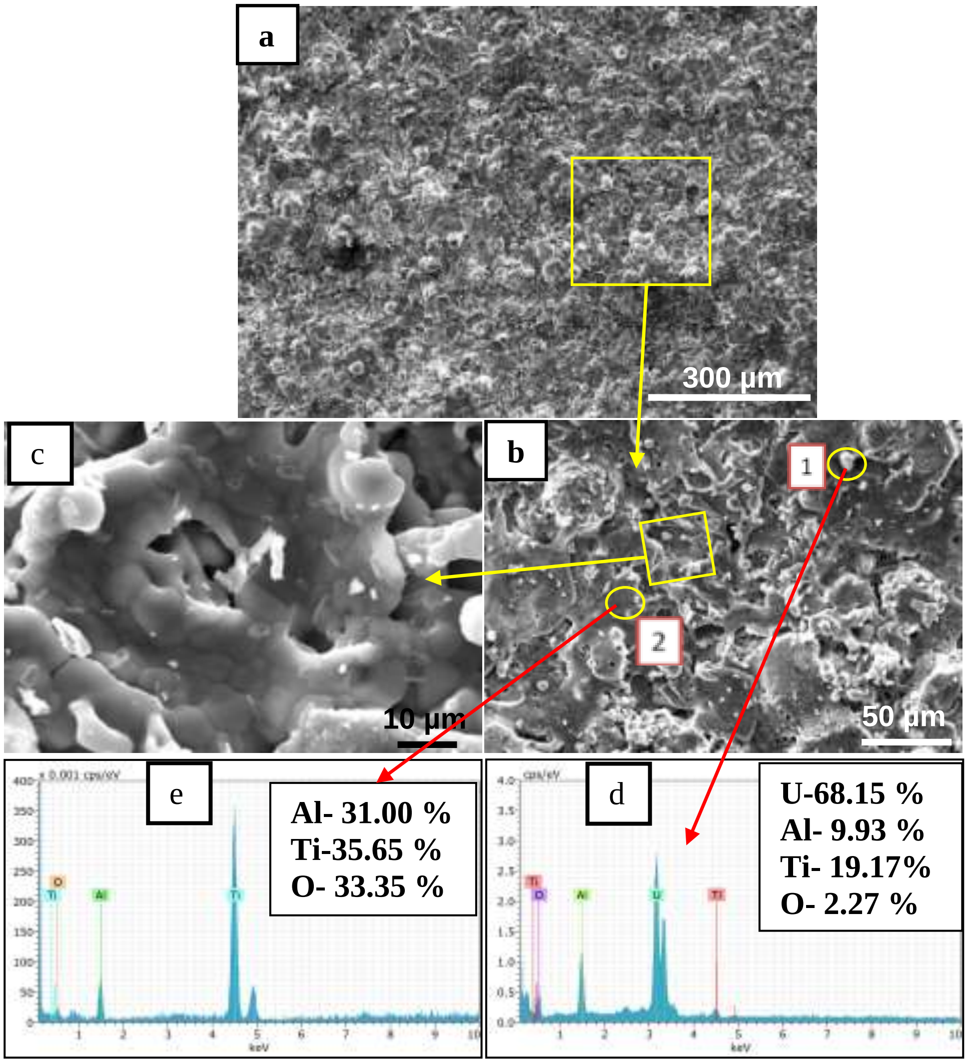

Fig. 5.26 Microstructures of A40T coating: (a,b & c) after single time uranium melting at lower and higher magnifications and selected regions of EDX spectra from (d) region -1and (e) region -2.

The EDX analysis performed on the coating region-2 (Fig. 5.26e) showed Al, Ti and O elements only and U was absent. The concentration of the elements shown in the EDX spectra (Fig. 5.26d and 5.26e) clearly indicated the maximum percentage of uranium element in region-1, while region-2 has only coating elements with high percentage of titanium after uranium melting. Similar analysis was performed on A40T coating after uranium melting for twice on the same spot and the coating microstructures and EDX spectra are shown in Fig. 5.27. The splat morphology observed on the microstructure of the as-sprayed A40T coating had changed to a consolidated microstructure (Figs. 5.27a and b) after melting for second time. The microstructure appeared to be of the one which was molten and solidified during the second run of uranium melting after absorbing sufficient energy from the melt. Figure 5.27c showed dense microstructural features which could be clearly distinguished from the microstructure seen in Fig. 5.26c. The wide pores/voids present in between the splats were minimized and the grain morphology was observed at higher magnification (Figs 5.26c and 5.27c). These kind of grain morphology has been expected to appear in heat treated ceramic coatings at very high temperatures. The grain growth was observed to increase from single to second time melting experiment on the A40T coating. The EDX analysis performed on the second time melted regions 3 and 4 of A40T coating are shown in Figs. 5.27d and 5.27e respectively. The spectra recorded on region-3 showed a high percentage of U along with ceramic coating elements (Fig. 5.27d). Region-4 showed only coating elements (Fig. 5.27e) indicating that the white regions observed on the coating after uranium melting are the signatures of U metal. The size and the distribution of U metal adhered to the coating in the second time melting experiment was higher compared to single melted A40T coating as observed from Figs. 5.26c and 5.27c.

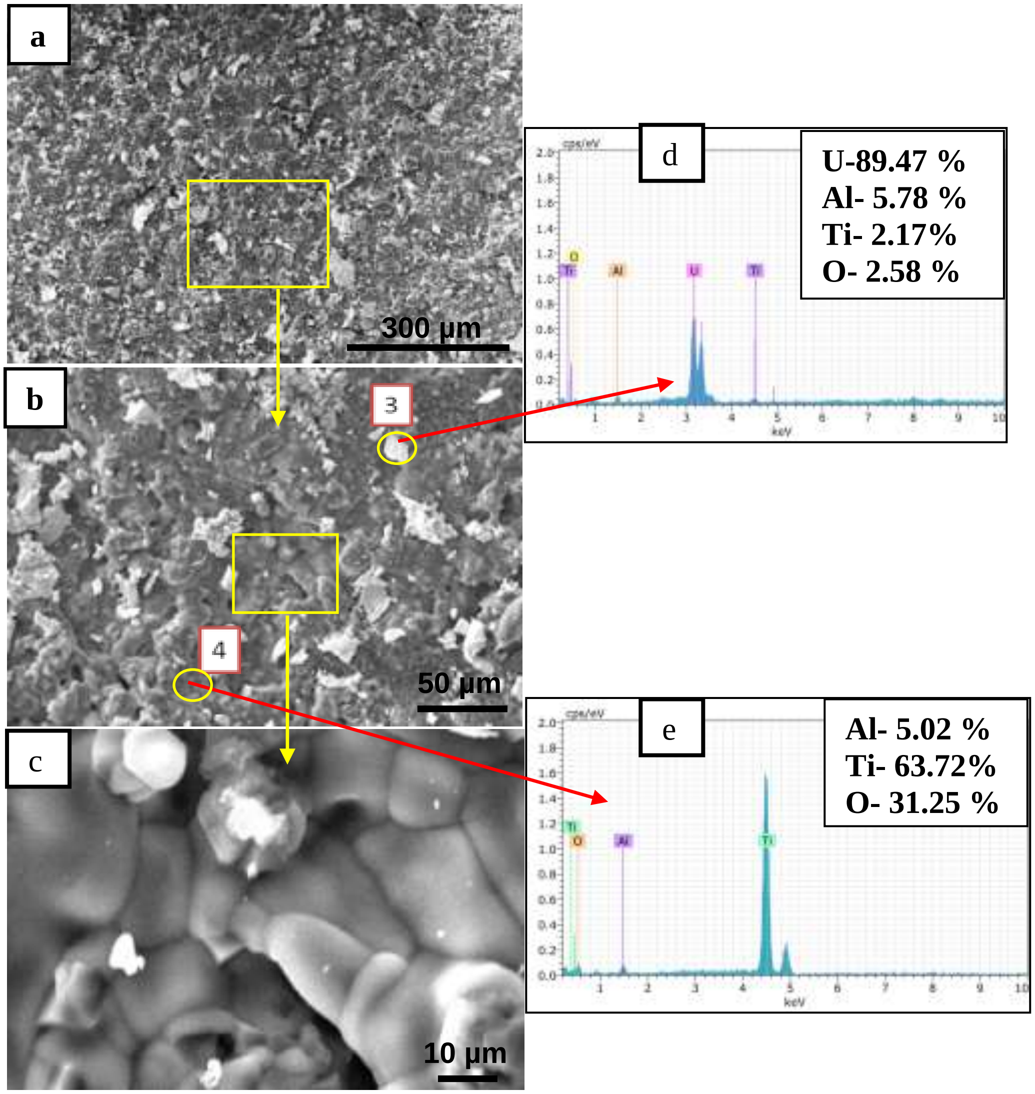

Fig. 5.27 (a, b & c) Microstructures of A40T coating after second time uranium melting experiment at lower and higher magnifications and selected regions of EDX spectra from (d) region-3 and (e) region-4.

Cross section morphologies of as-sprayed and uranium melted A40T coated HD graphite without bond coat are shown in Fig. 5.28a and b respectively. The typical pores present in the cross section of the as-sprayed coating got reduced after second time uranium melting. The as-sprayed A40T coating got densified after second time uranium melting. Along the cross section uranium element was not identified in EDX spectrum, as the molten uranium at 1623 K did not diffuse into the coating and it was adhered to the surface only. This observation was supported by the SEM images in Figs. 5.26c and 5.27c. The cross section of the as-sprayed A40T coated HD graphite with Cr_3C_2-NiCr bond coat is shown in Fig. 5.28c. The top coating layer completely delaminated from the graphite substrate after uranium melting at 1623 K (Fig. 5.28d) while removing the adhered uranium metal. The left out coating on the surface was analyzed by SEM and EDX. The morphology (Fig. 5.29d) clearly showed the porous nature and EDX analysis revealed the elemental composition as Cr-29.37 wt %, C-30.80 wt%, Ti- 3.31 wt %, Ni- 2.20 wt %, Si- 0.43 wt % and Fe- 0.77 wt %. This confirmed the presence of Cr_3C_2-NiCr bond coat remaining on the substrate. Si and Fe were found as impurities on the coating due to sand blasting of the substrate before coating by plasma spraying. These results revealed that A40T coating has poor adherence on graphite without and with the bond coat of Cr_3C_2-NiCr at the desired temperature for uranium melting. A40T coating without bond coat peeled off from some regions of graphite after second melting; hence, recoating after a few runs and cleaning of the graphite crucible walls to remove the adhered uranium is necessary. Due to poor adhesion and performance of uranium melting application further characterization on A40T coating was not performed with other analysis techniques.

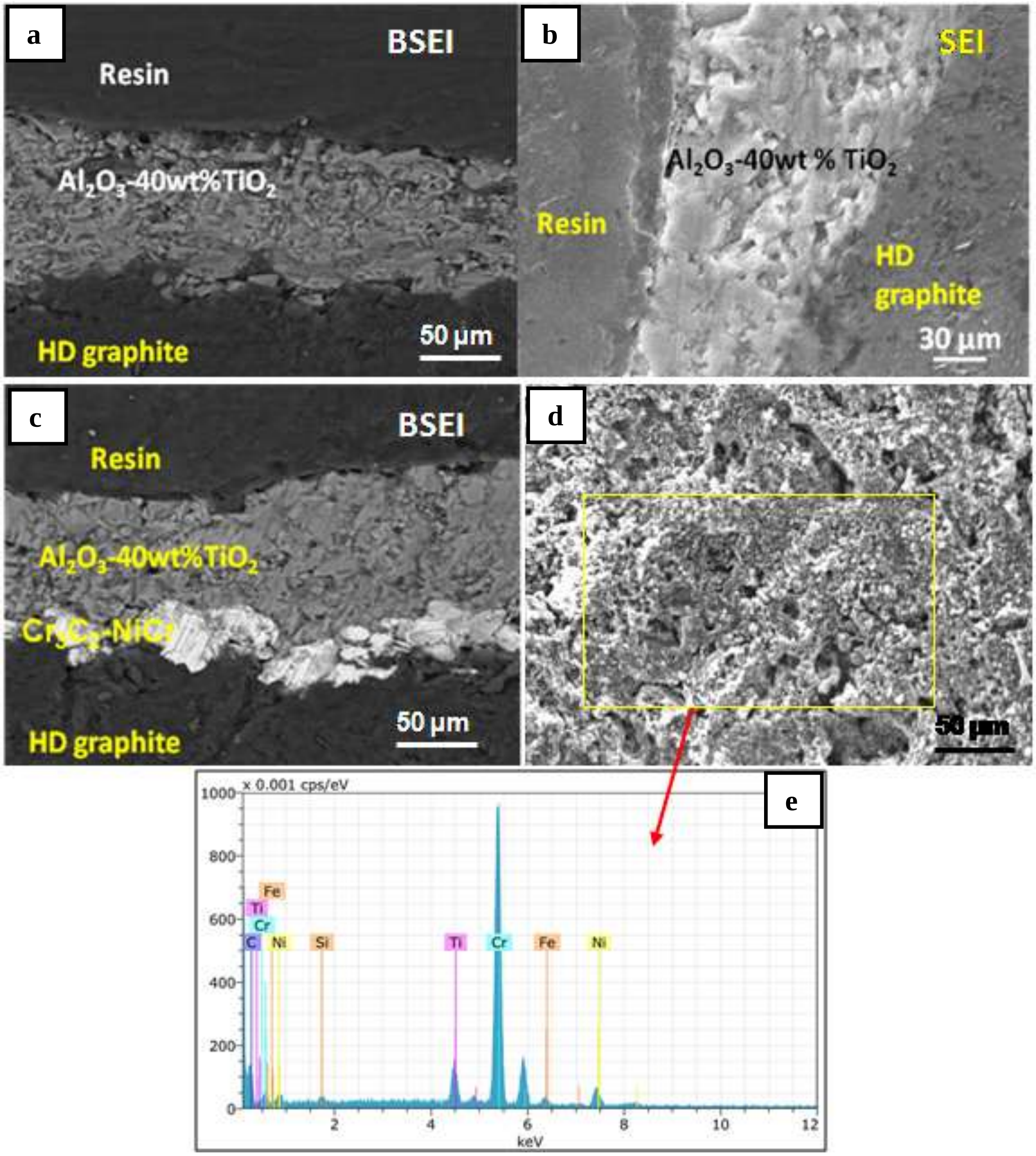

Fig. 5.28 Cross sections of (a) as-sprayed without bond coat (BSEI) and (b) uranium melted (SEI) A40T coatings on HD graphite; (c) A40T coated HD graphite with Cr_3C_2-NiCr bond coating (BSEI); and (d) Surface of A40T coating after spallation and (e) corresponding EDX spectrum.

5.3.5 Thermal cycling studies

The performance of A40T coating in molten LiCl-KCl salt and with molten uranium is not satisfactory due to poor adhesion to HD graphite and reaction with uranium metal. Based on these results it cannot be considered further for any application related to the pyroprocessing unless better processing conditions including different bond coating is necessary. However, in order to understand the durability of A40T coating on HD graphite thermal cycling studies were carried out at 873 K under vacuum.

5.3.5.1 Visual examination and weight loss studies

After thermal cycling experiments the A40T samples were visually examined to identify the surface changes and coating spallation or failure of the coating. The visual examination of samples without bond coat and with bond coat of A40T coated HD graphite samples showed spallation after thermal cycling for 80 and 60 cycles at 873 K respectively. The spallation of A40T coating clearly indicated that the top A40T coating has poor adhesion in both the cases (without and with bond coat). In case of bond coated sample the top coat spallation occurred at less number of cycles compared to the one without bond coating.

The weight loss of A40T coating without bond coat after 80 cycles and with Cr_3C_2-NiCr bond coated A40T coating after 60 cycles samples at 873 K are 70 % and 62 % respectively. The percentage weight losses observed in both cases are high due to complete failure of top A40T coating. The weight loss of A40T without bond coating sample is more compared to bond coated sample due to presence of Cr_3C_2-NiCr bond coat which remained on the graphite surface.

5.3.5.2 Morphology of thermal cycled A40Tcoating

The failure mechanisms of the coatings after thermal cycling related to the changes in the microstructures of the coating [65]. Usually, plasma sprayed A40T coating contains micro defects due to the characteristics of process of deposition. These imperfections play significant role in determining the life or durability of the coatings when subjected to thermal cycling. The surface morphology of as-sprayed A40T coating at higher magnification contained micro cracks between the molten splats as observed in Fig. 5.29. These microcracks became macrocracks in the coating; a catastrophic failure of coating occurred at certain number of cycles.

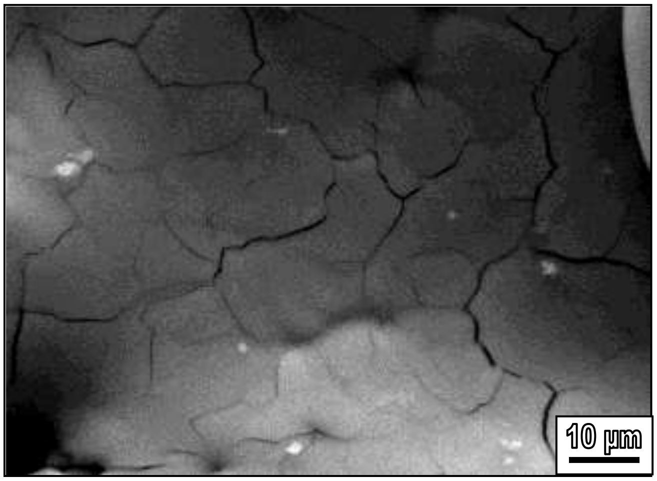

Fig. 5.29 The microstructure of A40T coating at higher magnification.

After thermal cycling test at 873 K for 80 cycles, A40T coating (without bond coat) surface exhibited blasted microstructure features like high surface irregularities and bumps (Fig. 5.30a). The splat morphology observed in as-sprayed coating was completely vanished. This observation confirms that the A40T coating got completely spalled out. At the higher magnification analysis of surface showed typical graphite morphology (Fig. 5.30b). The morphology of thermal cycled A40T coating with Cr_3C_2-NiCr bond coat at 873 K after 60 cycles exhibited porous microstructure as shown in Figs. 5.31a and b. At higher magnification also no substrate morphology was observed because of the presence of bond coat. It was confirmed in EDX analysis (Fig. 5.31c) that the elements present are Cr-30.51 wt %, Ni-15.48 wt %, C- 49.03 wt %, Ti-2.28 wt %, Fe-1.86 wt %, and Si- 0.84 wt %. The bond coat of Cr_3C_2-NiCr was not spalled from graphite substrate and only the top coating A40T failed and these results are agreement with the weight loss measurements. In the case of bond coated A40T sample failure was observed at the interface of A40T/Cr_3C_2-NiCr, and not at Cr_3C_2-NiCr/HD graphite. Cr_3C_2-NiCr bond coat is still adhered to the substrate, and the failure occurred in the top A40T coating. Similar kind of failure was observed in A40T coating tested in molten LiCl-KCl salt at 873 K and also in uranium melting testing at 1623 K as discussed earlier. The cross-section of as-sprayed A40T coating (Fig. 5.2 and Fig. 5.4) having interlamellar pores and voids because of this poor interlammelar structure, the top A40T coating was failed without and with Cr_3C_2-NiCr bond coating. These pre-existing inter-lamellar delimitations in the top coat generally act as crack embryos. The crack nucleation and propagation occurred in the A40T coating due to the opening up of such interlamellar delimitations [66]. In addition to the pre-existing interlamellar delaminations in the top coat, cracks may also nucleate at the interfacial regions during thermal cycling. Such crack initiation mechanisms are described in literature; crack initiation in the bond coat/top coat interface is most commonly attributed to the generation of thermal stress by mismatch in the thermal expansion between bond coat and top coat [66]. Similarly, there is a possibility of origin of stress at the interface of A40T/graphite leading to the failure of the coating. The failure of A40T coating is mainly due to the poor adhesion strength of the coating to the graphite as well as to the Cr_3C_2-NiCr bond coat.

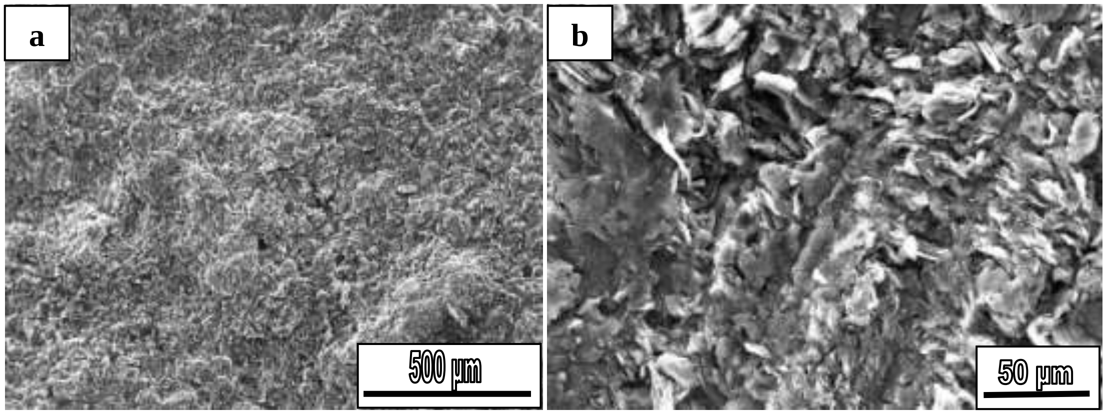

Fig. 5.30 (a) Surface morphologies of thermal cycled A40T coating (without bond coat) after 80 cycles, (d) typical graphite morphology after spallation of A40T coating.

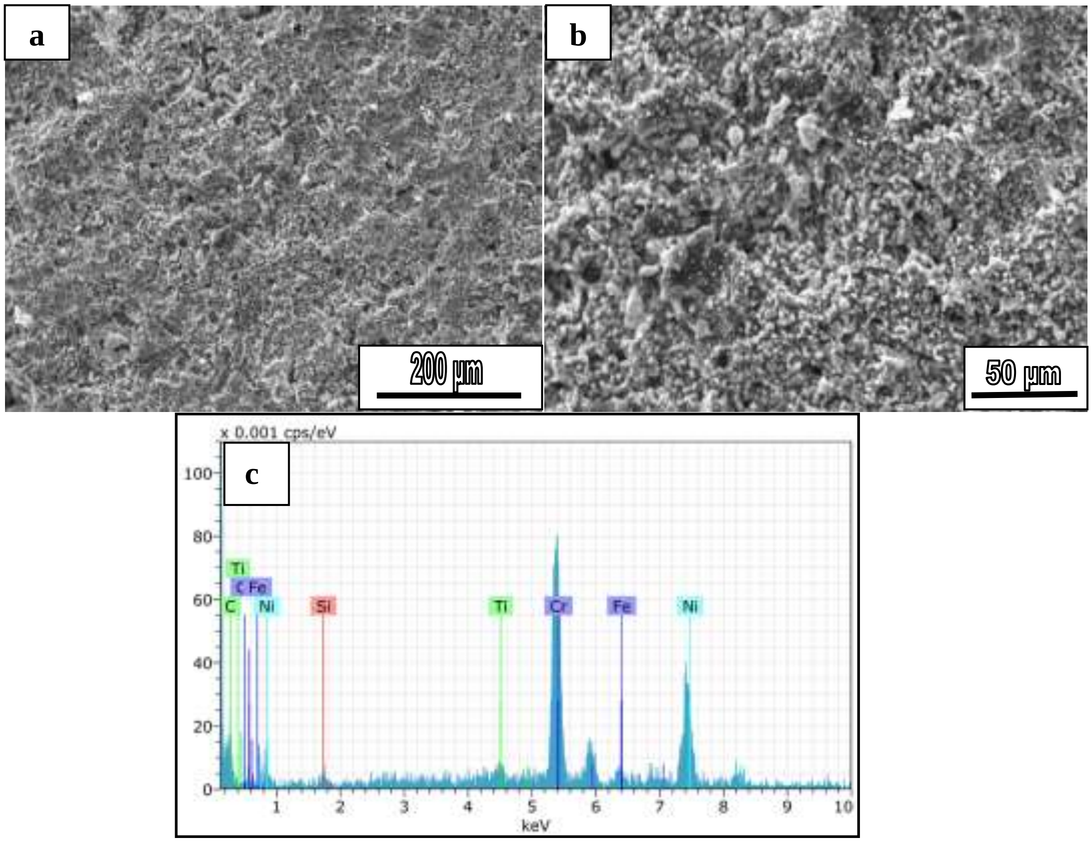

Fig. 5.31 Surface morphologies of thermal cycled A40T coating (with Cr_3C_2-NiCr bond coat) after 60 cycles, (b) morphology at higher magnification (after spallation) and corresponding (c) EDX spectrum.

One of the reasons for the delamination of A40T coatings from HD graphite after thermal cycling test is due to the ceramic nature of the cermet bond coat, Cr_3C_2-NiCr. The thermal expansion coefficient (α) of cermets is inferior compared to that of HD graphite substrate. Typical values of α for Cr_3C_2-NiCr (cermet) and HD graphite are $5.9 \times 10^{-6}\ K^{-1}$ and $10.9 \times 10^{-6}\ K^{-1}$ respectively, in the temperature range 293–1273 K. Further, the plastic flow and creep at high temperatures properties are not possessed by cermet bond coats.

5.4 Summary

The following results could be drawn based on the studies on the performance of A40T coating on HD graphite (tested under different conditions) with respect to the microstructure and phase changes:

The surface and cross sectional morphologies of the as-sprayed A40T coating characterized with SEM-EDX analysis confirmed the presence of partially and unmelted regions in the coatings. A40T coated HD graphite samples exposed to molten LiC-KCl salt for 500, 1000 and 2000 h revealed that the coating deposited with Cr_3C_2-NiCr bond coat had undergon a spllation and oxidation of bond coat due to salt penetration and attack; however, A40T coating without bond coat showed good corrosion resistance up to 500 h. Post treatments were performed on as-sprayed coating by annealing and pulsed laser melting to improve the surface properties and to eliminate the partially and unmelted regions of A40T coating. Laser melted coatings exhibited uniform microstructure owing to redution in the surface roughness and increase in microhardness. Laser melted A40T coating with two power densities exposed to molten LiCl-KCl salt revealed that the dense layer generated on the surface restricts the penetration of molten salt into the coating. As the power density increased the efficiency of corrosion protection was increased in terms of less salt deposit. Unstable phases observed in the as-sprayed coating like γ-Al_2O_3 were converted into stable phases like β-Al_2TiO_5 and α-Al_2O_3 by post spray treatments. Phase changes did not occur in the corrosion tseted as-sprayed as well as laser melted A40T coatings. Gibb's free energy calculation indicated that reaction is possible between uranium and A40T coating components. Uranium metal was adhered to coating and spllation of A40T coating observed after uranium melting experiments. Failure of the A40T coating was observed after thermal cycling for 80 cycles (without bond coat) and 60 cycles (Cr_3C_2-NiCr bond coated) due to interlammellar cracks and propagation of these cracks. The failure phenomenon observed for A40T coating clealy suggested that coating possessed less adhesion strength on HD graphite substrate.

References

[1] U. Kamachi Mudali, A. Ravi Shankar, S. Ningshen, G. Suresh, R. Sole and K. Thyagarajan, Energy Procedia. **7** (2011) 431-436.

[2] A. Ravi Shankar, U. Kamachi Mudali, Mater. Corros 59 (2008) 878-882.

[3] A. Ravi Shankar, S. Mathiya, K. Thyagarajan, U. Kamachi Mudali, Metall. Mater. Trans.A 41(2010) 1815-1825.

[4] J.E. Indacochea, J.L. Smith, K.R. Litko, E.J. Karell, J. Mater. Res 14 (1999) 1990-1995.

[5] A. Ravi Shankar, K. Thyagarajan, U. Kamachi Mudali, Corrosion 69 (2013) 655-665.

[6] P.S. Maiya, R.A. Erck, B.M. Moon, Surf. Coat. Technol. 102(1998) 218-222.

[7] N. Mesrati, H. Ajhrourh, D. Nguyen, D. Treheux, J. Thermal. Spray. Technol 9 (2000) 95-99.

[8] N. Mesrati, H. Ajhrourh, D. Nguyen, D. Treheux, Thermal spraying on graphite, in: C. Coddet (Eds.,), Thermal Spray: Meeting the Challenges of the 21st century, Proceedings

of the 15th International Thermal Spray Conference, ASM International, Ohio, 1998, pp.1507–1512.

[9] M. Takeuchi, T. Kato, K. Hanada, T. Koizumi, S. Aose, J. Phys. Chem. Solids. 66 (2005) 521-525.

[10] M.G. Lawson, F.S. Pettit, J.R. Blachere, J. Mater. Res. 8 (1993) 1964-1971.

[11] T. Hirata, K. Akiyama, H. Yamamoto, J. Mater. Sci. 36 (2001) 5927-5934.

[12] H.Y. Lee, K.H. Baik, Met. Mater. Int. 15 (2009) 783-787.

[13] V. Fervel, B. Normand, C. Coddet, Wear 230 (1999) 70-77.

[14] V. Fervel, B. Normand, H. Liao, C. Coddet, E. Beˆche, R. Berjoan, Surf. Coat. Technol. 111 (1999) 255-262.

[15] T.J. Steeper, W.L. Riggs II, A.J. Rotolico, J.E. Nerz, D.J. Varacalle, G.C. Wilson, in: T.F. Bernecki (Ed.), Thermal spray coatings: Properties, Processes and Applications, Proceedings of the Fourth National Thermal Spray Conference, Pittsburgh, Pennsylvania, ASM International, Ohio, 1991, pp.13-20.

[16] F.L. Toma, C.C. Stahr, L.M. Berger, S. Saaro, M. Herrmann, D. Deska, G. Michael, J. Therm. Spray Technol. 19 (2010) 137-147.

[17] D.J. Varacalle, H. Herman, G.A. Bancke, W.L. Riggs, Surf. Coat. Technol. 54-55 (1992)19-24.

[18] A. Afrasiabi, M. Saremi and A. Kobayashi, Mater. Sci. Eng. A, 478 (2008) 264-269.

[19] P.K. Sapra, S. Singh, S. Prakash, Hot corrosion behaviour of alumina titania coatings in molten sodium sulphate-vanadium pentoxide environment. Proc. Materials Science and Technology Conference and Exhibition, Pittsburgh, (2009) pp.2130-2135. ASM International, Ohio.

[20] S.H. Cho, S.B. Park, D.S. Kang, M.S. Jeong, H. Park, J.M. Hur , H.S. Lee, J. Nucl. Mater. 399 (2010) 212–218.

[21] Z. Chen, J. Mabon, J.G. Wen, R. Trice, J. Eur. Ceram. Soc. 29 (2009) 1647-1656.

[22] C. Batista, A. Portinhaa, R.M. Ribeiroa, V. Teixeira, and C.R. Oliveira, Surf. Coat. Technol. 200 (2006) 6783-6791.

[23] W.U. Weitoa, R. Streiff, W. Maocai, Mater. Sci. Eng A 121, (1989): p. 499.

[24] J.R. Davis and associates, ASM Handbook, 9, Metallography and microstructures, ASM international, Ohio, USA, 2004, pp.1038–1046.

[25] S.S. Chatha, H.S. Sidhu, B.S. Sidhu, Inter. J. Mater. Sci. Eng 2 (2011) Jan-Dec.

[26] G. Xie, X. Lin, K. Wang, X. Mo, D. Zhang, P. Lin, Corros. Sci. 49 (2007) 662-671.

[27] R. McPherson, Surf. Coat. Technol. 39-40 (1989) 173-181.

[28] A. Pawlowski, T. Czeppe, L. Gorski, W. Baliga, Arch. Metall. Mater. 50 (2005) 719-728.

[29] R. McPherson, J. Mater. Sci. 15 (1980) 3141-3149.

[30] W. Aihua, Z. Beidi, T. Zengyi, M. Xianyao, D. Shijun, C. Xudong, Surf. Coat. Technol. 57 (1993) 169-172.

[31] C. Sreedhar, G. Santhanakrishnan, CV. Gokularathnam, R. Krishnamurthy, J. Mater. Process. Technol 114 (2001) 246–51.

[32] H.L. Tsai, P.C. Tsai, J. Mater. Eng. Perform. 4 (1995) 689–96.

[33] R. Tomazek, L. Pawlowski, J. Zdanowski, J. Grimblot, J. Laureyns, Surf. Coat. Technol. 185 (2004) 137–49.

[34] A. Ibrahim, H. Salem, S. Sedky, Surf. Coat. Technol. 203 (2009) 3579–89.

[35] K.A. Khor, S. Jana, J. Mater. Process Technol. 66 (1997) 4–8.

[36] B.S. Sidhu, S. Prakash, Corrosion 61 (2005) 1098-1106.

[37] I. Smurov, A. Uglov, Y.U. Krivonogov, S. Sturlese, C. Bartuli, J. Mater. Sci 27 (1992) 4523-4530.

[38] J. W. Koger, C. E. Holcombe, J. G. Banker, Thin Solid Films 39 (1976) 297-303

[39] J.J. Asbury, Alumina titanate crucible for molten uranium, US Patent no: 3890140 (1975)

[40] U. Kamachi Mudali, A. Ravi Shankar, C. Mallika, K. Thyagarajan, S. Ningshen, B.P. Reddy, K. Nagarajan, Materials and Coating Technologies for Pyrochemical Reprocessing of Spent Metallic Fuel from Fast Breeder Reactors, Report: IGC/MMG/CSTG/2011. pp. 1-47.

[41] K.A. Habib, J.J. Saura, C. Ferrer, M.S. Damra, E. Giménez, L. Cabedo, Surf. Coat. Technol. 201(2006) 1436–1443.

[42] C.C. Berndt, J.H. Yi, in: D.L. Houck (Ed.), Thermal Spray: Advances in coating technology, Proceedings of the national thermal spray conference, Florida, ASM International, Ohio, 1987, pp. 297-308.

[43] S. Kuroda, T.W. Clyne, Thin Solid Films 200 (1991) 49-66.

[44] S. Kuroda, T. Dendo, S. Kitahara , J. Therm. Spray Technol. 4(1995) 75-84.

[45] A. Nishikata, H. Numata, T. Suru, Mater. Sci. Eng. A 146 (1991) 15-31.

[46] G.R. Heath, P. Heimgartner, G. Irons, R. Miller, S. Gustafsson, Mater. Sci. Forum. 251-254 (1997) 809-816.

[47] J.D. Reardon, R. Mignogna, F.N. Lonngo, Thin Solid Films (1981) 345-351.

[48] J.M. Guilemany, N. Espallargas, P.H. Suegama, A.V. Benedetti, Corros. Sci. 48 (2006) 2998–3013.

[49] M. Magnani, P.H. Suegama, N. Espallargas, C.S. Fugivara, S. Dosta, J.M. Guilemany, A.V. Benedetti, J. Therm. Spray. Technol. 18 (2009) 353-363.

[50] B. Normand, V. Fervel, C. Coddet, V. Nikitine, Surf. Coat. Technol. 123 (2000) 278-287.

[51] Z. Znamirowski, L. Pawlowski, T. Cichy, W. Czarczynski, Surf. Coat. Technol. 187 (2004) 37-46.

[52] V. Buscaglia, P. Nanni, J. Am. Ceram. Soc. 81 (1998) 2645-2653.

[53] L. Pawlowski, Surf. Coat. Technol. 31 (1987) 103-116.

[54] C.M. Wang, H.F. Sun, Q. Song, Key. Eng. Mater. 373-374 (2008) 47-50.

[55] P. Cheang, K.A. Khor, L.L. Teoh, S.C. Tam, Biomaterials17 (1996) 1901–1904.

[56] C. Batista, A. Portinha, R.M. Ribeiro, V. Teixeira, M.F. Costa, C.R. Oliveira, Appl. Surf. Sci. 247 (2005) 313–319.

[57] S.T. Picraux, L.E. Pope, Science 226 (1984) 615–622.

[58] A. Chehrghani, M.J. Torkamany, M.J. Hamedi, J. Sabbaghzadeh, Appl. Surf. Sci. 258 (2012) 2068-2076.

[59] A. Ravi Shankar, J. Babu, S. Ravikumar, U. Kamachi Mudali, H.S. Khatak, Surf. Eng. 23 (2007) 147–154.

[60] P.C. Tsai, J.H. Lee, C.S. Hsu, Surf. Coat. Technol. 201 (2007) 5143-5147.

[61] Y-l. Gao, C-s. Wang, M. Yao, H-b. Liu, Appl. Surf. Sci. 253 (2007) 5306–5311.

[62] Y. Yuanzheng, Z. Youlan, L. Zhengyi, C. Yuzhi, Mater. Sci. Eng A 291 (2000) 168–172.

[63] S.Y. Park, J.H. Kim, M.C. Kim, H.S. Song, C.G. Park, Surf. Coat. Technol 190 (2005) 357-365.

[64] X. Zhong, Y. Wang, Z. Xu, Y. Zhang, J. Zhang, X. Cao, Mater. Corros 60 (2009) 882-888.

[65] R. Vaßen, F. Traeger, D. Stöver, J. Thermal Spray Technol. 13 (2004) 396-404.

[66] R. Eriksson, Ph.D. thesis, High-temperature degradation of plasma sprayed thermal barrier coating systems, Linköping University, Linköping, Sweden (2011).

CHAPTER 6

PLASMA SPRAYED PARTIALLY STABILIZED ZIRCONIA COATING ON HIGH DENSITY GRAPHITE

Corrosion studies were performed on plasma sprayed partially stabilized zirconia (PSZ) coated high density (HD) graphite with NiCrAlY bond coat in molten LiCl-KCl eutectic salt at 873 K for periods of 250, 1000 and 2000 h under argon atmosphere. There is no significant attack and degradation of top PSZ coating in molten salt, however microcracks were observed at the bond coat-substrate interface after 2000 h of exposure. PSZ coated HD graphite exhibited excellent corrosion resistance in molten LiCl-KCl salt due to chemical stability and stable phases as confirmed from SEM and XRD studies. Laser Raman spectra (LRS) analysis of corrosion tested PSZ coating showed only tetragonal phase of zirconia irrespective of exposure time due to the absence of phase transformation even after 2000 h of exposure. However, reduction in the intensity of tetragonal phase as increasing upon exposure time was found from LRS mapping of molten salt exposed PSZ coating. Molten uranium interaction studies were carried out on the PSZ coated HD graphite by melting uranium metal at 1623 K using induction heating system. Microstructural analysis of PSZ coating by SEM, XRD and LRS after uranium melting demonstrated that PSZ did not form any significant reaction layers and products with molten uranium. Thermal cycling studies carried out at 873 and 1023 K up to 200 cycles did not show any failure of the coating. Segmented cracks were generated after 100 and 200 cycles at both the temperatures.

6.1 Introduction

High density (HD) graphite is proposed and sleeted as one of the candidate materials for various equipment in pyrochemical reprocessing plant (Chapter 1) for handling molten chloride salt as well as molten uranium at high temperature environment based on its corrosion behaviour as discussed in Chapter 4. Due to limited life of application as crucibles and liners, with the requirement of replacement and accumulation of solid waste, the use of HD graphite without coating becomes a critical issue as it will generate more solid waste. To avoid such circumstances, alumina-40wt% titania coating on HD graphite with and without bond coat attempted. The performance of alumina-40wt% titania coating was not up to the mark as discussed in Chapter 5. Hence it is necessary to select a ceramic coating meeting all f requirements and perform well without significant change in structure and property during service. Yttria stabilized zirconia (YSZ) is one of the internationally proved ceramic coating for high temperature molten salt applications [1]. Based on the international experience YSZ coating was chosen for current application for molten LiCl-KCl salt as well as for molten uranium with temperatures ranging from 773-1573 K. Zirconia and Yttria has stability in highly corrosive environments like Cl_2, O_2 and UO_2Cl_2+Cl_2 [2]. Partially stabilized zirconia (PSZ) with 8 wt % Y_2O_3 coating exhibited excellent thermal stability and maximum thermal cycle life [3]. The plasma spray process is an economical method for producing reproducible and durable thick PSZ coatings for molten salt applications [4]. Oxides are usually coated on graphite substrates by thermal spray process as mentioned in Chapter 5. The adhesion between oxides and graphite can be increased with suitable bond coat applied between them [5]. In the present investigation surface protection of HD graphite with PSZ coating as top coat and

NiCrAlY as bond coat was chosen because of excellent stability and corrosion resistance to molten salts [6-9].

Scanning electron microscopy (SEM) and X-ray diffraction (XRD) are the most common techniques used for characterization of corrosion tested YSZ coatings in molten LiCl-KCl salt. Laser Raman spectroscopy (LRS) is also an effective tool for studying the corrosion behaviour of YSZ coatings exposed to molten salt with respect to phase composition and stability [10,11]. Hamilton et al. [10] performed in-situ Raman study to understand the attack of YSZ by $Na_2V_2O_6$ molten salt and leaching of yttrium from the YSZ. Raman imaging is a powerful technique used for representation of Raman spectra information in a visual form that can be more easily understood [12]. Mayoral et al. [11] proposed Raman mapping as one of the wrathful techniques to detect the variation in the composition as well phase changes of the YSZ coating. Micro-Raman imaging studies were performed by Bowden et al. [13] to understand the stress induced phase transformation in MgO-stabilized zirconia ceramics; it was revealed that phase transformation will occur after indentation with a higher content of monoclinic phase at the grain boundary. Raman imaging was adapted to visualize the variation of phases present in the Raman spectra. There are a number of reports in the literature concerning Raman imaging studies on PSZ material/coatings to understand the mechanical behaviour after indentation processes [13-15]. Up to now, no study has been reported on the Raman microscopy and imaging of PSZ coatings exposed to molten LiCl-KCl salt. Hence, it was attempted to utilize Raman imaging technique for mapping of corrosion tested PSZ coatings to understand its corrosion behavior in detail.

Various coating materials were evaluated in order to achieve a durable coating which facilitate the ingot release, minimize contamination and loss of uranium metal for processing of molten uranium. The application of these materials including YSZ coating for uranium consolidation in cathode processor operation was already discussed in the literature review (Chapter 2). The processing steps involved in the pyroreprocessing are batch process. Therefore it necessary to study the effect of temperature gradient on coated structural material to understand the coating performance under such demanding conditions [16]. The plasma-sprayed ZrO_2-12 wt.% Y_2O_3 coatings subjected to thermal cycling at 1473 K with and without bond coats of Ni-Cr-Al-Zr in the atmosphere and the cracking behavior was correlated with acoustic emission technique data [17,18]. Joshi et al [19] studied extensively thermal cycling behaviour of YSZ coatings with the variation of following parameters: plasma arc current, spray distance, powder feed rate, coating thickness, bond coat material. Many groups/ researchers performed thermal cycling studies in air environment reported that oxidation of bond coat occurred at high temperatures due to the formation of thermally grown oxide (TGO) during thermal exposure at high temperature for a long time and the TGO grew further as the thermal cycles increased. This TGO growth is believed to play a crucial role to the life of the coating and induced the strain energy for the crack propagation during the spallation. The life of a thermal spray coating during furnace cycling greatly depends upon its microstructure [19]. Hence, studying the microstructure of the PSZ coating has great importance to understand the initiation of cracks and failure phenomenon of the coating. To our knowledge, no literature concerning the thermal cycling of NiCrAlY bond coat and top PSZ coating on HD graphite is available. In order to ascertain the performance of the coatings, coated substrates were subjected to repeat heating and cooling cycles. The failure mechanisms of the TBCs are different from that of the analysis of the present investigation and it cannot be comparable to that extent due to variation in testing environments and parameters. According to the specific requirement, the minimum number of thermal cycles required in order to pass the thermal cycling test is 200 cycles. Hence in the present thesis the thermal cycling test was carried up to 200 cycles.

The aim and objectives of this Chapter is to develop of PSZ coating on HD graphite and evaluation of coating performance under various conditions. This Chapter contains three sections related to the evaluation of PSZ coatings as: (1) Investigation of corrosion behaviuor in molten salt, (2) Compatibility with molten uranium and (3) Thermal cycling behavior up to 200 cycles.

6.2 Experimental

Different experiments were carried out to evaluate the performance of PSZ coatings in this Chapter (the detailed description about the testing and characterization techniques is provided in Chapter 3).

1. Deposition of PSZ coating on HD graphite by plasma spray process with NiCrAlY bond coat with optimized parameters and characterization with SEM-EDX, XRD and Raman spectroscopy techniques.
2. The corrosion studies were carried out on PSZ coated HD graphite in molten salt test assembly at 873 K for 500, 1000 and 2000 h by immersion in molten LiCl-KCl salt under ultra high pure (UHP) argon atmosphere. Corrosion tested PSZ coatings were characterization with visual examination, weight change and SEM-EDX, XRD and Raman spectroscopy techniques.
3. For in detailed understanding of corrosion performance of PSZ coating, Raman imaging studies were carried by Raman spectroscopy on all the exposed coatings.

4. Uranium metal melting experiments were carried out on PSZ coated HD graphite samples at 1623 K, after uranium melting the PSZ coatings were characterized with visual examination, SEM-EDX, XRD and Raman spectroscopy techniques.
5. The thermal cycling studies on PSZ coated HD graphite samples were conducted in an automated furnace at 873 and 1023 K under vacuum. Tested samples were characterized by weight loss, visual examination, SEM-EDX, XRD and Raman spectroscopy.

6.3 Results and Discussion

6.3.1 Corrosion behaviour in molten LiCl-KCl salt

6.3.1.1 Visual examination and weight change calculations

For comparing the corrosion behaviour of uncoated HD graphite with PSZ coated HD graphite, HD graphite samples were immersed in molten LiCl-KCl salt for 250, 1000 and 2000 h. Visual examination of uncoated HD graphite (Fig.6.1a) clearly showed the two distinct regions of molten salt immersion and vapour exposed regions compared to as-received graphite. Severe attack was observed at immersion region compared to the vapour exposed region. The attack was uniform throughout the immersion region.In case of PSZ coatings (Fig.6.1b) it can be seen two different regions of immersion and vapour exposed regions as compared to as-coated HD graphite. No detachment or thinning of the coating was observed in the immersion as well as in vapour exposed regions.

The weight change of the HD graphite and its PSZ coated specimens after the corrsion test in molten LiCl-KCl salt for various durations under UHP argon atmosphere was measured. The percentage weight loss of uncoated HD graphite for 250, 1000 and 2000 h were 0.033, 0.126 and 0.235 respectively. These results indicated that the weight loss (%)

increased linearly with increasing time of exposure. The PSZ coated HD graphite showed insignificant weight gain due to the presence of salt deposits over the surface. It can be inferred from the weight loss measurements that uncoated HD graphite suffered more corrosion attack, when compared to PSZ coated specimens. The weight change measurements revealed that PSZ coating perform very well in molten LiCl-KCl salt at 873K.

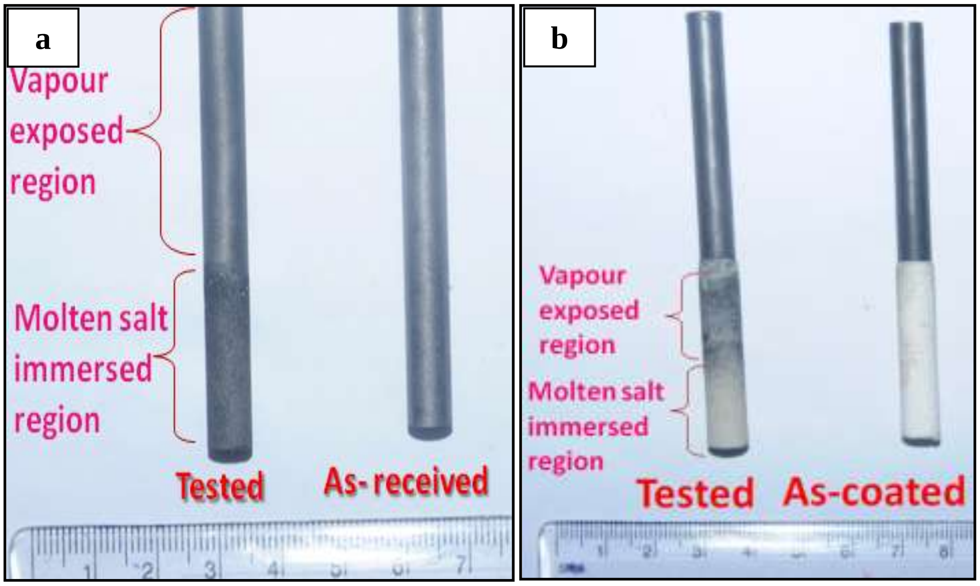

Fig. 6.1 Visual examination of (a) uncoated and (b) PSZ coated HD graphite rod samples before and after corrosion test in molten LiCl-KCl for 2000 h.

6.3.1.2 Surface morphology of immersion tested uncoated HD graphite

SEM micrographs of HD graphite under unexposed and exposed conditions are shown in Fig. 6.2. The increase of molten salt attack with time on HD graphite can be clearly seen from the SEM micrographs. The unexposed HD graphite surface contained pores and microcracks as shown in Fig. 6.2a. The surface morphology of 250 h exposed specimen showed lesser attack and initiation of graphite degradation was clearly seen in the micrograph (Fig. 6.2b) but the attack was significant in the case of 1000 h exposed (Fig. 6.2c) and was severe in 2000 h exposed specimens. The mechanism involved in the molten salt corrosion of graphite was explained in Chapter 4, section4.3.6. In the SEM image of 2000 h exposed sample (Fig. 6.2d) rough surface morphology was observed when compared to unexposed graphite. The graphite particles get dislodged from the surface into the molten salt as the salt have penetrated through the surface pores of the HD graphite [20].

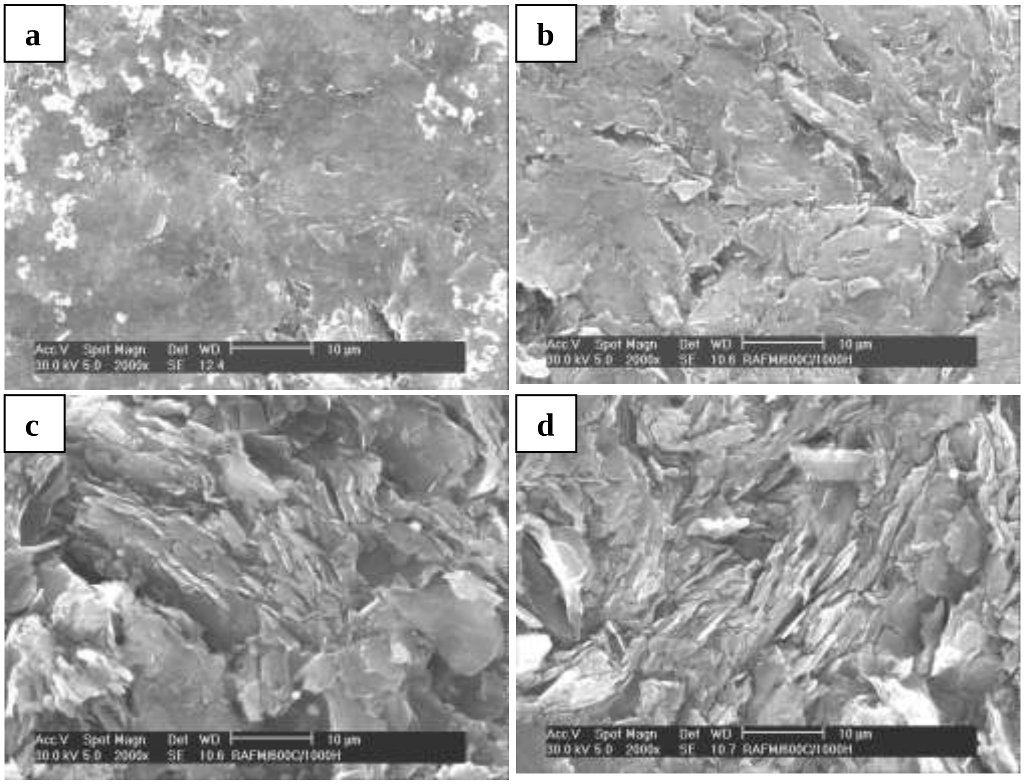

Fig. 6.2 SEM micrographs of as received and corrosion tested HD graphite in molten LiCl-KCl salt at 873 K (a) as received, (b) 250 h, (c) 1000 h and (d) 2000 h.

Hence, it can be inferred from the weight loss measurements and surface morphology results that graphite undergoes substantial attack in molten salt. Therefore with increase in time of exposure the carbon particles in graphite start to degrade, which caused material loss, grooves and cavities on the surface as shown in Fig. 6.2b-d. Throughout the exposed region uniform attack was found on the surface of HD graphite. The pores present in the unexposed graphite surface were more widened after corrosion test. Several oxidants and impurities present in the molten salts are responssible for accelerating the degradation of HD graphite in LiCl-KCl salt. Comparing the SEM micrographs of HD graphite, it was clear that porosity present in the unexposed graphite increased the weight loss with time of exposure to molten salt. The corrosion behaviour of HD graphite in molten salt suggested that protective coating was essential to avoid degradation in molten salt.

6.3.1.3 Surface morphology of immersion tested PSZ coated HD graphite

The surface morphology of as-sprayed coating (Fig.6.3a) exhibits typical splat morphology with pores, inter splat voids and microcracks. Figures 6.3b, c and d shows the surface morphology of PSZ coated HD graphite exposed to molten LiCl-KCl salt at 873 K for 250, 1000 and 2000 h respectively. Surface morphology of corrosion tested PSZ coating exposed for 2000 h in molten salt was similar to that of as-sprayed morphology. All the exposed samples exhibited the formation of dense outer layer and deposition of salt over the surface. It was observed that there was insignificant surface chages after corrosion testing in molten salt for 2000 h exposed coating (Fig. 6.3d). Comparing the surface morphology of corrosion tested YSZ coated on metallic substrate [6,7], it was clear that there was no significant degradation or changes in the surface morphology of YSZ top coat in both the cases. In general, the presence of impurities like moisture, water and oxygen present in the molten salts will accelerate the corrosion process by dissolution and leaching of the elements. Uniform corrosion, dissolution and leaching are the common form of molten salt corrosion among that selective leaching is very common form at high temperatures [21]. To identify the elemental composition of the coating; EDX spectra was collected on the 2000 h exposed top PSZ coatings as shown in Fig. 6.4. Although the intensity of Y peak was less, significant amount of yttrium was shown in the elemental composition. EDX spectrum of 2000 h exposed the coating (Fig. 6.4) showed Zr (61.89 wt%), O (28.32 wt%) and Y (9.78 wt%) elements similar to the as-sprayed coating. The presence of yttrium in the EDX analysis clearly indicated that no selective leaching and dissolution of yttrium occurred from coating into molten salt. This indicates that the absence of depletion of Y_2O_3 from PSZ in molten LiCl-KCl salt at 873 K.

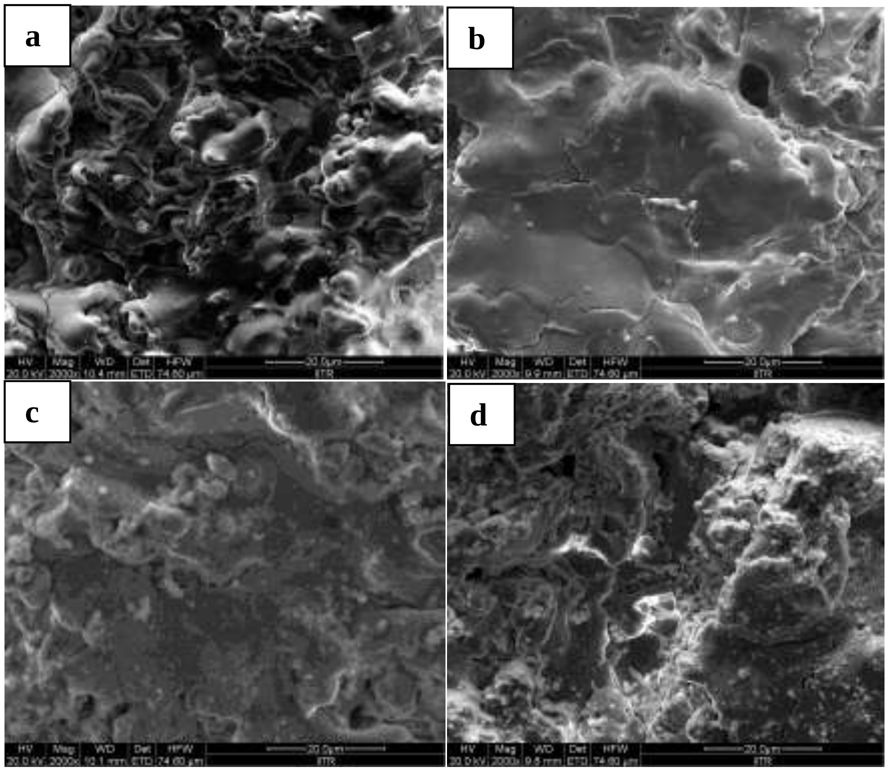

Fig. 6.3 Surface morphology of (a) as-sprayed and immersion tested PSZ coatings in molten LiCl–KCl salt at 873 K for (b) 250 h, (c) 1000 h and (d) 2000 h.

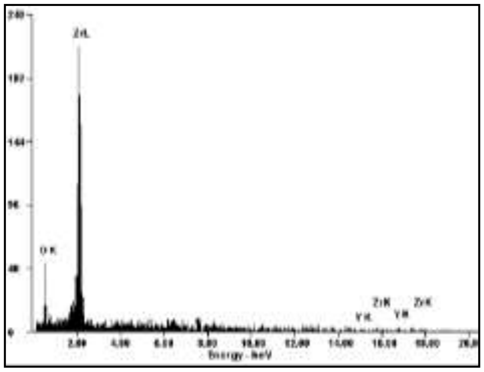

Fig. 6.4 EDX spectrum of PSZ coating after exposed to molten LiCl-KCl salt for 2000 h.

The possible reaction of ceramics with oxygen and chlorine containing salt was proposed by Haanappel et al. [22] as shown below:

$MO(s) + Cl_2(g) \rightarrow MCl_2(g) + \frac{1}{2}O_2(g) \rightarrow MO(s) + Cl_2(g)$ (Where M= Zr, Y) ……….. (1)

Oxides have better stability in chlorine environments and the standard Gibb's free enrgy change for the reaction of ZrO_2, Y_2O_3 with chlorine at 873 K is shown below [2]:

$\frac{1}{2}ZrO_2 + Cl_2(g) \rightarrow ZrCl_4(g) + \frac{1}{2}O_2(g)$ $\Delta G° = 79$ kJ/mol …………. (2)

$\frac{1}{3}Y_2O_3 + Cl_2(g) \rightarrow \frac{2}{3}YCl_3(g) + \frac{1}{2}O_2(g)$ $\Delta G° = 22$ kJ/mol ……….. (3)

These reactions clearly indicated that the YSZ has good stability. Various defects like pores, voids in between the splats, microcracks and thermal stresses were generated in the PSZ coatings (Fig. 6.3a) due to rapid solidification and shrinkage of ceramic particles during plasma spraying. Initially these microcracks and porosity present in the as-sprayed coatings act as penetration path for the molten salts. It was repoted that, the dense oxide layer formed on the surface during exposure would prevent further penetration of salt into the coating [8,9]. Thus the attack and dissolution of coating in molten salt has been prevented by the formation of protective dense layer on all the exposed surfaces. The present study revealed that PSZ coating exhibited better corrosion resistance in molten LiCl-KCl salt and provided superior protection to HD graphite.

6.3.1.4 Cross sectional morphologies of immersion tested PSZ coated HD graphite

Figure 6.5a shows the cross section of as-sprayed NiCrAlY bond coat followed by PSZ top coat on HD graphite. Top PSZ and bond coats exhibited laminar morphology, which is characteristic microstructural feature of plasma sprayed coatings. The bond coat generally improved the adhesion strength and coating integrity between top ceramic coat and substrate material [8]. X-ray elemental maps of as-sprayed coating shown in Fig. 6.5b clearly indicated that top coat mainly composed of ZrO_2 (Y_2O_3 stabilization) and the bond coat consisted of Ni, Cr, Al and Y. In order to understand the distribution of elements in the exposed coatings, EDX analysis was carried out on cross sections of 1000 and 2000 h samples.

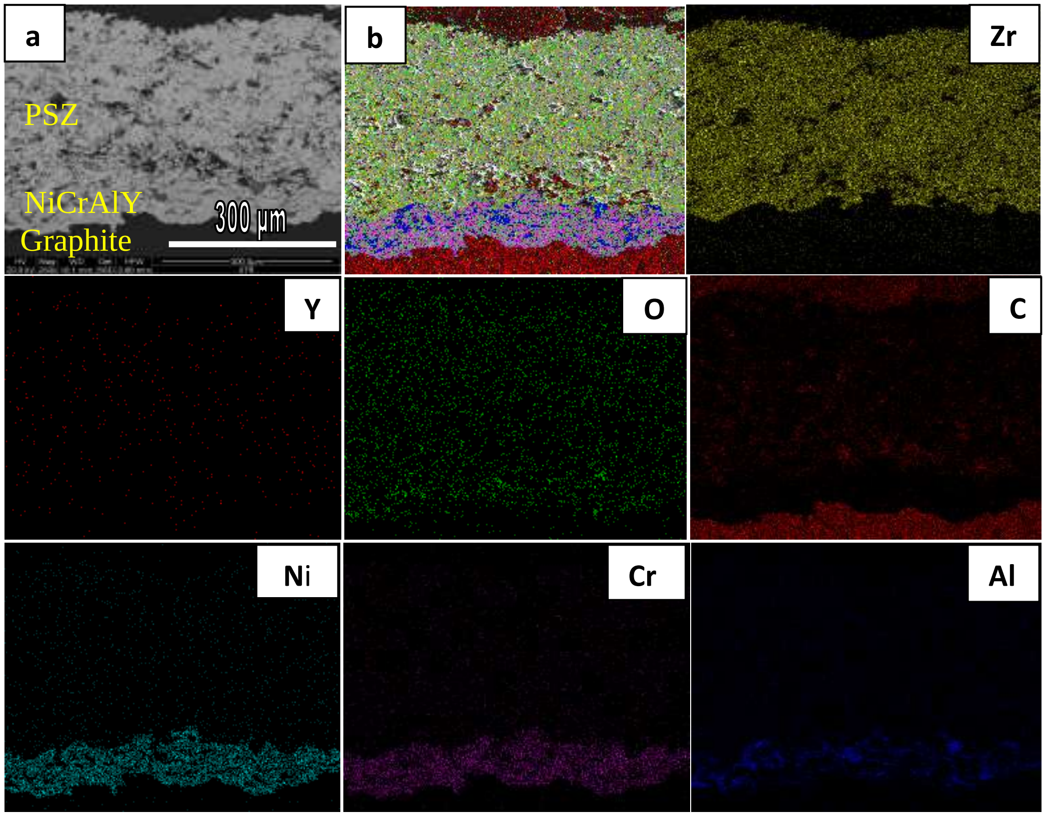

Fig. 6.5 (a) Cross sectional back scattered SEM images of as-sprayed PSZ coating on HD graphite and (b) X-ray elemental mapping of Zr, Y, O, C, Ni, Cr and Al.

The interfaces of PSZ/NiCrAlY and NiCrAlY/graphite were analysed by EDX line scans on 1000 (Fig. 6.6) and 2000 h (Fig. 6.7) exposed samples. The elements of Zr, O and Y were distributed in the top coating and, Ni, Cr, Al, Y were present in the bond coat even after the corrosion test for 1000 and 2000 h test in molten LiCl-KCl salt. But a variation in the distribution of elements in 2000 h exposed sample especially in the Cr and Al line profiles was observed (Fig. 6.7). Elements of metallic bond coat particularly Cr and Al were diffused into HD graphite substrate through pores on the substrate. Cross section SEM micrographs of immersion tested PSZ coated HD graphite after 1000 and 2000 h exposure in molten LiCl-KCl salt are shown in Fig .6.8. The top coat of PSZ showed few microcracks in 1000 (Fig. 6.8a) and 2000 h (Fig. 6.8b) exposed samples because of origin of stresses in the coating after exposure to molten salt [23]. Also in case of 2000 h exposed sample the bond coat was discontinuous along cross section and was merged with graphite substrate (Fig. 6.8b).

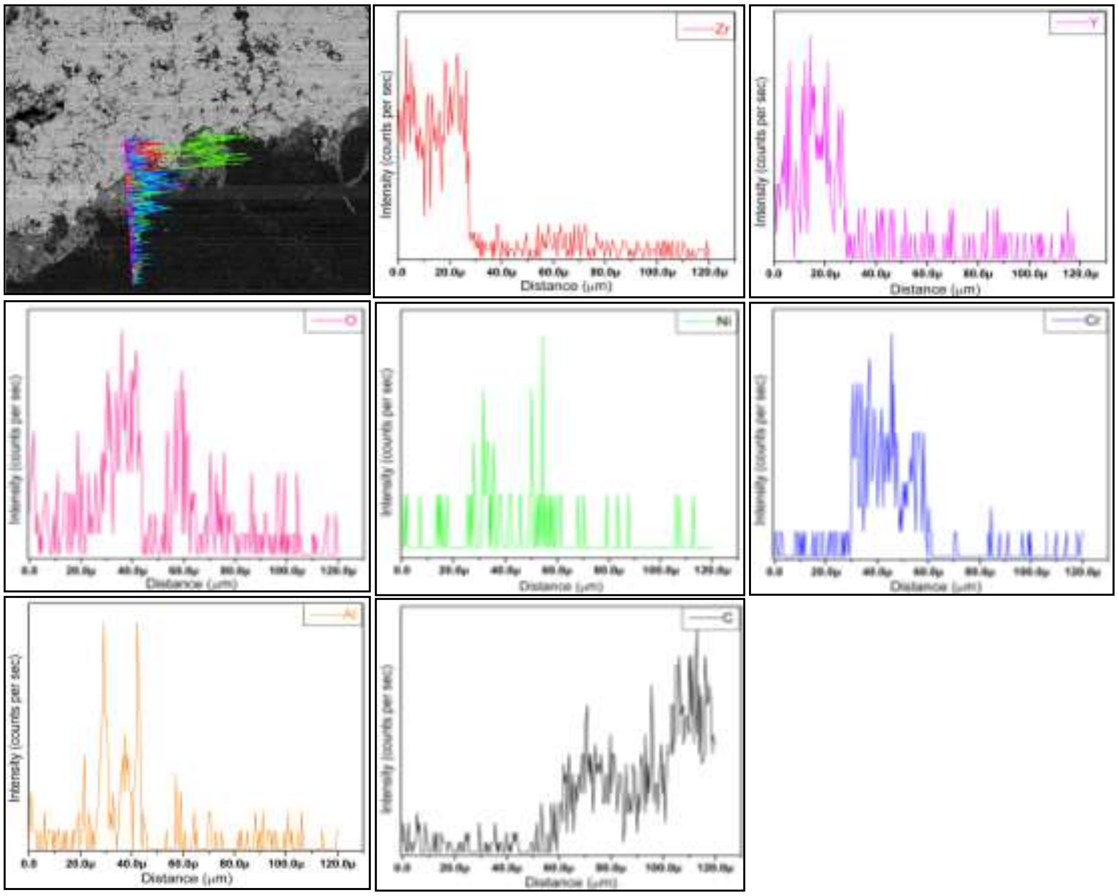

Fig. 6.6 Cross section of 1000 h exposed PSZ coated HD graphite with NiCrAlY bond coat and corresponding EDX line profiles of Zr, Y, O, Ni, Cr, Al and C elements.

The cross section micrographs does not show any degradation and penetration of salt through the PSZ coating cross section. However microcracks were identified at the interface of NiCrAlY/graphite and not at the NiCrAlY/PSZ interface. Formation of cracks in the coating was due to the development of stresses at the bond coat-graphite interface. The mismatch of thermal expansion coefficient between metallic bond coat and HD graphite lead to the development of such stresses at the interface [23]. But no spallation or peel off of coating was observed on HD graphite substrate even after 2000 h test in molten salt. Thus for further long term exposure to molten salt, PSZ coating on HD graphite with good bond coat is required to achieve good adhesion to the substrate.

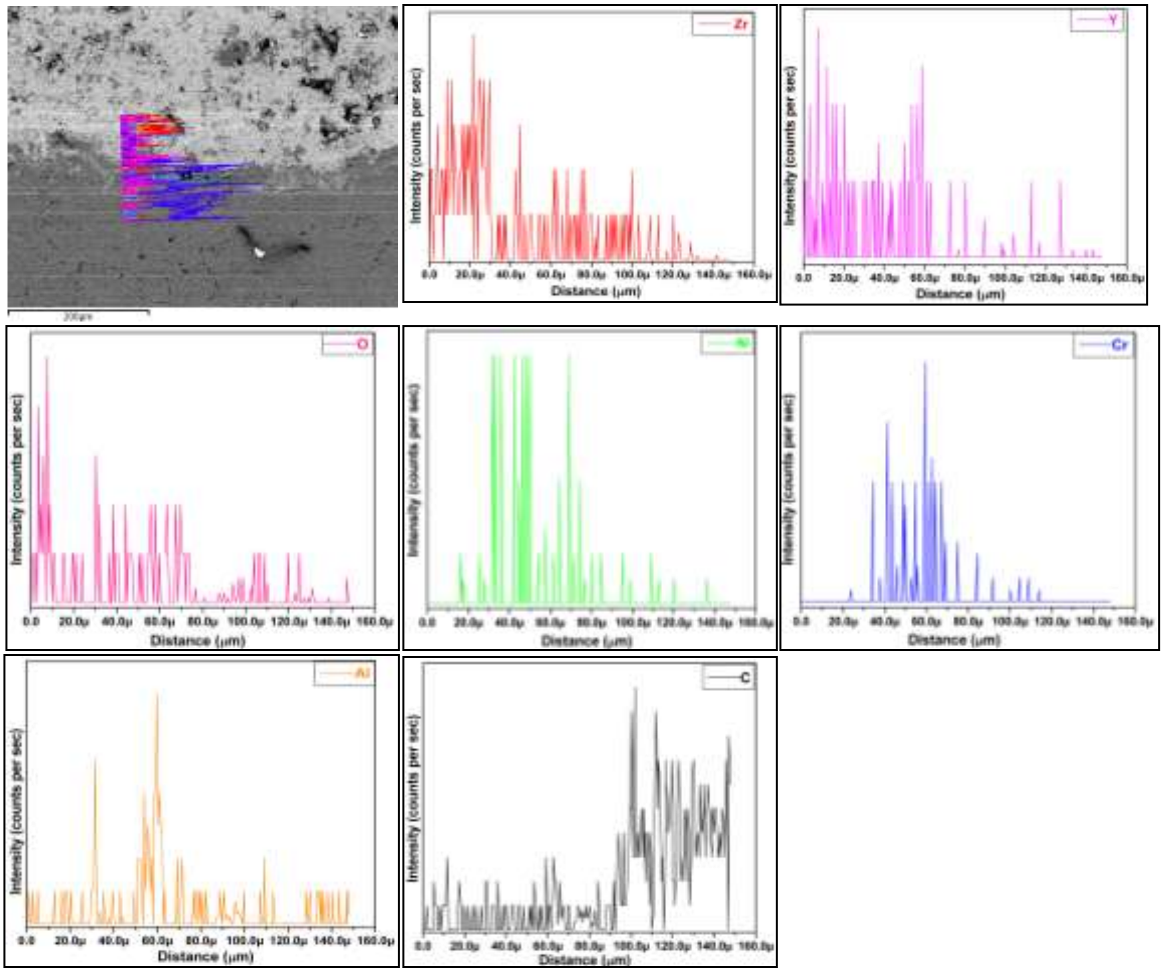

Fig. 6.7 **Cross section of 2000 h exposed PSZ coated HD graphite with NiCrAlY bond coat and corresponding EDX line profiles of Zr, Y, O, Ni, Cr, Al and C elements.**

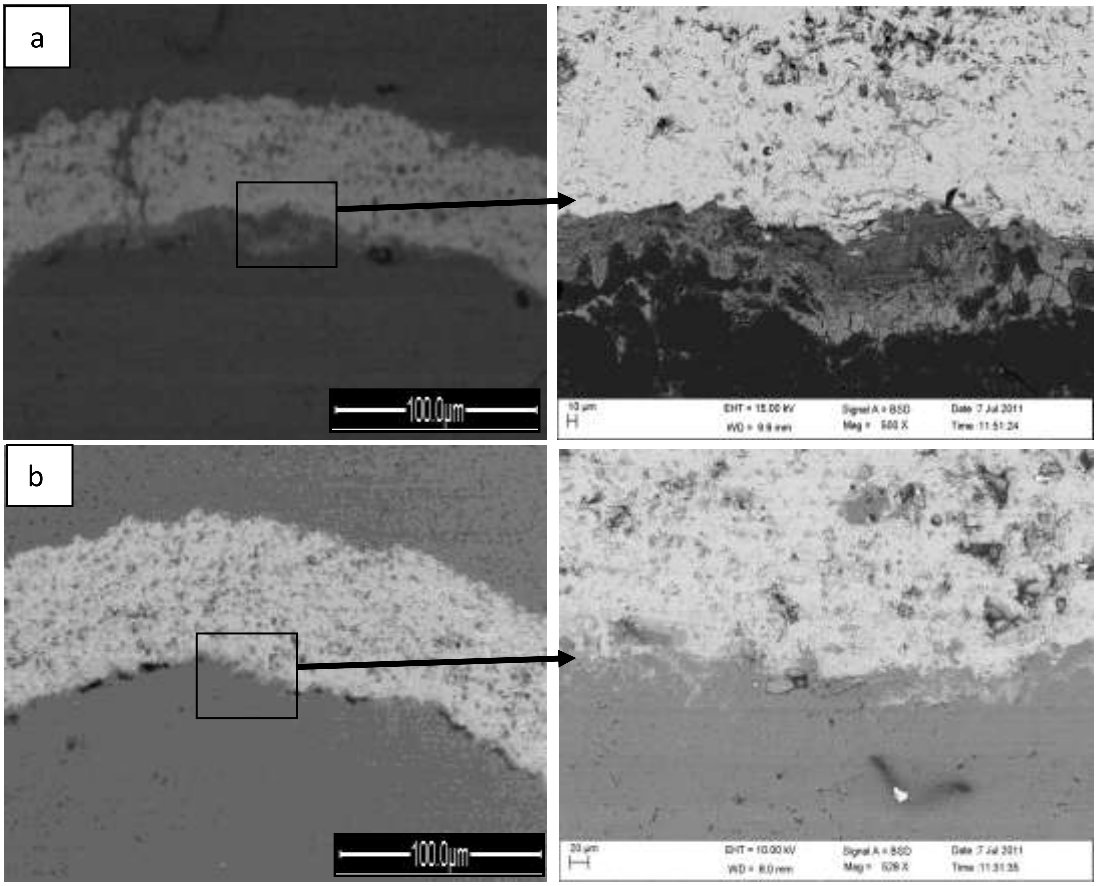

Fig. 6.8 Cross sections of corrosion tested PSZ coated HD graphite in molten LiCl–KCl salt at 873 K for (a) 1000 h and (b) 2000 h.

6.3.1.5 XRD studies on immersion tested PSZ coated HD graphite

XRD pattern of as-sprayed PSZ coating on HD graphite is shown in Fig. 6.9a. According to XRD results as-sprayed coatings consisted of tetragonal and cubic phases (Fig. 6.9a). In plasma sprayed PSZ coatings, zirconia transform to tetragonal modification (t´) phase in cubic fluorite matrix [24] due to rapid solidification of sprayed powders. This non transformable tetragonal phase has been responsible for excellent strength and crack toughness [3]. After molten salt corrosion, the XRD patterns of the surfaces of 250, 1000 and 2000 h samples are shown in Fig. 6.9b-d. No new phase corresponding to corrosion product was present in the coating after corrosion test for 2000 h indicating good chemical compatibility of PSZ coatings in molten LiCl-KCl salt. Corrosion studies performed in sodium metavanadate molten salts have reported phase transformation from cubic/tetragonal to monoclinic after corrosion test due to leaching of yttrium from the ceramic coating [24]. But no such phase transformation from tetragonal to monoclinic due to absence of leaching of yttrium was observed from XRD after corrosion test in the present study as shown in Fig. 6.9a-d. This result was supported by EDX analysis on the exposed PSZ coatings for 250, 1000 and 2000 h. The absence of corrosion products and phase transformations, clearly showed that YSZ on HD graphite was stable in molten LiCl-KCl salt.

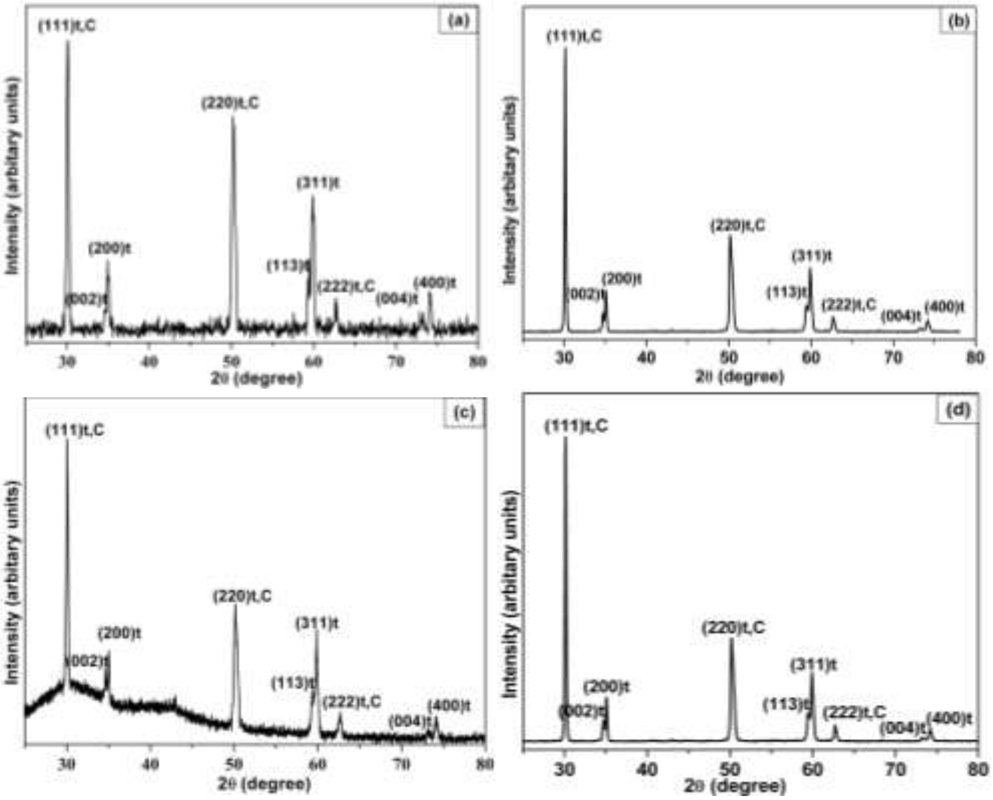

Fig. 6.9 XRD pattern of (a) as-sprayed, (b) 250 h, (c) 1000 h and (d) 2000 h corrosion tested PSZ coated HD graphite in LiCl-KCl salt.

6.3.1.6 Raman studies on immersion tested PSZ coated HD graphite

LRS is an effective tool for the characterization of YSZ coatings [10,11,25,26] to understand the attack of molten salt [10,24]. LRS is a useful tool to investigate the phase transformation in stabilized ZrO_2, because it determines the change in the bond length and the angle between the cation and anion [27]. Raman spectroscopy is one of the powerful techniques to identify phase changes in YSZ coatings exposed to highly aggressive environments [10]. Raman spectrum arises in YSZ mainly due to the polarizability associated with the oxygen ion vacancies produced by Y_2O_3 [28]. In the present investigation, LRS experiments were carried out on as-sprayed and corrosion tested PSZ coatings in molten LiCl-KCl salt at 873 K for 250, 1000 and 2000 h to identify the phase changes of PSZ coatings due to high sensitivity of Raman spectroscopy to these ceramics. The Raman spectra showed (Fig. 6.10) distinct peaks at 148, 250 and 638 cm^{-1} due to the presence of dominant tetragonal ZrO_2 phase [10,11]. In addition to that, weak peaks were obtained at 333 and 471 cm^{-1} which can be attributed to the tetragonal ZrO_2 phases. However, those peaks were shifted to a large wave number difference due to surface defects and heterogeneities. The designation of the modes according to Ref. [25] is as defined for PSZ with yttria system. Table 6.1 depicts the tentative assignments of the peaks seen in Raman spectra of as-sprayed and exposed PSZ coatings for 250, 1000 and 2000 h. One more observation was that all the Raman spectra were similar in terms of all spectral positions irrespective of the increase in exposure time to molten LiCl-KCl salt. Also, the peaks due to sp^2 carbon impurities were observed in all cases [29]. From Fig. 6.10, it was clear that Raman spectrum of as-sprayed coating was similar to that of corrosion tested samples and the phases present in the as-sprayed coating were still observed even after 2000 h at 873 K. The Raman spectra collected at different regions on corrosion tested PSZ coating revealed same spectral features as observed in Fig. 6.10. All the spectra contained tetragonal phase along with carbon impurities (Table 6.1), and no variation or change in spectral positions were observed.

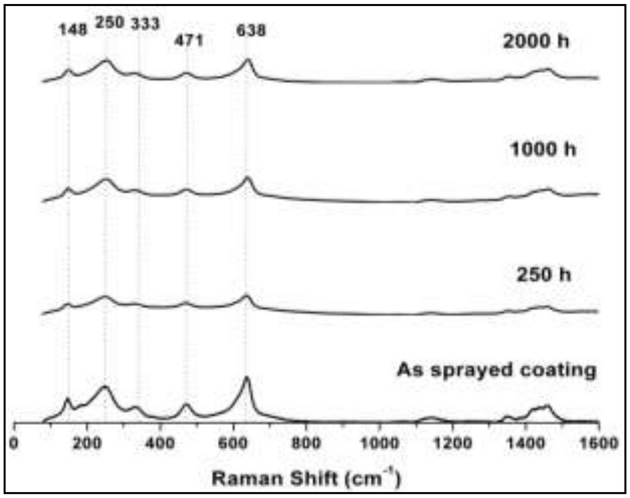

Fig. 6.10 Raman spectra of as-sprayed and corrosion tested PSZ coating over HD graphite for 250, 1000 and 2000 h in LiCl–KCl salt at 873 K.

The full width at half-maximum (FWHM) values of the Raman lines near 638 cm^{-1}of the characteristic peak of the tetragonal phase were measured to compare the structural disorder of the tetragonal phase in the as-sprayed coating to molten salt tested 1000 and 2000 h coatings. The FWHM of the Raman lines near 638 cm^{-1} in the as-sprayed coating is approximately 33.7 cm^{-1}; in the corrosion tested coatings were 33.8 and 34.9 cm^{-1} for 1000 and 2000 h exposed coatings respectively. The broadening of Raman line width indicated an increasing structural disorder of the tetragonal phase in the molten salt exposed coating [30]. The increase in FWHM was quite low (1.2 cm^{-1}) from as-sprayed to 2000 h exposed coatings and hence, much pronounced disorder was not observed in the tetragonal phase after exposure to molten LiCl-KCl salt. Stresses can also develop with time as a result of mechanical/physical property changes in the coating after exposure to aggressive molten salts

[23]. This microstructural feature was supported by a close observation of average Raman spectra of 2000 h exposed coating (Fig. 6.11) at 250 cm^{-1} which showed a shift in the peak position was due to the generation of stresses in the PSZ coating after exposure to molten salt.

Table 6.1 Raman peak assignments of as-sprayed and immersion tested PSZ coated on HD graphite specimens in molten LiCl-KCl salt for 250, 1000 and 2000 h.

Band (cm^{-1})	Assignments	Symmetry	Reference
148	tetragonal	E_g	[25]
250	tetragonal	E_g	[25]
333	tetragonal	A_g	[25]
471	tetragonal	B_g	[25]
638	tetragonal	B_g	[25]

From Raman analysis it was inferred that no phase transformation occurred even after exposure to corrosive molten LiCl-KCl salt environment, and that the top PSZ coatings exhibited excellent corrosion resistance towards molten LiCl-KCl salt.

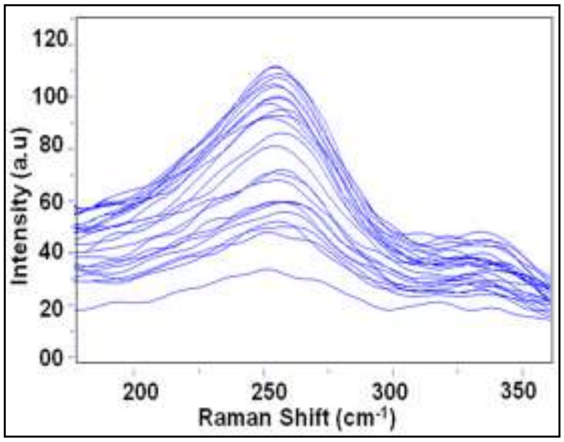

Fig. 6.11 Average Raman spectrum showing stresses distribution in PSZ coating exposed to molten LiCl-KCl salt for 2000 h.

6.3.1.7 Raman imaging/mapping studies on immersion tested PSZ coated HD graphite

Raman mapping was carried out on PSZ coatings after exposure to molten LiCl-KCl salt for 250, 1000 and 2000 h in order to understand in-depth the reason for disorder, microstructural and any phase change/variation information. The light microscopy images as shown in Fig. 6.12a, b and c represent the area of interest from which the average Raman spectra was collected. In Fig. 6.12 all three exposure time periods of PSZ coatings revealed tetragonal phase of zirconia only in the average Raman spectra. Single Raman spectra data was strongly supported by average Raman spectra. Generally, Raman map gives the intensity distributions of one particular spectral range from which the changes in the composition of a specific component can be determined. In the present study we selected 36 number of data points and hence the image obtained was coarse. Raman map represented the image distribution of one particular wave number range where as the light microscopic image depicts the distribution of all the components [31].

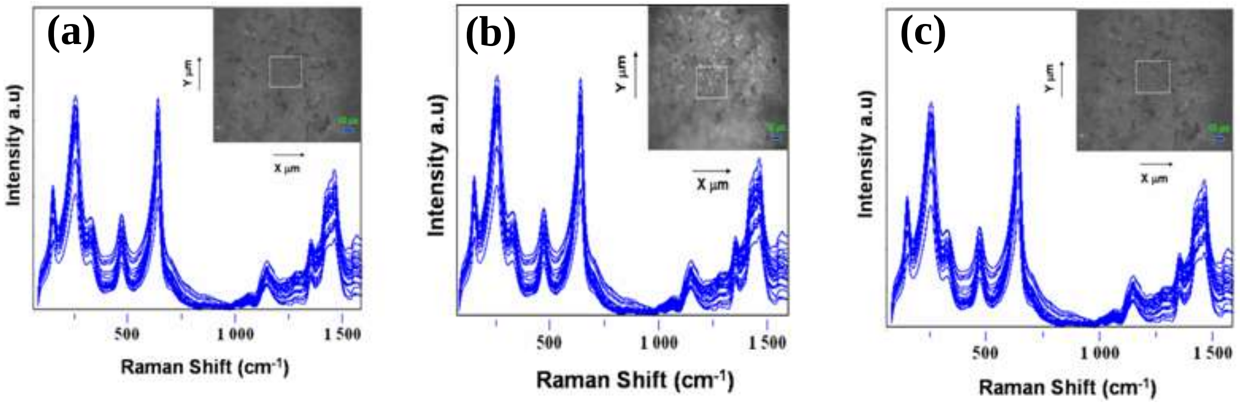

Fig. 6.12 Average Raman spectra and selected light microscopy area images of PSZ coatings after exposed to molten LiCl-KCl salt at 873 K for (a) 250, (b) 1000 and (c) 2000 h.

Raman maps were recorded from 131-167 cm^{-1} with a central peak position 150 cm^{-1} corresponds to tetragonal phase of zirconia [11]. The results of tetragonal Raman map at 150 cm^{-1} showed in Fig. 6.13b represents the change in the tetragonal phase with increasing the time of exposure to molten LiCl-KCl salt. As the exposure time increases molten LiCl-KCl salt created cracks, voids and pores in the PSZ coatings, and these features were indicated as white colour in the mapping images. The exposed PSZ coatings exhibited significant decrease in the intensity of tetragonal phase with increase in exposure time. The reduction in intensity is due to increase in microstructural inhomogeneities like cracks (Fig. 6.13a), voids, pores etc. Similar results have been recorded for Raman maps from 600-675cm^{-1} with a central peak position 638 cm^{-1} corresponding to tetragonal phase of zirconia as shown in Fig. 6.13c. The most important finding from Raman mapping was that average Raman spectra (Fig. 6.12) showed no phase other than tetragonal, however there was a change in the Raman imaging intensity of tetragonal phase from 250 to 2000 h (Figs. 6.13b and c). The molten LiCl-KCl salt exposure did create voids and cracks but did not favour leaching of yttrium leading to the formation of monoclinic phase. The decrease of tetragonal phase intensity in the Raman mapping was mainly due to the increase in the microstructural inhomogeneites as the exposure time increased from 250, 1000 and 2000 h as observed in SEM cross section images in Fig. 6.13a. These are represented as white colour region in the mapping results (Figs. 6.13b and c). Raman analysis in the present investigation was supported by XRD studies performed on YSZ coatings exposed to LiCl based molten salt at 600°C and their results revealed tetragonal phase only before and after corrosion test for different time period of exposure [8,9].

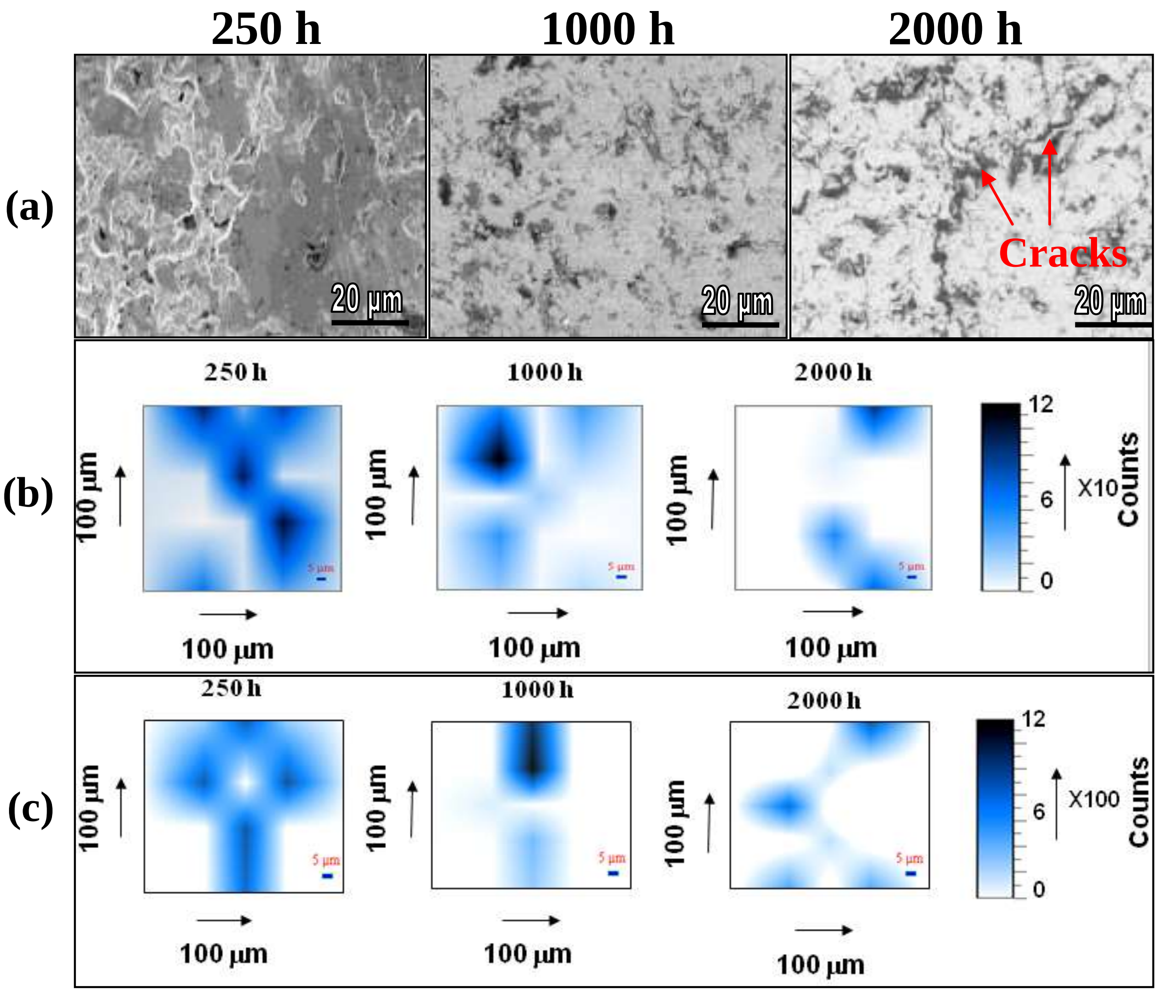

Fig. 6.13 (a) SEM micrographs on cross-section of exposed PSZ coating and Raman intensity mapping images corresponding to the (b) central peak position at 150 cm^{-1} and (c) at 638 cm^{-1} of PSZ coating tested in molten LiCl-KCl salt at 873 K for 250, 1000 and 2000 h. In Raman image, the coloured regions indicate the intensity of tetragonal phase and the white colour regions indicates the micro-cracks, voids and pores created regions and also carbon impurity.

6.3.2 Uranium melting

6.3.2.1 Compatibility studies based on Gibbs free energy and visual examination

Towards the chemical reactivity of molten uranium with the coating materials, the Gibbs free energy change (ΔG_R) was calculated using Factsage® version 6 software for the following reactions in the temperature range 300 - 2000 K.

$ZrO_2 + U \rightarrow UO_2 + Zr$ (4)

$Y_2O_3 + 1.5\ U \rightarrow 1.5\ UO_2 + 2Y$ (5)

ΔG_R values computed for the reactions (4) and (5) are plotted as a function of temperature in Fig. 6.14. The thermodynamic stability of the PSZ coating with respect to molten uranium can be ascertained from the values of Gibbs free energy change for the formation of all probable binary compounds from the constituents of coating materials and molten uranium in the temperature range of investigation. Figure 6.14 shows that the reaction between ZrO_2 and U is not feasible in the temperature range 300 to 2000 K as the value of Gibbs free energy change for reaction (4) is positive. The Gibbs free energy change for the reaction of Y_2O_3 with uranium is more positive than the values for the reaction (4). In temperature range of 300 - 2000 K, the Gibbs free energy change for these reactions (4) and (5) are positive and hence, the stability domain of YSZ showed lie within the ΔG_R - T plots between ZrO_2 and Y_2O_3 in Fig. 2, revealing that uranium will not react with YSZ. This fact is corroborated by the results reported in the literature that ZrO_2 and Y_2O_3 are chemically inert against the attack by uranium [32-34]. Thus, it is expected that coating of YSZ on graphite crucibles would eliminate the problem of interaction of molten U with the graphite container [32].

Figure 6.15 shows the pictures of PSZ coating on HD graphite before and after uranium melting experiments. Visual examination as-sprayed PSZ coating showed the change in colour from white to black after uranium melting. The region where uranium was melted could be identified on coating surface.

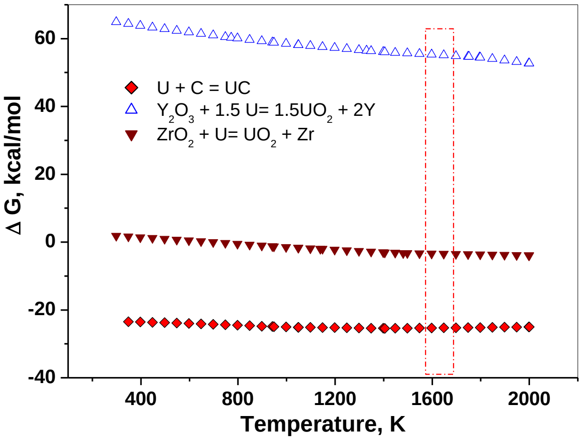

Fig. 6.14 Gibbs free energy change of possible chemical reactions as a function of temperature.

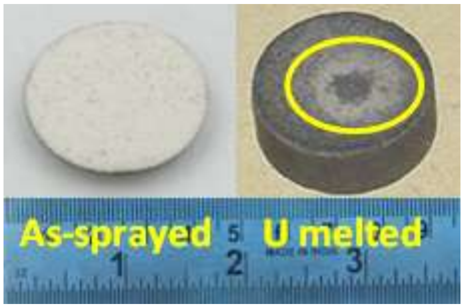

Fig. 6.15 Pictures of as-coated and double run uranium melted PSZ coating on HD graphite.

6.3.2.2 Morphology of uranium melted PSZ coatings

Figure 6.16a shows the surface features of a typical plasma sprayed PSZ coating. The splat morphology continued to be present in the PSZ coating after single uranium melting (Fig. 6.16b). After the second time uranium melting no reactive layer of uranium was formed on PSZ coated surface (Fig. 6.16c) due to the absence of reaction between U and PSZ. However, microcracks were generated on the surface of PSZ coating (Fig. 6.16d) due to rapid heating of PSZ coating and cooling to room temperature. Stresses can be generated in the microstructure (Fig. 6.16a) owing to the contraction of individual splats formed during rapid cooling (10^6-10^8 K/s) and resolidification on the colder substrate; or on a layer of previously solidified splats and these are called as ‘quenching stresses’ [35,36]. These stresses have strong influence on the microstructure and performance of coatings. Stresses were relaxed by forming microcracks in the coating due to the high heating rate of 90°C/min.

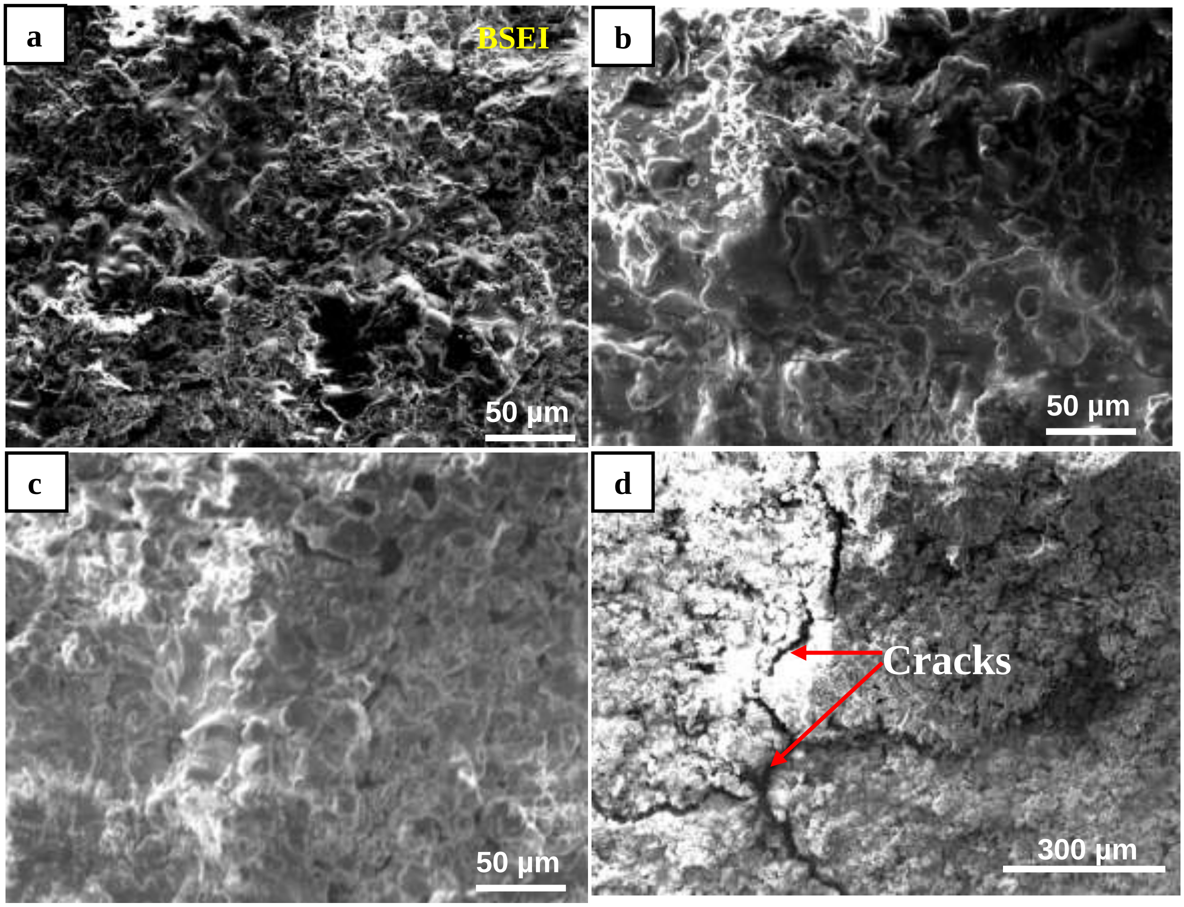

Fig. 6.16 Surface morphology of PSZ coating: (a) as-sprayed (BSEI), (b) single run and (c and d) double run uranium melted coatings.

Elemental analysis carried out by EDX (Fig. 6.17a) on selected regions of uranium melted coating (Fig. 6.17b) showed the presence of only coating elements Zr (67.41 wt %), Y (09.71 wt %) and O (22.88 wt %). Elemental peak of U was not identified on the tested coatings and the uranium (00.00 wt %) concentration is below the detection limits.

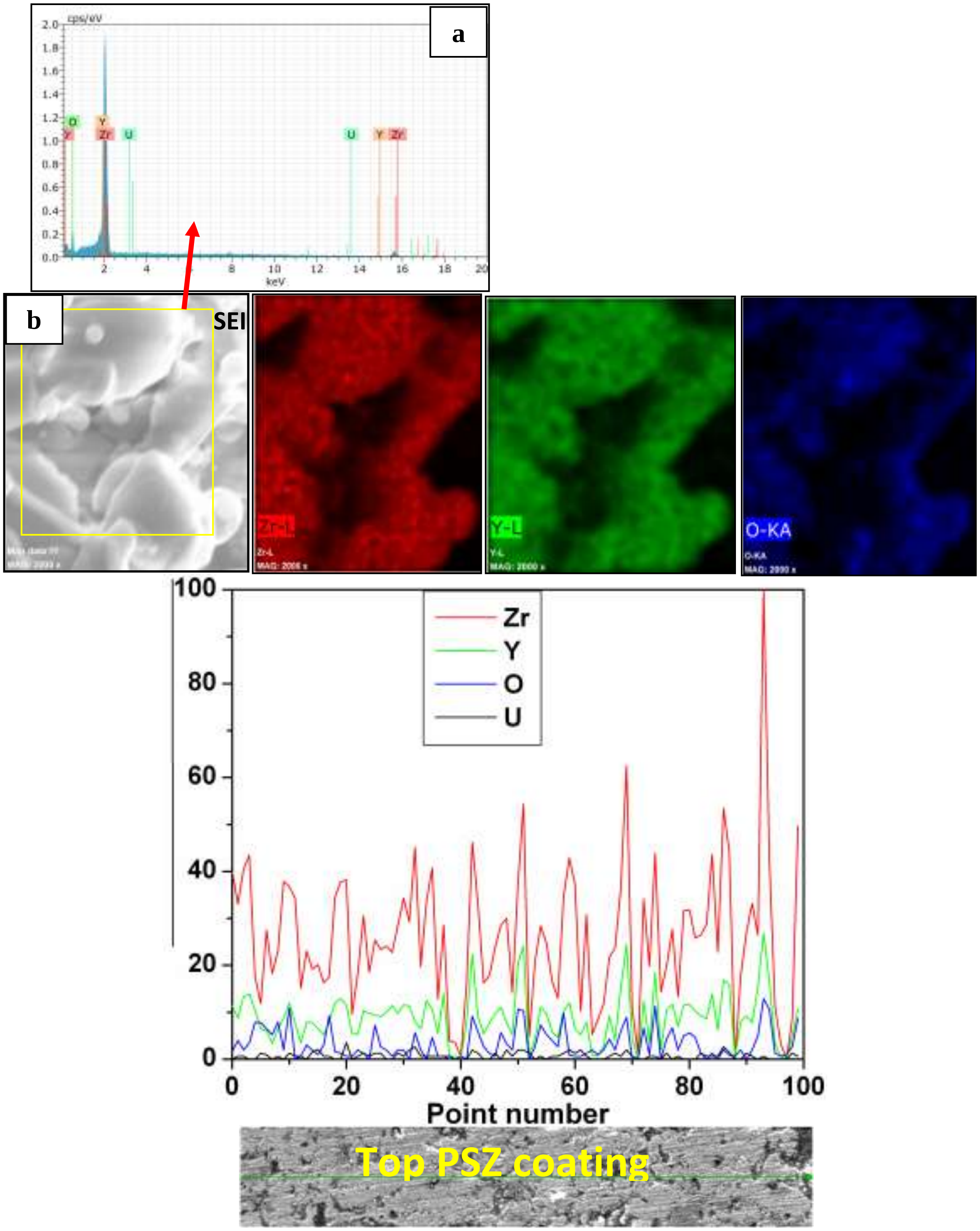

Fig. 6.17 (a) EDX spectrum of second time uranium melted PSZ coating surface of (b) selected area and corresponding EDX elemental mapping of Zr, Y and O and (c) line scan on the surface.

The evidence of absence of reaction between molten uranium and PSZ was further confirmed by X-ray elemental maps and lines scans on the surface of two times uranium melted coating. The elemental mapping of Zr, Y and O clearly showed the distribution of coating elements on the surface of PSZ coating after uranium melting. Black regions in the mapping images are unfocused regions due to surface irregularities and hence, no element was identified.

Figure 6.17c shows the line scans for different elements of coating along the top PSZ surface which clearly demonstrated that the uranium concentration was below the detection limits. The change in the signal intensity was possibly due to surface roughness. Even though uranium melting was performed with high heating rate no significant detachment of PSZ coating was observed from HD graphite after uranium melting experiments as could be seen in Figs. 6.18 and 6.19. Cross sectional micrograph of single time uranium melted PSZ coating in the secondary electron image (SEI) exhibited similar morphological features of as-sprayed coating like laminar morphology and pores on the top PSZ coating. Microcracks were not observed at the interfaces (Figs. 6.18b and 6.19) of PSZ/NiCrAlY and NiCrAlY/graphite after testing. But microcrcaks were observed within the ceramic coating due to relieved tensile stresses usually formed in the YSZ coating during the operation at high temperature. Extensive analysis was carried out along the cross-section of PSZ coated HD graphite to identify any diffusion or penetration of molten uranium and also morphological variations across the thickness of the coating and the results are presented in Figs. 6.18b, 6.19 and 6.20. X-ray elemental mapping (Figs. 6.18b and 6.19) was obtained on the cross section of SEI to find out variations in elemental composition after single uranium melting. It is evident from the results that the Ni, Cr, Al and Y were still present in the bond coat region and top coat comprised the elements Zr, Y and O. Line profiles and elemental mapping showed low intensity for Al and Y bond coat elements due to the low weight percentage of these two elements in the initial spray powder. From the line scan (Fig. 6.20) along the cross section of second time melted coating uranium concentration was found negligible in the PSZ coating on HD graphite (below the detection limits). This analysis was supported the EDX elemental mapping (Fig. 6.17b) and line scan (Fig. 6.17c) of the surface of PSZ after uranium melting. It was observed from the cross section micrographs of uranium melted PSZ coatings (Figs. 6.18, 6.19 and 6.20) that uranium has not penetrated through the pores on the surface. It was reported that penetration of liquid uranium into these pores was dependent on the surface tension and the contact angle [33]. Absence of reaction between uranium and PSZ in the EDX elemental mapping of uranium melted surface and cross section validated the discussion on the compatibility of U with PSZ based on Gibb’s free energy change as discussed in Section 6.3.2.1. Based on the results obtained in the presented work plasma sprayed PSZ is found compatible with molten uranium at 1623 K.

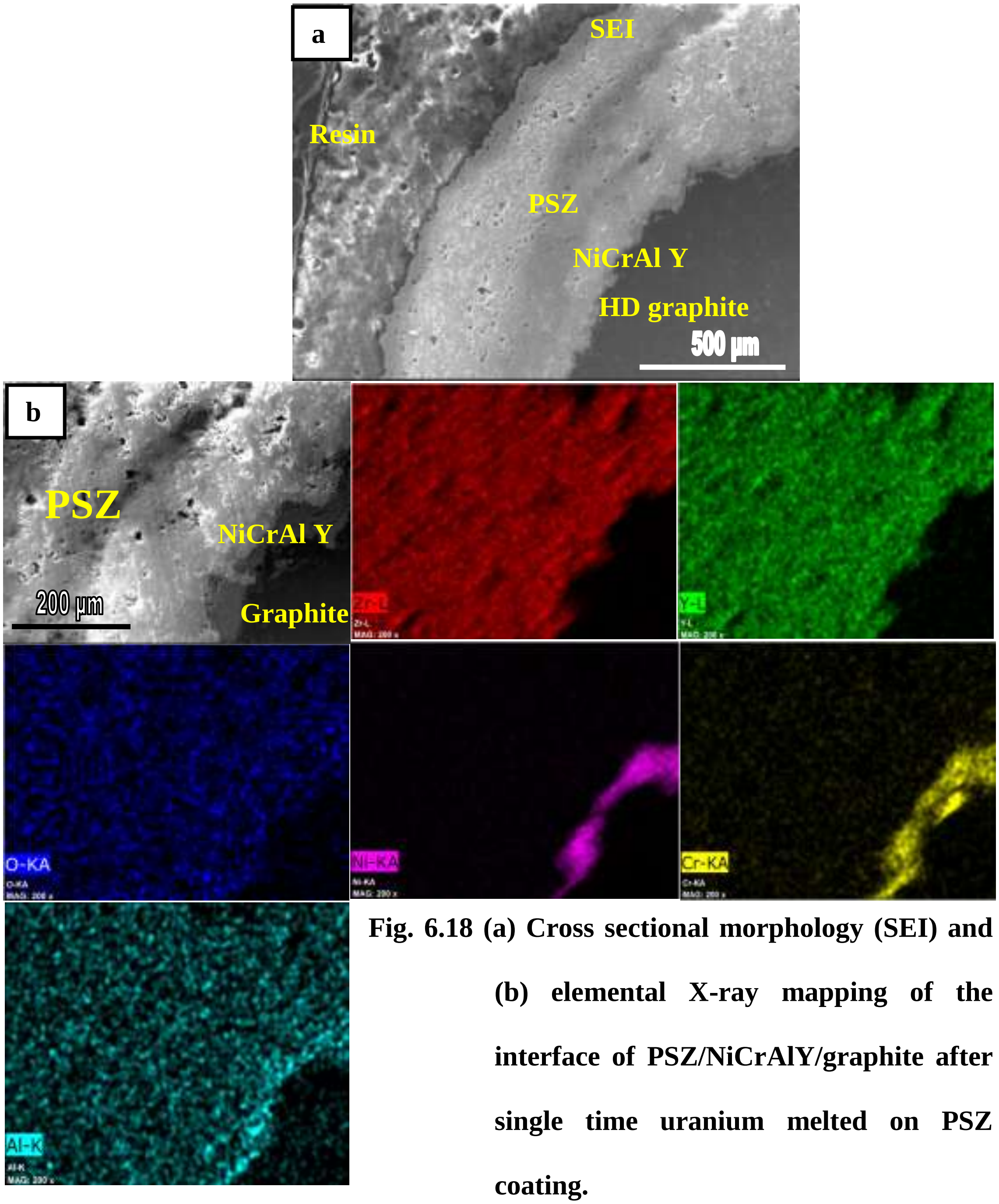

Fig. 6.18 (a) Cross sectional morphology (SEI) and (b) elemental X-ray mapping of the interface of PSZ/NiCrAlY/graphite after single time uranium melted on PSZ coating.

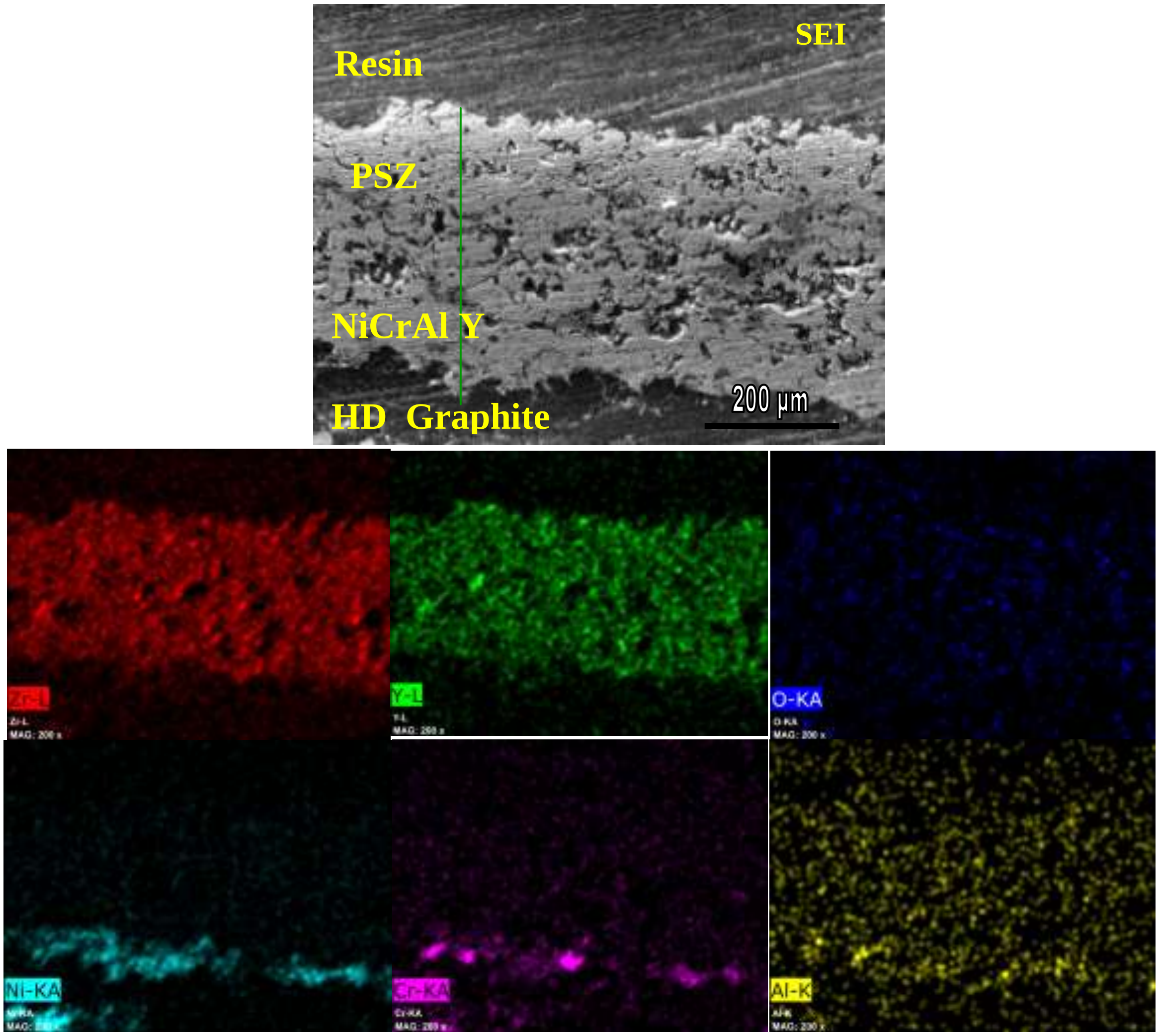

Fig. 6.19 Cross sectional morphology (SEI) and elemental X-ray mapping of the cross-section of PSZ coated HD graphite with NiCrAlY bond coating after second time uranium melting.

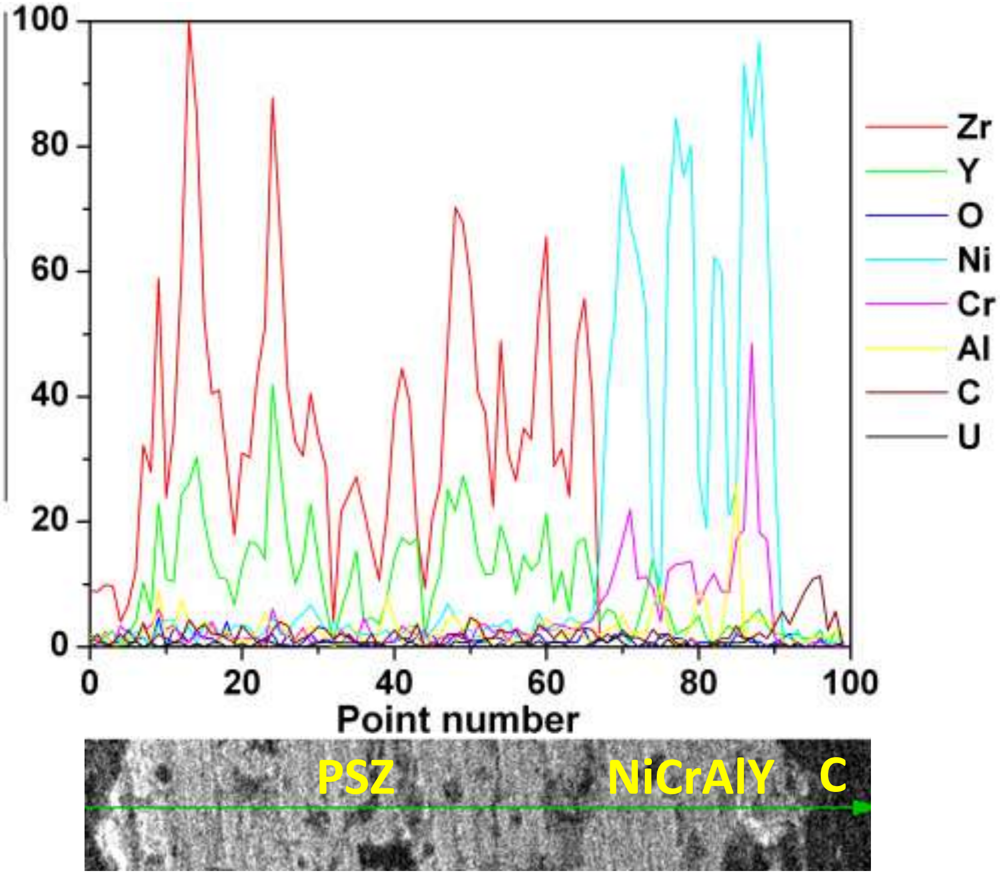

Fig. 6.20 Line scans of the cross-section of PSZ/NiCrAlY/graphite interface after second time uranium melting.

6.3.2.3 Phase analysis of uranium melted PSZ coatings

Figure 6.21a shows the XRD pattern of PSZ coating before and after uranium melting. Uranium melted PSZ coatings exhibited same crystallographic phases of as-sprayed coating. The existence of t´-form of tetragonal phase is too difficult to distinguish from the cubic phase by XRD analysis [37]. As per the phase diagram information on ZrO_2-Y_2O_3 system, in the temperature (1623 K) of interest in the present investigation of uranium melting the co-existence of non-transformable tetragonal (t´) and cubic phases in the plasma sprayed 8 wt% yttria doped zirconia was evident [38]. The predominance of the t´ phase in the coatings would be highly beneficial because of its high temperature stability and strength. The absence of any reaction product on the surface of PSZ coating after second uranium melting was confirmed by XRD analysis. It was reported that YSZ coatings were stable up to maximum temperature 1573 K in normal atmosphere. In the present study the melting was carried out in UHP argon atmosphere. Hence, there was no interaction of molten uranium with oxygen to form any compounds and inducing any phase change in the coating.

Raman spectra (Fig. 6.21b) of as-coated and uranium melted PSZ coatings showed tetragonal phase peaks only and these were designated according to the modes assigned in the literature [25]. The designation of peaks in the Raman spectra of PSZ coatings are listed in Table 1. In the tetragonal phase of zirconia each Zr atom is surrounded by eight oxygen atoms, four of which form an elongated tetrahedron and the remaining four a flattened tetrahedron. Upon exposure to high temperatures or molten salts or any aggressive media, there is a possibility of change in the Zr–O bond length and bond angle in PSZ and this brings out a change in the Raman active mode [28]. Unlike the XRD analysis of the phases in the PSZ, Raman spectroscopy showed only peaks corresponding to tetragonal phase because tetragonal phase modes are more active than the cubic phase in the chosen composition of PSZ (i.e. Y_2O_3 8 wt % in ZrO_2). The nature of the peaks and their position were found similar for as-coated and tested PSZ coatings. All the characteristic peaks of as-coated PSZ were also found to be present in the spectrum of uranium melted PSZ coating, though the peaks were marginally shifted by a few wave numbers and were more or less sharp as compared to that of the as-coated PSZ. This is due to generation and relaxation of stresses in the uranium melted PSZ coating during testing. This observation is in conformity with the SEM analysis (Fig. 6.16d) of uranium melted PSZ coating. Phase identification by XRD and Raman analysis on uranium melted PSZ coatings confirmed that the PSZ coating was intact without any phase change or formation of any corrosion/reaction product.

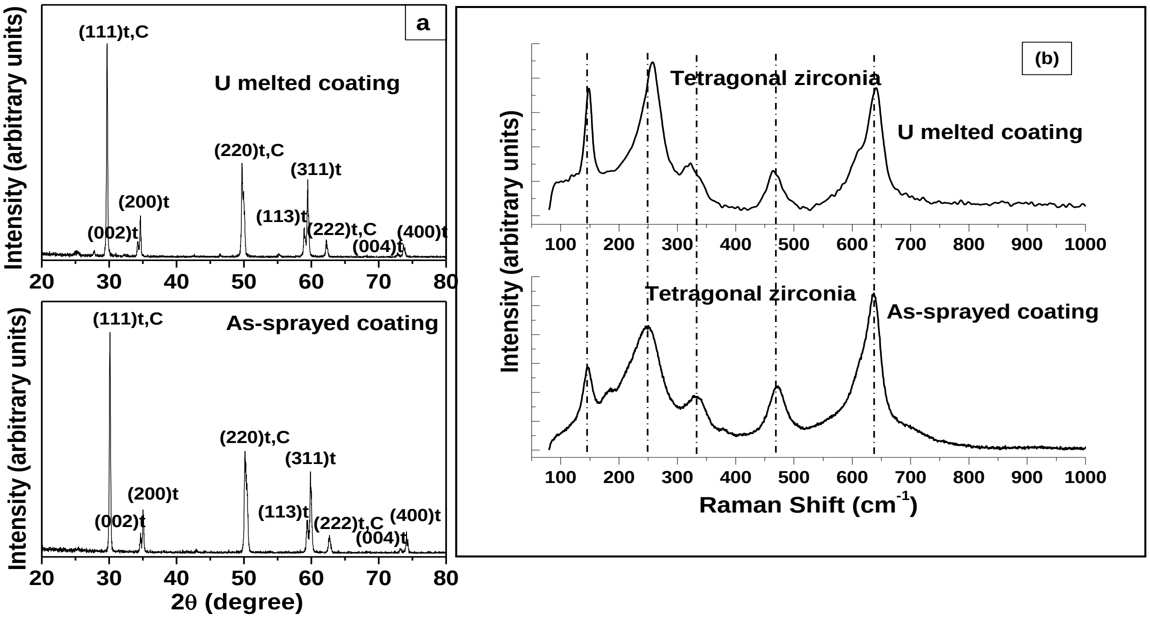

Fig. 6.21 (a) XRD pattern and (b) Raman spectra of as-sprayed and uranium melted PSZ coatings.

6.3.3 Thermal cycling studies

6.3.3.1 Porosity and visual examination

Plasma-sprayed coatings usually contain up to 10 % porosity. Optical micrograph of cross-section of PSZ coated HD graphite is shown in Fig. 6.22. The microstructure clearly distinguishes the laminar morphology of bond coat, top coat regions and top coat contained some level of porosity. Area percentage porosity measured by according to the ASTM E 2109-procedure A [39] indicated that the porosity of the top PSZ coating is around 10%. Porosity was an important parameter which determines various properties of coatings like thermal shock and thermal cycling resistance [40].

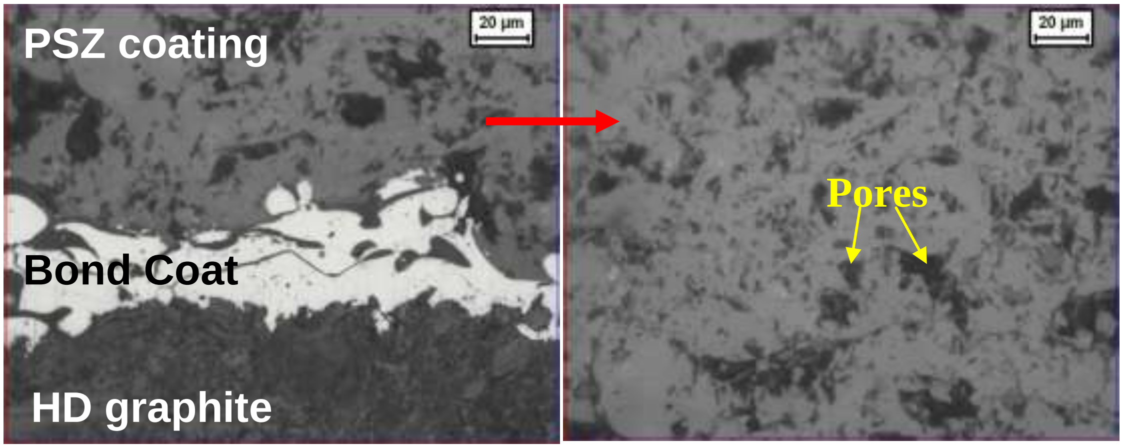

Fig. 6.22 Optical micrograph of as-coated cross section and top PSZ coating morphology for porosity measurement.

After thermal cycling the PSZ coating samples were visually examined to identify the surface changes and coating spallation and to identify the crack initiation and failure of the coating. Table 2 shows a photograph of PSZ coated HD graphite samples after thermal cycling for 50, 100 and 200 cycles at 873 and 1023 K. The visual examination of thermal cycled PSZ coating after 50 cycles at 873 and 1023 K coating turns to light dark colour, after 100 cycles the coating color changed to black color at both the temperatures. However, at 1023 K coating was blacker than the 873 K tested PSZ coating. It is well known that degassing occurs in graphite at high temperatures in very low P_{O_2} (vacuum) environment. As thermal cycling studies were performed in static vacuum, vapour of graphite would have deposited over YSZ coating and darkened its colour. It is also reported in literature that the colour of YSZ changes owing to loss of oxygen in YSZ in low oxygen and high temperature environments. Partially stabilized zirconia (PSZ) powder was used for top YSZ coating. In PSZ, the tetragonal phase of ZrO_2 is stabilized by the addition of 7-8 Y_2O_3 (by weight). As oxide ion vacancies already exist in PSZ, loss of very low quantity of oxygen is not expected to bring any deleterious effect. Nevertheless, YSZ coated graphite will be employed for applications in ultra high pure argon atmosphere and the problem of oxygen loss will not arise. Visually no macrocracking was observed on any of the PSZ coating surfaces tested up to 200 cycles.

Table 6.2 Visual examination of thermal cycled PSZ coated HD graphite at 873 and 1023 K for 50, 100 and 200 cycles.

Cycles ↓	Temperature	
	873 K	**1023 K**
50 cycles	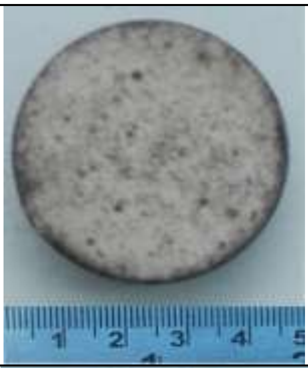	
100 cycles		
200 cycles		

6.3.3.2 Weight loss studies thermal cycled PSZ coating

The percentage of weight loss of PSZ coating plotted as a function of thermal cycles is shown in Fig. 6.23. The weight loss was calculated after 50, 100 and 200 cycles at two different temperatures of 873 and 1023 K. From Fig. 6.23 it was clear that as the number of cycles increased the weight loss of the coating was increased at both the temperatures. The weight loss observed owing to the loss of coating material during thermal cycling; however, the weight loss was not due to the failure of the coating.

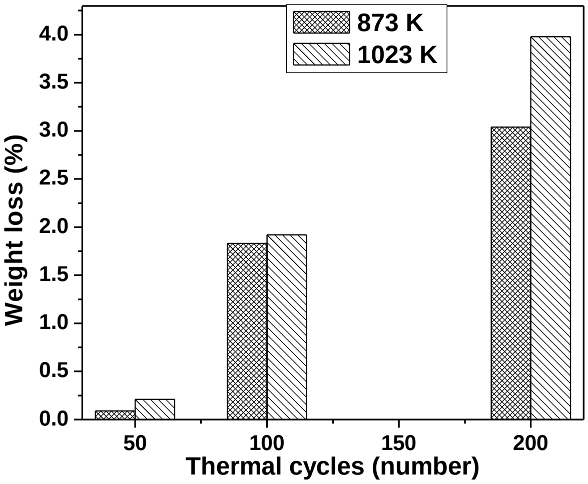

Fig. 6.23 Weight loss (%) of thermal cycled PSZ coated HD graphite.

6.3.3.3 Morphology of thermal cycled PSZ coatings

The as-sprayed PSZ coating surface morphology consists of splats, microcracks, voids between splats, unmelted oxides etc. (Fig. 6.24a). The morphology of the as-sprayed coating contain splat structures and splat is the ‘brick’ for the buildup of the deposit of coating [41]. These micro defects are common in plasma sprayed coatings due to the characteristics of process of deposition and they play significant role in determining the life or durability of the coatings when subjected to thermal cycling or thermal fatigue. According to Berndt et al. [17]

the failure mechanisms of plasma-sprayed TBCs are a complex function of imperfections contained within the oxide coating and at the interfacial region and the means by which these imperfections respond to thermal cycling. All failure mechanisms of the thermal cycled coatings are affected by the microstructures of the coating [42].

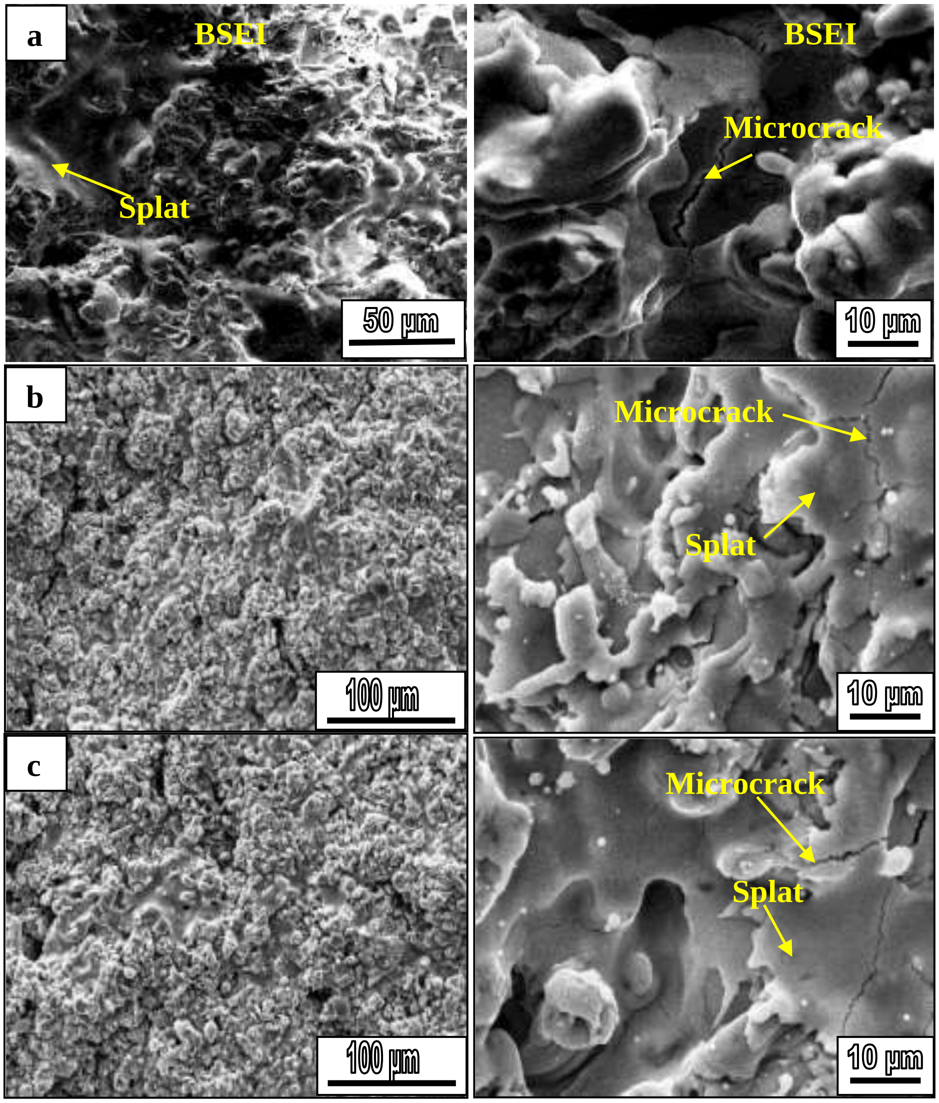

Fig. 6.24 Surface morphologies of PSZ coating: (a) BSEI of as-sprayed and after 50 cycles (b) at 873 and (c) 1023 K.

The variations in the microstructure lead to the spallation or detachment of the coating from the substrate. Hence, the microstructure of the thermal cycled PSZ coatings were studied in detail with possible characterization techniques.

The surface morphologies of thermal cycled PSZ coatings after 50, 100 and 200 cycles at 873 and 1023 K is shown in Figs. 6.24, 6.25 and 6.26 respectively. After 50 thermal cycles at 873 and 1023 K the surface morphology of PSZ coating did not show marked effect and microcracks were present between the splats and on the splats present as in the as-sprayed coating. There is no enlargement or propagation of crack or breaking of splats which are not observed in PSZ coatings after 50 cycles at 873 (Fig. 6.24a) and 1023 K (Fig. 6.24b). At a certain stress levels, cracks form between the already sprayed layers and freshly sprayed lamella (inter lamellar cracks) [42]. After 100 and 200 cycles crack propagation was clearly observed in the SEM study.

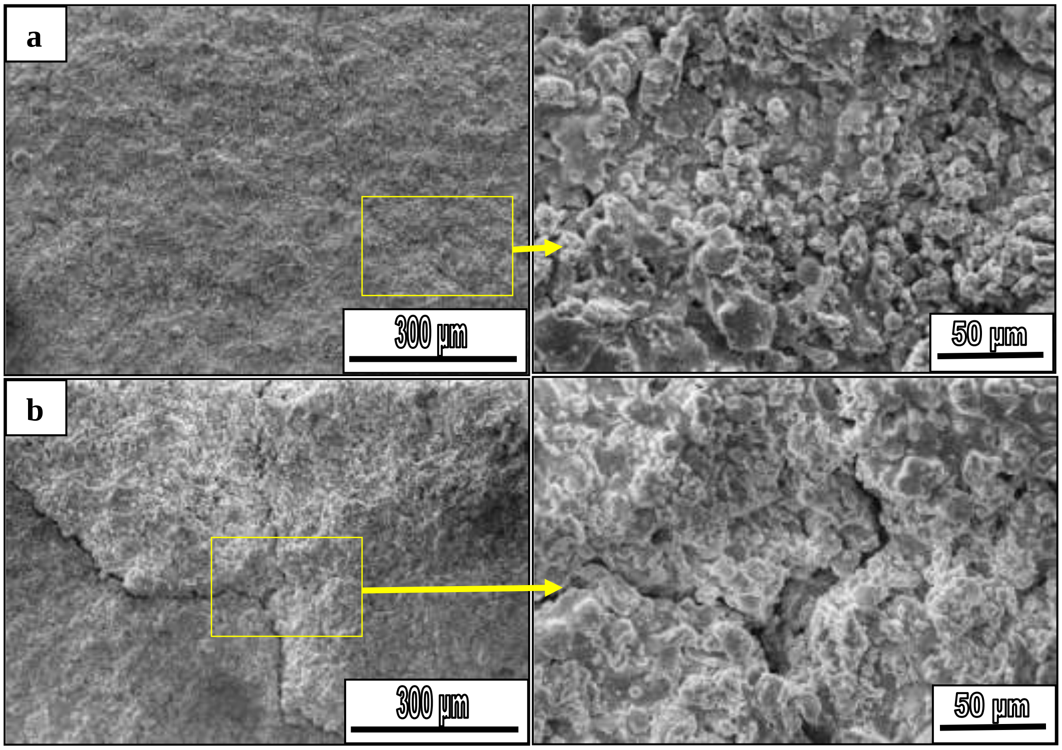

Fig. 6.25 Surface morphologies of PSZ coating after 100 cycles at (a) 873 and (b) 1023 K.

The microstructure of the PSZ coating after 100 cycles at 873 K (Fig. 6.25a) exhibited network of cracks generated on the surface which significantly propagated throughout the coating for samples tested at 1023 K (Fig. 6.25b). The surface morphology examined in SEM after thermal cycled for 200 cycles (Fig. 6.26) also exhibited segmented network of cracks in both the PSZ coatings tested at 873 and 1023 K. As compared to 873 K tested PSZ coatings, 1023 K tested coating showed deep cracking as observed at higher magnification in Figs. 6.25 and 6.26. Three different types of cracks can be observed in the plasma sprayed coatings subjected to thermal cycling and these can be defined as follows: (1) segmentation cracks (cracks running perpendicular to the coating surface and penetrating at least half the coating thickness); (2) branching cracks (cracks with the direction parallel to the coating plane, starting from segmentation cracks); (3) delamination cracks (oriented horizontal cracks occurring between individual splats or lamellae) [43].

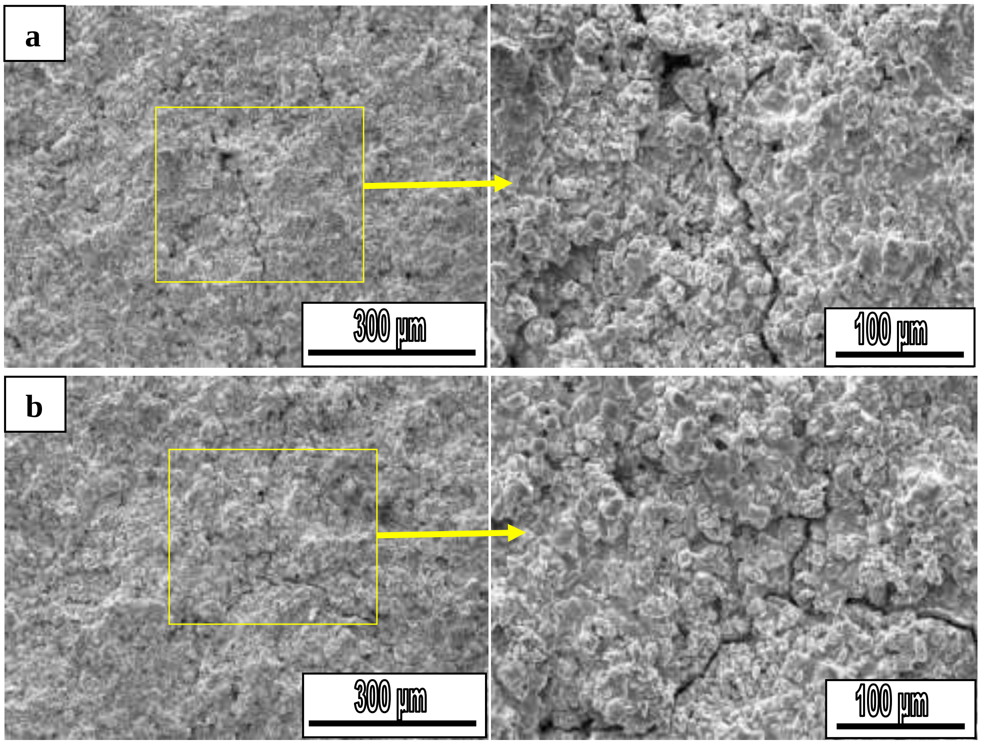

Fig. 6.26 Surface morphologies of PSZ coating after 200 cycles at (a) 873 and (b) 1023 K.

In case of 50 cycles tested PSZ coatings (Fig. 6.24) cracks are similar to the sprayed coating, but in case of 100 (Fig. 6.25) and 200 cycles (Fig. 6.26) tested PSZ coatings vertical cracks are observed in the thermal cycled PSZ coatings due to microcracking of splats during cooling. Two kinds of cracks observed in the 100 and 200 thermal cycled PSZ coatings are segmented cracks and branching cracks. Horizontal microrcaking lead to reduce thermal shock life [42,44] and these kind of delamination cracks are not observed in thermal cycled PSZ coatings up to 200 cycles. Once a single crack gets started, the crack encounters the stress fields associated with the geometrical arrays of cavities at most grain boundaries on the splats. Rapid crack link up takes place and macrocrack propagation occurs. The observed cracks on the surface of the coatings in SEM micrographs are microrcaks only and there was no macrocrack was observed visually on the PSZ coatings (Table 2). It was reported that catastrophic failure occurs at some stage when there was a transformation from the microcrack to a macrocrack network [18]. The interesting observation found in the present investigation was that with increase in thermal cycles the number of crack events were found increased in the coatings. Cracking and crack growth have been observed only in 100 and 200 cycles tested coatings.

Typical microstructures of as-deposited PSZ top coat with NiCrAlY bond coat by APS is shown in the backscattered electron image (BSEI) in Fig. 6.5. Porosity in the YSZ coating is considered advantageous for enhancing the coating life during thermal cycles [19]. The interlamellar porosity, resulting from poor adhesion between the splats, was evident. Porosity present in the coating and vertical microcracks generated during thermal cycling of the coatings gives the strain tolerance by lowering Young’s modulus of the coating [42,45]. Because of these features the coating will contain low stress values by stress relaxation process, without that features, the ceramic coating system would hardly able to withstand the stress levels arising during thermal cycling [42]. The primary failure modes observed in TBC systems subjected to the thermal cycling in oxidizing environment are: (i) cracking of the bond-coat/TGO at the interface; (ii) cracking within the top-coat; and (iii) linking of these microcracks by fracture of the TGO [46]. In the present study the crack was initiated in the top PSZ coating and was propagated within the coating perpendicular to the substrate and propagated to cracking of bond coat as shown in Fig. 6.27b. To identify the elemental composition variation X-ray elemental mapping (Fig. 6.27) was carried out. No variation in the elemental distribution was noticed and no thermally grown oxide at the bond coat region was observed. The change in the co-efficient of thermal expansion with temperature between substrate, bond coat and top ceramic coat also generate stresses near the interface during the thermal cycling studies. Due to thermal stresses generated by the temperature gradients, possibility exists to generate interface cracking. However, from cross-sectional microstructure (Fig. 6.27 and 6.28) analysis of PSZ coating thermal cycled for 200 cycles at 873 and 1023 K did not exhibit any microcracks at the HD graphite/NiCrAlY and NiCrAlY/PSZ interfaces. Crack was observed only in top coating due to the cracking of splats and it propagated through splats by breaking them. This indicated that up to 200 cycles at 873 and 1023 K the coating showed good adhesion to graphite substrate.

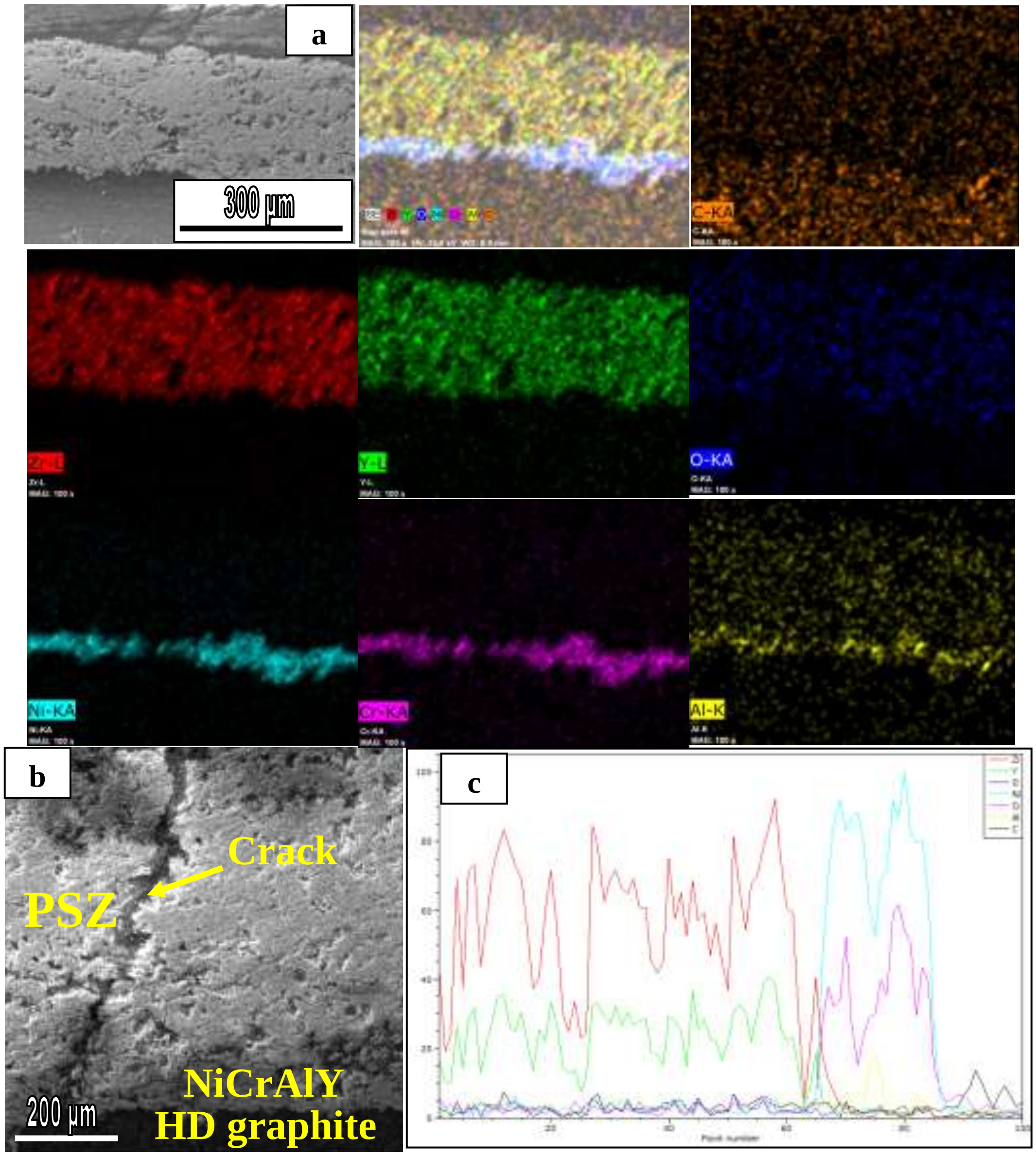

Fig. 6.27 (a) Cross-sectional SEM micrograph and X-ray elemental mapping, (b) generated crack and (c) line scan along the coating thickness of PSZ coating after 200 cycles at 873 K.

The PSZ coating contains two kinds of stresses: (i) compressive stress at ambient temperature when the coated substrate is heated during thermal cycling. (ii) At high temperature the compressive stresses become tensile stresses in the YSZ coating [47] and these stresses relieved by forming cracks in the coating (Fig. 6.27 and 6.28). The changes observed in the coatings are due to thermally induced changes only and there was no change in elemental composition was noticed. According to the literature, failure mechanisms of the thermal barrier PSZ coatings are closely associated with the oxidation of bond coat. In this study oxidation of the bond coat was not observed in elemental mapping or line scans carried out on tested PSZ coatings, because thermal cycling was carried out in vacuum to simulate the pyroprocessing plant conditions.

The generations of segmented cracks during thermal cycling studies will help to improve the life of coating by strain tolerance of the coating and increase the compliance of the coating. Many studies [43,48] reported that segmented crack densities generated in TBCs before or during the thermal cycling test improve in the thermal shock or thermal cycle resistance compared to the TBCs with low segmentation crack density or without segmentation cracks. The controlled porosity, internal microcracking and segmentation have been observed in the thermal cycled PSZ coatings gave enough strength to coating; to exhibit good resistance to thermal cycling up to 200 cycles and coating spallation was not observed at both the temperatures. YSZ coating did not spall-off due to the plastic flow and creep at high temperatures of metallic bond coat of NiCrAlY facilitate to relieve the thermal stresses significantly.

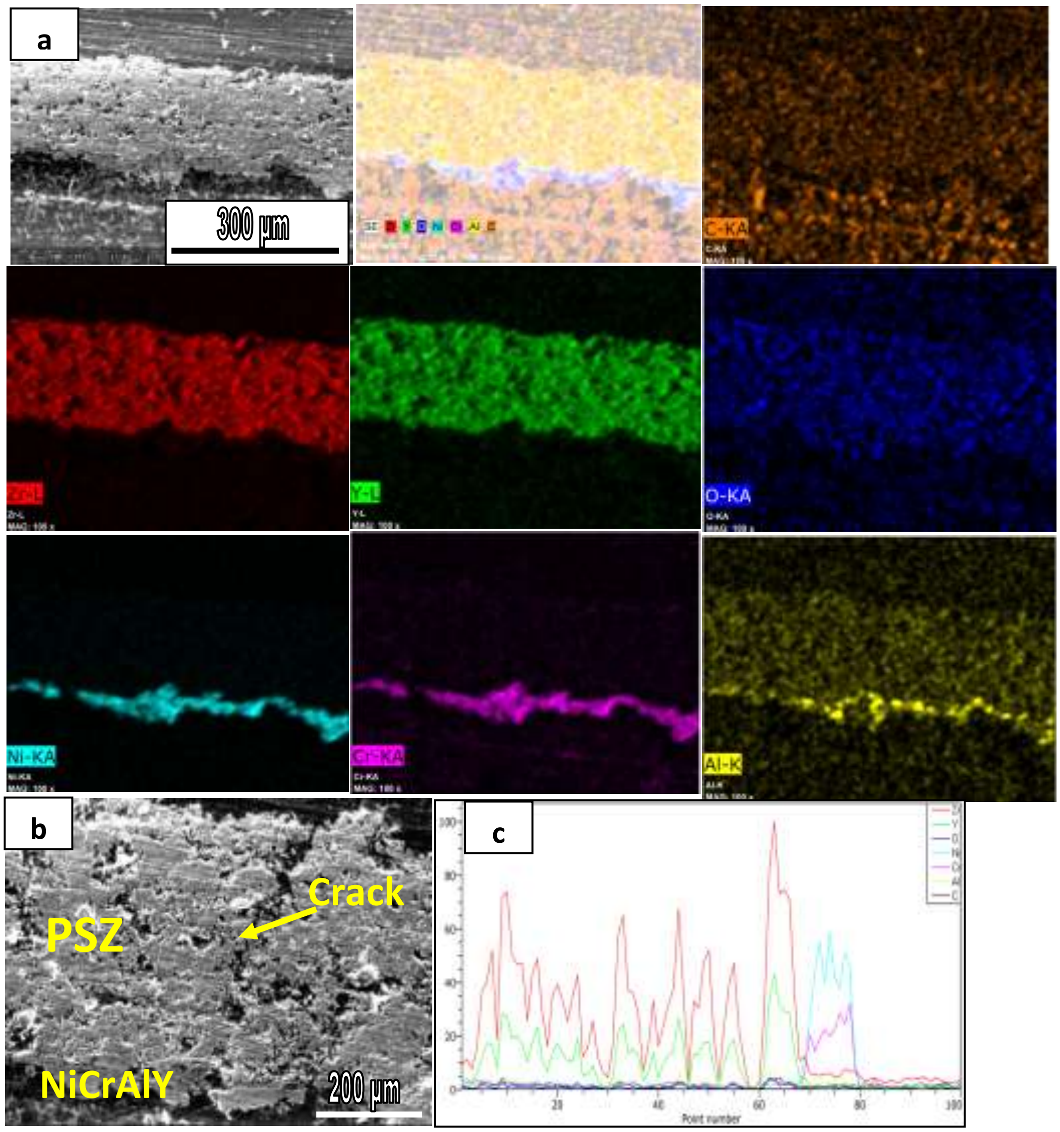

Fig. 6.28 (a) Cross-sectional SEM micrograph and X-ray elemental mapping, (b) generated crack and (c) line scan along the coating thickness of PSZ coating after 200 cycles at 1023 K.

6.3.3.4 Phase analysis of thermal cycled PSZ coatings

The diffraction patterns of thermal cycled PSZ coating at 873 and 1023 K for 50, 100 and 200 cycles are shown in Fig. 6.29a, b and c. All the thermal cycled PSZ coatings mostly consist of a nontransformable tetragonal (t′) phase along with cubic phase similar to the as-sprayed coating (Fig. 6.9a). In all three cases (50, 100 and 200 cycles) at two different temperatures it was observed that there was no phase change. It was pointed out from the diffraction patterns that difficult to resolve accurately the overlapping cubic and tetragonal phases in the XRD patterns because these are very similar and they are differentiated by the characteristic peak splitting of the tetranognal phases [3,49]. Monoclinic phase was not detected in any of the tested coatings for 50,100 and 200 thermal cycles. The t′ phase present in the thermal cycled PSZ coating will be highly beneficial because it gives excellent strength and crack toughness to the coating [3]. This is also one of the reasons for the coating having good thermal cycling resistance up to 200 cycles at 873 and 1023 K.

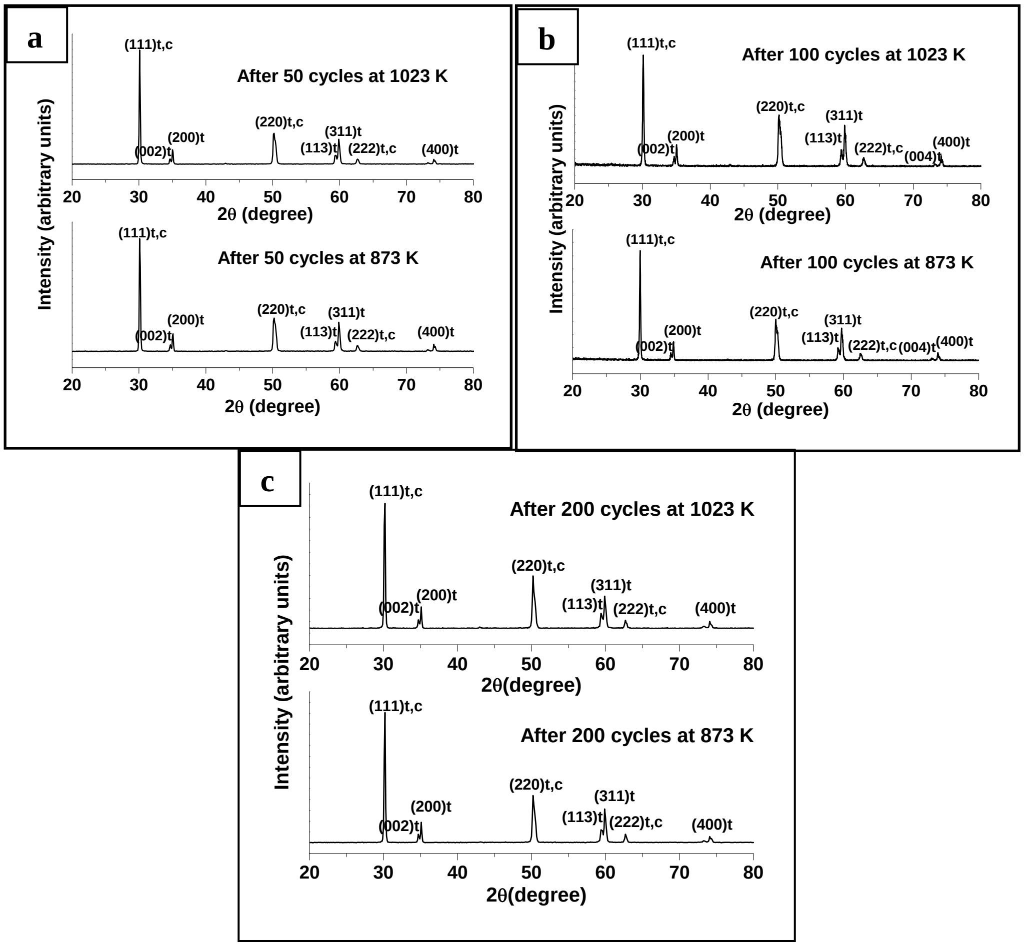

Fig. 6.29 XRD patterns of thermal cycles PSZ coatings at 873 and 1023 K after (a) 50, (b) 100 and (c) 200 cycles.

Raman spectra recorded from the surfaces of thermal cycled PSZ coatings after 200 cycles at 873 and 1023 K are shown in Fig. 6.30. Five bands observed in Raman spectra of all PSZ coatings and these five bands position (Table 1) confirms the presence of tetragonal zirconia present in the thermal cycled PSZ coatings similar to as-sprayed coating [50]. The peaks assignment was already discussed in Section 6.3.1.6. However, a minor shift in the peak position was observed due to the stresses in the thermal cycled PSZ coating. The segmented cracks formed in the coating observed in SEM indicated that stresses play a significant role in the thermal cycled samples. Due to these stresses Raman peaks were shifted from actual position to few wave numbers. This observation was in concurrence with the SEM analysis of the PSZ coating after thermal cycling. The temperatures of thermal cycling was carried are 873 and 1023 K. These temperatures are quite low for expecting phase change in YSZ system according to the phase diagram. Hence, the thermal cycling at these two temperatures not showed much marked effect on the stability of PSZ coatings up to 200 cycles. In general, the t′ phase transforms to the stable tetragonal phase (t) with low yttria content during the high temperature testing and subsequently to the monoclinic phase (m) during cooling to room temperature. The phase transformation of t to m is associated with a volume expansion of up to 5%. The volume expansion will deteriorate the integrity of PSZ topcoat and could hence cause the failure of coatings. Nevertheless, decomposition of t′ phase did not occur during thermal cycling studies. In the present investigation no phase transformation was observed up to 200 cycles at 873 and 1023 K in the XRD and Raman analysis. Therefore, it can be concluded that the absence of phase changes as evidenced in the present study did not cause any damage to the integrity of the PSZ coating system up to 200 cycles.

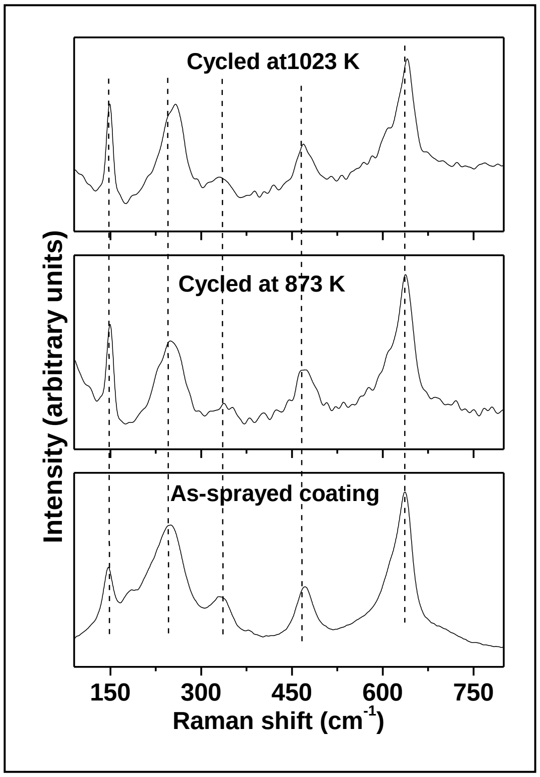

Fig. 6.30 Raman spectra of as-sprayed and thermal cycled PSZ coatings after 200 cycles at 873 K and 1023 K.

6.4 Summary

PSZ coatings were plasma sprayed on HD graphite with optimized process parameters and immersion tested in molten LiCl-KCl salt up to 2000 h under UHP argon atmosphere. PSZ coatings exhibited good corrosion resistance to molten LiCl-KCl salt even after 2000 h of exposure without spallation of coating and absence of phase transformation as evidenced in SEM-EDX and XRD analysis. Raman mapping of corrosion tested PSZ coatings for 250, 1000 and 2000 h results showed that as the exposure time increases the tetragonal phase intensity was decreased due to microstructural inhomogenities occurred in the coating after exposure. Molten uranium compatibility test with PSZ coatings at 1623 K proved that PSZ coating offer better stability and protection to HD graphite. Thermal cycling studies on PSZ coating at 873 and 1023 K up to 200 cycles did not show any failure of the coating and exhibited segmented cracks throughout the coating. Based on the results PSZ coating on HD graphite performed well in molten salt and uranium melting and no significant changes to the integrity of coating was observed. Hence, it can be considered as a best choice coating for these applications and can be evaluated further with large scale experiments.

References

[1] L.B. Chen, Surf. Rev. Lett. 13 (2006) 535–544.

[2] M. Takeuchi, T. Kato, K. Hanada, T. Koizumi, S. Aose, J. Phys. Chem. Solids 66 (2005) 521–525.

[3] R.L. Jones, Thermal barrier coatings, in: K.H. Stern (Ed.), Metallurgical and Ceramic Protective Coatings, Chapman and Hall, London, (1996), pp. 194–235.

[4] U. Kamachi Mudali, A. Ravi Shankar, S. Ningshen, Plasma sprayed thermal barrier coatings for molten chloride environment, Surface Modification Technologies XXV, T.S. Sudarshan, Per Nylen (Edts.,) VALAR Docs publications, 2012, pp. 235.

[5] N. Mesrati, H. Ajhrourh, N. Du, D. Treheux, J. Therm. Spray Technol. 9 (2000) 95–99.

[6] A. Ravi Shankar, U. Kamachi Mudali, R. Sole, H.S. Khatak, B. Raj, J. Nucl. Mater. 372 (2008) 226–232.

[7] A. Ravi Shankar, U. Kamachi Mudali, Mater. Corros. 59 (2008) 878–882.

[8] H.-Y. Lee, K.-H. Baik, Met. Mater. Int. 15 (2009) 783–787.

[9] S.-H. Cho, B.-H. Park, J.-M. Hur, H.-S. Lee, K.-C. Song, J.-H. Lee, Corros. Sci. 52 (2010) 2353–2364.

[10] J.C. Hamilton, A.S. Nagelberg, J. Am. Ceram. Soc. 67 (1984) 686–690.

[11] M.C. Mayoral, J.M. Andres, M.T. Bona, V. Higuera, F.J. Belzunce, Surf. Coat. Technol. 202 (2008) 5210–5216

[12] P.J. Treado and M.P. Nelson, in Handbook of vibrational spectroscopy, Edited J.M. Chalmers, P.R. Griffiths, John Wiley and sons Ltd. New York Vol.2 (2002), pp. 1429-1459.

[13] M. Bowden, G.D. Dickson, D.J. Gardiner and D.J. Wood, J. Mater. Sci. 28 (1993) 1031.

[14] A.M. Bolon, M.M. Gentleman, J. Am. Ceram. Soc. 94 (2011) 4478-4482.

[15] A. Paul, B. Vaidhyanathan, J. Binner, Adv. Appl. Ceram. 110 (2011) 114-119.

[16] U. Kamachi Mudali, A. Ravi Shankar, C. Mallika, K. Thyagarajan, S. Ningshen, B.P. Reddy and K. Nagarajan, Materials and Coating Technologies for Pyrochemical Reprocessing of Spent Metallic Fuel from Fast Breeder Reactors, Report: IGC/MMG/CSTG/2011. pp. 1–47.

[17] C.C. Berndt, H. Herman, Thin Solid Films 108 (1983) 427–437.

[18] C.C. Berndt, R.A. Miller, Thin Solid Films 119(1984) 173–184

[19] S.V. Joshi, M.P. Srivastava, Surf. Coat. Technol. 56 (1993) 215–224.

[20] V. Bernardet, S. Gomes, S. Delpeux, M. Dubois, K. Guerin, D. Avignant, G. Renaudin, L. Duclaux, J. Nucl. Mater. 384 (2009) 292–302.

[21] R.D. Kane, Molten salt corrosion, ASM Handbook, Volume 13A: Corrosion: Fundamentals, Testing, and Protection, S.D. Cramer, B.S. Covino, Jr., editors, pp. 216–219.

[22] V.A.C. Haanappel, T. Fransen, P.J. Gellings, High Temp. Mater. Processes 10 (1992) 67–90.

[23] G.R. Heath, P. Heimgartner, G. Irons, R. Miller, S. Gustafsson, Mater. Sci. Forum 251-254 (1997) 809–816.

[24] D.L. Porter, A.H. Heuer, J. Am. Ceram. Soc. 62 (1979) 298–305.

[25] C.H. Perry, D.W. Liu, R.P. Ingel, J. Am. Ceram. Soc. 68 (1985), C-184–C-187.

[26] P. Barberis, T. Merle-Mrjean, P. Quintard, J. Nucl. Mater. 246 (1997) 232–243.

[27] M. Ishigame, T. Sakurai, J. Am. Ceram. Soc. 60 (1977) 367-369.

[28] A. Ghosh, A.K. Suri, M. Pandey, S. Thomas, T.R. Rama Mohan, B.T. Rao, Materials Letters 60 (2006) 1170–1173.

[29] P.W. May, J.A. Smith, K.N. Rosser, Diamond Relat. Mater. 17 (2008) 199–203.

[30] B. Liang, C. Ding, H. Liao and C. Coddet, Surf. Coat. Technol. 200 (2006) 4549–4556.

[31] S. Ramya, R.P. George, R.V. Subba Rao and R.K. Dayal, Appl. Surf. Sci. 256 (2010) 5108–5115.

[32] C-h Cho, Y-s Lee, E-s Kim, J-g Kim, H-s Lee, J. Radioanal Nucl Chem 287 (2011) 485–490.

[33] N. Alangi, J. Mukherjee, P. Anupama, M.K. Verma, Y. Chakravarthy, P.V.A. Padmanabhan, A.K. Das, L.M. Gantayet, J. Nucl. Mater. 410 (2011) 39–45.

[34] P.V.A. Padmanabhan, S. Ramanathan, K.P. Sreekumar, R.U. Satpute, T.R.G. Kutty, M.R. Gonal, L.M. Gantayet, Mater. Chem. Phy. 106 (2007) 416–421.

[35] S. Kuroda, T.W. Clyne Thin Solid Films 200 (1991) 49–66.

[36] S. Kuroda, T. Dendo, S. Kitahara, J. Therm. Spray Technol. 4(1995) 75–84.

[37] E. Lugscheider, I. Kvernes, Thermal barrier coatings: powder spray process and coating technology, N.B. Dahotre, T.S. Sudarshan (Eds.), Intermetallic and Ceramic Coatings, Marcel Dekker Inc., New York/Basel (1999), pp. 267–306.

[38] J. Moon, H. Choi, H. Kim, C. Lee, Surf. Coat. Technol. 155 (2002) 1–10.

[39] ASTM E 2109-00 procedure A, test methods for determining area percentage porosity in thermal sprayed coatings.

[40] J.R. Davis and associates, Metallography Microstructure, Vol.9, ASM Handbook, ASM international, Materials Park, Ohio (2004) pp. 1038–1046.

[41] S. Sampath, X.Y Jiang, J Matejicek, A.C Leger, A. Vardelle, Mater. Sci. Eng. A 272 (1999) 181-188.

[42] R. Vaßen, F. Traeger, D. Stöver, J. Thermal Spray Technol. 13 (2004) 396–404.

[43] H.B. Guo, R. Vaßen, D. Stover, Surf. Coat. Technol. 192 (2005) 48–56.

[44] J. Wigren, J.-F. de Vries, D. Greving, Effects of Powder Morphology, Microstructure, and Residual Stresses on Thermal Barrier Coating Thermal Shock Performance, in Thermal Spray: Practical Solutions for Engineering Problems, C.C. Berndt, ed., ASM International, Materials Park, OH, 1996, pp. 855–861.

[45] J.A. Thompson, T.W. Clyne, Acta. Mater. 49 (2001) 1565–1575.

[46] K.W. Schlichting, N.P. Padture, E.H. Jordan, M. Gell, Mater. Sci. Eng. A 342 (2003) 120–130.

[47] G. McDonald, R.C. Hendricks, Effect of thermal cycling on ZrO_2-Y_2O_3 thermal barrier coatings, International conference on metallurgical coatings, San Diego, California, April (1980).

[48] H. Guo, H. Murakami, S. Kuroda, Mater. Trans. 47 (2006) 306–309.

[49] J.R. Brandon, R. Taylor, Surf. Coat. Technol. 46 (1991) 75–90.

[50] R. Srinivasan, M.B. Harris, S.F. Simpson, J. Mater. Res. 3 (1988) 787–797.

CHAPTER 7

CONCLUSIONS, SUMMARY AND SCOPE FOR FUTURE WORK

This Chapter provides important conclusions derived from the results of the investigations carried out on carbon materials and ceramic coatings developed on high density graphite for molten salt and uranium melting applications under pyroprocessing conditions. The corrosion behaviour of carbon materials and ceramic coatings in molten LiCl-KCl salt, the performance of ceramic coatings in uranium melting studies the thermal cycling behaviour of the investigated materials and detailed characterization of all the selected materials and coatings for the thesis work have been summarized in this Chapter. Apart from this, suggestions are provided for additional work to be continued in the near future for further evaluation of the performance of coatings at uranium melting temperatures and development of new coatings for such critical applications with better bond strength.

7.1 Conclusions

7.1.1 Corrosion Behaviour of Carbon Materials in Molten LiCl-KCl Salt

The major conclusions drawn from the study on the corrosion behaviour of carbon materials in molten LiCl-KCl salt up to 2000 h to understand their performance are the following:

1. Among the carbon materials low density graphite, high density graphite, glassy carbon and pyrolytic graphite excellent corrosion resistance was exhibited by pyrolytic graphite and glassy carbon when exposed to molten LiCl-KCl salt medium for 2000 h at 873 K under UHP argon atmosphere.

2. Morphology of carbon materials by SEM and AFM analysis revealed that the surface of low density graphite and high density graphite was severely attacked in molten LiCl-KCl salt due to the penetration and absorption of salt while the penetration of salt into glassy carbon and pyrolytic graphite was insignificant.
3. The as-deposited pyrolytic graphite exhibited a high preferred orientation along the (002) plane. The interlayer spacing (3.42 Å) and crystallite size (249.4 Å) indicated that pyrolytic graphite has a nearly ordered structure. Visual examination showed no surface attack on pyrolytic graphite and uniform attack was observed on the surfaces of low density graphite and high density graphite.
4. Leaching of carbon particles and surface degradation were absent in pyrolytic graphite exposed to molten LiCl–KCl salt. The study confirmed the excellent corrosion resistance of pyrolytic graphite in molten LiCl–KCl salt.
5. Pyrolytic graphite material/coating can be used for molten salt applications without any surface modification while high density graphite requires a protective ceramic coating on the surface.

Based on commercial availability and cost factor, high density graphite is preferred for plant applications. Corrosion of studies on high density graphite indicated that protective coating is essential on its surface to prevent its degradation in molten salt.For protecting high density graphite two types of ceramic coating materials were selected:

1. Alumina-40 wt% titania (A40T)
2. Yttria stabilized zirconia (YSZ)

7.1.2 Plasma Sprayed Alumina-40 wt% Titania (A40T) Coating on High Density Graphite

Following are the conclusions derived from the performance evaluation of "plasma sprayed alumina-40 wt% titania coating on high density graphite" in molten LiCl-KCl salt medium as well as in molten uranium and after thermal cycling studies.

1. Morphology of the as-sprayed A40T coating on high density graphite showed high surface roughness due to the formation of surface inhomogeneities. Molten salt corrosion experiments carried out at 873 K for various durations (500, 1000 and 2000 h) with and without bond coat under UHP argon atmosphere revealed that the coating was intact on the sample surface exposed up to 500 h, with the formation of cracks and salt deposits, while spallation of the coating occurred after 1000 and 2000 h exposure. XRD results indicated that phases present in the as-sprayed coating continued to be present in the spalled coating after corrosion test in molten salt for 1000 h.
2. A40T coating deposited along with the bond coat of Cr_3C_2-NiCr on high density graphite and exposed to molten LiCl-KCl salt at 873 K for 500 and 2000 h revealed that the top ceramic coat completely spalled off due to poor adhesion between the bond coat and A40T top coat and the bond coat subsequently got oxidized, as confirmed by the XRD and EDX analysis. Formation of porous chromium oxide from the chromium carbide bond coat which caused the spallation of top ceramic coating was evident from the microstructural characterization.
3. This study suggests that an improvement in A40T coating is required for better adhesion during long term exposure in molten salt. However, A40T coated on high

density graphite samples without bond coat and exposed only up to 500 h in molten salt showed good resistance to corrosion, as the coating did not spall off.

4. To improve the performance of A40T coating, post spray treatments were performed by vacuum annealing at 1373 K and pulsed laser melting. The lamellar morphology on the cross section of as-sprayed A40T coating got consolidated after laser melting. Annealed coatings did not show any major change in the microstructure, except agglomeration of unmelted particles and formation of clusters. It is evident that denser microstructure can be obtained by laser melting. The partially melted/unmelted regions present in the as-sprayed A40T coating were still present in vacuum annealed coatings, but they were completely eliminated in laser melted A40T coatings.
5. α-Al_2O_3 phase present in the starting material for coating was transformed into metastable γ-Al_2O_3 in the sprayed coating and was reverted to stable α-Al_2O_3 by post spray treatments. Laser melting coatings showed β-Al_2TiO_5 as the predominant phase when compared to the sprayed and vacuum annealed coatings. The reduction in average surface roughness (R_a) and increase in hardness implied that surface and microstructural modifications occurred in the laser melted A40T coatings.
6. The laser melted coatings exhibited improved corrosion resistance in molten LiCl-KCl salt medium at 873 K owing to their fully dense top layer, minimum defects and uniform distribution of the stable phases and their composition.
7. The molten salt corrosion of uncoated high density graphite, as-sprayed and laser melted A40T coatings on high density graphite was observed to follow the sequence: Un coated > as-sprayed A40T coating> laser melted coating with the power density 640 kW/cm^2 > laser remelted A40T coating with 800 kW/cm^2 powder density.

8. Laser melting of plasma sprayed coating is ideal for improving the surface homogeneity and for increasing the corrosion resistance of plasma sprayed A40T coatings in molten salt medium.
9. Computation of Gibb's free energy change for the reaction of U with Al_2O_3 and TiO_2 in the temperature range 300-2000 K indicated that Al_2O_3 and TiO_2 will be reduced by U to the respective metals. Uranium metal was adhered to the A40T coating surface after testing with molten uranium at 1623 K. The performance of A40T coating (with and without Cr_3C_2-NiCr bond coat) was not satisfactory in uranium melting experiments at 1623 K because of poor adhesion to graphite substrate, spallation as well as sticking of U metal on the coating layer.
10. Thermal cycling studies on A40T coated high density graphite with bond coat of Cr_3C_2-NiCr at 873 K under vacuum revealed failure of the top coating after 60 cycles due to thermal stress build up and brittle nature of Cr_3C_2-NiCr bond coat. The A40T coated sample without bond coat showed spllation of coating and exhibited graphite morphology after 80 thermal cycles.

7.1.3 Plasma Sprayed Partially Stabilized Zirconia (PSZ) Coating on High Density Graphite

Partially stabilized zirconia coating was developed using plasma spraying on high density graphite and its performance was evaluated after studying the corrosion behaviour in molten LiCl-KCl salt medium as well as in molten uranium and after the thermal cycling test. The conclusions drawn from this study are listed below:

1. Immersion studies performed on high density graphite and PSZ coated high density graphite in molten LiCl-KCl salt at 873 K under UHP argon for 250, 1000 and 2000 h

revealed that high density graphite had undergone degradation in molten salt while PSZ coated high density graphite showed weight gain due to deposition of salt on the exposed surface.

2. SEM micrographs of high density graphite showed severe attack with increase in exposure time due to penetration of salt through pores and subsequent removal of carbon particles into molten salt. Surface morphology of corrosion tested PSZ coatings for 250, 1000 and 2000 h confirmed the absence of degradation or attack on the surface of exposed coating to molten LiCl-KCl salt.
3. Cross section examination revealed that microcracks were formed at the interface between bond coat and high density graphite due to difference in thermal expansion coefficient. The influence of stable and beneficial non transformable tetragonal zirconia phase in the coating providing superior corrosion resistance to high density graphite was confirmed by XRD and Raman analysis. This study hinted that a suitable bond coat with near thermal expansion coefficient as that of the top YSZ coat is required to achieve good adhesion on high density graphite.
4. The average Raman spectra collected on the surface as a function of exposure time of PSZ coating showed only tetragonal phase of zirconia. Though there was variation in the intensity of tetragonal phase of zirconia as the exposure time increased, Raman imaging did not reveal any phase change up to 2000 h of exposure.
5. Computation of Gibb's free energy change for the reactions of U with ZrO_2 and Y_2O_3 in the temperature range 300-2000 K indicated that ZrO_2 and Y_2O_3 are chemically inert to uranium.

6. Visual examination revealed the change in colour from white to black when uranium was melted at 1623 K on YSZ coated high density graphite. Surface morphology of uranium melted PSZ coating was similar to that of as-sprayed coating; however, micro cracks were generated due to thermal stresses. Cross section SEM micrographs of the PSZ coated samples indicated good coating adherence on high density graphite.
7. PSZ coating maintained its integrity without any phase change in the coating after uranium melting at 1623 K and no reaction with uranium was apparent as inferred from SEM/EDX, XRD and Raman studies.
8. Plasma sprayed PSZ coatings on high density graphite were subjected to thermal cycling studies at 873 and 1023 K up to 200 cycles under vacuum. The microstructural analysis of PSZ coating tested for 50 cycles showed no evidence of modification of the structure. Morphological variations like generation of segmented cracks and propagation throughout the PSZ coating were observed in the coated samples subjected to 100 and 200 cycles. Cross-sectional micrographs confirmed crack network along the coating thickness after 200 cycles at 873 and 1023 K. However, elemental composition did not vary. Phase analysis by XRD and Raman revealed the presence of tetragonal phase alone in all the thermal cycled samples irrespective of temperature and number of cycles.

7.2 Summary

The salient features of the present thesis work on “Corrosion behaviour of carbon materials and development of ceramic coatings on graphite crucibles for molten salt based applications” by exposing them to molten salt and molten uranium at high temperature and characterizing them for corrosion attack and surface/cross-sectional morphology are summarized as follows:

Corrosion evaluation of the carbon materials low density graphite, high density graphite, GC and pyrolytic graphite exposed to molten LiCl-KCl salt for 2000 h at 873 K showed that the corrosion resistance of these carbon materials follows the order: low density graphite < high density graphite < GC < pyrolytic graphite. The adhesion strength of A40T coating on high density graphite substrate was poor under all the tested conditions i.e. in molten LiCl-KCl salt as well as in uranium melting test. To improve the performance of A40T coating, post spray treatments (vacuum annealing and laser melting) were carried out for surface modification and marginal improvement in corrosion resistance to molten salt was observed for laser melted plasma sprayed coating. Thermal cycling of A40T coating at 873 K resulted in the spallation of coating after 80 cycles due to thermal stress build up as well as brittle nature of Cr_3C_2-NiCr bond coat. Degradation of PSZ coating on high density graphite in molten salt test at 873 K was not significant. Uranium melting studies with PSZ coated high density graphite indicated that no reaction had occurred between uranium and PSZ coating at 1623 K, thereby upholding the choice of PSZ coated high density graphite crucible for cathode processor application. The PSZ coated high density graphite performed well even after thermal cycling at 873 and 1023 K upto 200 cycles. The delamination of A40T coatings from high density graphite after thermal cycling test was due to the poor adhesion strength. The results of the present investigation on the corrosion behavior of YSZ coatings in molten LiCl-KCl salt up to 2000 h and in uranium melting experiments gave the confidence for developing PSZ coating on engineering scale high density graphite crucibles by air plasma spray process. It is essential to demonstrate the performance of PSZ coating in uranium melting experiments in engineering scale using these PSZ coated high density graphite crucibles in order to consider them for plant applications and these tests are under way. Two such coated crucibles with different dimensions shown in Figs. 7.1a and b.

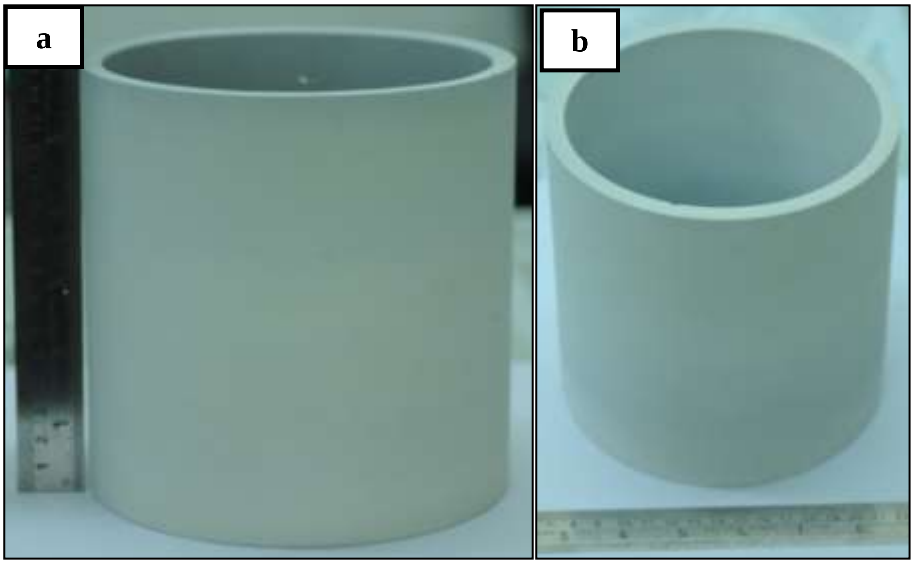

Fig. 7.1 PSZ coated engineering scale high density graphite crucibles with dimensions: (a) H x OD x ID = 150 x150 x 135 mm and (b) H x OD x ID = 100 x 100 x 85 mm.

These coated crucibles will be employed for the purification of uranium from the molten salt by melting at 1623 K in the cathode processing unit of pyrochemical reprocessing plant.

7.3 Scope for future work

1. Since, PSZ coating on high density graphite exposed to molten salt for 2000 h showed micro-cracks at the interface of bond coat/high density graphite due to thermal expansion mismatch, it is suggested that silicon carbide can be used as bond coat before spraying top ceramic coating and the performance may be evaluated in molten salt up to 2000 h.

2. In the present study, ceramic coated high density graphite samples were tested in molten chloride salt and molten uranium independently. Under actual plant conditions, these two environments prevail together. Hence it is essential to evaluate the combined effect of molten salt and uranium on ceramic coated high density graphite crucibles at and above 1573 K.
3. The present thesis work relied only on the morphological variations; phase analysis and thermal cycling up to the minimum requirement of 200 cycles at 873 and 1023 K for qualifying PSZ coatings developed on high density graphite for pyroreprocessing application. Based on the experience gained in this study, it is felt that mechanical properties of the coatings also contribute to adhesion strength in high temperature thermal cycling. Hence, attempts should be made to evaluate the adhesion strength etc. of the coatings according to the ASTM C633 test method as a function of temperature.
4. The performance of ceramic coated high density graphite (actual component) requires to be evaluated under the plant operating conditions in the range of 1273 -1700 K and in the combined presence of molten salt and uranium. Life prediction of the coated components may be tried by testing them in molten salt beyond 2000 h and until the coating delamination occurs completely.
5. As Y_2O_3 is thermodynamically more stable than ZrO_2 with uranium, development of Y_2O_3 coating on high density graphite and the coating performance in combined molten salt and uranium at 1623 K can be evaluated.
6. Nanostructured materials offer significant improvement in engineering properties based on the improvement in physical and mechanical properties compared to the present engineering materials. Outstanding properties have been observed in thermal-

sprayed coatings derived from nanostructured powders. Hence, nanostructured ceramic coatings can be developed on high density graphite with suitable bond coat for pyroreprocessing applications.

7. The results of the present study revealed that pyrolytic graphite in molten salt has superior corrosion resistance. Hence, pyrolytic graphite / pyrolytic carbon coating can be developed by chemical vapour deposition/chemical vapour infiltration on high density graphite and its detailed corrosion behaviour may be investigated for plant applications.